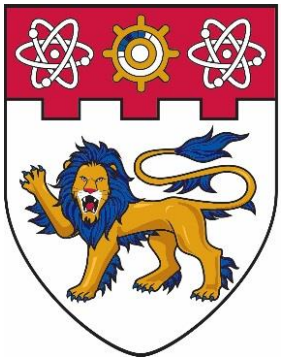

NANYANG TECHNOLOGICAL UNIVERSITY
SINGAPORE

3D MICROENVIRONMENTS FOR *IN VITRO* MODELING OF ALZHEIMER'S DISEASE

RANJAN VIVEK DAMODAR
Interdisciplinary Graduate School
NTU Institute for Health Technologies

2020

3D MICROENVIRONMENTS FOR *IN VITRO* MODELING OF ALZHEIMER'S DISEASE

RANJAN VIVEK DAMODAR

Interdisciplinary Graduate School
NTU Institute for Health Technologies

A thesis submitted to the Nanyang Technological University in partial fulfillment of the requirement for the degree of Doctor of Philosophy

2020

Statement of Originality

I hereby certify that the work embodied in this thesis is the result of original research, is free of plagiarised materials, and has not been submitted for a higher degree to any other University or Institution.

25/08/2020

. . . . . .
Date

. . . . . .
Ranjan Vivek Damodar

Supervisor Declaration Statement

I have reviewed the content and presentation style of this thesis and declare it is free of plagiarism and of sufficient grammatical clarity to be examined. To the best of my knowledge, the research and writing are those of the candidate except as acknowledged in the Author Attribution Statement. I confirm that the investigations were conducted in accord with the ethics, policies and integrity standards of Nanyang Technological University and that the research data are presented honestly and without prejudice.

25/08/2020

. . . . . .
Date

. . . . . .
Assoc Prof. Huang Weimin

Authorship Attribution Statement

This thesis contains material from 4 papers published in the following peer-reviewed journals in which I am listed as an author.

Chapter 2 is published as **Ranjan, V. D.**, Qiu, L., Tan, E. K., Zeng, L., & Zhang, Y. (2018). Modelling Alzheimer's disease: Insights from *in vivo* to *in vitro* three-dimensional culture platforms. *J Tissue Eng Regen Med*, 12(9), 1944-1958. DOI: 10.1002/term.2728

The contributions of the co-authors are as follows:

- Asst Prof. Zhang Yilei and Assoc Prof. Zeng Li provided the initial direction to write the review and edited the manuscript.
- I prepared the manuscript drafts and revised the same after discussions with Dr. Qiu Lifeng, Asst Prof. Zhang Yilei and Assoc Prof. Zeng Li.
- Asst Prof. Zhang Yilei, Assoc Prof. Zeng Li and Prof. Eng King Tan provided valuable suggestions and insights to improve the quality of the review.

Chapter 3 is published as Chen, X., **Ranjan, V. D.**, Liu, S., Hu, S., & Zhang, Y. (2021). *In situ* formation of 3D conductive and cell-laden graphene hydrogel for electrically regulating cellular behaviour. *Macromolecular Bioscience* (2021) 202000374. DOI: 10.1002/mabi.202000374

The contributions of the co-authors are as follows:

- Dr. Chen Xuelong and I conceived and designed the study (co-first author).
- Dr. Chen Xuelong fabricated the graphene oxide hydrogel-based samples.

- Dr. Chen Xuelong carried out the material characterization analysis with assistance from Dr. Liu Sijun.
- I carried out the cell culture experiments, electrical stimulation experiments, data analysis, immunocytochemistry and confocal microscopy.
- Dr. Chen Xuelong and I prepared the manuscript drafts and revised the same after discussions with other co-authors.
- Asst Prof. Zhang Yilei and Prof. Hu Xiao oversaw the whole project and provided valuable insights to improve the quality of the manuscript.

Chapter 4 is published as **Ranjan, V. D.**, Zeng, P., Li, B., & Zhang, Y. (2020). *In vitro* cell culture in hollow microfibers with porous structures. *Biomaterials Science*, 8(8), 2175-2188. DOI: 10.1039/C9BM01986C

The contributions of the co-authors are as follows:

- Asst Prof. Zhang Yilei and I conceived and designed the study.
- Peiqin Zeng and Boyuan Li carried out the fabrication process and performed DOE for optimizing the parameters with my assistance.
- I carried out the cell culture experiments, performed imaging and analysed the data together with Peiqin Zeng and Boyuan Li.
- I prepared the manuscript drafts and revised the same after discussions with Asst Prof. Zhang Yilei .
- Asst Prof. Zhang Yilei oversaw the whole project and provided valuable insights to improve the quality of the manuscript.

Chapters 5 and **6** are published as **Ranjan, V. D.**, Qiu, L., Lee, J. W.-L., Chen, X., Jang, S. E., Chou, C., Lim, K. L., Tan, E.-K., Zhang, Y., Huang, W. M., & Zeng, L.

(2020). A microfiber scaffold-based 3D *in vitro* human neuronal culture model of Alzheimer's disease. *Biomaterials Science*. DOI: 10.1039/D0BM00833H

The contributions of the co-authors are as follows:

- Dr. Qiu Lifeng, Asst Prof. Zhang Yilei, Assoc Prof. Weimin Huang, Assoc Prof. Li Zeng and I conceived and designed the study.
- Dr. Qiu Lifeng, Jolene Wei-Ling Lee, Dr. Chai Chou and I performed the cell-culture experiments, immunocytochemistry, confocal microscopy and gene expression analysis.
- I fabricated the 3D electrospun microfiber scaffolds, performed the material characterization, data analysis and scanning electron microscopy.
- Dr. Chen Xuelong performed the XPS characterization.
- I prepared the manuscript drafts and revised the same after discussions with Dr. Qiu Lifeng, Dr. Jang Se Eun, Asst Prof. Zhang Yilei, Assoc Prof. Weimin Huang, Prof. Lim Kah Leong, Prof. Eng King Tan and Assoc Prof. Zeng Li.
- Asst Prof. Zhang Yilei and Assoc Prof. Zeng Li oversaw the whole project and provided valuable insights to improve the quality of the manuscript.

25/08/2020

. . . . . .
Date

. . . . . .
Ranjan Vivek Damodar

Acknowledgements

It gives me great pleasure at this point to acknowledge and thank the people who have been involved throughout the course of my studies and research.

First and foremost, I would like to express my sincere gratitude to my supervisor **Assoc Prof. Huang Weimin** and my co-supervisor **Assoc Prof. Zeng Li** for their invaluable mentorship, friendly advice and motivation throughout my research.

I am grateful to my TAC members **Assoc Prof. Scott Rice** and **Prof. Tan Eng King** for their guidance and encouragement.

I would like to thank **Asst Prof. Zhang Yilei**, **Dr. Qiu Lifeng, Dr. Chen Xuelong**, **Dr. Shreyas Kuddannaya and Ms. Jolene Lee** for their constant support, training and assistance which have been invaluable in giving me a comfortable start. They helped me learn the basics of my research domain, without which I might have had a challenging time.

I would also like to thank my parents, friends and family members for their love, support and encouragement during this long academic endeavour.

Finally, I would like to acknowledge the Interdisciplinary Graduate School, HealthTech NTU and the Neural Stem Cell Research Laboratory, National Neuroscience Institute (NNI) for the necessary financial and technical support required for my research.

Table of Contents

Abstract

Alzheimer's disease (AD) has become increasingly prevalent owing to the rise in aging population, heightening life-expectancy, and lack of effective treatments. Understanding AD pathogenesis requires the development and study of model systems which can ideally mirror all aspects of the disease. Increasing evidence indicates the superiority of three-dimensional (3D) *in vitro* cell culture platforms over conventionally used two-dimensional (2D) monolayer cultures in mimicking native *in vivo* microenvironments. However, existing 3D culture models of AD rely on engineered cell lines which overexpress mutant genes or aggregate-based cultures with heterogeneities in composition, biological properties and cell differentiation stages. These limitations motivate exploration of alternative *in vitro* substrate-based human neuronal AD models with better reproducibility and matrix uniformity.

In this study, tissue engineering techniques are leveraged on for fabrication of three novel biomaterial-based scaffolding platforms for achieving *in vitro* 3D neuronal culture. These include: a graphene oxide hydrogel-based electroconductive substrate fabricated via physical crosslinking; a synthetic polymer-based hollow microfiber substrate fabricated via core-shell electrospinning; and a synthetic polymer-based, non-woven fibrillar substrate fabricated via wet electrospinning. All three platforms were evaluated in terms of cell encapsulation, distribution, viability, proliferation, neuronal differentiation and neurite formation to determine their feasibility for facilitating long-term 3D neuronal culture. Data from immunocytochemistry clearly indicate wet electrospun, non-woven poly(lactic-co-glycolic acid) (PLGA) microtopographic scaffolds to be the most suitable substrate in terms of design criteria encompassing both physical and biological properties. The highly porous fibrillar scaffolds supported enhanced infiltration, uniform distribution and long-

term survival of human stem cell-derived neurons. In addition, the microfiber scaffold stiffness was found to mimic the elasticity of native brain tissue, indicating its capability to promote realistic physiological responses in cellular phenotypes.

Next, key neural stem cell features including proliferation and differentiation in 3D culture were compared with Petri dish-based 2D monolayer controls. The 3D fibrillar microenvironment reduced cell proliferation and significantly accelerated both neuronal and glial differentiation within seven days of culture. Finally, the scaffolds were interfaced with familial AD (FAD) patient induced pluripotent stem cells (iPSC)-derived neurons for *in vitro* modeling of early-stage AD pathogenesis. The differentiated neurons in 3D PLGA scaffold-based culture exhibited significant amplification in pathogenic amyloid-beta 42 (Aβ42) and phospho-tau (p-tau) levels between diseased and age-matched controls. Furthermore, spontaneous expression levels of these pathogenic markers in 3D culture were more pronounced compared with corresponding 2D monolayer control cultures.

Taken together, the present findings represent the first demonstration of interfacing 3D synthetic polymer-based fibrillar scaffolds with iPSC-derived human neuronal cultures to robustly recapitulate and accelerate early-stage AD pathogenesis. Moreover, it serves as a simple, standardisable and easy to implement *in vitro* platform, which facilitates highly efficient neuronal differentiation and significantly faster maturation compared with conventional monolayer cultures. This platform can be further broadened for modeling of other complex neurodegenerative diseases as well as evaluation of prospective therapeutic candidates.

List of Figures

List of Tables

List of Abbreviations

2D	Two-dimensional
3D	Three-dimensional
AD	Alzheimer's disease
aGSK-3β	Active glycogen synthase kinase-3β
ANOVA	Analysis of variance
APOE	Apolipoprotein E
APP	Amyloid precursor protein
Aβ	Amyloid-β
Aβ42	Amyloid-beta 42
BACE1	β-secretase
BFCNs	Basal forebrain cholinergic neurons
BSA	Bovine serum albumin
BSC	Biosafety cabinet
CC3	Cleaved caspase 3
CRISPR	Clustered regularly interspaced short palindromic repeats
DAPI	Diamidino-2-phenylindole dihydrochloride
DI	Deionized
DMEM	Dulbecco's Modified Eagle Medium
DMF	Dimethylformamide
DOE	Design of experiments
DS	Down syndrome
EB	Embryonic body
ECM	Extracellular matrix
ELISA	Enzyme-linked immunosorbent assay
ER	Endoplasmic reticulum
ES	Electrical simulation
FACS	Fluorescence-activated cell sorting
FAD	Familial AD
FBS	Fetal bovine serum
FE-SEM	Field emission scanning electron microscopy

FTD	Frontotemporal dementia
FTIR	Fourier transform infrared spectroscopy
GO	Graphene oxide
hESC	Human embryonic stem cells
hMSC	Human mesenchymal stem cells
hNPC	Human neural precursor cells
HTS	High-throughput screening
iPSC	Induced pluripotent stem cells
lt-NES	long-term self-renewing Neuroepithelial stem cells
MAP2	Microtubule-associated protein 2
MIPC	Multi-interfacial polyelectrolyte complexation
NaCl	Sodium chloride
NFTs	Neurofibrillary tangles
NGF	Nerve growth factor
NHP	Non-human primates
NPC	Neural progenitor cell
NSC	Neural stem cell
PAni	Polyaniline
PBS	Phosphate buffered saline
PC12	Pheochromocytoma 12
PCLF	Polycaprolactone fumarate
PDA	Polydopamine
PDL	Poly-d-lysine
PEO	Polyethylene oxide
PEGDA	Poly(ethylene glycol) diacrylate
PGD	Pre-implantation genetic diagnostic
PLCL	Poly(l-lactide-co-ε-caprolactone)
PLGA	Poly(lactic-co-glycolic acid)
PLLA	Poly(l-lactic acid)
PLO	Poly-l-ornithine
PPy	Polypyrrole
PSEN1	Presenilin 1

PSEN2	Presenilin 2
p-tau	Phospho-tau
PVA	Polyvinyl alcohol
ReN	ReNcell VM
rGO	Reduced graphene oxide
rGO-PDA	PDA functionalized rGO
ROI	Region of interest
RTPCR	Reverse transcription polymerase chain reaction
SAD	Sporadic AD
SD	Standard deviation
SEM	Scanning electron microscopy
TALENs	Transcription activator-like effector nucleases
TUNEL	Terminal deoxynucleotidyl transferase tdt-mediated dutp nick end labeling
UV	Ultraviolet
XPS	X-ray photoelectron spectroscopy

List of Publications

1. **V.D. Ranjan**, L. Qiu, E.K. Tan, L. Zeng, Y. Zhang, Modelling Alzheimer's disease: Insights from *in vivo* to *in vitro* three-dimensional culture platforms, J Tissue Eng Regen Med 12(9) (2018) 1944-1958.
2. **V.D. Ranjan**, P. Zeng, B. Li, Y. Zhang, *In vitro* cell culture in hollow microfibers with porous structures, Biomaterials Science 8(8) (2020) 2175-2188.
3. **V.D. Ranjan**, L. Qiu, J.W.-L. Lee, X. Chen, S.E. Jang, C. Chai, K.-L. Lim, E.-K. Tan, Y. Zhang, W.M. Huang, L. Zeng, A microfiber scaffold-based 3D in vitro human neuronal culture model of Alzheimer's disease, Biomaterials Science 8 (17) (2020) 4861-4874.
4. X. Chen, **V.D. Ranjan**, S. Liu, X. Hu, Y. Zhang, In situ formation of 3D conductive and cell-laden graphene hydrogel for electrically regulating cellular behavior, Macromolecular Bioscience (2021) 202000374.
5. Y. Wu, **V.D. Ranjan**, Y. Zhang, A Living 3D *In Vitro* Neuronal Network Cultured Inside Hollow Electrospun Microfibers, Advanced Biosystems 2(5) (2018) 1700218.
6. X. Chen, Y. Wu, **V.D. Ranjan**, Y. Zhang, Three-dimensional electrical conductive scaffold from biomaterial-based carbon microfiber sponge with bioinspired coating for cell proliferation and differentiation, Carbon 134 (2018) 174-182.
7. Y. Wu, Y. Peng, H. Bohra, J. Zou, **V.D. Ranjan**, Y. Zhang, Q. Zhang, M. Wang, Photoconductive Micro/Nanoscale Interfaces of a Semiconducting

Polymer for Wireless Stimulation of Neuron-Like Cells, ACS applied materials & interfaces 11(5) (2019) 4833-4841.

8. S. Sreejith, R. Kishor, A. Abbas, R. Thomas, T. Yeo, **V.D. Ranjan**, R. Vaidyanathan, Y.P. Seah, B. Xing, Z. Wang, L. Zeng, Y. Zheng, C.T. Lim, Nanomechanical Microfluidic Mixing and Rapid Labeling of Silica Nanoparticles using Allenamide-Thiol Covalent Linkage for Bioimaging, ACS applied materials & interfaces 11(5) (2019) 4867-4875.

Conference Abstract

1. **V.D. Ranjan**, L. Qiu, E.-K. Tan, Y. Zhang, W.M. Huang, L. Zeng, Design & Development of a 3D *in vitro* Model for Alzheimer's Disease, eCM Online Periodical, 2019, Collection 2; ScSB Conference Abstracts (page 13)

CHAPTER 1 Introduction

1.1 Background

Alzheimer's disease (AD) presently occupies the topmost position among the most commonly diagnosed neurodegenerative diseases worldwide with the number of affected people forecasted to reach 100 million by 2050 [1]. According to the latest statistics, nearly 44 million people in the world suffer from AD or a related dementia [2], with only one in four being diagnosed [3]. AD also ranks first among the most frequently observed causes of dementia in Singapore [4]. It is characterized by progressive memory loss, inability to perform activities of daily life, and culminates in total impairment of cognitive functions [5]. Multiple risk factors linked to both genetic and environmental origins have been implicated in the emergence of AD, with advancing age being identified as the most significant among them [6]. Besides its multifactorial and heterogeneous nature, AD is progressive i.e. the symptoms gradually worsen with the passage of years. The average clinical duration ranges between eight and ten years, typically extending over 20 years including both preclinical and prodromal stages [7].

Basic and clinical research conducted over the last few decades has made substantial progress in unraveling the molecular basis and clinical course of AD, including its salient pathological features; nevertheless, AD pathogenesis is not fully understood and presently has no cure available, except for palliative treatments which offer relief from some symptoms. The key to understanding aetiology lies in developing effective models which should ideally recapitulate all aspects of the disease. Furthermore, high inaccessibility to the human brain makes it desirable to study neuronal function and degeneration on appropriate model systems of brain cultures closely mimicking *in vivo* conditions. Over the years, a plethora of techniques

including *in vivo* and *in vitro* platforms have been utilized for developing disease models of AD (**Figure 1-1**). They have proven beneficial in interpreting several aspects of AD and have also helped in developing potential diagnostic and therapeutic measures [8].

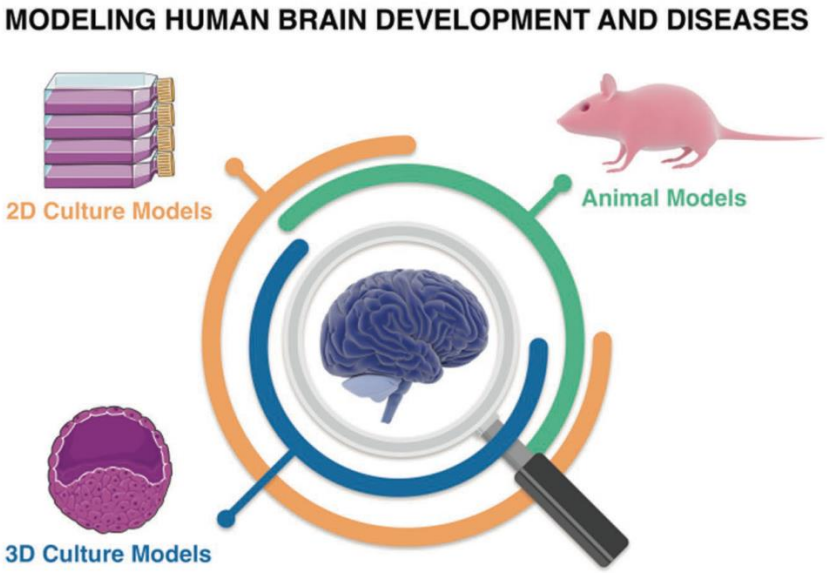

Figure 1-1. Schematic representation of modeling the human brain development and its diseases (Adapted from [9])

Research into AD pathogenesis has predominantly focused on either animal models or on two-dimensional (2D) *in vitro* cell culture systems. Although both approaches have provided valuable insights into AD aetiology, neither has fully reproduced all the pathological events observed in human AD patients [10]. Animal models based mainly on transgenic mice were unsuccessful owing to fundamental biological differences between rodent and human brains [11, 12]. Despite providing the required complexity, they are incapable of accurately recapitulating human AD pathophysiology. On the other hand, Petri dish-based 2D monolayer human neuronal cultures fail at mimicking the complexity of the human brain including its unique features [13, 14]. They are unable to emulate the spatial organization and complex cell-cell interactions present inside native extracellular matrix (ECM), and force

cells in culture to adapt to flat, rigid plastic or glass surfaces [15]. Moreover, a growing body of evidence indicates that 2D monolayer cultures do not have the same morphology [16], proliferation [17], migration [18], gene expression [19] or differentiation [20] observed in *in vivo* conditions. This has prompted the development of three-dimensional (3D) culture platforms to overcome aforementioned limitations as well as strike a balance between experimental tractability and physiological relevance (**Figure 1-2**) in biological model systems for disease modeling applications.

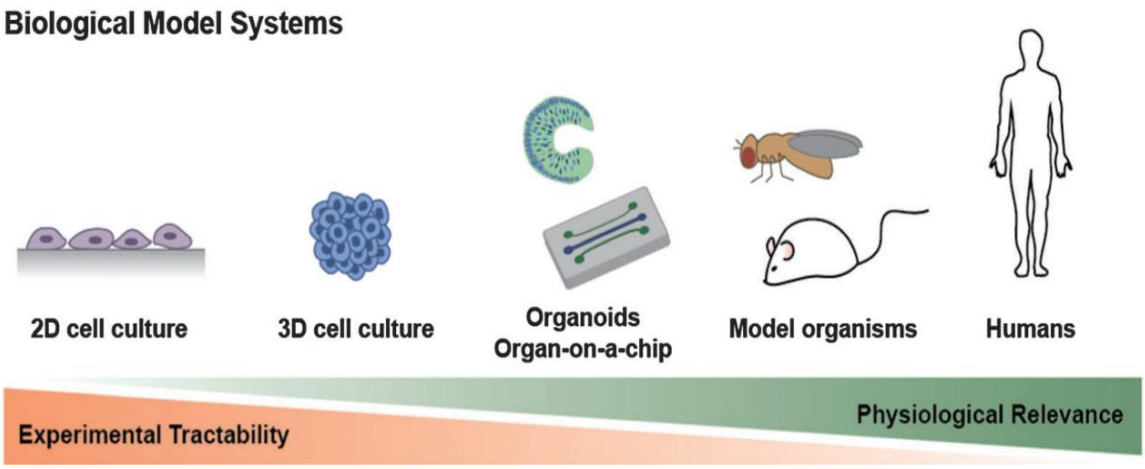

Figure 1-2. Spectrum of biological model systems used in disease modeling applications (Adapted from [21])

These state-of-the-art 3D human cell culture models of AD hold great promise as a novel platform for studying disease mechanisms in a human brain-like environment including high-throughput screening (HTS) of potential drug candidates. A 3D microenvironment affects the shape, polarity and motility of cells, which in turn can translate into several secondary tissue-specific consequences. Not only are they more representative of *in vivo* environments, they also are highly customizable and can be tailored to have a range of properties depending on the application.

1.2 Research gap and Motivation

Combining tissue engineering techniques with stem cell technologies has spurred the development of novel 3D neuronal culture platforms recapitulating key AD pathogenic hallmarks such as amyloid-β (Aβ) plaques and phospho tau (p-tau) accumulation. Researchers have utilized both scaffold-free and scaffold-based techniques to create 3D *in vitro* disease models of AD. The former relies on self-organization of AD patient-derived induced pluripotent stem cells (iPSCs) into 3D brain organoids or neuro-spheroids [22-24]. However, organoid growth typically stalls after few months due to lack of vascularization [25], causing low diffusion of oxygen, essential nutrients and metabolites to inner regions resulting in cell death and necrotic cores [26]. Moreover, the self-organizing nature of organoids renders them difficult to control and reproduce, leading to variable cell microenvironments depending on depth from the surface [27]. On the other hand, scaffold-based approaches have mainly relied on encapsulating immortalized ReNcell VM (ReN) human neural progenitor cells (hNPCs) inside a Matrigel matrix [28-30]. Accelerated neuronal differentiation, neuron–glia interactions, Aβ deposition and p-tau aggregation were achieved using this platform [29, 30]. However, these studies artificially elevated AD pathologies via gene manipulation and used engineered cell lines which is not representative of early stage pathogenesis observed in the AD human brain [28]. Moreover, Matrigel is animal-derived and composed of a heterogenous and ill-defined mixture of complex proteins [10, 31]. These limitations motivate exploration of alternative synthetic biomaterial-based substrates with better reproducibility and matrix uniformity for *in vitro* modeling of AD. The development of such a platform would not only provide a more accurate picture, but also help bridge research gaps encountered in former approaches.

1.3 Objectives and Scope

The overall goal of this thesis is to develop a proof-of-concept *in vitro* microenvironment facilitating 3D neuronal culture for modeling early-stage AD pathogenesis. The specific objectives and scope of this study are mentioned below:

1. To perform a comprehensive literature review of existing models of AD to understand design criteria and identify research gap.
    - Study the genesis, evolution and significance of the principal approaches utilized for modeling AD and compare their advantages and limitations.
    - Review state-of-the-art 2D and 3D *in vitro* models of AD and identify the key challenges faced in terms of material and functionality.
2. To fabricate *in vitro* substrates facilitating 3D neuronal culture and evaluate their functionality based on the design criteria.
    - Fabrication and characterization of novel, tuneable and scalable substrates capable of supporting 3D neuronal culture.
    - Characterization of cell encapsulation, distribution, viability, proliferation, neuronal differentiation and neurite formation.
3. To utilize the most suitable substrate for 3D culture of human stem cell-derived neurons for assessing recapitulation of early-stage AD pathologies.
    - Characterization and comparison of neural stem cell (NSC) proliferation and neuronal/glial differentiation with 2D monolayer controls.
    - Characterization and comparison of Aβ and p-tau AD pathologies in 3D FAD neuronal culture with non-demented as well as 2D monolayer controls.

1.4 Novelty and Significance

3D *in vitro* modeling of neurodegenerative diseases is currently in its infant stages. Existing scaffold-based models of AD utilize thin hydrogel matrices to bring about the third dimension, and rely on manipulating gene expression in immortalized cell lines for robust recapitulation of disease pathologies [10]. Although this approach has served as a starting point for 3D *in vitro* studies into AD pathogenesis, they fail at physiologically mirroring the disease progression observed in the human AD brain. This necessitates further exploration into state-of-the-art tissue engineering techniques in conjunction with patient-derived iPSC technologies for creating more precise 3D human neuronal culture models of AD.

In this regard, we developed three separate, novel biomaterial-based scaffolding platforms for achieving 3D cellular culture, each approach specifically aimed at supporting neuronal differentiation and long-term neuronal culture. These include: a graphene oxide hydrogel-based electroconductive substrate; a synthetic polymer-based, hollow microfiber substrate fabricated via core-shell electrospinning; and a synthetic polymer-based, non-woven, wet-electrospun fibrillar substrate. The first two techniques involve direct fabrication of cell-scaffold structure, where cell encapsulation is achieved as and when the scaffold is produced. In contrast, the third technique requires passive cell seeding as the scaffold is fabricated separately, thereby providing greater leeway for surface functionalization of the substrate.

Firstly, we evaluate all three platforms in terms of cell encapsulation, distribution, viability, proliferation, neuronal differentiation and neurite formation to determine the most suitable substrate for facilitating 3D neuronal culture. Next, we interface this substrate with human stem cell-derived neural progenitor cells (NPC) to compare key cellular phenotypes including viability, proliferation and neuronal/glial

differentiation in 3D culture with conventional 2D monolayer controls. Lastly, we investigate whether 3D culture enhances pathogenic Aβ42 and p-tau levels in differentiated neurons carrying familial AD (FAD) mutations, compared with age-matched healthy controls. Furthermore, the results have been compared with Petri dish-based 2D monolayer cultures to establish the advantages offered by a 3D microenvironment in terms of expression of neuronal markers as well as recapitulation of key disease phenotypes.

Overall, we present a simple, standardisable, scalable and easy to implement 3D culture platform to facilitate highly efficient neuronal differentiation, accelerated maturation and robust recapitulation of disease phenotypes. Although electrospun scaffolds have widely been used in neural tissue engineering platforms [32-34], the present findings represent the first description of interfacing polymer-based fibrillar scaffolds with FAD patient iPSC-derived neurons so as to robustly recapitulate and accelerate early-stage AD pathogenesis. The scaffolds are optimized to have a large pore size and porosity, allowing deeper cellular infiltration and uniform distribution from the seeding surface compared with most existing platforms where cell infiltration mostly ranges between 200-800 μm [35-37]. The stiffness of the fibrous substrate was comparable with the elasticity of brain tissue which plays a significant role in promoting realistic physiological responses for regulation of cell fate, survival and growth *in vitro* [38].

This platform can also be broadened to model other complex neurodegenerative diseases including evaluation and characterization of prospective therapeutic candidates. It could be also be utilized in *in vivo* transplantation studies to generate differentiated cells for regenerative medicine applications.

1.5 Organization of thesis

The structure of the thesis is as illustrated below (**Figure 1-3**) and is divided into seven chapters, based on the progression of my research as described below.

Chapter 1 gives some background into AD modeling and briefly describes the various platforms utilized to study disease pathogenesis. Next, the limitations of current 3D *in vitro* models are discussed along with potential merits of using biomaterial-based substrates in addressing these issues. In addition, the objectives and scope of the work are outlined including its novelty and significance. Finally, an overview of the thesis structure is provided along with a brief outline of the constituent chapters.

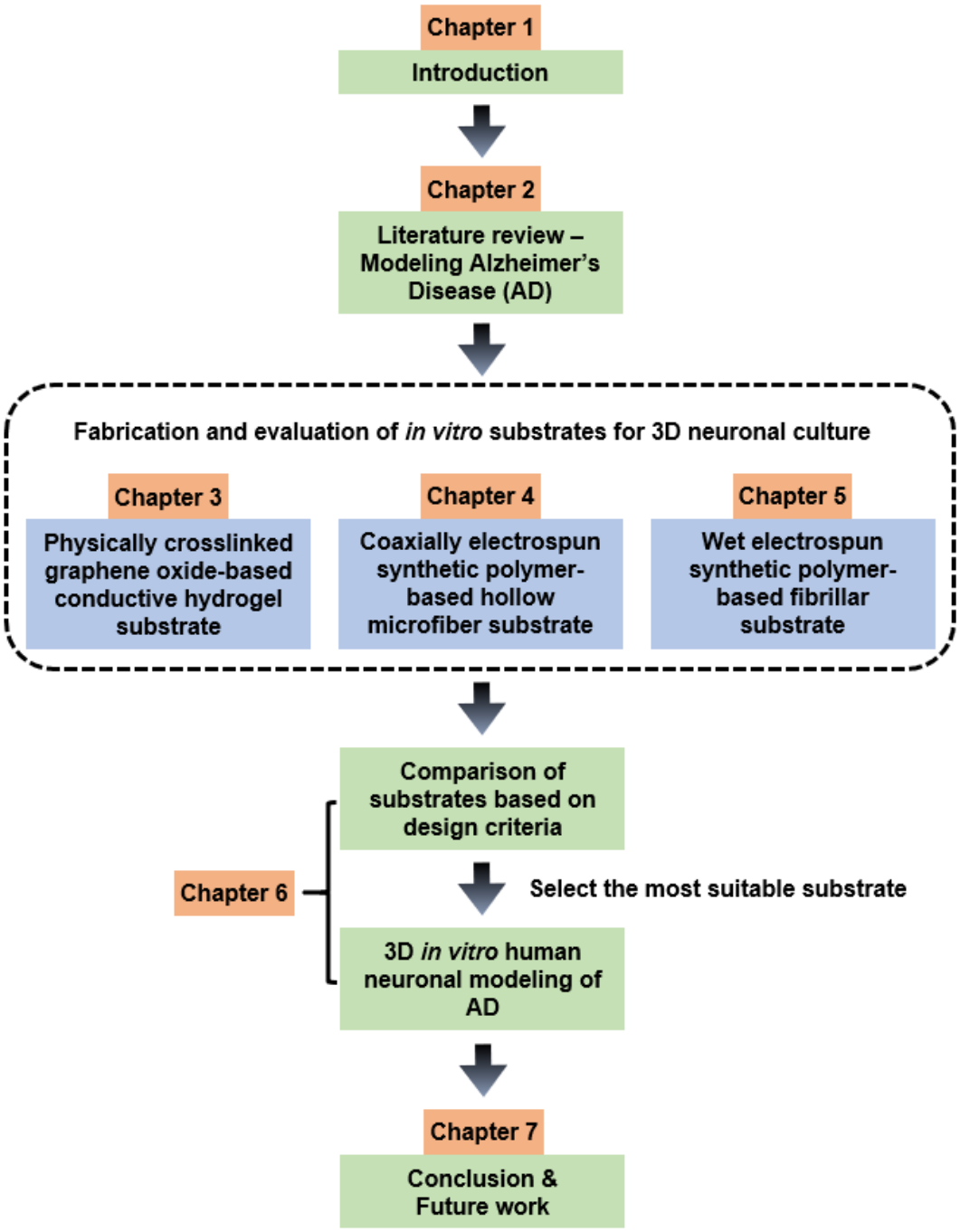

Figure 1-3. Schematic of thesis outline.

Chapter 2 delves into the genesis, evolution and significance of the principal approaches utilized for modeling AD. An extensive analysis of state-of-the-art 2D and 3D *in vitro* models of AD is provided along with the challenges and limitations faced in their application. Furthermore, strategies to mitigate these issues were

identified and potential advantages of our proposed 3D platform have been highlighted.

Chapters 3-5 are themed topic chapters describing the development and characterization of three separate, novel biomaterial-based scaffolding platforms for achieving 3D cellular culture, each approach specifically aimed at supporting neuronal differentiation and long-term neuronal culture. These include: a graphene oxide hydrogel-based electroconductive substrate; a synthetic polymer-based hollow microfiber substrate fabricated via core-shell electrospinning; and a synthetic polymer-based, non-woven, wet-electrospun fibrillar substrate. The platforms are evaluated in terms of cell encapsulation, cell viability and neuronal differentiation.

Chapter 6 is divided into 2 key sections. The first section involves the comparison of all the above-mentioned substrates in terms of meeting the scaffold design criteria (both physical and biological properties). In the next section, only the most suitable substrate among the 3 platforms which best satisfies all requirements is picked for application in human neuronal modeling of AD. In this case, the wet-electrospun microfiber substrate was clearly the most optimum platform for supporting 3D neuronal culture and was therefore selected for *in vitro* modeling of AD. Human embryonic stem-cell (hESC) derived neural progenitors were encapsulated within the substrate for assessment of cell viability, proliferation and neuronal differentiation. Finally, the substrate was interfaced with FAD patient iPSC-derived neurons to determine, compare and study the expression levels of key AD pathological hallmarks in 3D culture with conventional 2D monolayer controls.

Chapter 7 provides a summary of the key inferences drawn from **Chapters 3-6** and outlines the major findings of this study in line with the proposed objectives. In

addition, the key limitations of the study along with recommendations for future work are discussed based on the outcomes and learnings of the project.

References

[1] R. Brookmeyer, E. Johnson, K. Ziegler-Graham, H.M. Arrighi, Forecasting the global burden of Alzheimer's disease, Alzheimers Dement 3(3) (2007) 186-91.

[2] Alzheimer's Statistics, 2017. http://www.alzheimers.net/resources/alzheimers-statistics/.

[3] B.T. Hyman, C.H. Phelps, T.G. Beach, E.H. Bigio, N.J. Cairns, M.C. Carrillo, D.W. Dickson, C. Duyckaerts, M.P. Frosch, E. Masliah, S.S. Mirra, P.T. Nelson, J.A. Schneider, D.R. Thal, B. Thies, J.Q. Trojanowski, H.V. Vinters, T.J. Montine, National Institute on Aging-Alzheimer's Association guidelines for the neuropathologic assessment of Alzheimer's disease, Alzheimers Dement 8(1) (2012) 1-13.

[4] Parkinson Disease and Movement Disorders, 2017. https://www.nni.com.sg/PatientsandVisitors/Conditions-Treatments/Pages/Parkinson-Disease-and-Movement-Disorders.aspx.

[5] L. Bertram, R.E. Tanzi, Thirty years of Alzheimer's disease genetics: the implications of systematic meta-analyses, Nature Reviews Neuroscience 9(10) (2008) 768-778.

[6] Alzheimer's & Dementia Risk Factors | Alzheimer's Association, (2017).

[7] C.L. Masters, R. Bateman, K. Blennow, C.C. Rowe, R.A. Sperling, J.L. Cummings, Alzheimer's disease, Nature Reviews Disease Primers 1(1) (2015) 15056.

[8] K.H. Benam, S. Dauth, B. Hassell, A. Herland, A. Jain, K.J. Jang, K. Karalis, H.J. Kim, L. MacQueen, R. Mahmoodian, S. Musah, Y.S. Torisawa, A.D. van der Meer, R. Villenave, M. Yadid, K.K. Parker, D.E. Ingber, Engineered in vitro disease models, Annu Rev Pathol 10 (2015) 195-262.

[9] M. Jorfi, C. D'Avanzo, D.Y. Kim, D. Irimia, Three-Dimensional Models of the Human Brain Development and Diseases, Adv Healthc Mater 7(1) (2018).

[10] S.H. Choi, Y.H. Kim, L. Quinti, R.E. Tanzi, D.Y. Kim, 3D culture models of Alzheimer's disease: a road map to a "cure-in-a-dish", Mol Neurodegener 11(1) (2016) 75.

[11] S.E. Cavanaugh, Animal models of Alzheimer disease: historical pitfalls and a path forward, Altex 31(3) (2014) 279-302.

[12] M. Sarasa, P. Pesini, Natural non-trasgenic animal models for research in Alzheimer's disease, Current Alzheimer research 6(2) (2009) 171-8.
[13] M.A. Israel, S.H. Yuan, C. Bardy, S.M. Reyna, Y. Mu, C. Herrera, M.P. Hefferan, S. Van Gorp, K.L. Nazor, F.S. Boscolo, C.T. Carson, L.C. Laurent, M. Marsala, F.H. Gage, A.M. Remes, E.H. Koo, L.S. Goldstein, Probing sporadic and familial Alzheimer's disease using induced pluripotent stem cells, Nature 482(7384) (2012) 216-20.
[14] T. Yagi, D. Ito, Y. Okada, W. Akamatsu, Y. Nihei, T. Yoshizaki, S. Yamanaka, H. Okano, N. Suzuki, Modeling familial Alzheimer's disease with induced pluripotent stem cells, Hum Mol Genet 20(23) (2011) 4530-9.
[15] C. D'Avanzo, J. Aronson, Y.H. Kim, S.H. Choi, R.E. Tanzi, D.Y. Kim, Alzheimer's in 3D culture: challenges and perspectives, Bioessays 37(10) (2015) 1139-48.
[16] E. Cukierman, R. Pankov, D.R. Stevens, K.M. Yamada, Taking cell-matrix adhesions to the third dimension, Science (New York, N.Y.) 294(5547) (2001) 1708-12.
[17] M. Hindié, M. Vayssade, M. Dufresne, S. Quéant, R. Warocquier-Clérout, G. Legeay, P. Vigneron, V. Olivier, J.L. Duval, M.D. Nagel, Interactions of B16F10 melanoma cells aggregated on a cellulose substrate, Journal of Cellular Biochemistry 99(1) (2006) 96-104.
[18] P. Friedl, K.S. Zänker, E.-B. Bröcker, Cell migration strategies in 3-D extracellular matrix: Differences in morphology, cell matrix interactions, and integrin function, Microscopy Research and Technique 43(5) (1998) 369-378.
[19] A. Birgersdotter, R. Sandberg, I. Ernberg, Gene expression perturbation in vitro—A growing case for three-dimensional (3D) culture systems, Seminars in Cancer Biology 15(5) (2005) 405-412.
[20] T.-H. Chun, K.B. Hotary, F. Sabeh, A.R. Saltiel, E.D. Allen, S.J. Weiss, A Pericellular Collagenase Directs the 3-Dimensional Development of White Adipose Tissue, Cell 125(3) (2006) 577-591.
[21] E.L. Jackson, H. Lu, Three-dimensional models for studying development and disease: moving on from organisms to organs-on-a-chip and organoids, Integrative Biology 8(6) (2016) 672-683.
[22] H.K. Lee, C. Velazquez Sanchez, M. Chen, P.J. Morin, J.M. Wells, E.B. Hanlon, W. Xia, Three Dimensional Human Neuro-Spheroid Model of Alzheimer's Disease

Based on Differentiated Induced Pluripotent Stem Cells, PLoS One 11(9) (2016) e0163072.
[23] W.K. Raja, A.E. Mungenast, Y.T. Lin, T. Ko, F. Abdurrob, J. Seo, L.H. Tsai, Self-Organizing 3D Human Neural Tissue Derived from Induced Pluripotent Stem Cells Recapitulate Alzheimer's Disease Phenotypes, PLoS One 11(9) (2016) e0161969.
[24] M. Jorfi, C. D'Avanzo, R.E. Tanzi, D.Y. Kim, D. Irimia, Human Neurospheroid Arrays for In Vitro Studies of Alzheimer's Disease, Sci Rep 8(1) (2018) 2450.
[25] M.A. Lancaster, J.A. Knoblich, Generation of cerebral organoids from human pluripotent stem cells, Nat Protoc 9(10) (2014) 2329-40.
[26] H. Wang, Modeling Neurological Diseases With Human Brain Organoids, Front Synaptic Neurosci 10 (2018) 15-15.
[27] F. Yu, W. Hunziker, D. Choudhury, Engineering Microfluidic Organoid-on-a-Chip Platforms, Micromachines (Basel) 10(3) (2019) 165.
[28] Y.H. Kim, S.H. Choi, C. D'Avanzo, M. Hebisch, C. Sliwinski, E. Bylykbashi, K.J. Washicosky, J.B. Klee, O. Brustle, R.E. Tanzi, D.Y. Kim, A 3D human neural cell culture system for modeling Alzheimer's disease, Nat Protoc 10(7) (2015) 985-1006.
[29] J. Park, I. Wetzel, I. Marriott, D. Dréau, C. D'Avanzo, D.Y. Kim, R.E. Tanzi, H. Cho, A 3D human triculture system modeling neurodegeneration and neuroinflammation in Alzheimer's disease, Nature Neuroscience 21(7) (2018) 941-951.
[30] S.H. Choi, Y.H. Kim, M. Hebisch, C. Sliwinski, S. Lee, C. D'Avanzo, H. Chen, B. Hooli, C. Asselin, J. Muffat, J.B. Klee, C. Zhang, B.J. Wainger, M. Peitz, D.M. Kovacs, C.J. Woolf, S.L. Wagner, R.E. Tanzi, D.Y. Kim, A three-dimensional human neural cell culture model of Alzheimer's disease, Nature 515(7526) (2014) 274-8.
[31] Y. Fang, R.M. Eglen, Three-Dimensional Cell Cultures in Drug Discovery and Development, SLAS Discov 22(5) (2017) 456-472.
[32] J.I. Kim, T.I. Hwang, L.E. Aguilar, C.H. Park, C.S. Kim, A Controlled Design of Aligned and Random Nanofibers for 3D Bi-functionalized Nerve Conduits Fabricated via a Novel Electrospinning Set-up, Scientific Reports 6(1) (2016) 23761.
[33] M. Kim, G. Kim, Highly porous electrospun 3D polycaprolactone/β-TCP biocomposites for tissue regeneration, Materials Letters 120 (2014) 246-250.

[34] Y.-S. Lee, T. Livingston Arinzeh, Electrospun Nanofibrous Materials for Neural Tissue Engineering, Polymers 3(1) (2011) 413-426.
[35] J. Wu, Y. Hong, Enhancing cell infiltration of electrospun fibrous scaffolds in tissue regeneration, Bioactive Materials 1(1) (2016) 56-64.
[36] Q.L. Loh, C. Choong, Three-Dimensional Scaffolds for Tissue Engineering Applications: Role of Porosity and Pore Size, Tissue Engineering Part B: Reviews 19(6) (2013) 485-502.
[37] D. Zhang, M. Pekkanen-Mattila, M. Shahsavani, A. Falk, A.I. Teixeira, A. Herland, A 3D Alzheimer's disease culture model and the induction of P21-activated kinase mediated sensing in iPSC derived neurons, Biomaterials 35(5) (2014) 1420-8.
[38] K. Saha, A.J. Keung, E.F. Irwin, Y. Li, L. Little, D.V. Schaffer, K.E. Healy, Substrate modulus directs neural stem cell behavior, Biophysical journal 95(9) (2008) 4426-38.

CHAPTER 2 Literature review

The work presented in **Chapter 2** is largely based on the following publication: Vivek Damodar Ranjan, Lifeng Qiu, Eng King Tan, Li Zeng, Yilei Zhang. "Modelling Alzheimer's disease: Insights from *in vivo* to *in vitro* three-dimensional culture platforms." *J Tissue Eng Regen Med* 12, no. 9 (Sep 2018): 1944-58. http://dx.doi.org/10.1002/term.2728.

2.1 Overview of Alzheimer's Disease

AD can either be familial (usually early-onset) or sporadic (usually late-onset) in nature. Familial forms of AD (FAD) normally occur within 60-65 years of age, are not very prevalent (<10 percent), and are inherited in an autosomal-dominant fashion [1, 2]. FAD can be caused by any among over 200 mutations [3] in the following three genes i.e. amyloid precursor protein (APP), presenilin 1 (PSEN1), or presenilin 2 (PSEN2) genes [4, 5]. Despite its low frequency of occurrence, FAD has helped researchers in identifying and analyzing several important pathogenetic avenues associated with the disease [2]. Sporadic AD (SAD) is the more frequently occurring form of the disease (> 90 percent), its origin being difficult to pinpoint owing to the multiple genetic and environmental risk factors governing it [1, 5]. Unlike the familial form of the disease, SAD does not exhibit autosomal dominant inheritance, and a high risk for developing the latter has been associated with the inheritance of the ε4 allele of the apolipoprotein E (APOE) [6, 7].

The principal pathological hallmarks of AD include neuronal cell death, synapse loss, neuroinflammation, oxidative stress, senile plaques (amyloid/neuritic plaques), and neurofibrillary tangles (NFTs) [2, 8]. The senile plaques are extracellular amyloid filaments composed of peptides (36-43 amino acids in length) called

amyloid-beta (Aβ), which in turn are the products of a larger protein i.e. amyloid precursor protein (APP), formed as a result of its sequential proteolytic cleavages by the proteases, β-secretase (BACE1) and γ-secretase [9]. The γ-secretase generates Aβ42 (42 amino acids in length) which is particularly important in AD pathogenesis owing to its tendency to form insoluble toxic fibrils, which make up the amyloid plaques [1]. NFTs are composed of highly phosphorylated forms of the microtubule-associated highly soluble protein tau [10], which accumulates within the cell body and dendrites as a result of the imbalance between phosphatases and activities of protein kinases [5].

The presence of these abnormal, insoluble protein deposits constituting extracellular amyloid plaques and intracellular p-tau tangles have led to the development of two alternate hypotheses propounding the mechanism of AD, which differ mainly on the primary causative factor of the disease. Recent research mostly supports the amyloid cascade hypothesis where Aβ is argued to trigger pathogenesis, with tau functioning downstream. In contrast, the tau hypothesis states that abnormal phosphorylation of tau is the initiating factor of the disease, and is based on the lack of correlation between Aβ deposition and neuronal loss [11]. Lately, the amyloid hypothesis has been revised with greater emphasis being given to soluble Aβ oligomers, which have been identified to be more neurotoxic compared with the later-stage insoluble plaques. This toxicity of these oligomers is assumed to result from their innate misfolded nature, as they present the cellular environment with chemical groups, usually inaccessible under normal physiological circumstances [12, 13]. AD pathogenesis is not completely understood despite decades of research; nevertheless, substantial progress has been made in unraveling the molecular basis of the disease including certain key pathological features as elucidated previously. Since it is not

feasible to conduct experimental investigations directly on humans, several disease modeling approaches have been developed over the years to help recapitulate events underlying the emergence and progression of AD [14].

2.2 Modeling Alzheimer's disease

There are three primary approaches for modeling diseases including AD i.e. *in vivo*, *in vitro* and *in silico* methods as shown in **Figure 2-1**. *In vivo* approaches refer to studies performed using animals as model organisms, whereas *in vitro* approaches involve 2D/3D culture of cells outside of the living organism, usually in a dish. *In silico* approaches make use of computational methods and simulations to recreate cellular models of the disease outside of a laboratory setting [15].

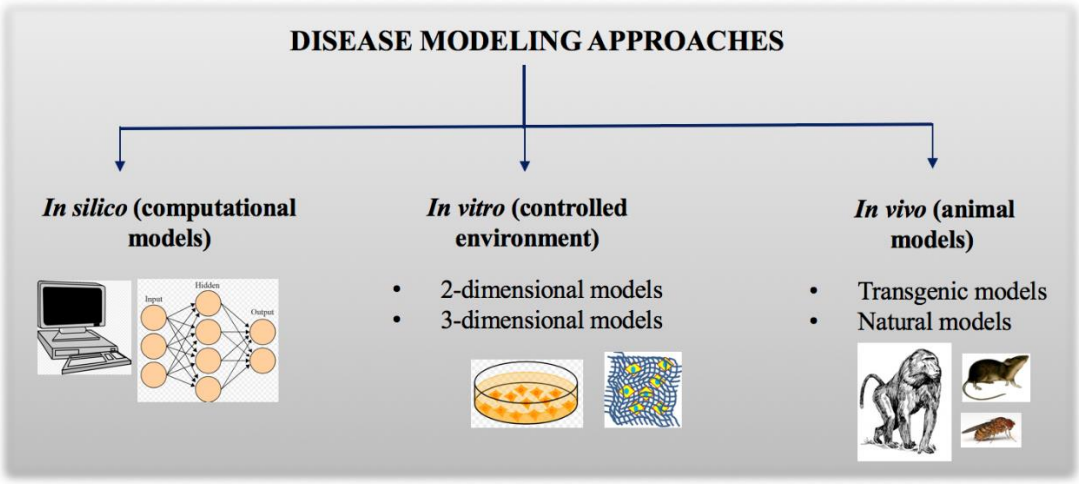

Figure 2-1. Current approaches utilized in modeling AD (Adapted from [16]).

Animal models of AD were the first to provide critical insights into the pathological events involved in disease progression. The next avenue explored by researchers focused on 2D *in vitro* adherent neuronal culture models involving attachment of cells on flat, stiff, functionalized synthetic surfaces [17, 18]. Over the last decade, research has advanced into 3D culture systems to bridge the gaps left by former approaches. In terms of imitating native *in vivo* microenvironments, 3D culture

platforms in combination with tissue engineering techniques are believed to be superior to monolayer based 2D cultures [19, 20]. **Figure 2-2** illustrates the temporal evolution of modeling approaches deployed by researchers for modeling AD.

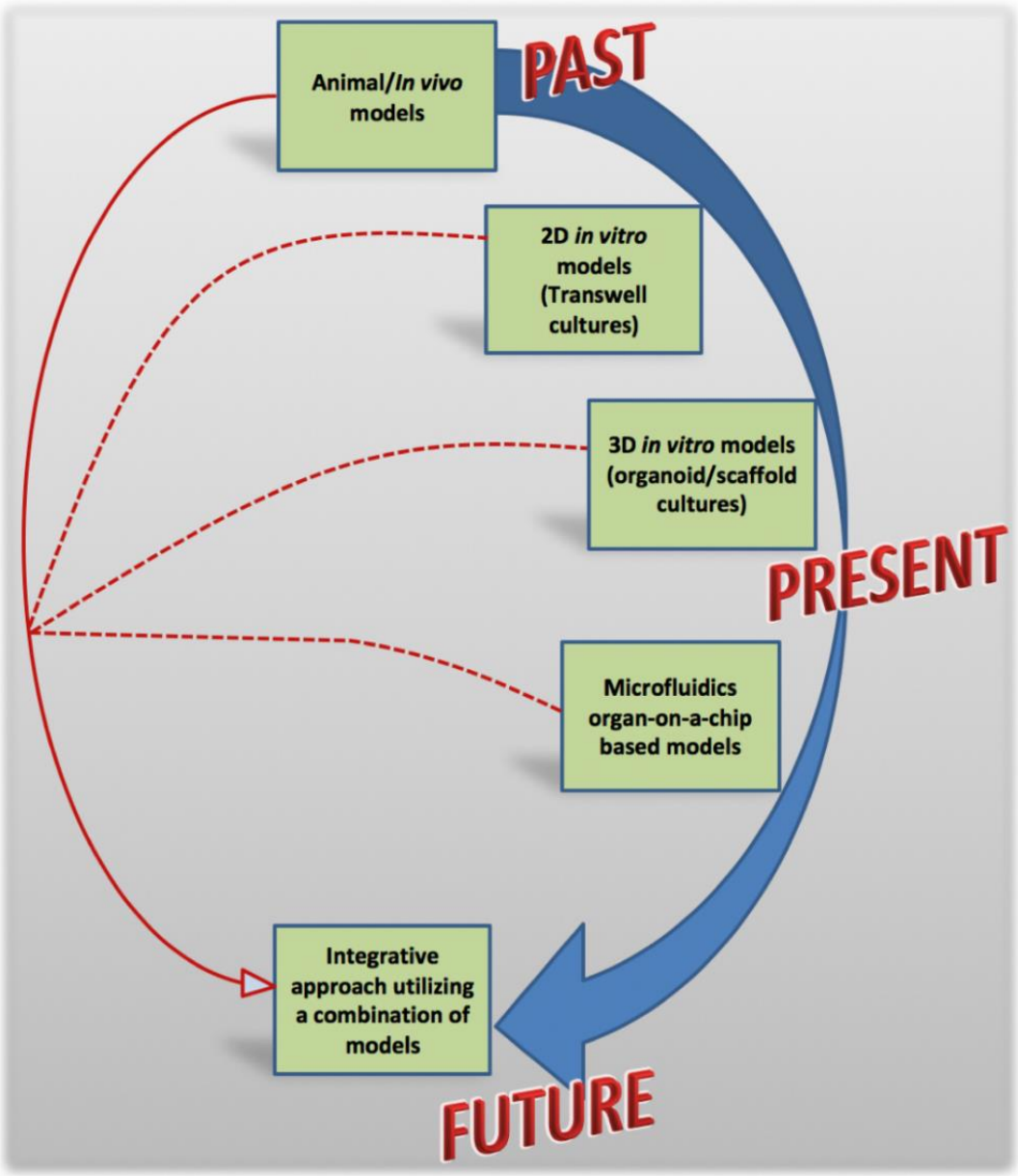

Figure 2-2. Evolution of AD modeling (Adapted from [16]).

There are several excellent reviews on animal models of AD [21-25] and the reader is advised to go through the same for more details. This review will dwell briefly on animal models and focuses on the advances, challenges and future directions of *in vitro* modeling of AD.

2.3 *In vivo* models of AD

In vivo models continue to play a significant role in Alzheimer's research and are broadly classified into two categories i.e. transgenic (genetically modified) and non-transgenic (natural) animal models. Both vertebrate and non-vertebrate animal species have been utilized as model organisms; the two most frequently used organisms being mice and rats, both belonging to the rodent family [21, 23]. Several advantages underlie the use of these rodents such as their small size, high birth rates, easy maintenance and low expenses owing to their short reproductive cycles [23]. Most transgenic animal models rely on single or multiple genetic mutations associated with the familial form of the disease i.e. FAD [22]. Higher the number of mutations utilized, faster is the rate of Aβ accumulation as observed in transgenic mice models [24].

2.3.1 Transgenic AD animal models

Knocking in/out of mutated genes that encode proteins like APP, ApoE, α- secretase and presenilins associated with AD, form the cornerstone in transgenic animal model research. For example, transgenic mice overexpressing APP show age-dependent Aβ accumulation in the form of plaques outside affected cells similar to that observed in diseased human brains [21]. The surplus Aβ levels were found to result in synaptic dysfunction and subsequent impairment of cognition, although neuronal loss and neurofibrillary tangles were absent. On the other hand, tau continued to remain soluble without substantial hyperphosphorylation and not aggregating into tangles in these models [21]. To overcome this absence of pathological tau and study its interaction with Aβ, a triple transgenic mice model was developed by Oddo et al. which harbored mutations in PSEN1, APP, and the tau protein [26]. The key observations in this model include manifestation of synaptic dysfunction prior to

plaques/tangles formation as well as appearance of Aβ related alterations preceding tauopathy, which corroborates the amyloid cascade hypothesis.

2.3.2 Non-transgenic AD animal models

Non-transgenic (natural) animal models of AD include both non-human primates (NHP) and other non-primates. These models are usually induced by administration of soluble Aβ oligomers [27], streptozotocin [28] or other AD related neurotoxins into the brains of the animals. Since these models do not utilize specific mutations to induce AD pathology, they are argued to be more representative of the sporadic form of the disease (SAD). NHPs such as macaques are both genetically and anatomically closer to humans compared with the rodents utilized in transgenic animal models; they also age in a similar fashion to humans and are therefore considered to be better candidates for modeling AD [29]. Moreover, changes observed in the structure and biochemistry of the aging NHP brain are similar to the aging human brain [30].

2.3.3 Limitations of AD animal models

Despite the multitude of studies conducted over 20 years across a variety of animal species, several inconsistencies remain in these models [31-33]. Firstly, transgenic AD models rely on FAD mutations and is therefore not representative of the more prevalent SAD. The mice models showed Aβ plaques and Aβ induced memory impairments but failed at recapitulating robust NFT pathology [3, 24]. Only double and triple transgenic models have reproduced NFTs and subsequent neuronal death, but they incorporate both FAD as well as frontotemporal dementia (FTD) associated tau mutations [31, 34]. They utilize abnormally high levels of expression of mutated genes and a variety of promoters which could lead to unforeseeable and inconsistent cell responses [24]. Moreover, neuronal death in human AD is progressive in nature,

which gradually increases with age, whereas brain atrophy in transgenic mice models occurs much earlier [35, 36]. On the other hand, non-transgenic models of AD do not take into account the intrinsic genetic factors involved in the disease. In addition, AD is identified to be a disorder exclusive to humans [37, 38]. Even though age-associated pathologies such as plaques and tau related alterations were observed in some NHP models, several dissimilarities in their phenotypes were also noted when compared with human AD pathologies [38-40]. Furthermore, it is challenging to study age-related disease pathologies in NHP species owing to their longevity, management costs, difficulty in incorporating genetic mutations as well as the legal and ethical problems involved in using them for research [29, 41]. In summary, animal models of AD have provided a good start to understanding the relationships between Aβ and tau pathologies and have helped initiate therapeutic strategies including clinical trials. However, these models for the most part have inconsistencies still remaining in the comprehensive recapitulation of disease phenotypes. This is attributed to the imperfect replication of human AD in other animal species as well as the differential vulnerability of rodent cells to human disease transgenes [42]. In this regard, human stem-cell derived *in vitro* cellular models are being utilized by researchers for filling in the knowledge gaps in the replication of *in vivo* disease pathogenesis and progression observed in existing animal models of AD [20]. *In vitro* tools such as scaffold-based cultures and organoids (miniature, simplified versions of human organs), have recently garnered a lot of attention in complementing and informing decisions in animal models.

2.4 *In vitro* models of AD

An effective *in vitro* model of AD is one which utilizes an appropriate cell type corresponding to the specific brain region, and then recapitulates all relevant

pathological features in a reproducible manner over a reasonably practicable culture duration [43]. In general, *in vitro* modeling of AD involves: introduction of synthetic compounds like Aβ peptides into cells, insertion of AD associated genes into cells via gene delivery technologies, or utilization of AD patient-derived cells [44].

2.4.1 Using cell lines to model AD

The first requirement in developing an *in vitro* model of AD is a cell line which has the potential to differentiate into neurons. In the past, the most commonly used cells for modeling AD were primary culture cell lines derived from rodents such as the immortal rat hippocampal cells [45] and the human neuroblastoma (SH-SY5Y) cells [46]. Despite their easy availability, use of such traditional cell lines rely on immortalized or cancerous cells which are cultured for several generations. This can lead to variations in genetic and physiological attributes, making their application in modeling of primary tissue cells questionable [18]. Long term *in vitro* sub-culturing of cell lines results in genetic adaptation to specific culture conditions, which leads to disparities among different batches of the same cell line. Moreover, it has been shown that rodent cells lines do not fully mimic the pathogenesis observed in human AD [44].

In view of these limitations, there was a pressing need to develop more reliable disease models utilizing human cells, which paved the way for stem cell-based modeling of AD. The obvious approach would be to use human embryonic stem cells (hES cells) obtained from embryos carrying the disease-causing mutation and derive neurons from them. However, this requires advance pre-implantation genetic diagnostic (PGD) assessment of the embryos to determine the embryos harboring the specific genetic disease [47, 48] (AD in this case). Due to the difficulties involved in generation of accurate patient-specific ES cells along with other ethical

concerns surrounding their application in research, the discovery of induced pluripotent stem cells (iPSCs) by Yamanaka's team in 2006 proved a better alternative for disease modeling [49]. Using this technology, adult human cells harvested from patients could be directly converted into pluripotent stem cells by introduction of four specific genes [50]. Furthermore, the development of highly efficient differentiation protocols such as dual SMAD inhibition [51] made it easier for deriving neurons from human stem cells, which is a prerequisite for modeling neurodegenerative diseases and drug screening as illustrated in **Figure 2-3**.

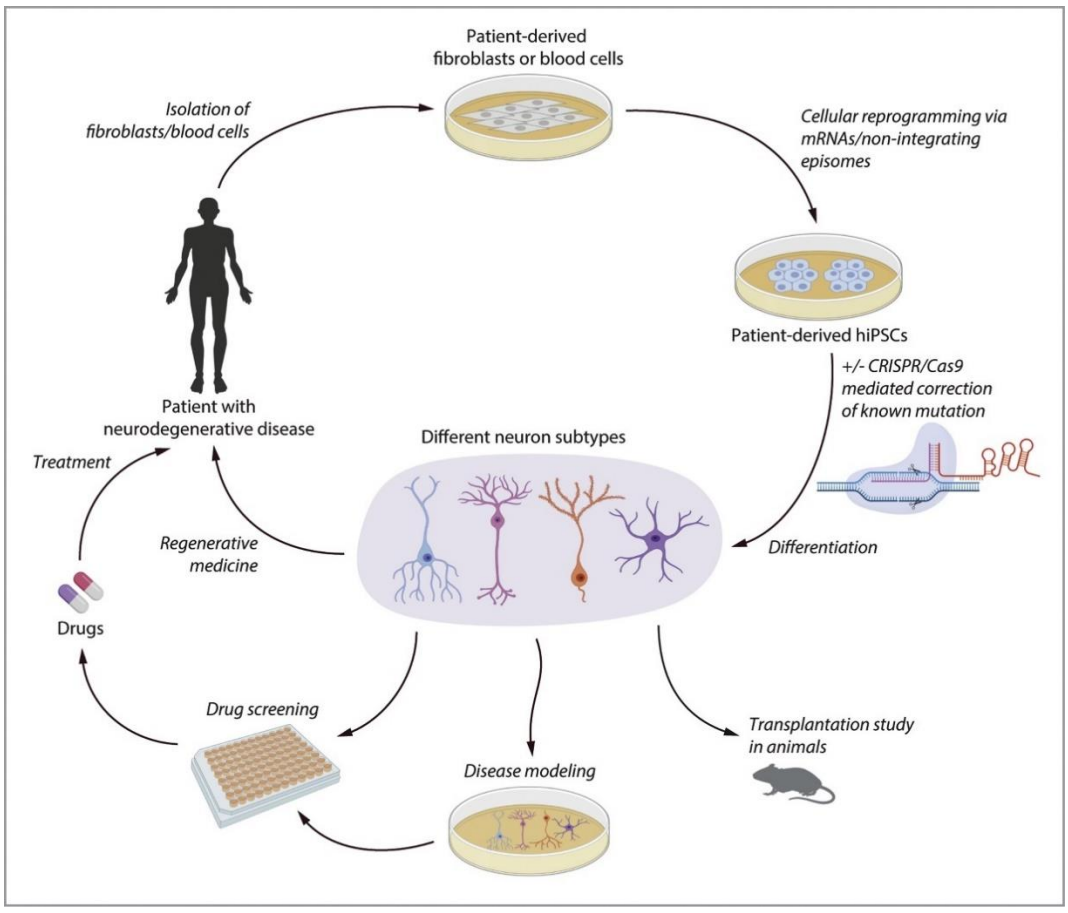

Figure 2-3. Cellular reprogramming for hiPSC generation and pathway for hiPSC-based disease modeling and drug discovery (Adapted from [52]).

2.4.2 Using iPSC-derived 2D culture platforms to model AD

Several *in vitro* models of AD employing 2D monolayer cultures of iPSC-derived neurons and encompassing both familial and sporadic forms of the disease have been

developed over the years. Some of the key models and findings using this approach are highlighted in **Table 2-1**.

Table 2-1. iPSC based 2D *in vitro* models of AD [16].

Type of AD	Key Results	Reference
FAD	Increased Aβ42 levels; γ-secretase inhibitor treatment modulated Aβ42 levels	[53]
FAD & SAD	Increased Aβ, aGSK-3β and p-tau levels; β-secretase inhibitor treatment reduced Aβ, aGSK-3β and p-tau levels whereas γ-secretase inhibitor treatment reduced Aβ levels only	[54]
AD	Generation of disease specific iPSC lines from patients	[55]
FAD & SAD	Formation and accumulation of Aβ oligomers inducing ER and oxidative stress; docosahexaenoic acid (DHA) treatment alleviated the stress responses	[56]
AD (DS)	Cells derived from Down syndrome (DS) patients developed AD pathologies over months in culture; production of Aβ42 peptides and hyperphosphorylated tau; γ-secretase inhibitor treatment blocked Aβ42 production	[43]
FAD	Increased Aβ42 to Aβ40 ratios; 14 genes showing altered expressions relative to controls	[57]
FAD	Increased APPsβ, Aβ, total tau and phosphorylated tau levels; Aβ-specific antibody treatment early in culture reverses the phenotype of increased total tau levels	[58]
FAD & SAD	Derivation of basal forebrain cholinergic neurons (BFCNs); increased Aβ42 to Aβ40 ratios; γ-secretase inhibitor treatment showed altered responses in Aβ40 production with an increase seen in SAD lines	[59]
FAD	Knock-in early onset Alzheimer's disease mutations into iPS cells using CRISPR/Cas9 technology;	[60]

Yagi et al. were the first to generate iPSC-derived neurons from FAD patients harboring mutations in PSEN1 and PSEN2, and demonstrated increased Aβ42 secretion along with elevated Aβ42 to Aβ40 ratios compared with non-AD controls [53]. Israel et al. probed both familial and sporadic forms of AD, generating iPSC lines by transducing fibroblasts with retroviruses [54]. They reported the presence

of significantly higher levels of Aβ40, active glycogen synthase kinase-3β (aGSK-3β) as well as hyperphosphorylation of tau. Another study by Kondo et al. showed intracellular accumulation of Aβ oligomers in both FAD (APP mutation) and SAD cases, inducing both endoplasmic reticulum (ER) and oxidative stress in the iPSC derived neurons [56]. Muratore et al. showed that elevation in tau levels could be reversed by treatment with Aβ-specific antibodies in iPSC-derived neurons harboring FAD mutations [58]. In addition to FAD patient-derived neurons, Paquet et al. reported generation of knock-in human neurons, which harbor heterozygous and homozygous FAD mutations (APP, PSEN1), by using modified CRISPR/Cas9 (Clustered regularly interspaced short palindromic repeats) gene editing technology [60]. The APP knock-in neurons demonstrated increase in total Aβ levels, while the PSEN1 neurons displayed a near twofold increase in Aβ42/Aβ40 ratios. Since these neurons were acquired from non-AD patients, the results clearly indicate that APP or PSEN1 FAD mutations are sufficient to increase pathogenic Aβ species in neurons [60].

Several challenges remain in accurate reproduction of AD hallmarks in 2D *in vitro* models resulting from multiple factors. For instance, Aβ levels generated in these models were insufficient for formation of plaques including other downstream pathological features [3]. This is presumed to be a result of higher diffusion of Aβ species into cell culture media and its subsequent removal during media changes. The neurons derived from the stem cells were not mature enough to replicate age-dependent pathogenic events seen in the AD human brain. The amount of neuronal degeneration and synapse loss observed in monolayer cultures is also significantly lower than *in vivo* conditions. More importantly, 2D cell culture platforms fall short in imitating the complex 3D microenvironments present inside the human brain,

which is vital for accelerating various cellular behaviors including neuronal differentiation, maturation, development of synapse connections and formation of neural circuits [3]. These limitations paved the way for development of novel 3D *in vitro* culture models of AD to complement and advance findings obtained using previous animal/2D culture-based models.

2.4.3 Using 3D culture platforms to model AD

3D cellular culture aims at bridging knowledge gaps between *in vivo* and traditionally used 2D *in vitro* cultures, thereby providing a platform which is more physiologically representative of native microenvironments. The various advantages offered by 3D over 2D cellular cultures have been well acknowledged in recent literature [61, 62], especially in provision of cues regulating cell structure, adhesion, proliferation, differentiation, signaling and mechanotransduction [63]. This is also relevant in neuronal cultures where 3D substrates can help improve both cell yield [64] and neuronal differentiation [65] compared with conventionally used Petri dish-based monolayer cultures. 2D cultures of AD also ignore astrocytes and microglia which are reported to play a supporting role in AD pathogenesis [66, 67]. In contrast, 3D culture allows functional cell-to-cell interactions between neurons and glia and is a better imitation of the complex interdependence/interplay of cells inside the human brain. Moreover, the spatial configuration of neurons may affect cytoskeletal dynamics such as binding of tau to microtubules [68], which is better mimicked using 3D culture platforms. **Figure 2-4** highlights the key approaches utilized by researchers in realizing a 3D microenvironment for *in vitro* cell culture in the context of disease modeling [17, 19, 20].

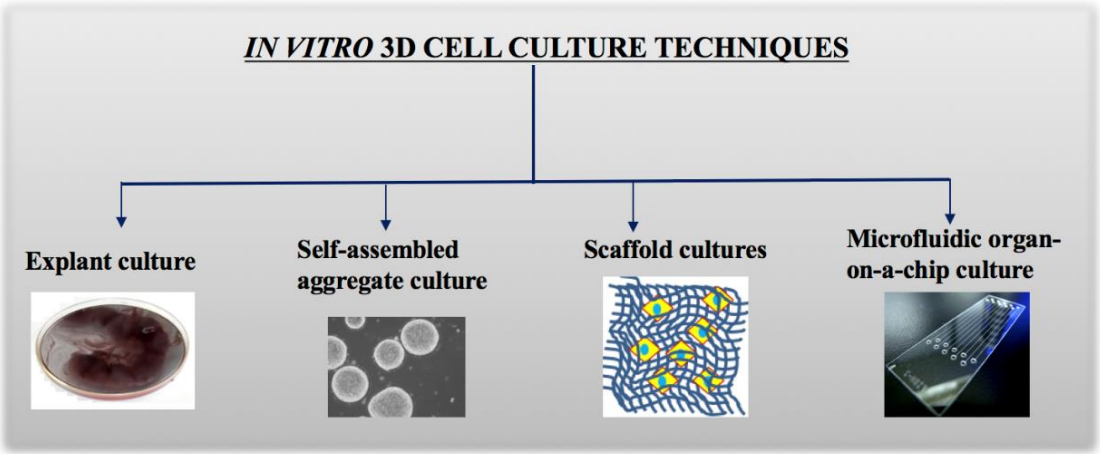

Figure 2-4. Principal 3D cell culture techniques (Adapted from [16]).

AD models have mainly utilized aggregate-based and scaffold-based techniques to culture cells in 3D. Aggregate-based models are comprised of organoid or neurospheroidal cultures relying on self-organization of patient-derived pluripotent stem cells or neural progenitor cells (NPC) into clump-like structures, and represent a simplified, miniature version of an organ [69]. These cell aggregates can be dispersed within a matrix, on a matrix or in a suspension medium [70]. Scaffold-based models rely on encapsulating cells inside highly porous, biocompatible, biodegradable matrices capable of promoting cellular outgrowth along all three dimensions as well as regulating cellular functions via physicochemical cues [71]. They can either be produced by passive seeding of cells on an acellular solid matrix or by dispersing cells inside a liquid matrix which is subsequently solidified to form a 3D cell-scaffold structure [70]. The materials used to fabricate these scaffolds/matrices can either be biologically derived or synthetic in nature.

An exhaustive list of the prominent *in vitro* 3D culture-based disease models of AD developed until now has been provided in **Table 2-2**. Most of the studies listed also feature 2D monolayer cultures for purposes of comparison or as controls.

Table 2-2. 3D *in vitro* models of AD [16].

3D Approach utilized	Methodology/ Cell culture type	Initial cell type	Differentiated cell type	Duration of culture and key focus	Reference
Aggregate based	Organotypic-like spheroid culture	SH-SY5Y (3 lines)	-	5-7 days, Tau pathology	[72]
Aggregate based	Networked neurosphere culture	Prenatal rat cortical neurons (NPC)	Neurons	10 days, Aβ pathology	[73]
Scaffold based	Matrigel matrix based thin and thick layer culture	ReNcell VM (ReN) human neural precursor (hNPC) cells	Neurons and glia	10-14 weeks, Aβ and Tau pathology	[34, 74]
Microfluidics + Aggregate based	Brain-on-a-chip neurospheroidal culture	Prenatal rat cortical neurons (NPC)	Neurons	10 days, Aβ pathology	[75]
Scaffold based	Self-assembling peptide hydrogel matrix-based culture	Healthy human iPSC derived neuroepithelial stem cells (lt-NES)	Neurons	2 days, P21-activated kinase modulation	[76]
Aggregate based	Cortical neurospheroidal culture	SAD Human iPSC derived from blood cells	Neurons	9 weeks, Aβ and Tau pathology	[68]
Aggregate based	Neural organoid culture	FAD Human iPSC derived from fibroblasts	NPC and neurons	90 days, Aβ and Tau pathology	[77]
Scaffold based	Matrigel matrix based thin layer culture	Healthy human iPSC derived from epithelial cells, fibroblasts	Layer V cortical neurons	40 days, Tau pathology	[78]
Scaffold based	Collagen matrix-based culture	PC-12 cells, SH-SY5Y cells	-	4-6 days, Aβ pathology	[79]
Aggregate + Scaffold based	Neurospheroids suspended in Matrigel matrix	ReN hNPCs and human iPSC-derived NPCs	Neurons and glia	8 weeks, Aβ and Tau pathology	[80]
Microfluidics + Scaffold based	Matrigel matrix based triculture system inside a 3D microfluidic platform	ReN hNPCs, human iPSC-derived NPCs and human microglia SV40	Neurons and glia	3–9 weeks, Aβ and Tau pathology, Neuroinflammatory response	[81]

The first 3D culture model of AD using a human cell line (ReN) was developed in 2014, and managed to recapitulate both senile plaques and NFTs which has not been feasible in transgenic mouse models [34, 74]. A 3D Matrigel matrix composed of brain ECM proteins was utilized for encapsulating cells and closely mimicking *in vivo* conditions. The human neuronal progenitor cells (hNPCs) cells were genetically engineered to overexpress both human APP and PSEN1 by harboring multiple FAD mutations, and therefore resulted in the production of very high levels of Aβ40 (~9-fold), Aβ42 (~17-fold) as well as elevated Aβ42/Aβ40 ratios (~5-fold) compared with controls. Next, fluorescence-activated cell sorting (FACS) enrichment protocols were utilized to generate FAD ReN cell lines producing nearly 1000-fold higher levels of Aβ compared with iPSC-derived FAD neurons used in other models [5]. The differentiation of the ReN cells into both neurons and glia, induction of tau pathology without utilizing FTD tau mutations, and exhibition of dystrophic morphology by neurites were other key aspects seen in this model. The addition of β-secretase or γ-secretase inhibitors suppressed Aβ generation, lowering Aβ plaque levels and resulted in the attenuation of tau pathology, thereby supporting the amyloid hypothesis. Recently, researchers from this group generated uniformly-sized neurospheroids using ReN cells with FAD mutations inside microwell-based arrays, which displayed both Aβ plaques and p-tau after eight weeks of culture [80]. Matrigel matrix was added into the microwells to hold the neurospheroids in place and initiate differentiation of cells, imitating a 3D microenvironment comparable to the brain ECM [82]. This technique was further developed and optimized for construction of a triculture model composed of AD neurons, astrocytes and microglia inside a 3D microfluidic platform, enabling neuron–glia interactions and

neuroinflammatory activity along with the recapitulation of AD hallmarks such as Aβ and p-tau [81].

Lee et al. developed the first AD patient-derived iPSC differentiated 3D culture model composed of neurospheroids; the iPSC lines were obtained from five patients diagnosed with sporadic AD (named as AD1-AD5) [68]. They cultured cells using both traditional 2D and spheroid-based 3D formats and exposed them to BACE1 and γ-secretase inhibitor drugs. Aβ40 and Aβ42 levels decreased significantly in all five cell lines for 2D; however, in 3D neurospheroid culture, significant reduction was observed only in AD2-AD5 [68]. They theorized that differences in individual genetic backgrounds (APOE genotypes) of patients may be responsible for variation in efficacy of the inhibitor [68]. Another study performed on a 3D organoid-based model utilized iPSC cells derived from FAD patients (APP duplication), and reported recapitulation of both amyloid and tau pathology along with abnormal endosome phenotypes [77]. Treatment with BACE1 and γ-secretase inhibitors initially led to a reduction in Aβ, after which a decrease in tau hyperphosphorylation was seen, indicating that Aβ accumulation precedes tauopathy.

Other research groups have utilized the Matrigel matrix-based approach [74] in further optimizing and advancing 3D modeling of AD. For instance, Medda et al. cultured iPSC derived cortical neurons obtained from healthy individuals, and induced principal tauopathy hallmarks via overexpression of mutant tau [78]. They focused on reproducibility, scalability and optimization of the culture protocol, aimed at providing a high-throughput assay to consistently bring about tau aggregation. More recently, another group cultured patient iPSC-derived neurons harboring a mutation in the PSEN1 gene inside Matrigel to study the initial stages of disease progression. They reported the production of Aβ oligomers by neurons

after 2 weeks of differentiation in the absence of both mutation induction and synthetic Aβ exposure [83].

2.4.4 Current challenges and missing links in 3D *in vitro* models of AD

It is clear from the above studies that 3D cell culture platforms have advanced *in vitro* modeling of AD and bridged several gaps observed in preceding *in vivo* as well as 2D monolayer-based culture models. At the same time, the limited number of 3D models of AD developed as of now indicates the infancy of this approach, and much work remains to done in realizing their full potential. Several challenges remain in both scaffold-free and scaffold-based techniques used for 3D modeling of AD including use of immortalized cell lines, lack of an adequate sample size, lack of data regarding the role of glial cells, use of promoters and the use of inappropriate controls. The lack of patterning cues and body axes which are absent in *in vitro* microenvironments limits organoids in organizing themselves into patterns seen in *in vivo* conditions [84]. Their self-assembling nature makes them difficult to control and significant differences in cell microenvironments are observed depending on depth from the surface [76]. Although this self-organizing phenotype of organoids imparts them with greater *in vivo* relevance at the cellular level [71, 85], single-cell transcriptomics have shown that cells constituting cerebral organoids use gene expression programs remarkably close to fetal tissue for assembling into cortex-like regions [85, 86]. Moreover, the lack of vascularization within organoids results in reduced infiltration of nutrients, signaling molecules and oxygen into inner regions once they reach a certain size, and leads to core tissue necrosis which impairs later stage development including neurogenesis [77, 87]. This affects drug screening owing to reduced penetration and leads to varied drug concentrations along the radius. It also leads to heterogeneities between batches, taking into account the wide

variety of differentiation protocols used by different research groups, which makes comparison and reproduction of data very difficult [88]. Although microfluidic perfusion chambers enable fluid flow via micro-scale channels to substitute *in vivo* vasculature, these devices have their own limitations such as flow induced shear stress, susceptibility to contamination, permeability, solubility and diffusibility of gas, absorption, adsorption, desorption and evaporation, all of which have adverse effects on cell growth and viability [69, 89, 90]. The large number of device designs available necessitates further standardization and validation of microfluidic 3D culture platforms incorporating iPSC technology [91, 92]. Furthermore, integration of vascular structures within *in vitro* organoids or scaffold-based cell constructs using organs-on-chip devices to ensure controlled supply of oxygen and other essential nutrients via diffusion is still a major challenge [93].

Scaffold-based 3D cultures utilizing hydrogels are susceptible to matrix disruption due to the long culture durations and multiple media changes involved in modeling of neurodegenerative diseases [76]. Most differentiation protocols also do not consider the regions of the brain specifically affected by AD, such as the limbic system including the cerebral cortex and hippocampus. This is important for the creation of accurate models, where the stem cells must be differentiated into neurons and glia specific to the disease affected brain region. Although 3D models of AD utilizing Matrigel matrix have produced 10~1000-fold higher levels of Aβ compared to iPSC-derived FAD neurons [3, 74], they utilize FACS enrichment protocols to generate FAD ReN cells, an immortalized hNPC line producing high levels of pathogenic Aβ species by overexpressing human APP and PSEN1 with multiple FAD mutations [5]. This artificial elevation of pathologies via gene manipulation and engineered cell lines is not representative of early stage pathogenesis observed

in the AD human brain. Moreover, Matrigel is animal-derived and composed of a heterogenous and ill-defined mixture of complex proteins [94]. These limitations motivate the exploration of "state-of-the-art" tissue engineering techniques utilizing alternative synthetic biomaterial-based substrates with better reproducibility and matrix uniformity in combination with patient-derived iPS cells for 3D *in vitro* modeling of AD.

2.5 Using tissue engineering strategies for 3D *in vitro* modeling of AD

Tissue engineering is an interdisciplinary field which brings together principles of biology, engineering, materials science and medicine to find solutions to clinical problems [17]. The goal here is to assemble functional constructs by combining biomaterial-based scaffolds, cells and bioactive molecules as biological substitutes to study, model, maintain or restore tissue function as illustrated in **Figure 2-5** [95].

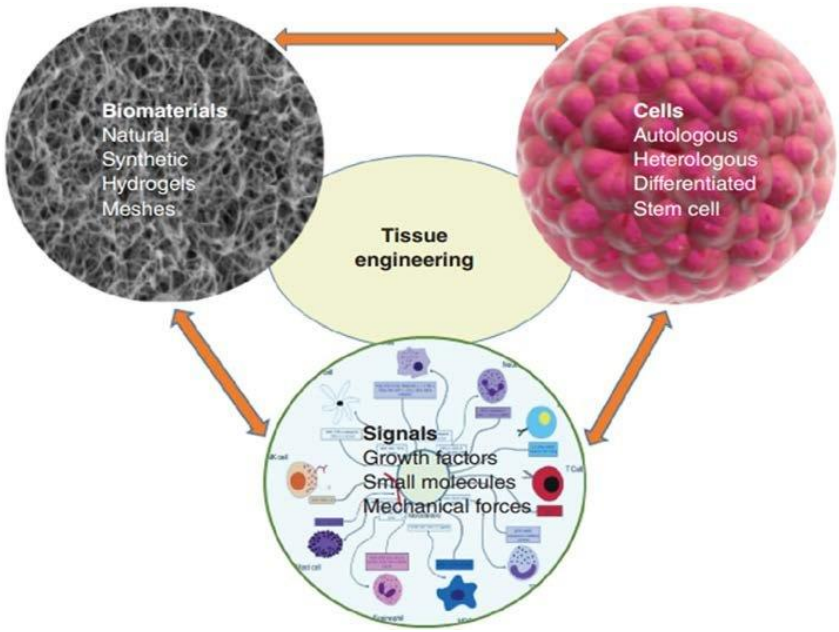

Figure 2-5. Tissue engineering triad (Adapted from [96]).

2.5.1 Design and fabrication of 3D scaffolds

Scaffolds are required to mimic the ECM present inside actual tissue, serving as a mechanical platform for cells to attach and grow in 3D. The ideal design

requirements for *in vitro* scaffolding of various neural systems and the criteria necessary for their assessment have been extensively studied over the years [97, 98]. Some of the key criteria are ease of fabrication, scalability, biodegradability, high porosity, interconnected pore network, suitable surface functionality as well as mechanical properties comparable with corresponding *in vivo* conditions. In addition, they should support cell infiltration, distribution, encapsulation, adhesion, viability, proliferation and differentiation [99]. At present, there is no 'gold standard' for fabricating 3D scaffolds, and a plethora of approaches have been developed over the years such as gelation, phase separation, gas foaming, salt leaching, 3D printing, freeze drying, electrospinning etc. (**Figure 2-6).** Most processes are capable of producing nano/micro-topographical scaffolds composed of a highly porous 3D microstructure with a tunable pore size.

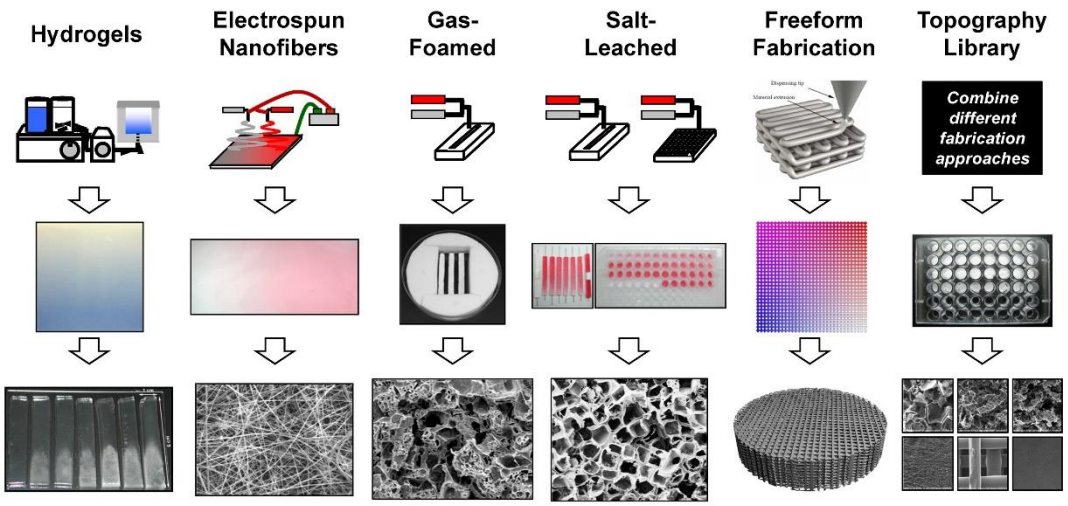

Figure 2-6. Tissue engineering techniques for fabrication of 3D scaffolds (Adapted from [100]).

The structure of the brain is both complex and intricate, composed of a dense network of interconnected neurons interacting with the ECM. The density of cells in the brain is so high that extracellular space occupies only about 20% of the total volume, the ECM accounting for another 20-30% and composed mainly of

hyaluronan, tenascins and proteoglycans [17, 101]. The elastic modulus of brain tissue is quite low ranging around 0.5-1 kPa [102]. Substrate stiffness plays a significant role in regulating neuronal stem cell fate including migration, differentiation and neurite formation [103]. The 3D substrate developed needs to be soft and mimic the mechanical properties of neural tissue to obtain appropriate cell responses upon encapsulation [103]. In this regard, hydrogels and electrospun fibers are popularly used tissue engineering techniques for fabricating soft matrices for 3D *in vitro* neuronal applications [17].

Hydrogels are a group of soft materials composed of water-swollen 3D networks of hydrophilic species, and have been explored as scaffolds for various biomedical applications owing to their excellent biocompatibility, high permeability and similarity to native soft tissues [104, 105]. A variety of hydrogel materials with diverse mechanical properties, crosslinking mechanisms, bio-responses have been utilized for cell culture applications [106, 107]. Cellular experiments performed using hydrogels either typically involve cell encapsulation within the material or the use of molds to fabricate substrates on which cells are later seeded. Hydrogel formation involves physical (non-covalent) or chemical (covalent) crosslinking for transition of liquid precursor solutions into solid materials [108].

Electrospinning is another straightforward for fabricating soft 3D fibrillar matrices, as it can produce uniform and continuous fibers which are structurally similar to native ECM proteins [109]. Electrospinning involves the creation of a strong electric field between a positively charged capillary filled with polymer solution and a grounded collector [83]. Once the electrostatic charge built up inside the solution at the tip of the needle exceeds its surface tension, a Taylor cone is formed, and the polymer solution shoots towards the collector in the form of a fine jet (**Figure 2-7**).

The solvent evaporates during this process and the polymer deposits on the collector in the form of thin fibers.

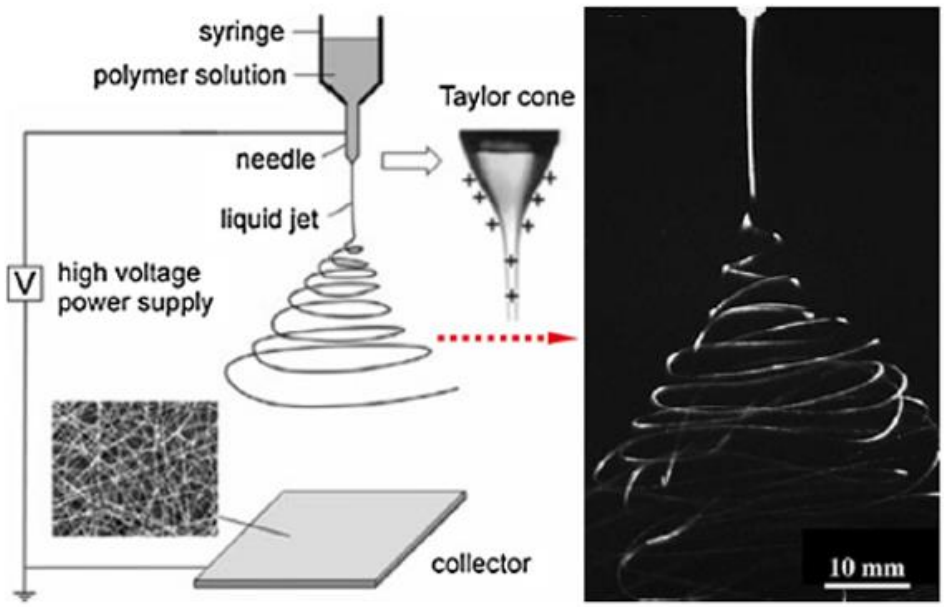

Figure 2-7. Schematic of electrospinning (Adapted from [110]).

The type of collector used can be varied to create fibers having different structures as well as orientation depending on the application. A flat plate can be used to obtain random fibers in the form of a 2D mat, whereas a rotating cylindrical shaped collector can be used to fabricate aligned fibers [83]. A liquid-based collector consisting of a low surface tension liquid such as ethanol can be used to fabricate non-woven, 3D macroporous scaffolds [85]. The fabrication of 3D polymer-based scaffolds via electrospinning has been shown to support neuronal culture and formation of neural networks in both *in vivo* [111] and *in vitro* [112] studies. Some of the key parameters to be considered in the electrospinning process and their effect on fiber morphology have been discussed in **Table 2-3** [113]. **Table 2-4** highlights properties of the polymer solution and their consequences on fiber formation.

Table 2-3. Electrospinning parameters and their effects.

Parameters	Influence	Effects
Voltage	Higher the voltage: higher the repulsive force, higher the acceleration and higher volumes of solution drawn.	Greater stretching, fiber diameter reduction, faster solvent evaporation, induces greater crystallinity, may also cause beads.
Feed rate	Greater the feed rate, greater is the volume of solution drawn from the needle.	Increases fiber diameter; longer time to dry may cause web formation due to residual solvents causing fibers to fuse together.
Temperature	Increases rate of evaporation, reduces viscosity of polymer solution.	Greater polymer solubility, smaller and more uniform fiber diameter.
Effect of collector	Typically made of conductive material.	Results in high packing density, non-conducting material could result in 3D structures due to repulsive forces.
Diameter of needle orifice	Low orifice diameters reduce clogging along with presence of beads.	Decrease in fiber diameter and bead formation.
Distance between needle tip and collector	Influences flight time and electric field strength.	Lower the distance, greater is the acceleration, hence lesser time for evaporation resulting in merging of fibers causing an interconnected network.
Ambient conditions	Humidity.	Causes pore formation on the surface.

Table 2-4. Properties of polymer solution affecting electrospinning.

Properties	Dependence	Consequences
Viscosity	Polymer concentration. Polymer solubility. Molecular weight of polymer.	Related to the extent of polymer molecule chains entanglement within the solution. There is a critical entanglement concentration below which electrospraying occurs and the likelihood of occurrence of beaded fibers instead of smooth ones.
Volatility	Rate of solvent evaporation.	If volatility is too low, then fibers may not be formed, and a thin film of polymer solution is deposited on the collector.
Surface tension	Temperature.	May cause solution to break into droplets, also may cause the formation of beads.
Electrical Conductivity	Ability of solution to carry charges (to overcome surface tension).	Can be increased significantly by mixing chemically non-interacting components.

2.5.2 Use of biomaterials in 3D scaffolds

The tremendous progress made in this area over the last decade has brought to the fore an assortment of novel biomaterials which are capable of actively supporting cell growth as well as modulating cell behavior by replicating the functions of native ECM [114]. They also provide additional growth factors and adhesion proteins facilitating accelerated maturation of neurons, maintaining culture stability and synaptic connectivity of neurons in 3D [58, 78]. These materials include both organic and inorganic materials which can be of synthetic or natural origins [99]. In terms of composition, naturally derived materials such as Matrigel (murine origin) resemble complex *in vivo* microenvironments present inside the ECM of several tissues. This ability to provide physiological relevance has resulted in their popular use in many 3D cellular culture platforms including *in vitro* models of AD [5]. However, natural materials also usually possess poor intrinsic mechanical properties, diverse compositions, batch-to-batch variability and immunogenicity issues which limit their use in scaffolding [108]. In contrast, synthetic materials can easily be tailored to impart them with biochemical and mechanical properties which meet application specific requirements [97, 98]. Subsequent use of these materials for fabrication of biocompatible *in vitro* scaffolds also enables development of 3D microtopographic structures capable of imitating *in vivo* microenvironments in a controlled setting.

2.6 Conclusion

The key to understanding AD aetiology lies in developing effective disease models, which should ideally recapitulate all aspects pertaining to the disease. Three key modeling approaches have been employed by researchers over the years in unraveling AD pathogenesis as well as initiating research into potential therapeutic

interventions. Every approach has its own specific advantages and limitations as highlighted in **Table 2-5,** and in turn has addressed different aspects of AD progression. In this review, we have provided details into the genesis, evolution, and significance of the principal approaches utilized by researchers for modeling AD. The salient features of animal based transgenic and natural models are listed, which helps improve our understanding of the challenges faced by *in vivo* platforms in mimicking disease pathogenesis and progression. Given the growing interest in use of *in vitro* platforms for disease modeling, this review further provides an extensive analysis of the latest 2D and 3D based *in vitro* AD models, and therefore stimulate much-needed research validation in this area.

Inaccessibility of the human brain makes it desirable to study AD pathogenesis on appropriate 3D model systems of brain cultures to bridge knowledge gaps encountered in preceding animal/2D models. Increasing evidence indicates superiority of 3D *in vitro* cell culture platforms over conventionally used Petri dish-based 2D monolayer cultures in mimicking native *in vivo* microenvironments. However, existing 3D neuronal culture models of AD utilize engineered cell lines, overexpress mutant genes or possess heterogeneities in composition, biological properties and cell differentiation stages. In this regard, the exploration of "state-of-the-art" tissue engineering techniques for development of alternative synthetic biomaterial-based 3D *in vitro* substrates in combination with AD patient-derived iPS cells could facilitate a more accurate and comprehensive study of early-stage AD pathogenesis. The key to deciphering AD lies in synergy i.e. primarily building on previous research, integrating the pros and cons of every technique, and combining available platforms aimed at developing more comprehensive paradigms of the disease.

Table 2-5. Current scope of AD modeling approaches [16].

	Modeling Alzheimer's Disease (AD)		
	In silico	***In vitro***	***In vivo***
ADVANTAGES	• Is inexpensive, does not require animal facilities or sophisticated laboratories. • High-throughput • Ability to complement *in vitro* and *in vivo* studies to speed up research process • Reproducibility • Can be used to improve efficiency of clinical trials	• Enables use of stem cell technology making it more relevant to humans • High-throughput • Recapitulation of both Aβ and tau pathology • Demonstration of elevated ER and oxidative stress levels • Drug screening • Use of microfluidic platforms and biomaterial scaffolds in mimicking the native microenvironment of the brain	• Recapitulation of Aβ pathology • Cognitive deficits can be analyzed • More suitable for long-term research • Therapeutic screening • Structure and biochemistry of the aging NHP brain is similar to aging human brain • Physiological relevance
LIMITATIONS	• Selection of a plausible set of parameters is complex and involves cross-disciplinary work • Modeling a complete set of parameters including both biological and non-biological factors using current technology is very difficult, if not impossible • Brain dynamics involve interlinked features, many of which are yet to be discovered and thus a computational model of the same could be inadequate by itself	• Still in its infancy • Scalability and standardization of iPS cell culture platforms • Heterogeneity, tumorigenicity of iPS cell cultures • Lack of vascularization leading to necrosis in the cores of organoid based models • Variability in cell lines and culture protocols among research groups resulting in low reproducibility • Limited human AD cell sources • Long term culture is difficult and expensive • Current scope of *in vitro* culture is at cellular and tissue levels • Difficulty in performing imaging studies for 3D cultures • Use of promoters as well as inappropriate controls could lead to inconsistent results	• Robust NFT replication requires additional mutations • Variation in features of hallmarks between models as well as dissimilarities in AD phenotypes compared to AD human brain • Lower levels of neuronal loss observed • Low reproducibility • High maintenance costs involved • Differential vulnerability of animal cells to human disease transgenes • Abnormally high levels of expression of mutated genes to induce pathogenesis • Ethical and legal problems

References

[1] L. Bertram, R.E. Tanzi, Thirty years of Alzheimer's disease genetics: the implications of systematic meta-analyses, Nat Rev Neurosci 9(10) (2008) 768-78.

[2] R.L. Nussbaum, C.E. Ellis, Alzheimer's disease and Parkinson's disease, The New England journal of medicine 348(14) (2003) 1356-64.

[3] C. D'Avanzo, J. Aronson, Y.H. Kim, S.H. Choi, R.E. Tanzi, D.Y. Kim, Alzheimer's in 3D culture: challenges and perspectives, Bioessays 37(10) (2015) 1139-48.

[4] M. Kim, J. Suh, D. Romano, M.H. Truong, K. Mullin, B. Hooli, D. Norton, G. Tesco, K. Elliott, S.L. Wagner, R.D. Moir, K.D. Becker, R.E. Tanzi, Potential late-onset Alzheimer's disease-associated mutations in the ADAM10 gene attenuate {alpha}-secretase activity, Hum Mol Genet 18(20) (2009) 3987-96.

[5] S.H. Choi, Y.H. Kim, L. Quinti, R.E. Tanzi, D.Y. Kim, 3D culture models of Alzheimer's disease: a road map to a "cure-in-a-dish", Mol Neurodegener 11(1) (2016) 75.

[6] C.C. Liu, T. Kanekiyo, H. Xu, G. Bu, Apolipoprotein E and Alzheimer disease: risk, mechanisms and therapy, Nat Rev Neurol 9(2) (2013) 106-18.

[7] J.M. Castellano, J. Kim, F.R. Stewart, H. Jiang, R.B. DeMattos, B.W. Patterson, A.M. Fagan, J.C. Morris, K.G. Mawuenyega, C. Cruchaga, A.M. Goate, K.R. Bales, S.M. Paul, R.J. Bateman, D.M. Holtzman, Human apoE Isoforms Differentially Regulate Brain Amyloid-β Peptide Clearance, Science Translational Medicine 3(89) (2011) 89ra57-89ra57.

[8] J. Yang, S. Li, X.B. He, C. Cheng, W. Le, Induced pluripotent stem cells in Alzheimer's disease: applications for disease modeling and cell-replacement therapy, Mol Neurodegener 11(1) (2016) 39.

[9] D.J. Selkoe, J. Hardy, The amyloid hypothesis of Alzheimer's disease at 25 years, EMBO Mol Med 8(6) (2016) 595-608.

[10] L.M. Ittner, J. Gotz, Amyloid-beta and tau--a toxic pas de deux in Alzheimer's disease, Nat Rev Neurosci 12(2) (2011) 65-72.

[11] C. Schmitz, B.P.F. Rutten, A. Pielen, S. Schäfer, O. Wirths, G. Tremp, C. Czech, V. Blanchard, G. Multhaup, P. Rezaie, H. Korr, H.W.M. Steinbusch, L. Pradier, T.A. Bayer, Hippocampal Neuron Loss Exceeds Amyloid Plaque Load in a Transgenic

Mouse Model of Alzheimer's Disease, The American Journal of Pathology 164(4) (2004) 1495-1502.
[12] T.P. Knowles, M. Vendruscolo, C.M. Dobson, The amyloid state and its association with protein misfolding diseases, Nat Rev Mol Cell Biol 15(6) (2014) 384-96.
[13] S. Campioni, B. Mannini, M. Zampagni, A. Pensalfini, C. Parrini, E. Evangelisti, A. Relini, M. Stefani, C.M. Dobson, C. Cecchi, F. Chiti, A causative link between the structure of aberrant protein oligomers and their toxicity, Nat Chem Biol 6(2) (2010) 140-7.
[14] K.H. Benam, S. Dauth, B. Hassell, A. Herland, A. Jain, K.J. Jang, K. Karalis, H.J. Kim, L. MacQueen, R. Mahmoodian, S. Musah, Y.S. Torisawa, A.D. van der Meer, R. Villenave, M. Yadid, K.K. Parker, D.E. Ingber, Engineered in vitro disease models, Annu Rev Pathol 10 (2015) 195-262.
[15] Trisilowati, D.G. Mallet, In silico experimental modeling of cancer treatment, ISRN Oncol 2012 (2012) 828701.
[16] V.D. Ranjan, L. Qiu, E.K. Tan, L. Zeng, Y. Zhang, Modelling Alzheimer's disease: Insights from in vivo to in vitro three-dimensional culture platforms, J Tissue Eng Regen Med 12(9) (2018) 1944-1958.
[17] A.M. Hopkins, E. DeSimone, K. Chwalek, D.L. Kaplan, 3D in vitro modeling of the central nervous system, Prog Neurobiol 125 (2015) 1-25.
[18] P. Horvath, N. Aulner, M. Bickle, A.M. Davies, E.D. Nery, D. Ebner, M.C. Montoya, P. Ostling, V. Pietiainen, L.S. Price, S.L. Shorte, G. Turcatti, C. von Schantz, N.O. Carragher, Screening out irrelevant cell-based models of disease, Nat Rev Drug Discov 15(11) (2016) 751-769.
[19] D.B. Edelman, E.W. Keefer, A cultural renaissance: in vitro cell biology embraces three-dimensional context, Exp Neurol 192(1) (2005) 1-6.
[20] K.R. Ko, J.P. Frampton, Developments in 3D neural cell culture models: the future of neurotherapeutics testing?, Expert Rev Neurother 16(7) (2016) 739-41.
[21] F.M. LaFerla, K.N. Green, Animal models of Alzheimer disease, Cold Spring Harb Perspect Med 2(11) (2012).
[22] J. Gotz, L.M. Ittner, Animal models of Alzheimer's disease and frontotemporal dementia, Nat Rev Neurosci 9(7) (2008) 532-44.
[23] M. Sarasa, P. Pesini, Natural non-trasgenic animal models for research in Alzheimer's disease, Current Alzheimer research 6(2) (2009) 171-8.

[24] S.E. Cavanaugh, Animal models of Alzheimer disease: historical pitfalls and a path forward, Altex 31(3) (2014) 279-302.
[25] J. Blesa, S. Phani, V. Jackson-Lewis, S. Przedborski, Classic and new animal models of Parkinson's disease, J Biomed Biotechnol 2012 (2012) 845618.
[26] S. Oddo, A. Caccamo, J.D. Shepherd, M.P. Murphy, T.E. Golde, R. Kayed, R. Metherate, M.P. Mattson, Y. Akbari, F.M. LaFerla, Triple-Transgenic Model of Alzheimer's Disease with Plaques and Tangles, Neuron 39(3) (2003) 409-421.
[27] L. Forny-Germano, N.M. Lyra e Silva, A.F. Batista, J. Brito-Moreira, M. Gralle, S.E. Boehnke, B.C. Coe, A. Lablans, S.A. Marques, A.M. Martinez, W.L. Klein, J.C. Houzel, S.T. Ferreira, D.P. Munoz, F.G. De Felice, Alzheimer's disease-like pathology induced by amyloid-beta oligomers in nonhuman primates, J Neurosci 34(41) (2014) 13629-43.
[28] Y. Chen, Z. Liang, J. Blanchard, C.L. Dai, S. Sun, M.H. Lee, I. Grundke-Iqbal, K. Iqbal, F. Liu, C.X. Gong, A non-transgenic mouse model (icv-STZ mouse) of Alzheimer's disease: similarities to and differences from the transgenic model (3xTg-AD mouse), Mol Neurobiol 47(2) (2013) 711-25.
[29] J.M. Verdier, I. Acquatella, C. Lautier, G. Devau, S. Trouche, C. Lasbleiz, N. Mestre-Frances, Lessons from the analysis of nonhuman primates for understanding human aging and neurodegenerative diseases, Front Neurosci 9 (2015) 64.
[30] D. Van Dam, P.P. De Deyn, Non human primate models for Alzheimer's disease-related research and drug discovery, Expert Opin Drug Discov 12(2) (2017) 187-200.
[31] S.H. Choi, Y.H. Kim, C. D'Avanzo, J. Aronson, R.E. Tanzi, D.Y. Kim, Recapitulating amyloid beta and tau pathology in human neural cell culture models: clinical implications, US Neurol 11(2) (2015) 102-105.
[32] J.K. Chambers, T. Tokuda, K. Uchida, R. Ishii, H. Tatebe, E. Takahashi, T. Tomiyama, Y. Une, H. Nakayama, The domestic cat as a natural animal model of Alzheimer's disease, Acta Neuropathol Commun 3 (2015) 78.
[33] F.T. Merkle, K. Eggan, Modeling human disease with pluripotent stem cells: from genome association to function, Cell Stem Cell 12(6) (2013) 656-68.
[34] Y.H. Kim, S.H. Choi, C. D'Avanzo, M. Hebisch, C. Sliwinski, E. Bylykbashi, K.J. Washicosky, J.B. Klee, O. Brustle, R.E. Tanzi, D.Y. Kim, A 3D human neural cell culture system for modeling Alzheimer's disease, Nat Protoc 10(7) (2015) 985-1006.

[35] J.C. Dodart, C. Mathis, J. Saura, K.R. Bales, S.M. Paul, A. Ungerer, Neuroanatomical abnormalities in behaviorally characterized APP(V717F) transgenic mice, Neurobiol Dis 7(2) (2000) 71-85.
[36] J.M. Redwine, B. Kosofsky, R.E. Jacobs, D. Games, J.F. Reilly, J.H. Morrison, W.G. Young, F.E. Bloom, Dentate gyrus volume is reduced before onset of plaque formation in PDAPP mice: a magnetic resonance microscopy and stereologic analysis, Proc Natl Acad Sci U S A 100(3) (2003) 1381-6.
[37] A. Toledano, M.I. Álvarez, A.B. López-Rodríguez, A. Toledano-Díaz, C.I. Fernández-Verdecia, Does Alzheimer disease exist in all primates? Alzheimer pathology in non-human primates and its pathophysiological implications (II), Neurología (English Edition) 29(1) (2014) 42-55.
[38] T.L. Platt, V.L. Reeves, M.P. Murphy, Transgenic models of Alzheimer's disease: better utilization of existing models through viral transgenesis, Biochim Biophys Acta 1832(9) (2013) 1437-48.
[39] E. Heuer, R.F. Rosen, A. Cintron, L.C. Walker, Nonhuman primate models of Alzheimer-like cerebral proteopathy, Current pharmaceutical design 18(8) (2012) 1159-69.
[40] N. Oikawa, N. Kimura, K. Yanagisawa, Alzheimer-type tau pathology in advanced aged nonhuman primate brains harboring substantial amyloid deposition, Brain Res 1315 (2010) 137-49.
[41] J.D. Jebelli, T.M. Piers, Amyloid-beta oligomers unveil a novel primate model of sporadic Alzheimer's disease, Front Neurosci 9 (2015) 47.
[42] R.J. Jakel, B.L. Schneider, C.N. Svendsen, Using human neural stem cells to model neurological disease, Nat Rev Genet 5(2) (2004) 136-44.
[43] Y. Shi, P. Kirwan, J. Smith, G. MacLean, S.H. Orkin, F.J. Livesey, A human stem cell model of early Alzheimer's disease pathology in Down syndrome, Sci Transl Med 4(124) (2012) 124ra29.
[44] M.N. Carolindah, R. Rosli, A. Adam, N. Nordin, An overview of in vitro research models for Alzheimer's disease, Regenerative Research 2(2) (2013) 8-13.
[45] K.L. Anderson, N.U.C.I. Institute for Neuroscience, A. Ferreira, N.U.C.I. Institute for Neuroscience, C. Department of, F.S.o.M.N.U.C.I. Molecular Biology, S.B.R.E.S.S.C.I.L. Northwestern Institute for Neuroscience, α1 integrin activation: A link between β-amyloid deposition and neuronal death in aging hippocampal neurons, Journal of Neuroscience Research 75(5) (2017) 688-697.

[46] S. Stoppelkamp, H.S. Bell, J. Palacios-Filardo, D.A. Shewan, G. Riedel, B. Platt, In vitro modelling of Alzheimer's disease: degeneration and cell death induced by viral delivery of amyloid and tau, Exp Neurol 229(2) (2011) 226-37.
[47] J. Sandoe, K. Eggan, Opportunities and challenges of pluripotent stem cell neurodegenerative disease models, Nat Neurosci 16(7) (2013) 780-9.
[48] G. Hargus, M. Ehrlich, A.L. Hallmann, T. Kuhlmann, Human stem cell models of neurodegeneration: a novel approach to study mechanisms of disease development, Acta Neuropathol 127(2) (2013) 151-73.
[49] K. Takahashi, S. Yamanaka, Induction of pluripotent stem cells from mouse embryonic and adult fibroblast cultures by defined factors, Cell 126(4) (2006) 663-76.
[50] K. Takahashi, K. Tanabe, M. Ohnuki, M. Narita, T. Ichisaka, K. Tomoda, S. Yamanaka, Induction of pluripotent stem cells from adult human fibroblasts by defined factors, Cell 131(5) (2007) 861-72.
[51] S.M. Chambers, C.A. Fasano, E.P. Papapetrou, M. Tomishima, M. Sadelain, L. Studer, Highly efficient neural conversion of human ES and iPS cells by dual inhibition of SMAD signaling, Nat Biotechnol 27(3) (2009) 275-80.
[52] E. Seranova, A.M. Palhegyi, S. Verma, S. Dimova, R. Lasry, M. Naama, C. Sun, T. Barrett, T.R. Rosenstock, D. Kumar, M.A. Cohen, Y. Buganim, S. Sarkar, Human Induced Pluripotent Stem Cell Models of Neurodegenerative Disorders for Studying the Biomedical Implications of Autophagy, Journal of Molecular Biology 432(8) (2020) 2754-2798.
[53] T. Yagi, D. Ito, Y. Okada, W. Akamatsu, Y. Nihei, T. Yoshizaki, S. Yamanaka, H. Okano, N. Suzuki, Modeling familial Alzheimer's disease with induced pluripotent stem cells, Hum Mol Genet 20(23) (2011) 4530-9.
[54] M.A. Israel, S.H. Yuan, C. Bardy, S.M. Reyna, Y. Mu, C. Herrera, M.P. Hefferan, S. Van Gorp, K.L. Nazor, F.S. Boscolo, C.T. Carson, L.C. Laurent, M. Marsala, F.H. Gage, A.M. Remes, E.H. Koo, L.S. Goldstein, Probing sporadic and familial Alzheimer's disease using induced pluripotent stem cells, Nature 482(7384) (2012) 216-20.
[55] J. Jang, J.E. Yoo, J.A. Lee, D.R. Lee, J.Y. Kim, Y.J. Huh, D.S. Kim, C.Y. Park, D.Y. Hwang, H.S. Kim, H.C. Kang, D.W. Kim, Disease-specific induced pluripotent stem cells: a platform for human disease modeling and drug discovery, Exp Mol Med 44(3) (2012) 202-13.

[56] T. Kondo, M. Asai, K. Tsukita, Y. Kutoku, Y. Ohsawa, Y. Sunada, K. Imamura, N. Egawa, N. Yahata, K. Okita, K. Takahashi, I. Asaka, T. Aoi, A. Watanabe, K. Watanabe, C. Kadoya, R. Nakano, D. Watanabe, K. Maruyama, O. Hori, S. Hibino, T. Choshi, T. Nakahata, H. Hioki, T. Kaneko, M. Naitoh, K. Yoshikawa, S. Yamawaki, S. Suzuki, R. Hata, S. Ueno, T. Seki, K. Kobayashi, T. Toda, K. Murakami, K. Irie, W.L. Klein, H. Mori, T. Asada, R. Takahashi, N. Iwata, S. Yamanaka, H. Inoue, Modeling Alzheimer's disease with iPSCs reveals stress phenotypes associated with intracellular Abeta and differential drug responsiveness, Cell Stem Cell 12(4) (2013) 487-96.

[57] A.A. Sproul, S. Jacob, D. Pre, S.H. Kim, M.W. Nestor, M. Navarro-Sobrino, I. Santa-Maria, M. Zimmer, S. Aubry, J.W. Steele, D.J. Kahler, A. Dranovsky, O. Arancio, J.F. Crary, S. Gandy, S.A. Noggle, Characterization and molecular profiling of PSEN1 familial Alzheimer's disease iPSC-derived neural progenitors, PLoS One 9(1) (2014) e84547.

[58] C.R. Muratore, H.C. Rice, P. Srikanth, D.G. Callahan, T. Shin, L.N. Benjamin, D.M. Walsh, D.J. Selkoe, T.L. Young-Pearse, The familial Alzheimer's disease APPV717I mutation alters APP processing and Tau expression in iPSC-derived neurons, Hum Mol Genet 23(13) (2014) 3523-36.

[59] L. Duan, B.J. Bhattacharyya, A. Belmadani, L. Pan, R.J. Miller, J.A. Kessler, Stem cell derived basal forebrain cholinergic neurons from Alzheimer’s disease patients are more susceptible to cell death, Mol Neurodegener2014, p. 3.

[60] D. Paquet, D. Kwart, A. Chen, A. Sproul, S. Jacob, S. Teo, K.M. Olsen, A. Gregg, S. Noggle, M. Tessier-Lavigne, Efficient introduction of specific homozygous and heterozygous mutations using CRISPR/Cas9, Nature 533(7601) (2016) 125-9.

[61] M. Ravi, V. Paramesh, S.R. Kaviya, E. Anuradha, F.D. Solomon, 3D cell culture systems: advantages and applications, J Cell Physiol 230(1) (2015) 16-26.

[62] F. Pampaloni, E.G. Reynaud, E.H.K. Stelzer, The third dimension bridges the gap between cell culture and live tissue, Nat Rev Mol Cell Biol 8(10) (2007) 839-845.

[63] B.M. Baker, C.S. Chen, Deconstructing the third dimension: how 3D culture microenvironments alter cellular cues, J Cell Sci 125(Pt 13) (2012) 3015-24.

[64] A. Liedmann, S. Frech, P.J. Morgan, A. Rolfs, M.J. Frech, Differentiation of human neural progenitor cells in functionalized hydrogel matrices, Biores Open Access 1(1) (2012) 16-24.
[65] Z.N. Zhang, B.C. Freitas, H. Qian, J. Lux, A. Acab, C.A. Trujillo, R.H. Herai, V.A. Nguyen Huu, J.H. Wen, S. Joshi-Barr, J.V. Karpiak, A.J. Engler, X.D. Fu, A.R. Muotri, A. Almutairi, Layered hydrogels accelerate iPSC-derived neuronal maturation and reveal migration defects caused by MeCP2 dysfunction, Proc Natl Acad Sci U S A 113(12) (2016) 3185-90.
[66] E. Solito, M. Sastre, Microglia function in Alzheimer's disease, Front Pharmacol 3 (2012) 14.
[67] C.J. Garwood, L.E. Ratcliffe, J.E. Simpson, P.R. Heath, P.G. Ince, S.B. Wharton, Review: Astrocytes in Alzheimer's disease and other age-associated dementias; a supporting player with a central role, Neuropathol Appl Neurobiol (2016).
[68] H.K. Lee, C. Velazquez Sanchez, M. Chen, P.J. Morin, J.M. Wells, E.B. Hanlon, W. Xia, Three Dimensional Human Neuro-Spheroid Model of Alzheimer's Disease Based on Differentiated Induced Pluripotent Stem Cells, PLoS One 11(9) (2016) e0163072.
[69] M. Jorfi, C. D'Avanzo, D.Y. Kim, D. Irimia, Three-Dimensional Models of the Human Brain Development and Diseases, Advanced healthcare materials 7(1) (2017).
[70] R. Edmondson, J.J. Broglie, A.F. Adcock, L. Yang, Three-dimensional cell culture systems and their applications in drug discovery and cell-based biosensors, Assay Drug Dev Technol 12(4) (2014) 207-218.
[71] C. Arber, C. Lovejoy, S. Wray, Stem cell models of Alzheimer’s disease: progress and challenges, Alzheimer's Research & Therapy 9 (2017) 42.
[72] D. Seidel, D. Krinke, H.G. Jahnke, A. Hirche, D. Kloss, T.G. Mack, F. Striggow, A. Robitzki, Induced tauopathy in a novel 3D-culture model mediates neurodegenerative processes: a real-time study on biochips, PLoS One 7(11) (2012) e49150.
[73] Y.J. Choi, J. Park, S.H. Lee, Size-controllable networked neurospheres as a 3D neuronal tissue model for Alzheimer's disease studies, Biomaterials 34(12) (2013) 2938-46.

[74] S.H. Choi, Y.H. Kim, M. Hebisch, C. Sliwinski, S. Lee, C. D'Avanzo, H. Chen, B. Hooli, C. Asselin, J. Muffat, J.B. Klee, C. Zhang, B.J. Wainger, M. Peitz, D.M. Kovacs, C.J. Woolf, S.L. Wagner, R.E. Tanzi, D.Y. Kim, A three-dimensional human neural cell culture model of Alzheimer's disease, Nature 515(7526) (2014) 274-8.

[75] J. Park, B.K. Lee, G.S. Jeong, J.K. Hyun, C.J. Lee, S.H. Lee, Three-dimensional brain-on-a-chip with an interstitial level of flow and its application as an in vitro model of Alzheimer's disease, Lab Chip 15(1) (2015) 141-50.

[76] D. Zhang, M. Pekkanen-Mattila, M. Shahsavani, A. Falk, A.I. Teixeira, A. Herland, A 3D Alzheimer's disease culture model and the induction of P21-activated kinase mediated sensing in iPSC derived neurons, Biomaterials 35(5) (2014) 1420-8.

[77] W.K. Raja, A.E. Mungenast, Y.T. Lin, T. Ko, F. Abdurrob, J. Seo, L.H. Tsai, Self-Organizing 3D Human Neural Tissue Derived from Induced Pluripotent Stem Cells Recapitulate Alzheimer's Disease Phenotypes, PLoS One 11(9) (2016) e0161969.

[78] X. Medda, L. Mertens, S. Versweyveld, A. Diels, L. Barnham, A. Bretteville, A. Buist, A. Verheyen, I. Royaux, A. Ebneth, A. Cabrera-Socorro, Development of a Scalable, High-Throughput-Compatible Assay to Detect Tau Aggregates Using iPSC-Derived Cortical Neurons Maintained in a Three-Dimensional Culture Format, J Biomol Screen 21(8) (2016) 804-15.

[79] M.N. Labour, S. Vigier, D. Lerner, A. Marcilhac, E. Belamie, 3D compartmented model to study the neurite-related toxicity of Abeta aggregates included in collagen gels of adaptable porosity, Acta Biomater 37 (2016) 38-49.

[80] M. Jorfi, C. D'Avanzo, R.E. Tanzi, D.Y. Kim, D. Irimia, Human Neurospheroid Arrays for In Vitro Studies of Alzheimer's Disease, Sci Rep 8(1) (2018) 2450.

[81] J. Park, I. Wetzel, I. Marriott, D. Dréau, C. D'Avanzo, D.Y. Kim, R.E. Tanzi, H. Cho, A 3D human triculture system modeling neurodegeneration and neuroinflammation in Alzheimer's disease, Nature Neuroscience 21(7) (2018) 941-951.

[82] M.J. Irimia, D.A. Carla, E.T. Rudolph, K. Doo Yeon, Daniel, Human Neurospheroid Arrays for In Vitro Studies of Alzheimer's Disease, Scientific Reports 8(1) (2018) 2450.

[83] M.A. Hernández-Sapiéns, E.E. Reza-Zaldívar, R.R. Cevallos, A.L. Márquez-Aguirre, K. Gazarian, A.A. Canales-Aguirre, A Three-Dimensional Alzheimer's Disease Cell Culture Model Using iPSC-Derived Neurons Carrying A246E Mutation in PSEN1, Frontiers in Cellular Neuroscience 14(151) (2020).

[84] M.A. Lancaster, M. Renner, C.A. Martin, D. Wenzel, L.S. Bicknell, M.E. Hurles, T. Homfray, J.M. Penninger, A.P. Jackson, J.A. Knoblich, Cerebral organoids model human brain development and microcephaly, Nature 501(7467) (2013) 373-9.

[85] I. Kelava, M.A. Lancaster, Dishing out mini-brains: Current progress and future prospects in brain organoid research, Developmental Biology 420(2) (2016) 199-209.

[86] J.G. Camp, F. Badsha, M. Florio, S. Kanton, T. Gerber, M. Wilsch-Brauninger, E. Lewitus, A. Sykes, W. Hevers, M. Lancaster, J.A. Knoblich, R. Lachmann, S. Paabo, W.B. Huttner, B. Treutlein, Human cerebral organoids recapitulate gene expression programs of fetal neocortex development, Proc Natl Acad Sci U S A 112(51) (2015) 15672-7.

[87] G. Quadrato, J. Brown, P. Arlotta, The promises and challenges of human brain organoids as models of neuropsychiatric disease, Nature medicine 22(11) (2016) 1220-1228.

[88] X. Qian, H.N. Nguyen, M.M. Song, C. Hadiono, S.C. Ogden, C. Hammack, B. Yao, G.R. Hamersky, F. Jacob, C. Zhong, K.J. Yoon, W. Jeang, L. Lin, Y. Li, J. Thakor, D.A. Berg, C. Zhang, E. Kang, M. Chickering, D. Nauen, C.Y. Ho, Z. Wen, K.M. Christian, P.Y. Shi, B.J. Maher, H. Wu, P. Jin, H. Tang, H. Song, G.L. Ming, Brain-Region-Specific Organoids Using Mini-bioreactors for Modeling ZIKV Exposure, Cell 165(5) (2016) 1238-1254.

[89] L.J. Millet, M.U. Gillette, New perspectives on neuronal development via microfluidic environments, Trends Neurosci 35(12) (2012) 752-61.

[90] S.N. Bhatia, D.E. Ingber, Microfluidic organs-on-chips, Nat Biotechnol 32(8) (2014) 760-72.

[91] S. Halldorsson, E. Lucumi, R. Gomez-Sjoberg, R.M.T. Fleming, Advantages and challenges of microfluidic cell culture in polydimethylsiloxane devices, Biosensors & bioelectronics 63 (2014) 218-231.

[92] V. van Duinen, S.J. Trietsch, J. Joore, P. Vulto, T. Hankemeier, Microfluidic 3D cell culture: from tools to tissue models, Curr Opin Biotechnol 35 (2015) 118-26.
[93] X. Yin, B.E. Mead, H. Safaee, R. Langer, J.M. Karp, O. Levy, Stem Cell Organoid Engineering, Cell Stem Cell 18(1) (2016) 25-38.
[94] Y. Fang, R.M. Eglen, Three-Dimensional Cell Cultures in Drug Discovery and Development, SLAS Discov 22(5) (2017) 456-472.
[95] J.L. Olson, A. Atala, J.J. Yoo, Tissue engineering: current strategies and future directions, Chonnam Med J 47(1) (2011) 1-13.
[96] N. Almouemen, H.M. Kelly, C. O'Leary, Tissue Engineering: Understanding the Role of Biomaterials and Biophysical Forces on Cell Functionality Through Computational and Structural Biotechnology Analytical Methods, Computational and Structural Biotechnology Journal 17 (2019) 591-598.
[97] G. Orive, E. Anitua, J.L. Pedraz, D.F. Emerich, Biomaterials for promoting brain protection, repair and regeneration, Nat Rev Neurosci 10(9) (2009) 682-692.
[98] Manuel Pérez-Garnes, J.A. Barcia, U. Gómez-Pinedo, M. Pradas, Ana, Vallés-Lluch, Materials for Central Nervous System Tissue Engineering, Intech2014.
[99] D.W. Hutmacher, Scaffold design and fabrication technologies for engineering tissues--state of the art and future perspectives, Journal of biomaterials science. Polymer edition 12(1) (2001) 107-24.
[100] NIST, Scaffold Fabrication: Airbrushed Scaffolds & Combinatorial Methods. https://www.nist.gov/mml/bbd/biomaterials/scaffold-fabrication-airbrushed-scaffolds-combinatorial-methods. 2020).
[101] N. Charles, Diffusion and related transport mechanisms in brain tissue, Reports on Progress in Physics 64(7) (2001) 815.
[102] B.S. Elkin, E.U. Azeloglu, K.D. Costa, B. Morrison, 3rd, Mechanical heterogeneity of the rat hippocampus measured by atomic force microscope indentation, Journal of neurotrauma 24(5) (2007) 812-22.
[103] A.J. Engler, S. Sen, H.L. Sweeney, D.E. Discher, Matrix elasticity directs stem cell lineage specification, Cell 126(4) (2006) 677-89.
[104] S. Liu, X. Chen, Y. Zhang, Hydrogels and hydrogel composites for 3D and 4D printing applications, 3D and 4D Printing of Polymer Nanocomposite Materials, Elsevier2020, pp. 427-465.

[105] N. Annabi, A. Tamayol, J.A. Uquillas, M. Akbari, L.E. Bertassoni, C. Cha, G. Camci-Unal, M.R. Dokmeci, N.A. Peppas, A. Khademhosseini, 25th anniversary article: Rational design and applications of hydrogels in regenerative medicine, Advanced materials 26(1) (2014) 85-124.
[106] B.V. Slaughter, S.S. Khurshid, O.Z. Fisher, A. Khademhosseini, N.A. Peppas, Hydrogels in regenerative medicine, Advanced materials 21(32-33) (2009) 3307-3329.
[107] Y. Li, J. Rodrigues, H. Tomas, Injectable and biodegradable hydrogels: gelation, biodegradation and biomedical applications, Chemical Society Reviews 41(6) (2012) 2193-2221.
[108] S.R. Caliari, J.A. Burdick, A practical guide to hydrogels for cell culture, Nature methods 13(5) (2016) 405-414.
[109] C.P. Barnes, S.A. Sell, E.D. Boland, D.G. Simpson, G.L. Bowlin, Nanofiber technology: designing the next generation of tissue engineering scaffolds, Advanced drug delivery reviews 59(14) (2007) 1413-33.
[110] X. Wang, B. Ding, G. Sun, M. Wang, J. Yu, Electro-spinning/netting: A strategy for the fabrication of three-dimensional polymer nano-fiber/nets, Progress in Materials Science 58(8) (2013) 1173-1243.
[111] A.L. Carlson, N.K. Bennett, N.L. Francis, A. Halikere, S. Clarke, J.C. Moore, R.P. Hart, K. Paradiso, M. Wernig, J. Kohn, Z.P. Pang, P.V. Moghe, Generation and transplantation of reprogrammed human neurons in the brain using 3D microtopographic scaffolds, Nat Commun 7 (2016) 10862.
[112] T.B. Puschmann, Y. de Pablo, C. Zanden, J. Liu, M. Pekny, A novel method for three-dimensional culture of central nervous system neurons, Tissue engineering. Part C, Methods 20(6) (2013) 485-92.
[113] G.C. Ingavle, J.K. Leach, Advancements in electrospinning of polymeric nanofibrous scaffolds for tissue engineering, Tissue engineering. Part B, Reviews 20(4) (2013) 277-93.
[114] A. Khademhosseini, R. Langer, A decade of progress in tissue engineering, Nat Protoc 11(10) (2016) 1775-81.

CHAPTER 3 Physically crosslinked graphene oxide-based conductive hydrogel substrate

The work presented in **Chapter 3** is largely based on the following publication: Xuelong Chen, Vivek Damodar Ranjan, Sijun Liu, Xiao Hu, Yilei Zhang. "*In situ* formation of 3D conductive and cell-laden graphene hydrogel for electrically regulating cellular behavior." *Macromolecular Bioscience.* (2021) 202000374. https://doi.org/10.1002/mabi.202000374

3.1 Background

Hydrogels are a group of soft materials composed of 3D hydrated networks of hydrophilic species, and have been widely explored as substrates for various tissue engineering applications owing to their excellent biocompatibility, high permeability and structural similarity to native extracellular matrix (ECM) [1, 2]. A plethora of hydrogel materials with diverse mechanical properties, crosslinking mechanisms and biological responses have been utilized for both *in vitro* as well as *in vivo* cell culture applications [3, 4]. Electroconductive hydrogels which harness conductive materials capable of regulating cell behavior are drawing great interest due to their ability to render scaffolds with both electrical and biological properties. Application of electrical stimulation via conductive hydrogels has been reported to enhance cell proliferation, migration and differentiation and at the same time, provides a valuable platform for study of electroactive tissues such as cardiac, neuronal and skeletal muscle [5, 6]. Various types of conductive fillers such as metal nanoparticles or nanowires [7-9] and carbon-based materials [10, 11] including graphene, fullerenes and carbon nanotubes (CNTs) have been utilized to fabricate electroconductive nanocomposite hydrogels. In addition, conjugated polymers with inherent electrical conductance such as polypyrrole [12], polythiophene [13],

polyaniline [14, 15] and poly(3,4-ethylenedioxythiophene) [16, 17] have also been used in producing electroconductive hydrogels.

In situ-forming hydrogels work on the principle of premixing cells with aqueous polymeric solutions before injecting it into defect sites and undergoing gelation [18]. It is advantageous over traditional pre-formed hydrogels because it is both minimally invasive during surgery and can also reach deep tissue defects with excellent adaptation to defect margins [19]. In this context, the development of electroconductive and injectable hydrogel-based scaffolds which are biocompatible, noncytotoxic and easy to synthesize is highly desirable. The purpose of this study is to fabricate a novel hydrogel satisfying aforementioned criteria and explore the feasibility of using it as a 3D *in vitro* cell culture platform. Herein, a new type of reduced graphene oxide (rGO) hydrogel crosslinked using polyvinyl alcohol (PVA) was prepared. The gelation of the physical hydrogel is mainly driven by hydrogen bonding between PVA and modified rGO whose main purpose is to form the structural component of the hydrogel. PVA is a synthetic polymeric, water-soluble biomaterial whose cytocompatibility is well-documented in various tissue engineering applications [20, 21]. Graphene is a 2-dimensional (2D) nanomaterial and its derivatives such as graphene oxide (GO), graphene quantum dots (GQDs), and rGO have emerged as new tools in tissue engineering and biomedical applications owing to their porous structure, abundant surface chemistry and tunable thermal/electric properties [22-25]. The rGO in this work was reduced from graphene oxide by polymerization of dopamine at the surface of GO. PDA has been reported to effectively reduce GO into rGO by undergoing self-polymerization, acting both as a reducing agent as well as a functionalization agent [26]. The purpose of using polydopamine as the reducing agent over other conventionally used

reagents such as hydrazine, $NaBH_4$, dimethylhydrazine, hydroquinone is its non-toxic/non-hazardous nature. Dopamine can also be polymerized under mild conditions and both dopamine/polydopamine are non-cytotoxic and biocompatible. In addition, simultaneous grafting of self-polymerized PDA on rGO due to its inherent strong adhesion to bulk substrates could enhance the hydrophilicity of the resulting scaffold and render it amenable to further surface functionalization via biomolecules [27]. Taking advantage of the sol-gel process, PC12 cells were loaded and dispersed in sol before gelation to realize instantaneous 3D uniform spatial distribution of cells within the hydrogel. Furthermore, the novel PDA engineered rGO/PVA hydrogel supported long-term cell viability, proliferation as well as highly efficient neuronal differentiation, even in the absence of external growth factors. This demonstrates the suitability of this platform as a biocompatible and electroconductive 3D *in vitro* substrate for tissue engineering applications. Besides, the physical hydrogel can also be squeezed out of a needle syringe without clogging, indicating its potential as a promising candidate for *in vivo* cell delivery/transplantation.

3.2 Materials and Methods

3.2.1 Preparation of PDA grafted GO

Purified natural flake graphite powder was supplied by Superior Graphite Company, USA. Potassium permanganate and PVA (Mw 85000~124000, 87~89% hydrolyzed) were purchased from Sigma Aldrich. Sodium nitrate and dopamine hydrochloride (99%) were purchased from Alfa Aesar. Sulfuric acid (95~97%) was bought from Honeywell. Hydrogen peroxide (30% in water) was bought from VWR. Hydrochloric acid, PBS solution and tris buffer solution were provided by Merck, Gibco and Regent Chemicals Pte Ltd respectively.

Graphene oxide (GO) was prepared according to the modified Hummer's method (**Appendix A1**) [28]. To prepare PDA modified GO, 30 mg as prepared GO solution (6.3 mg/ml, 189 mg in total) was mixed with 450 ml autoclaved PBS. At the same time, 94.5 mg dopamine was dissolved in 20 ml PBS and filtered by 100 nm sized filter, after which it was transferred into GO/PBS solution, giving GO/PVA mass ratio 1: 0.5. 5 mg tris solution was also filtered and added into the solution to trigger the reaction. Then, the solution was allowed for reaction at 60^{o}C for 2 hours, followed by 100^{o}C for 10 min for sterilization. Afterwards, the PDA modified GO (PDA-GO) was concentrated by centrifuge (10000 rpm, 10 min for each cycle) and obtain the final solution with concentration around 8~9 mg/ml. To determine the concentration, 0.5 ml solution was transferred into a vial and weighed after completely dried in the oven overnight. Note that the concentration of pure PBS solution should be taken into account i.e., 11.287mg/ml, in order to obtain the true value of PDA-GO concentration.

3.2.2 Synthesis of hydrogel

PVA was dissolved in PBS solution by magnetic stirring at an elevated temperature. The hydrogel without cell seeding was prepared by mixing specific amounts of rGO-PDA and PVA solution (mass ratios of 10:1, 5:1, 2:1 with rGO-PDA at a final concentration 6 mg/ml) and shaken by hand for several seconds. PVA solution was prepared in accordance with the concentration of rGO-PDA. A mass ratio of PDA-GO/PVA = 5: 1 and volume of 500 µl was used in the final 3D rGO-PDA-PVA hydrogel scaffold utilized for cell culture.

3.2.3 Characterization

The as prepared GO was examined by transmission electron microscope (Carl Zeiss Libra 120 Plus). The morphology of GO and rGO-PDA was studied by field

emission scanning electron microscopy (FESEM) (JEOL JSM-7600F). The samples were prepared by dropping the solutions onto copper tape and dried at 60^{o}C in vacuum oven for evaporation, resulting in self-standing sample films which were then fixed to the SEM sample holder using copper tape for observation. EDS was conducted under 20 kV using JEOL JSM-7600F. Fourier transform infrared spectroscopy (FTIR) spectra were recorded by PerkinElmer Frontier spectrometers, with resolution of 2 cm^{-1} for 32 scans. X-ray photoelectron spectroscopy (XPS) measurement was carried out on an AXIS Supra X-ray photoelectron spectrometer (Kratos Analytical Ltd. U.K.). The spectra were calibrated with reference to C1s at 284.8 eV. The viscoelastic properties of hydrogels were measured by a Discovery hybrid rheometer (DHR-3, TA Instruments, USA). The tests were performed at oscillation mode using a 25 mm parallel plate, with frequency from 0.01 to 100 Hz and 2.5% strain at room temperature. The sheet resistance was measured using Four-point probes (Mitsubishi Loresta GP).

3.2.4 Cell culture

Rat pheochromocytoma 12 (PC12) cells used in this experiment were purchased from the Institute of Biochemistry and Cell Biology, SIBS, CAS (Shanghai, China). The cells were cultured in maintenance media composed of high glucose-DMEM medium supplemented with 10% fetal bovine serum, 5% horse serum, and 1% penicillin–streptomycin. All cells were passaged using trypsin/EDTA 0.25% w/v trypsin/0.02% EDTA) and incubated in a humidified atmosphere incubator with 5% CO2, 37oC, and 95% humidity. To encapsulate cells inside the hydrogel, the PVA solution is first mixed with the required number of cells. The PDA-GO solution is pipetted into each well of a sterile 24-well plate after which the PVA solution containing cells is added; the final volume of the mixture is always maintained at

500 µl. The mixture is then shaken to ensure uniform distribution of cells as well as triggering gelation, thus resulting in the formation of rGO-PDA-PVA hydrogel with encapsulated cells in a single step. The cell seeding density was optimized to 5×106 cells per hydrogel scaffold to ensure an even spatial distribution of cells in all regions of the scaffold. 1.5 ml of fresh culture media was then added to each well and then placed in the incubator. Media change was performed daily for the duration of cell culture. Glass coverslips coated with Poly-L-Ornithine (PLO) (Sigma) solution were used as 2D controls for assessing cell differentiation. Coverslips were placed in a 24-well plate during culture and cell seeding density used was 0.4×10^6 per coverslip.

3.2.5 Electrical Stimulation

To study the effect of electrical stimulation (ES) on cell culture, PC12 cells were encapsulated inside the hydrogel scaffolds using a self-made bioreactor with a direct coupling set-up inside each culture well [29]. A continuous 100-Hz pulsed waveform of 100 mV/cm was applied across the electrodes using a function generator (AFG3022C, Tektronix) for 4 h every day in the incubator starting from day 1 (**Appendix A2**). Stainless steel needles were used as electrodes and were kept in direct contact with the graphene-based hydrogel containing cells. The cells were incubated for 7 days with media change being done on daily basis prior to electrical stimulation (ES). The maintenance media was replaced with differentiation media composed of high glucose-DMEM medium supplemented with 1% horse serum, and 1% penicillin–streptomycin from day 1. NGF (NGF 2.5S Life Technologies) at a concentration of 100 ng/ml was added to the differentiation media to stimulate neuronal differentiation as required.

3.2.6 *In vitro* cytoactive assays

PC12 cell proliferation was evaluated and quantified using PrestoBlue (Life Technologies) assay according to manufacturer's instructions on days 1, 3 and 5. Suitable sized hydrogel scaffolds were fabricated using a 96-well plate with a cell seeding density of 1×10^5 cells per well and cultured for specific durations. Cell nuclei were stained with 4′,6-diamidino-2-phenylindole dihydrochloride (DAPI) (1:200) and stored at 4°C overnight. Cells were washed thrice with 1×PBS and visualized after sectioning of the scaffold using both brightfield and fluorescence microscopy (Nikon, TI-DH, Japan). Simultaneous evaluation of cytoplasmic function and membrane integrity was carried out using the Live/Dead Viability/Cytotoxicity Kit (Life Technologies) for mammalian cells. Cells were rinsed twice with PBS, and cell viability was assessed according to the manufacturer's protocol. Viability of encapsulated cells in different hydrogel scaffolds, both with and without electrical stimulation were measured in triplicate and quantified.

3.2.7 Immunocytochemistry

Immunofluorescence staining was carried out to characterize cell phenotypic changes which occurred over the course of proliferation/differentiation culture. Both 2D coverslips and cell-laden 3D hydrogel samples were rinsed in 1×PBS and fixed using 4% paraformaldehyde (Hito) for 30 min at room temperature. Next, cells were permeabilized in 0.1% Triton X-100 (Biochemica) for 30 min and blocked in 1% bovine serum albumin (BSA) (Sigma) for 45 min at room temperature. Cells were then incubated with antibodies overnight at 4ºC with commercially available primary antibodies: mouse anti-microtubule-associated protein-2 (MAP2) (1:250, Sigma), rabbit anti-Ki67 (1:200, Abcam). Finally, they were fluorescently labelled

with appropriate secondary antibodies: goat anti-rabbit Alexa Fluor 555 (1:250, Invitrogen) and donkey anti-mouse Alexa Fluor 488 (1:250, Invitrogen) overnight at 4ºC, after which they were counterstained with fluorescent nuclear dye DAPI (1:200, Sigma).

3.2.8 Cryosectioning and Imaging

Labelled cell-laden hydrogel scaffolds were embedded in Tissue-Tek O.C.T. Compound (Sakura) and placed at -20ºC. Frozen sections of 50 μm thickness were sectioned using a cryotome and mounted on poly-lysine adhesive glass slides using Dako fluorescent mounting medium. Thereafter, confocal laser scanning microscopy (Olympus Fluoview FV1000) was used to visualize fluorescence/bright-field images of both 2D coverslips as well as 3D scaffold sections at desired magnification. The immunofluorescent images were quantitatively analyzed using ImageJ. Constant image size, magnification, and imaging parameters were used for all measurements. Three random, separate fields for each sample were recorded followed by image analysis using custom ImageJ macros for region of interest (ROI) selection and cell counting. Positive cells were identified as cells with fluorescence intensity thrice or more above background level. First, the images were split into separate channels using stack viewing option in ImageJ [30]. The images were then converted to binary style and the pixel intensity threshold values were adjusted to a suitable level to identify individual cells. In the case of images containing densely packed cells, the watershed segmentation algorithm within ImageJ was used to delineate nuclear boundaries in both 2D and 3D binary images after converting them to masks [31]. Next, the Analyze Particles tool was used to filter out different sizes of particles and count only those objects which are very circular by adjusting the Circularity range numbers in the segmented images. This process of cell counting was done for all

channels in each image which correspond to the specific antibodies stained including DAPI. Finally, the average percentage ratios of the total cell number stained for each marker to that of DAPI were determined and the corresponding data were plotted using bar charts for the respective groups (2D and 3D). The morphology of PC12 cells cultured on different scaffolds was also observed via scanning electron microscopy (SEM). On day 7 after cell seeding, the samples were fixed with 3% glutaraldehyde for 2h and washed thrice with 1×PBS. Samples were subsequently dehydrated using graded concentrations (50, 70, 90, and 100% v/v) of ethanol for 15 min each. Samples were then subjected to critical point drying after which they were sputter coated with a thin layer of gold for 20s using a current of 20 mA (JEOL JFC 1600 Auto Fine Coater). Cell morphology was observed using a scanning electron microscope (SEM, JSM-6701F, JEOL) at an accelerating voltage of 10 kV.

3.2.9 Statistical analysis

The results presented are representative data sets and all experiments were performed in triplicates at a minimum of three independent events. Statistical analysis was done using unpaired Student's two-tailed t-test. Quantitative data were expressed as mean ± standard deviation (SD). Differences were considered statistically significant when $p^* < 0.05$ (GraphPad Prism).

3.3 Results and Discussion

3.3.1 Fabrication of rGO-PDA

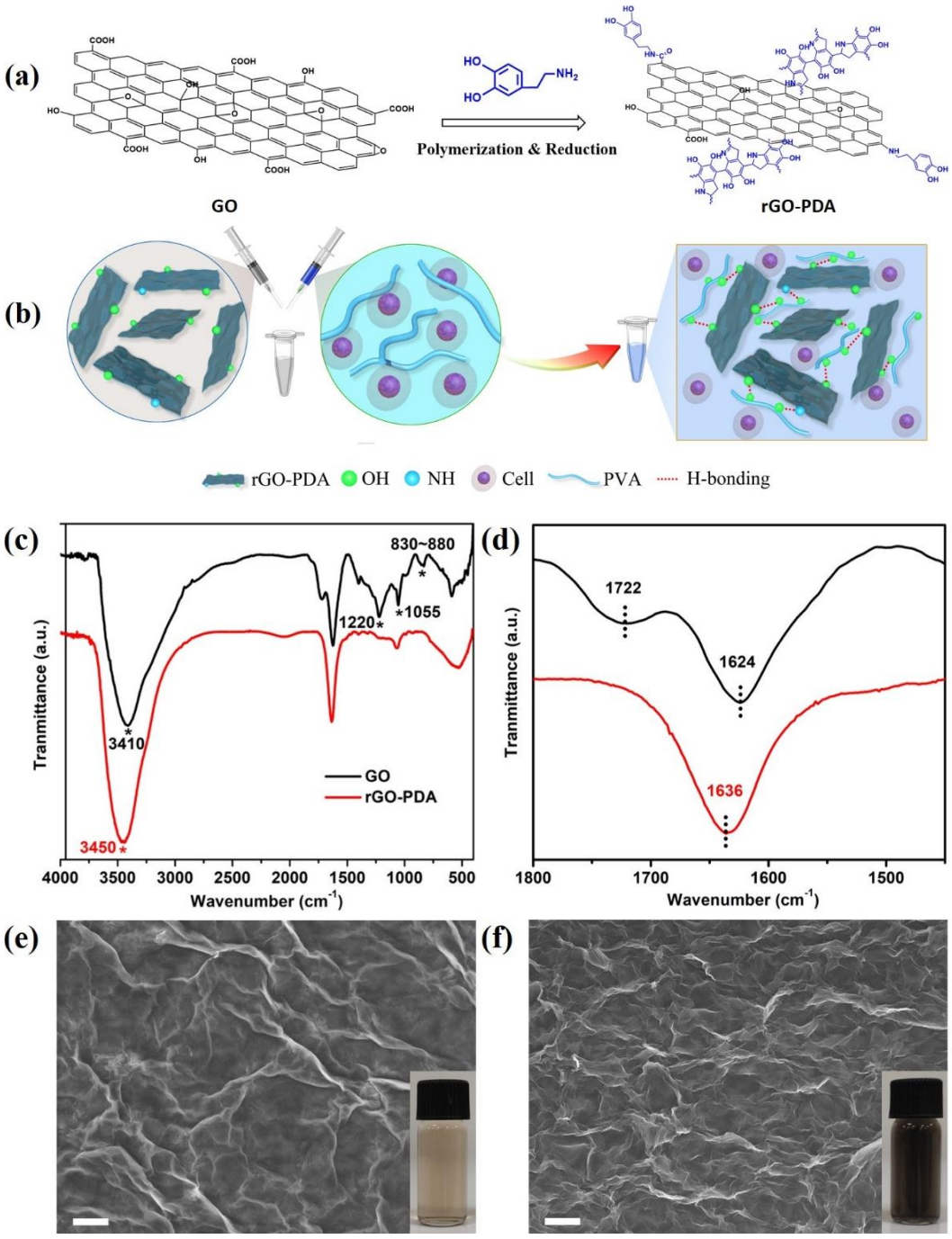

Figure 3-1. Fabrication of novel 3D conductive, cell-laden hydrogel. Schematic illustration of fabrication of (a) rGO-PDA, graphene oxide was reduced by dopamine to restore the electrical conductivity of graphene, while simultaneously enhancing both hydrophilicity and biocompatibility of reduced graphene oxide; (b) 3D conductive cell-laden hydrogel, which can be formed by simply mixing cell-containing PVA solution and PDA functionalized rGO, instantly achieving a 3D spatially distributed cells in the hydrogel; FTIR spectra of GO and rGO-PDA with

wavenumber (c) 4000~500 cm-1 (d) and 1800~ 1450 cm-1; (e, f) SEM image of GO and rGO-PDA (insets show digital images of dilute GO and rGO-PDA solution, scale bar is 10 μm).

The objective of this work is to fabricate an electroconductive and injectable hydrogel that can be used as a cell culture platform. The two constituents of the hydrogel are graphene derivative and PVA, which is hypothesized to be connected via hydrogen bonding. Firstly, the starting material GO (**Appendix A1**) underwent reaction with dopamine (**Figure 3-1a**), whose purpose is to reduce GO and restore electrical conductivity and at the same time, also improve the cytocompatibility by increasing hydrophilicity via self-polymerized PDA coating on the surface. To achieve injectability as well as instantaneous uniform spatial cell distribution within the hydrogel construct, the cells were pre-dispersed in PVA solution at pre-defined cell density prior to mixing with the rGO solution (**Figure 3-1b**). Though oxygen containing groups were significantly removed during the reduction process, the PDA wrapping on rGO surface provided a plenitude of hydroxyl and amine moieties, which can undergo hydrogen bonding with PVA after shaking. FTIR was used to study the functional groups on GO and rGO-PDA with results shown in **Figure 3-1c-d**. There are plenty of oxygen-containing groups on surface of GO. The peak at 1722 cm^{-1} is ascribed to the C=O group while peaks at 1220, 1055 and 830~880 cm^{-1} are contributed by the absorption of C-O in various groups. These peaks disappeared or significantly reduced in rGO-PDA, suggesting the successful reduction reaction of GO by dopamine. The peak at 1624 cm^{-1} due to C=C in aromatic structure of GO shifted to 1636 cm^{-1} because of the combination with N-H absorption after reaction with dopamine. The strong and wide peaks at 3410 and 3450 cm^{-1} are due to the existence of O-H in GO and coexistence of O-H and N-H in rGO-PDA respectively.

The morphologies of GO and rGO-PDA are different. One droplet of GO and rGO-PDA in water was dropped on copper tape, dried and observed by SEM, with results shown in **Figure 3-1e-f**. Compared with GO, the rGO-PDA seems to be porous and rougher. This is probably because GO possesses large number of functional groups which can form strong interactions between its layers, and these multiple layers could stick to each other firmly thus after solvent evaporation. In contrast, after reduction reaction by DA, functional groups are significantly removed leading to weak interaction between layers. In addition, the excessive DA self-polymerized particles/layers can also serve as barriers between rGO layers. The inset images show GO and rGO-PDA solution with similar concentrations. The GO solution is typical light yellow while rGO-PDA turns into black, indicating the successful coating of PDA on the surface of reduced GO. TEM of GO and rGO-PDA is illustrated in **Appendix A3**.

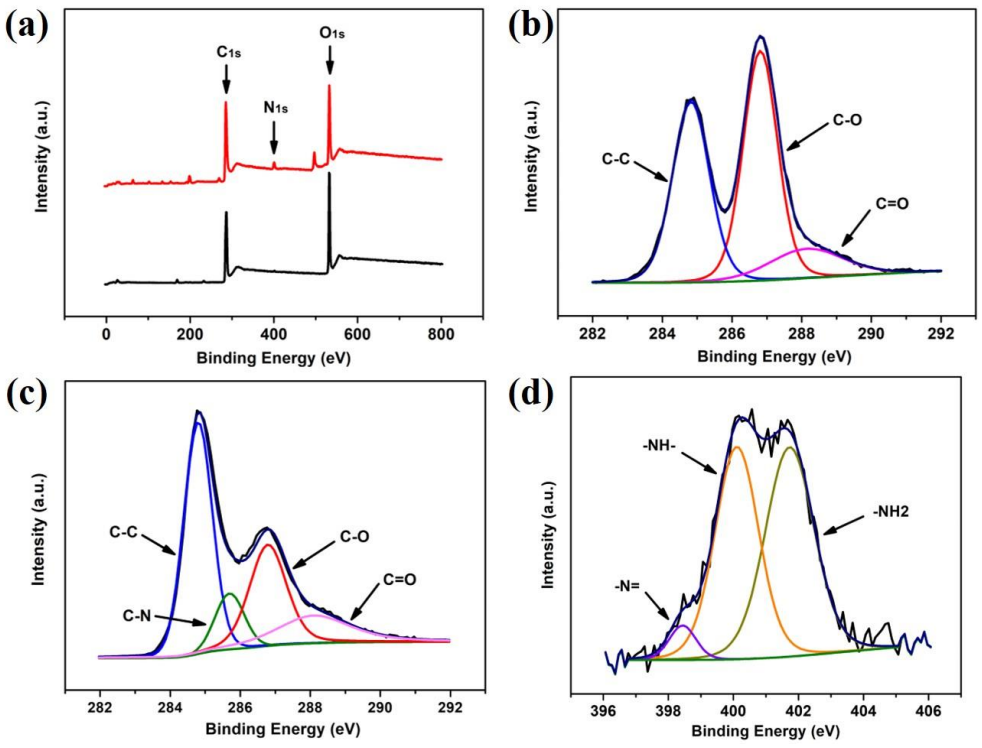

Figure 3-2. XPS spectra of GO and rGO-PDA; (a) wide scan; (b) convoluted C1s of GO (c) convoluted C1s of rGO-PDA; and (d) convoluted N1s of rGO-PDA.

Element analysis for samples before and after reaction was carried out using XPS; the results are shown in **Figure 3-2**. It is seen that after reaction with dopamine (**Figure 3-2a**) the C/O ratio increased, along with the emergence of nitrogen peak because of PDA wrapping on the surface of GO. The presence of many weak peaks in rGO-PDA spectrum are due to sodium, phosphorus, chlorine etc. present in PBS solution as the reaction between GO and dopamine is conducted in PBS medium. Typical high resolution C1s spectrum of GO (**Figure 3-2b**) can be fitted into three peaks at 284.8 eV, 286.8 eV and 288.1 eV, which correspond to C-C, C-O and C=O species respectively [32]. After reaction with dopamine, the oxygen containing groups significantly decreased, as shown in **Figure 3-2c**, indicating the successful reduction of GO. The new peak appears at 285.7 eV and is attributed to the C-N bonding. The convoluted N1s in rGO-PDA (Figure 2d) contains three peaks at 398.4 eV, 400.1 eV and 401.7 eV, which are ascribed to -N=, -NH- and -NH_2, respectively. All these groups combined with hydroxyl groups on PDA will be able to induce hydrogen bonding with PVA molecules, facilitating the formation of hydrogel.

3.3.2 Fabrication of rGO-PDA-PVA hydrogel

The rGO-PDA-PVA composite hydrogel was prepared by mixing rGO-PDA and PVA solution followed by vigorous shaking for a few seconds to disperse these two components into each other. Specific volumes of rGO-PDA and PVA solution were used to make up the total volume of 500 µl composed of rGO-PDA: PVA at mass ratios of 10:1, 5:1 and 2:1 respectively. The formation of hydrogel was examined by the tube inversion method as shown in **Figure 3-3a**. It was observed that hydrogel formation can occur when mass ratios are 10:1 and 5:1, while no stable hydrogel was observed for 2:1 with the solution flowing down along the bottle wall in this case. As control sample, the rGO-PDA solution cannot undergo gelation with PBS

solution in the absence of PVA. The hydrogen bonding interactions between rGO-PDA nanosheet and linear PVA chains is believed to be the dominant crosslinking mechanism leading to gelation. It is reported that as-prepared GO without reduction is able to form hydrogels with PVA and Pluronic solution mainly through hydrogen bonding [33, 34]. Graphite oxide could also form hydrogen bonding with PVA via the large amount of hydroxyl and carboxyl group on the surface [35]. Though oxygen containing groups were largely removed during the reduction process, the wrapping of PDA replenishes plenty functional moieties, such as hydroxyl, amine groups etc., that are capable of creating hydrogen bonding with PVA molecules resulting in gelation between PVA and rGO-PDA; see schematic illustration in **Figure 3-3b**.

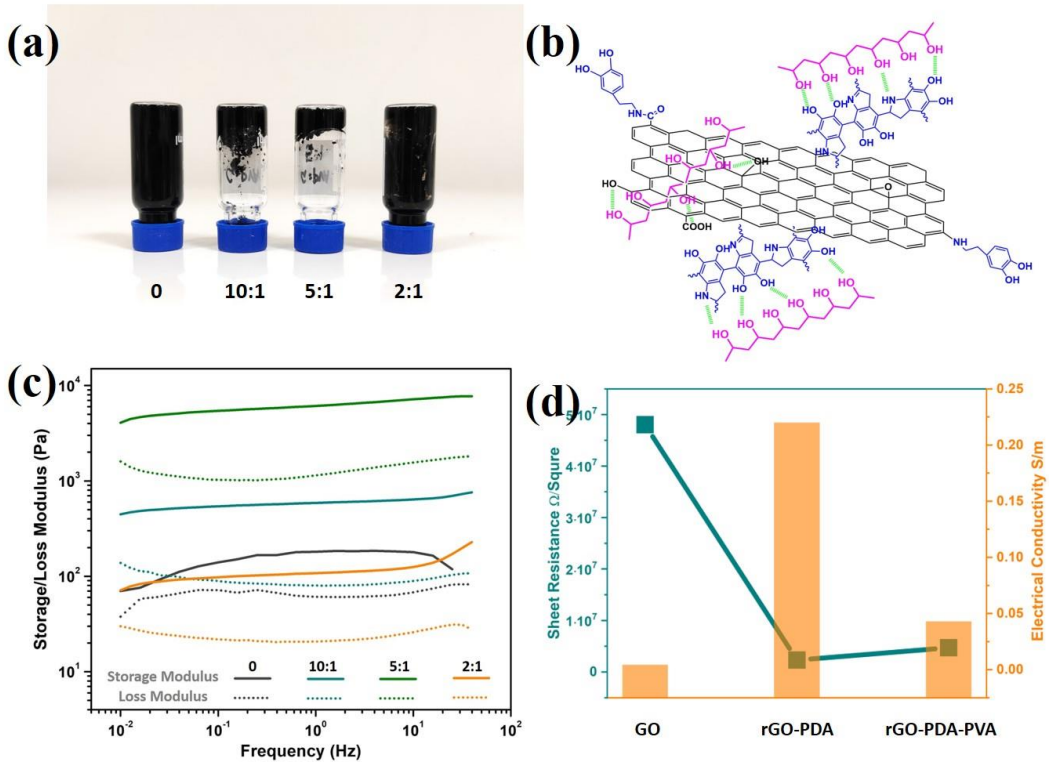

Figure 3-3. (a) Photographs of rGO-PDA mixed with PVA solution using different mass ratios showing the gelation; (b) Schematic representation of formation of hydrogen-bonded network between PVA and rGO-PDA nanosheet; (c) Viscoelastic properties of hydrogel; (d) sheet resistance and electrical conductivity of GO, rGO-PDA and dried hydrogel (rGO-PDA-PVA).

The viscoelastic properties of hydrogel were studied using a rheometer with storage and loss modulus as shown in **Figure 3-3c**. It was observed that the storage moduli for mass ratios 10:1 and 5:1 were quite high, owing to the crosslinking of PVA and rGO-PDA. Moreover, the hydrogel with mass ratio 5:1 had the highest mechanical performance, better than those with higher (2:1) or lower PVA (10:1) loading, which seems to indicate that there is an optimum ratio between PVA and rGO-PDA. With lower loading of PVA, the PVA molecules can serve as valid crosslinker between two or multiple reduced graphene sheets. Thus, with the increase in PVA loading, a stronger network could be expected. However, at higher loading excessive PVA chains are unable to directly connect with graphene sheet and exist as free molecules, weakening its capability for hydrogel formation and leading to weaker hydrogel as observed by its poorer mechanical properties. Other factors may also affect the hydrogel strength. For example, smaller GO platelets and shorter polymer crosslinker are unfavorable in forming hydrogels, as the former tend to form a less stable network and the latter has less probability to connect two or more graphene sheets [36]. The cationic ions in the PBS solution could form coordination bond with electronegative oxygen in rGO, which may also affect the hydrogen bonding between rGO and PVA and thus influence the hydrogel strength.

The sheet resistance of GO, rGO-PDA and hydrogel was measured using the four-probe method to assess the electrical conductivity of GO before and after PDA reduction treatment (**Figure 3-3c**). Each sample was tested thrice, and average values were calculated. The sheet resistance (R_s) of GO, rGO-PDA and rGO-PDA-PVA are 48, 2.3 and 4.6 M Ω/sq respectively. According to $Rs = \rho / t$ and $\sigma = 1 / \rho$, where ρ is the electrical resistivity, the electrical conductivity σ of all three samples were then determined i.e. 4.2×10^{-3}, 0.22 and 4.3×10^{-2} S/m respectively.

It is obvious that after PDA reduction, the electrical conductivity of rGO increases significantly owing to the restoration of the crystalline structure of graphene. Considering the fact that the dopamine is excessive in the reaction and the excess polymerized PDA is coated on the surface, the real electrical conductivity of rGO should be much higher. After the introduction of PVA, the electrical conductivity decreases, due to the intrinsic insulation of PVA. It must be noted that during cell culture, the electrical impulses could be directly transferred from the conductive PBS solution to reduced graphene oxide. The conductivity values of rGO-PDA and rGO-PDA-PVA are comparable with existing modified polymer-based conductive scaffolds which were utilized for *in vitro* cell culture. For instance, Moroder et al. fabricated conductive polymer composite-based scaffolds composed of polycaprolactone fumarate and polypyrrole (PCLF-PPy) with conductivity values ranging between 0.17~0.6 S/m, which in turn supported cell attachment, proliferation and neurite extension [37]. Similarly, Guarino et al. synthesized conductive poly(ethylene glycol) diacrylate-polyaniline (PEGDA-PAni) hybrid materials with a conductivity of $(1.1 \pm 0.5) \times 10^{-3}$ mS/cm and demonstrated enhanced cell-material response in both PC12 and hMSC cells using this scaffold [38]. On these lines, the rGO-PDA-PVA hydrogel scaffold was assessed in terms of its suitability for 3D cellular culture as well as application of electrical stimulation to regulate cell behavior.

3.3.3 *In vitro* cell culture: Cell viability and proliferation

The application and performance of the hydrogel for *in vitro* cell culture was evaluated using the PC12 cell line, which can differentiate into neuron-like cells in response to specific environmental cues [39]. DAPI live fluorescence staining of the cell nuclei was utilized to visualize cells encapsulated inside the scaffold 12 hours

after hydrogel formation as shown in **Figure 3-4a**. The images clearly confirm the ability of the hydrogel to encapsulate cells in large numbers along with a uniform spatial distribution of cells throughout the scaffold. Few free-floating cells were observed in the culture media (data not shown) indicating that majority of seeded cells were entrapped inside the hydrogel as desired. Next, growth and proliferation of the encapsulated PC12 cells was then assessed and compared using PrestoBlue assay on days 1, 3 and 5 after cell seeding (**Figure 3-4c**). Results were normalized to the cell number data obtained for day 1 which was set at 100%. A significant increase in cell proliferation was observed on both days 3 ($p < 0.01$) and 5 ($p < 0.001$) with cell numbers increasing by 285% and 364% respectively. However, increase in cell number was found to be lower between days 3 and 5 ($p < 0.05$) compared to that between days 1 and 3 ($p < 0.01$). Increased cell clumping was observed by day 5, possibly owing to the large number of cells present in the hydrogel and the tendency of the PC12 cells to form floating cell aggregates [40].

Finally, viability of encapsulated cells was assessed using Live/Dead staining assay to evaluate the cytotoxicity of the 3D hydrogel scaffold, both with and without electrical stimulation on days 1, 3 and 5. Living cells stain for calcein-AM (green) and dead cells stain for ethidium homodimer (red). Representative fluorescence images are illustrated in **Figure 3-4b**, and percentage fractions of live cells for both conditions are presented in **Figure 3-4d** for quantitative comparison. The results indicate that nearly 99% of seeded cells were viable one day after seeding which clearly demonstrates the non-cytotoxicity of the 3D hydrogel scaffold for PC12 cells. Furthermore, ~93% and ~90% of cells stained positive for Calcein-AM (green) on days 3 and 5 respectively, with no significant difference observed between those scaffolds subjected to electrical stimulation and those without. This suggests that the

application of pulsed electrical stimulation for the duration of culture did not negatively impact the cells or result in cell death. Taken together, the cell viability results demonstrate the *in vitro* cytocompatibility of the rGO-PDA-PVA hydrogel substrate for long term 3D cellular culture which is consistent with previous studies using graphene-based scaffolds [41-43].

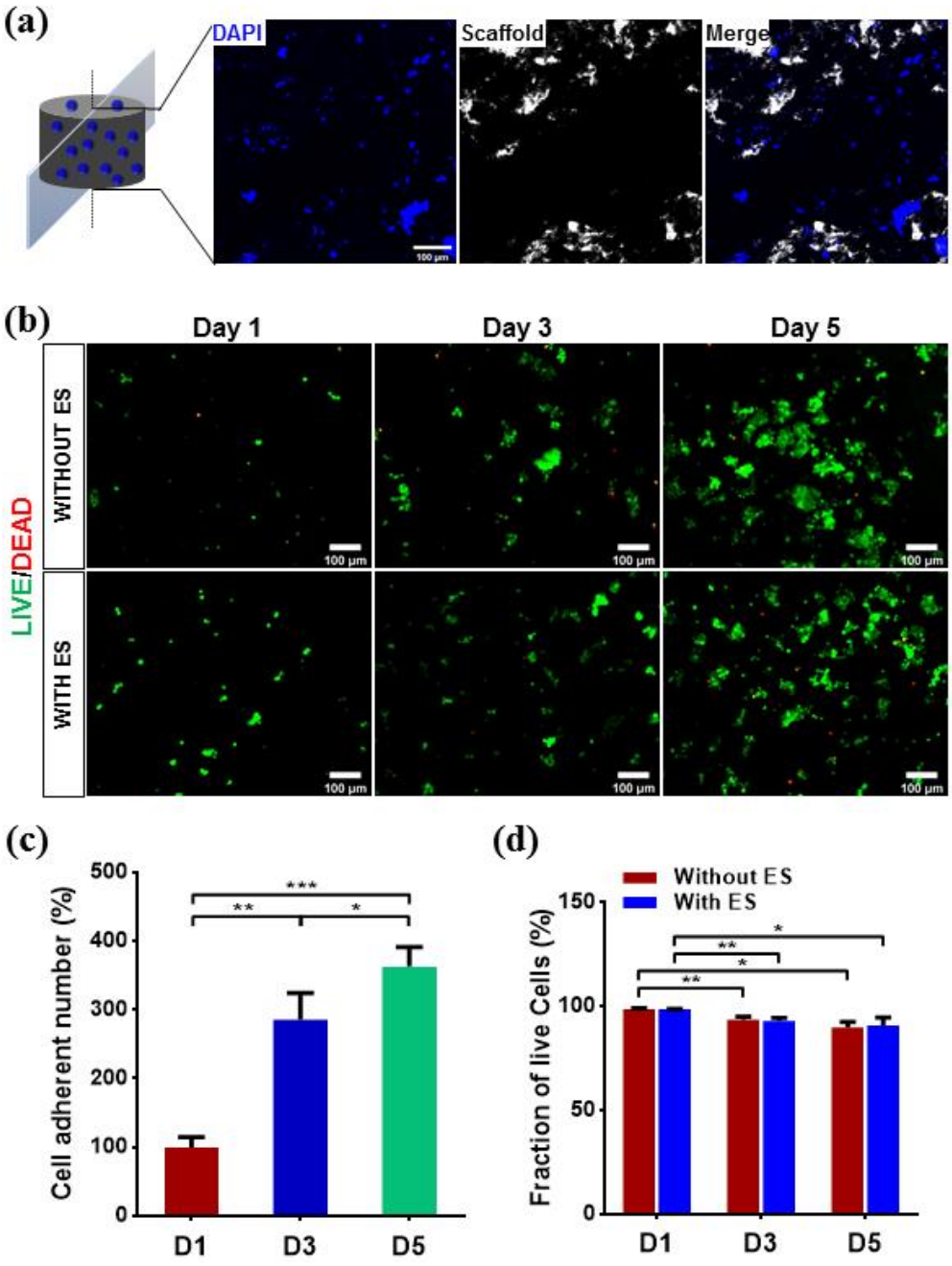

Figure 3-4. (a) Confocal fluorescent microscopy images showing PC12 cells encapsulated inside scaffold cross-section 12h after cell seeding - nuclei were

counterstained with DAPI (blue); (b) Fluorescence microscopy images indicating cell viability: Live\dead viability test performed on days 1, 3 and 5 after cell seeding (green: Calcein-AM indicating live cells; red: ethidium homodimer indicating dead cells); (c) Quantification of PrestoBlue assay results indicating relative number of PC12 cells adhered to scaffold on days 1, 3 and 5 after cell seeding; (D) Quantification of live/dead staining results showing percentage of live cells present inside the scaffold on days 1,3 and 5 after cell seeding; Data are expressed as mean ± SD (n = 3), *$p < 0.05$, **$p < 0.01$, ***$p < 0.001$.

3.3.4 Enhanced neuronal differentiation in 3D rGO-PDA-PVA hydrogel scaffolds

The influence of the 3D graphene-based hydrogel scaffold in regulating neuronal differentiation of PC12 cells was assessed via immunocytochemistry and compared with 2D monolayer culture. It is well reported that the treatment of PC12 cells with nerve growth factor (NGF) induces cessation of cell division, neurite extension, electrical excitability and expression of neuronal markers [39, 44, 45]. In this regard, the differentiation of cells in 2D and 3D cultures was examined by staining for microtubule-associated protein 2 (MAP2), both with and without application of NGF after 7 days of culture. MAP2 is a neuronal cell marker expressed specifically in their perikarya and dendrites [46]. In addition, Ki-67 marker was utilized to stain for proliferating cells, thereby distinguishing them from differentiating cells. Representative confocal microscopy images of labelled cells for both cases are illustrated in **Figure 3-5a**, and the corresponding percentage of differentiating cells identified by positive MAP2 staining on D7 has been quantified as illustrated in **Figure 3-5b**. In the case of 2D culture, cells differentiated only with the application of NGF, whereas untreated cells continue to proliferate, staining positive only for Ki67 marker. In contrast, 3D culture of PC12 cells encapsulated within the rGO-PDA-PVA hydrogel resulted in 52.72 ± 7.79% of total cells showing $MAP2^+$ staining without NGF treatment, which is significantly higher ($p < 0.001$) than the 2D

cultures which did not show cell differentiation as expected. After treatment with NGF, 66.44 ± 7.97% and 78.31 ± 7.00% cells stained positive for MAP2 in 2D and 3D cultures respectively, increased neuronal differentiation again observed in the scaffold-based culture.

The results clearly demonstrate that 3D culture within the hydrogel-based scaffolds are able to induce neuronal differentiation of PC12 cells, negating the need for expensive NGF treatment which is necessary in the case of 2D monolayer cultures. However, neurite formation and extension in differentiated cells was observed only in the case of 2D culture, the cell bodies showing a flat, spread-out morphology. Cells encapsulated in the hydrogel retained a spherical morphology and aggregated to form large clusters after a few days of culture. The coverslips are coated with PLO which promotes cell adherence, whereas in 3D culture, the cells tend to aggregate and exhibit poor attachment due to their inherent inability to adhere to non-coated surfaces [40, 47]. Moreover, the hydrophobicity of the reduced graphene oxide is not conducive for cell adherence as well as neurite outgrowth in spite of incorporating bioinspired PDA, and thus needs to be improved in terms of surface functionalization. Nevertheless, rGO-PDA-PVA hydrogel-based 3D culture enhanced neuronal differentiation of PC12 cells compared with monolayer culture conditions, which is possibly the result of cell-material interactions including the physicochemical interplay of cells with the graphene-based microenvironment [48]. The molecular mechanisms underlying graphene induced cellular neurogenesis have not fully been revealed, although, increased neuronal differentiation in graphene substrates have been attributed to the influence of numerous factors such as: micro-scale topographic features including surface roughness, curvature and anisotropicity [41]; complex 3D microarchitecture with interconnected pores mimicking *in vivo*

conditions [49]; elasticity and stiffness of the scaffold [50]; upregulation of genes related to calcium signaling pathways [42]; as well as higher capability of rGO for electron transfer [51].

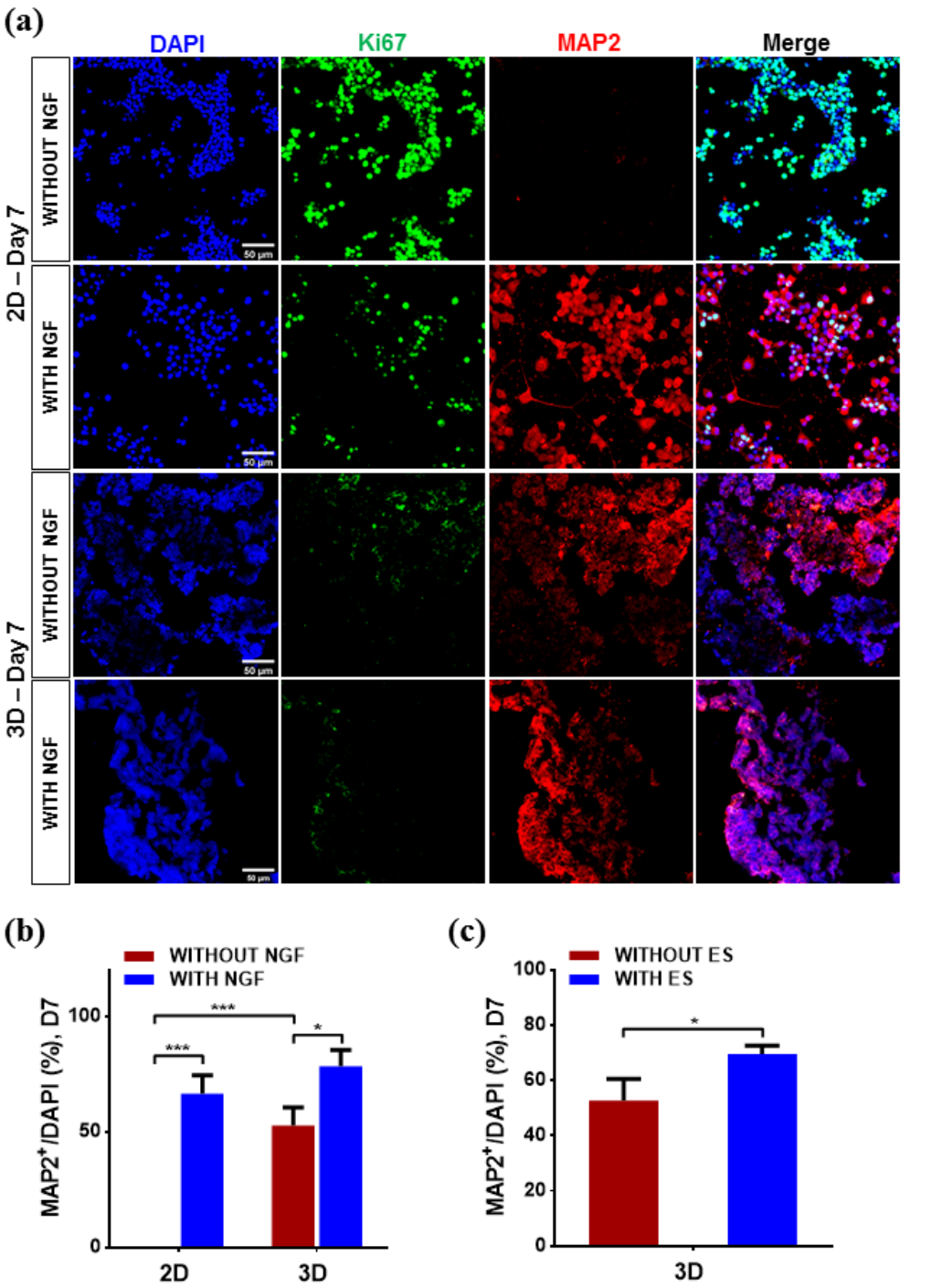

Figure 3-5. (a) Confocal fluorescent microscopy images indicating PC12 cell proliferation and differentiation in 2D and 3D cultures as stained for Ki67 (green) marker and MAP2 (red) marker respectively on D7 without and with application of NGF; Nuclei were counterstained with DAPI (blue); Quantification of immunostaining

results showing percentage positive staining of neuronal differentiation marker MAP2 normalized to DAPI on D7 (b) for 2D and 3D culture – without and with application of NGF and (c) for 3D culture – without and with electrical stimulation; Data are expressed as mean ± SD (n = 3), *$p < 0.05$, **$p < 0.01$, ***$p < 0.001$.

The application of electrical stimuli as a biophysical cue in regulating *in vitro* cell behavior including proliferation, differentiation as well as neurite outgrowth and extension is well reported in tissue engineering [52, 53]. In this regard, the influence of ES on neuronal differentiation of PC12 cells cultured within the conductive rGO-PDA-PVA substrate for a duration of one week was investigated using immunocytochemistry and compared with controls cultured without ES using setup depicted in **Appendix A2**. The percentage of differentiated cells identified by MAP2 positive staining in both cases were quantified as shown in **Figure 3-5c**. 69.56 ± 3.01% of total cells cultured with ES showed $MAP2^+$ staining, significantly higher ($p < 0.05$) than controls where 52.72 ± 7.79% of total cells were $MAP2^+$. This is consistent with previous studies where application of ES in the absence of NGF resulted in neuronal differentiation of PC12 cells [54], including extension of neurites via activation of *c-fos* mRNA expression [55]. However, visualization of cellular morphology of differentiated cells using SEM revealed the absence of neurites in both cases (with and without ES) as shown in **Appendix A4**. The high-resolution SEM images of the hydrogel cross-section clearly show that cells retained a spherical morphology even after differentiation or application of ES. Furthermore, majority of the cells were clustered together throughout the hydrogel confirming the tendency of cells to form clumps/clusters as observed in the immunofluorescence images. The hydrophobicity of the rGO scaffold along with the lack of ECM protein-based surface functionalization may have also caused the absence of neurite formation in addition to poor cell adherence. Nevertheless, the rGO-PDA-PVA

hydrogel substrate demonstrates great potential as a 3D electroconductive substrate for *in vitro* cellular culture, capable of supporting enhanced cell encapsulation, excellent cell viability, and highly efficient neuronal differentiation.

3.4 Conclusion

Electroconductive and injectable hydrogel-based scaffolds are attracting increasing attention in the study of electrically induced regulation of cell behavior, tissue engineering of electroactive tissues as well as achieving minimum invasiveness during tissue repair. In this work, a novel reduced graphene oxide (rGO)/polyvinyl alcohol (PVA) composite hydrogel was prepared, intended as a 3D electroconductive substrate for electrical stimulation of cells in culture. Graphene oxide was reduced and functionalized by dopamine to restore the electrical conductivity of graphene, while simultaneously enhancing hydrophilicity and biocompatibility. Cell encapsulation within the hydrogel was achieved by simply mixing the polydopamine (PDA) functionalized rGO (rGO-PDA) solution with the PVA solution containing dispersed cells. Instantaneous and uniform 3D spatial distribution of cells was achieved during hydrogen bonding-induced hydrogel formation on shaking the mixture. Furthermore, successful *in vitro* culture of PC12 cells encapsulated within the substrate demonstrates the biocompatibility and non-cytotoxicity of this composite hydrogel in supporting long-term cell growth and proliferation. Highly efficient neuronal differentiation was also observed, both with and without electrical stimulation indicating the potential of this novel 3D graphene-based hydrogel platform for tissue engineering of electroactive tissues.

References

[1] S. Liu, X. Chen, Y. Zhang, Hydrogels and hydrogel composites for 3D and 4D printing applications, 3D and 4D Printing of Polymer Nanocomposite Materials, Elsevier2020, pp. 427-465.

[2] N. Annabi, A. Tamayol, J.A. Uquillas, M. Akbari, L.E. Bertassoni, C. Cha, G. Camci‐Unal, M.R. Dokmeci, N.A. Peppas, A. Khademhosseini, 25th anniversary article: Rational design and applications of hydrogels in regenerative medicine, Advanced materials 26(1) (2014) 85-124.

[3] B.V. Slaughter, S.S. Khurshid, O.Z. Fisher, A. Khademhosseini, N.A. Peppas, Hydrogels in regenerative medicine, Advanced materials 21(32‐33) (2009) 3307-3329.

[4] Y. Li, J. Rodrigues, H. Tomas, Injectable and biodegradable hydrogels: gelation, biodegradation and biomedical applications, Chemical Society Reviews 41(6) (2012) 2193-2221.

[5] B.W. Walker, R.P. Lara, E. Mogadam, C.H. Yu, W. Kimball, N. Annabi, Rational design of microfabricated electroconductive hydrogels for biomedical applications, Progress in Polymer Science (2019).

[6] X. Liu, A.L. Miller, S. Park, B.E. Waletzki, Z. Zhou, A. Terzic, L. Lu, Functionalized carbon nanotube and graphene oxide embedded electrically conductive hydrogel synergistically stimulates nerve cell differentiation, ACS applied materials & interfaces 9(17) (2017) 14677-14690.

[7] C. García-Astrain, C. Chen, M.a. Burón, T. Palomares, A. Eceiza, L. Fruk, M.Á. Corcuera, N. Gabilondo, Biocompatible hydrogel nanocomposite with covalently embedded silver nanoparticles, Biomacromolecules 16(4) (2015) 1301-1310.

[8] S. Ahadian, R.B. Sadeghian, S. Yaginuma, J. Ramón-Azcón, Y. Nashimoto, X. Liang, H. Bae, K. Nakajima, H. Shiku, T. Matsue, Hydrogels containing metallic glass sub-micron wires for regulating skeletal muscle cell behaviour, Biomaterials science 3(11) (2015) 1449-1458.

[9] Y. Ahn, H. Lee, D. Lee, Y. Lee, Highly conductive and flexible silver nanowire-based microelectrodes on biocompatible hydrogel, ACS applied materials & interfaces 6(21) (2014) 18401-18407.

[10] S. Sayyar, E. Murray, B. Thompson, J. Chung, D.L. Officer, S. Gambhir, G.M. Spinks, G.G. Wallace, Processable conducting graphene/chitosan hydrogels for tissue engineering, Journal of Materials Chemistry B 3(3) (2015) 481-490.
[11] S.R. Shin, S.M. Jung, M. Zalabany, K. Kim, P. Zorlutuna, S.B. Kim, M. Nikkhah, M. Khabiry, M. Azize, J. Kong, Carbon-nanotube-embedded hydrogel sheets for engineering cardiac constructs and bioactuators, ACS nano 7(3) (2013) 2369-2380.
[12] J. Hur, K. Im, S.W. Kim, J. Kim, D.-Y. Chung, T.-H. Kim, K.H. Jo, J.H. Hahn, Z. Bao, S. Hwang, Polypyrrole/agarose-based electronically conductive and reversibly restorable hydrogel, ACS nano 8(10) (2014) 10066-10076.
[13] D. Pattavarakorn, P. Youngta, S. Jaesrichai, S. Thongbor, P. Chaimongkol, Electroactive Performances of Conductive Polythiophene/hydrogel Hybrid Artificial Muscle, Energy Procedia 34 (2013) 673-681.
[14] Y. Xia, H. Zhu, Polyaniline nanofiber-reinforced conducting hydrogel with unique pH-sensitivity, Soft Matter 7(19) (2011) 9388-9393.
[15] X. Zhao, P. Li, B. Guo, P.X. Ma, Antibacterial and conductive injectable hydrogels based on quaternized chitosan-graft-polyaniline/oxidized dextran for tissue engineering, Acta biomaterialia 26 (2015) 236-248.
[16] Y.S. Kim, K. Cho, H.J. Lee, S. Chang, H. Lee, J.H. Kim, W.-G. Koh, Highly conductive and hydrated PEG-based hydrogels for the potential application of a tissue engineering scaffold, Reactive and Functional Polymers 109 (2016) 15-22.
[17] A.R. Spencer, A. Primbetova, A.N. Koppes, R.A. Koppes, H. Fenniri, N. Annabi, Electroconductive Gelatin Methacryloyl-PEDOT: PSS Composite Hydrogels: Design, Synthesis, and Properties, ACS Biomaterials Science & Engineering 4(5) (2018) 1558-1567.
[18] U.P. Shinde, B. Yeon, B. Jeong, Recent progress of in situ formed gels for biomedical applications, Progress in polymer science 38(3-4) (2013) 672-701.
[19] A. Sivashanmugam, R.A. Kumar, M.V. Priya, S.V. Nair, R. Jayakumar, An overview of injectable polymeric hydrogels for tissue engineering, European Polymer Journal 72 (2015) 543-565.
[20] N. Alexandre, J. Ribeiro, A. Gärtner, T. Pereira, I. Amorim, J. Fragoso, A. Lopes, J. Fernandes, E. Costa, A. Santos-Silva, M. Rodrigues, J.D. Santos, A.C. Maurício, A.L. Luís, Biocompatibility and hemocompatibility of polyvinyl alcohol

hydrogel used for vascular grafting--In vitro and in vivo studies, Journal of biomedical materials research. Part A 102(12) (2014) 4262-75.
[21] G. Paradossi, F. Cavalieri, E. Chiessi, C. Spagnoli, M.K. Cowman, Poly(vinyl alcohol) as versatile biomaterial for potential biomedical applications, Journal of Materials Science: Materials in Medicine 14(8) (2003) 687-691.
[22] W.C. Lee, C.H.Y. Lim, H. Shi, L.A. Tang, Y. Wang, C.T. Lim, K.P. Loh, Origin of enhanced stem cell growth and differentiation on graphene and graphene oxide, ACS nano 5(9) (2011) 7334-7341.
[23] P. Bajaj, J.A. Rivera, D. Marchwiany, V. Solovyeva, R. Bashir, Graphene‐based patterning and differentiation of C2C12 myoblasts, Advanced healthcare materials 3(7) (2014) 995-1000.
[24] T.R. Nayak, H. Andersen, V.S. Makam, C. Khaw, S. Bae, X. Xu, P.-L.R. Ee, J.-H. Ahn, B.H. Hong, G. Pastorin, Graphene for controlled and accelerated osteogenic differentiation of human mesenchymal stem cells, ACS nano 5(6) (2011) 4670-4678.
[25] E. Krueger, A.N. Chang, D. Brown, J. Eixenberger, R. Brown, S. Rastegar, K.M. Yocham, K.D. Cantley, D. Estrada, Graphene foam as a three-dimensional platform for myotube growth, ACS biomaterials science & engineering 2(8) (2016) 1234-1241.
[26] L.Q. Xu, W.J. Yang, K.-G. Neoh, E.-T. Kang, G.D. Fu, Dopamine-Induced Reduction and Functionalization of Graphene Oxide Nanosheets, Macromolecules 43(20) (2010) 8336-8339.
[27] C. Silva, F. Simon, P. Friedel, P. Pötschke, C. Zimmerer, Elucidating the Chemistry behind the Reduction of Graphene Oxide Using a Green Approach with Polydopamine, Nanomaterials (Basel, Switzerland) 9(6) (2019) 902.
[28] W.S. Hummers, R.E. Offeman, Preparation of Graphitic Oxide, Journal of the American Chemical Society 80(6) (1958) 1339-1339.
[29] C. Chen, X. Bai, Y. Ding, I.S. Lee, Electrical stimulation as a novel tool for regulating cell behavior in tissue engineering, Biomater Res 23 (2019) 25.
[30] J. Schindelin, I. Arganda-Carreras, E. Frise, V. Kaynig, M. Longair, T. Pietzsch, S. Preibisch, C. Rueden, S. Saalfeld, B. Schmid, J.-Y. Tinevez, D.J. White, V. Hartenstein, K. Eliceiri, P. Tomancak, A. Cardona, Fiji: an open-source platform for biological-image analysis, Nature Methods 9 (2012) 676.

[31] L. Vincent, P. Soille, Watersheds in digital spaces: an efficient algorithm based on immersion simulations, IEEE Transactions on Pattern Analysis and Machine Intelligence 13(6) (1991) 583-598.
[32] X.-Z. Tang, C. Mu, W. Zhu, X. Yan, X. Hu, J. Yang, Flexible polyurethane composites prepared by incorporation of polyethylenimine-modified slightly reduced graphene oxide, Carbon 98 (2016) 432-440.
[33] H. Bai, C. Li, X. Wang, G. Shi, A pH-sensitive graphene oxide composite hydrogel, Chemical Communications 46(14) (2010) 2376-2378.
[34] A. Sahu, W.I. Choi, G. Tae, A stimuli-sensitive injectable graphene oxide composite hydrogel, Chemical Communications 48(47) (2012) 5820-5822.
[35] K. Manna, S.K. Srivastava, V. Mittal, Role of enhanced hydrogen bonding of selectively reduced graphite oxide in fabrication of poly (vinyl alcohol) nanocomposites in water as EMI shielding material, The Journal of Physical Chemistry C 120(30) (2016) 17011-17023.
[36] H. Bai, C. Li, X. Wang, G. Shi, On the gelation of graphene oxide, The Journal of Physical Chemistry C 115(13) (2011) 5545-5551.
[37] P. Moroder, M.B. Runge, H. Wang, T. Ruesink, L. Lu, R.J. Spinner, A.J. Windebank, M.J. Yaszemski, Material properties and electrical stimulation regimens of polycaprolactone fumarate-polypyrrole scaffolds as potential conductive nerve conduits, Acta biomaterialia 7(3) (2011) 944-953.
[38] V. Guarino, M.A. Alvarez-Perez, A. Borriello, T. Napolitano, L. Ambrosio, Conductive PANi/PEGDA Macroporous Hydrogels For Nerve Regeneration, Advanced Healthcare Materials 2(1) (2013) 218-227.
[39] G. Guroff, PC12 Cells as a Model of Neuronal Differentiation, in: J.E. Bottenstein, G. Sato (Eds.), Cell Culture in the Neurosciences, Springer US, Boston, MA, 1985, pp. 245-272.
[40] A. Orlowska, P.T. Perera, M. Al Kobaisi, A. Dias, H.K.D. Nguyen, S. Ghanaati, V. Baulin, R.J. Crawford, E.P. Ivanova, The Effect of Coatings and Nerve Growth Factor on Attachment and Differentiation of Pheochromocytoma Cells, Materials (Basel, Switzerland) 11(1) (2017).
[41] N. Li, Q. Zhang, S. Gao, Q. Song, R. Huang, L. Wang, L. Liu, J. Dai, M. Tang, G. Cheng, Three-dimensional graphene foam as a biocompatible and conductive scaffold for neural stem cells, Sci Rep 3 (2013) 1604.

[42] S.Y. Park, J. Park, S.H. Sim, M.G. Sung, K.S. Kim, B.H. Hong, S. Hong, Enhanced Differentiation of Human Neural Stem Cells into Neurons on Graphene, Advanced Materials 23(36) (2011) H263-H267.
[43] A.T. Nguyen, S. Mattiassi, M. Loeblein, E. Chin, D. Ma, P. Coquet, V. Viasnoff, E.H.T. Teo, E.L. Goh, E.K.F. Yim, Human Rett-derived neuronal progenitor cells in 3D graphene scaffold as an in vitro platform to study the effect of electrical stimulation on neuronal differentiation, Biomedical materials (Bristol, England) 13(3) (2018) 034111.
[44] L.J. Klesse, K.A. Meyers, C.J. Marshall, L.F. Parada, Nerve growth factor induces survival and differentiation through two distinct signaling cascades in PC12 cells, Oncogene 18(12) (1999) 2055-2068.
[45] L.A. Greene, A.S. Tischler, Establishment of a noradrenergic clonal line of rat adrenal pheochromocytoma cells which respond to nerve growth factor, Proc Natl Acad Sci U S A 73(7) (1976) 2424-8.
[46] M.H. Soltani, R. Pichardo, Z. Song, N. Sangha, F. Camacho, K. Satyamoorthy, O.P. Sangueza, V. Setaluri, Microtubule-associated protein 2, a marker of neuronal differentiation, induces mitotic defects, inhibits growth of melanoma cells, and predicts metastatic potential of cutaneous melanoma, Am J Pathol 166(6) (2005) 1841-50.
[47] B. Wiatrak, A. Kubis-Kubiak, A. Piwowar, E. Barg, PC12 Cell Line: Cell Types, Coating of Culture Vessels, Differentiation and Other Culture Conditions, Cells 9(4) (2020).
[48] T. Bouzid, A. Sinitskii, J.Y. Lim, Graphene platform for neural regenerative medicine, Neural regeneration research 11(6) (2016) 894-5.
[49] M. Serrano, J. Patiño, C. García-rama, M.L. Ferrer, J. Fierro, A. Tamayo, J. Collazos-castro, F. Monte, M. Gutiérrez, 3D free-standing porous scaffolds made of graphene oxide as substrates for neural cell growth, J. Mater. Chem. B 2 (2014).
[50] Q. Ma, L. Yang, Z. Jiang, Q. Song, M. Xiao, D. Zhang, X. Ma, T. Wen, G. Cheng, Three-Dimensional Stiff Graphene Scaffold on Neural Stem Cells Behavior, ACS applied materials & interfaces 8(50) (2016) 34227-34233.
[51] O. Akhavan, E. Ghaderi, E. Abouei, S. Hatamie, E. Ghasemi, Accelerated differentiation of neural stem cells into neurons on ginseng-reduced graphene oxide sheets, Carbon 66 (2014) 395-406.

[52] C. Chen, X. Bai, Y. Ding, I.-S. Lee, Electrical stimulation as a novel tool for regulating cell behavior in tissue engineering, Biomaterials Research 23(1) (2019) 25.
[53] W. Jing, Y. Zhang, Q. Cai, G. Chen, L. Wang, X. Yang, W. Zhong, Study of Electrical Stimulation with Different Electric-Field Intensities in the Regulation of the Differentiation of PC12 Cells, ACS Chemical Neuroscience 10(1) (2019) 348-357.
[54] X. Chen, Y. Wu, V.D. Ranjan, Y. Zhang, Three-dimensional electrical conductive scaffold from biomaterial-based carbon microfiber sponge with bioinspired coating for cell proliferation and differentiation, Carbon 134 (2018) 174-182.
[55] K. Kimura, Y. Yanagida, T. Haruyama, E. Kobatake, M. Aizawa, Gene expression in the electrically stimulated differentiation of PC12 cells, Journal of Biotechnology 63(1) (1998) 55-65.

CHAPTER 4 Coaxially electrospun synthetic polymer-based hollow microfiber substrate

The work presented in **Chapter 4** is largely based on the following publication: Vivek Damodar Ranjan, Peiqin Zeng, Boyuan Li and Yilei Zhang. "*In vitro* cell culture in hollow microfibers with porous structures." *Biomaterials Science* 8, no. 8 (2020): 2175-88. http://dx.doi.org/10.1039/C9BM01986C.

4.1 Background

Polymeric fibrous scaffolds have attracted significant attention in the field of biological engineering for *in vitro* neuronal culture, owing to their structural similarity to ECM proteins present inside native *in vivo* tissues as well as their ability to provide neurite contact guidance [1, 2]. Electrospinning is one of the most convenient and cost-effective methods for producing continuous and uniform fibers, with diameters ranging from few nanometers to several micrometers [3, 4]. It offers several advantages compared to other fiber fabrication techniques such as simplicity, low costs, material versatility, ease of fiber functionalization as well as the capability to tune fiber diameter via small adjustments in process parameters [5-8]. Variations of this technique have been developed for fabricating a range of 2D fibrous substrates composed of aligned or randomly oriented fibers depending on the application [9-11].

In conventional electrospinning, fibers are continuously deposited on a flat plate or aluminum foil collector, eventually forming a 2D structure with closely packed fibers [12]. In this format, cells can only grow on the top surface and cannot penetrate into the interior of the scaffold, similar to traditionally used Petri-dish based monolayer cultures [13]. This limitation has spurred modifications in

conventional electrospinning for fabrication of 3D fibrous platforms where cells can infiltrate and distribute throughout the scaffold [14-18]. For example, wet electrospinning (discussed in **Chapter 5**) involves the use of a liquid bath collector comprised of ethanol instead of a solid flat plate, allowing fibers to sink inside the liquid, thus creating more space between adjacent layers and resulting in a 3D structure [17–19]. Electrospinning combined with salting-out/foaming can be used to prepare scaffolds which have both nano and micron-sized pores utilizing sodium chloride (NaCl) particles as a porogen [19]. Porous fibrous scaffolds also can be obtained by using water-soluble polymer fiber precipitation [20]. Fibers with high porosity and large specific surface area are not only beneficial for the transportation of nutrients, oxygen and metabolites, but also promote cellular activities such as migration, proliferation and differentiation, and inducing formation of neuronal connections and networks in the case of nerve cells [21-23].

Another technique developed recently involves combining two immiscible polymer solutions and spinning them through a co-axial nozzle, creating a core-sheath structure made of two fibers having a common axis [24-26]. Subsequent removal of the core polymer results in the creation of hollow fibers. We have shown that cells can attach and grow on the inner surface of the hollow microfibers when the core polymer solution is mixed with living cells and the shell is made of a biocompatible material [27]. Cell encapsulation within microfibers has also been achieved via techniques such as extrusion [28], laminar flow [29-31] and multi-interfacial polyelectrolyte complexation (MIPC) methods [32-34], especially aimed at reconstructing three-dimensional vascular and neural networks [35, 36]. However, these techniques involve fabrication of cell-laden microfibers on alginate-based materials and hydrogels via utilization of micronozzle arrays and sophisticated

microfluidic channels with programmed flow controls [37-39]. Although microfibers produced by extrusion methods require a simple setup, it cannot precisely control fiber diameter and is also limited to a simple fiber geometry [36]. The more popular laminar flow method offers more accurate control of fiber diameter; however, it necessitates changes in microfluidic channel dimension and/or flow rates of pre-gel and gelator solutions, thus requiring microchannel fabrication and clean room facilities [36]. MIPC methods do not need syringe pumps or microfluidic channels, but they are limited to polyion complex materials [34, 36]. Broadening the type of material used for creating such cell encapsulated microfibers via simple, cost-effective and easy to use instruments has nevertheless remained a challenge [36]. At the same time, the diffusion rate of nutrients, oxygen and other essential biomolecules into the interior of the existing 3D microfiber constructs is limited, resulting in cell death and adversely affecting long-term culture [38].

Although, cell electrospinning has been investigated as an alternative in successfully achieving cell-laden fibrous scaffolds [40, 41], there are very few studies utilizing biocompatible and biodegradable materials currently available within the scope of electrospinning [42]. The material used governs various physical and biological properties of the scaffold such as surface wettability, mechanical stiffness, degradation, immunogenicity, biocompatibility etc. Poly (lactic-co-glycolic acid) (PLGA), a synthetic polymer-based biomaterial has been documented extensively as an *in vitro* substrate in neural tissue engineering for promoting neural stem cell survival [43], adhesion [44], self-renewal [45], neuronal differentiation [46], neurite formation [47] and generation of neural networks [48]. It is an aliphatic polyester which undergoes degradation via hydrolysis of ester linkages [49], whose presence also renders the polymer amenable for surface functionalization via biomolecules

[2]. On degradation, the monomeric components of PLGA can be removed by natural pathways. PLA can be cleared through the tricarboxylic acid cycle, whereas PGA is converted to metabolites or eliminated by other mechanisms [50]. Polyvinyl alcohol (PVA) is a suitable core material because it is non-cytotoxic as well as water soluble, whose viscosity can easily be adjusted for process optimization. Both PLGA and PVA are biocompatible and biodegradable polymers approved by FDA for clinical use in humans, and have been extensively used as biomaterials in drug delivery and tissue engineering applications [51-53].

In this study, a novel coaxial electrospinning process with a mixture of PLGA and polyethylene oxide (PEO) for sheath along with PVA for core were used to produce 3D core-sheath microfibers. Subsequent removal of PVA and PEO by dissolution in water resulted in the formation of hollow fibers containing pores inside the shell. These small pores could enhance transportation of nutrients, oxygen and other metabolites into the interior of the hollow fibers [54, 55]. Design of Experiments (DOE) methodology was utilized for optimizing experimental parameters and building a model to determine the key electrospinning variables influencing coaxial fiber diameter. The parameters which significantly influence fiber diameter as reported in literature are applied voltage (electric field strength), concentration and flow rate of polymer solutions [56, 57]. In addition, a regression model was built to show the mathematical relationships and interdependence between process variables and the response. Next, the feasibility of this 3D hollow microfiber platform for *in vitro* cell culture was assessed by encapsulating and culturing pheochromocytoma 12 (PC12) cells. The cells attach and grow inside the hollow microfibers, instead of on the outside surface of the fibers. The shell fiber protects the encapsulated cells from the external environment and can also provide contact guidance for directional

growth. Depending on the size of the fiber diameter produced, the duration of cell culture and the cell type used, cells can subsequently form a 2D or a 3D network.

4.2 Materials and Methods

4.2.1 Materials

PLGA (L-lactide/Glycolide ratio of 82/18; inherent viscosity midpoint = 1.8 dl/g) was purchased from Purac. Poly (ethylene oxide) (PEO), M_w=10065 and Polyvinyl alcohol (PVA), Average M_w=85000–146000 were purchased from Sigma Aldrich, Chloroform (contains 100-200 ppm amylenes as stabilizer, ≥99.5%) was purchased from Sigma Aldrich, Dulbecco's Modified Eagle's Medium (DMEM), fetal bovine serum (FBS), horse serum, penicillin/streptomycin mixture, phosphate buffered saline (PBS), DAPI (4',6-diamidino-2-phenylindole) were purchased from Life Technologies.

4.2.2 Fabrication of hollow microfibers without/with cell encapsulation

PLGA/PEO were separately dissolved in chloroform with different concentrations (10%, 12.5%, 15%) by magnetic stirring for 12 h. PVA was separately dissolved in deionized (DI) water/cell culture media at a concentration of 6% by magnetic stirring for 12 h under sterile conditions. For experiments involving cell culture study, PC12 cells were mixed with PVA solution at a concentration of 5×10^5-10^6 cells per ml. The prepared PLGA(PEO)/PVA solutions were placed in separate 1 ml syringes connected to a coaxial 17G/13G needle (2 mm/1 mm in diameter). The solution was pumped out of the syringes (KDS100, NanoNC) at a rate of 30 ml/h and 10ml/h respectively using a syringe pump (Longer pump LSP01-1A). A grounded aluminum foil/glass coverslip was used to collect the fibers released from the syringe. Voltages of 10, 12 and 14 kV were applied to the syringe using a high voltage device (Dongwen High Voltage). All experiments were carried out at room

temperature inside a biosafety cabinet (BSC) to ensure sterile conditions. For SEM observation, the samples were air-dried and observed using a scanning electron microscope (SEM, JSM-6701F, JEOL) at an accelerating voltage of 10 kV. Before placing the fiber samples into the SEM chamber, they were sputter coated with a thin layer of gold using coating device (JFC-1600 Auto Fine Coater, JEOL). Cells were observed before and after staining using brightfield and fluorescence microscopy respectively (Nikon, TI-DH).

4.2.3 Cell culture

Rat pheochromocytoma 12 (PC12) cells used in this experiment were purchased from the Institute of Biochemistry and Cell Biology, SIBS, CAS (Shanghai, China). The cells were cultured in high glucose-DMEM medium supplemented with 10% fetal bovine serum, 5% horse serum and 1% penicillin–streptomycin in T-75 cell culture flasks. All cells were incubated in a humidified atmosphere incubator with 5% CO_2 and 37^{o}C. After electrospinning, the polymer-cell hollow microfibers were immediately transferred into 6-well plates and washed thrice with phosphate buffered saline (PBS) gently, with care being taken to avoid disturbing encapsulated cells. Next, 2 ml of fresh culture media was added to each well and the 6-well plates were transferred to the 37°C incubator for the duration of cell culture.

4.2.4 Live/Dead cell viability assay

Simultaneous evaluation of cytoplasmic function and membrane integrity was carried out using the Live/Dead viability/cytotoxicity kit for mammalian cells (Life Technologies Holdings Pte Ltd). This assay provides information about the functional status of the cell by detecting cytoplasmic esterase activity. The kit consists of two fluorescent dyes - calcein AM and ethidium homodimer. When hydrolyzed by cytoplasmic esterase present in live cells, calcein AM shows intense

green fluorescence at an emission wavelength of 515 nm, whereas ethidium homodimer shows a bright red fluorescence at an emission wavelength of 617 nm after binding to DNA in cells where the cell membrane is disrupted (dead cells). The microfiber-cell samples were rinsed twice with PBS, and cell viability was assessed using the kit according to the manufacturer's protocol.

4.3 Results and Discussion

4.3.1 Fabrication and characterization of hollow, porous PLGA microfibers

The principle of coaxial electrospinning is the same as conventional electrospinning, except for modifications in the nozzle. It has 2 separate nozzles i.e. an inner and outer coaxial spinneret which renders it capable of simultaneously spinning two different polymer solutions to obtain a core-shell fiber structure [4]. PLGA was chosen as the shell polymer and the water-soluble PVA as the core. PLGA has been used extensively in tissue engineering and found to have good biocompatibility with many kinds of cells, the degradation products being lactic acid and glycolic acid, which are byproducts of human metabolism and has no major side effects when used as a biological material [50]. PVA is also has no obvious biological toxicity and is easily soluble in water but is insoluble in organic solvents [52]**.** These features make it convenient for PVA to be removed during subsequent steps via dissolution in DI water/PBS, leading to the creation of hollow fibers. PEO, a polymer which is soluble in both water and organic solvents was used as the porogen in this process. It was mixed with the shell solution prior to electrospinning, and then dissolved and removed along with PVA subsequently using an aqueous solution. On removal of PEO, apertures are created inside the shell structure now composed only of biodegradable PLGA, which makes enhanced transfer of nutrients and other necessary molecules possible, into the interior of the fiber during cell culture.

Figure 4-1A is a schematic of coaxial electrospinning process involving living cells: PVA is dissolved in water/culture media and mixed with PC12 cells at a pre-defined density, thereby forming the inner core solution; PLGA/PEO are dissolved in chloroform and serve as the outer shell solution. The two solutions are loaded into separate syringes and then pushed through the cylindrical coaxial needle by the double-clip thrust pump at specified flow rates. Electrospinning is performed under the influence of a high-voltage electric field, and results in the production of cell-encapsulated micron-sized core-shell fibers. Finally, PVA and PEO are selectively removed by washing with DI water/PBS or incubating fibers in cell-culture media overnight, resulting in the creation of hollow and porous fibers with PC12 cells attached to its inside surface. By optimizing electrospinning conditions, uniform microfibers with an average diameter of 75 μm (outer) were obtained using a PLGA concentration of 15%, PVA concentration of 6%, a tip-to-collector distance of 5 cm and a voltage of 10 kV. The flow rates for the shell and core solutions were maintained at 50 ml/h and 10 ml/h respectively; this was dependent on the fiber diameter produced, with lower flow rates being utilized to fabricated smaller diameter fibers and vice versa. **Figure 4-1B-C** shows optical microscope images of coaxial fibers fabricated at optimized electrospinning parameters and indicates the hollow structure of the fiber on dissolution of core polymer. **Figure 4-1D-E** shows SEM images of individual microfibers confirming their porous and hollow structure respectively. The optical microscope images (**Figure 4-1F**) demonstrate the hollow structure of the microfiber after removal of the core fiber, with water flowing inside the shell as shown below. The results demonstrate that the hollow microfibers retain mechanical integrity and are liquid permeable, capable of facilitating movement of culture media required for cell growth and exchange of nutrients/waste.

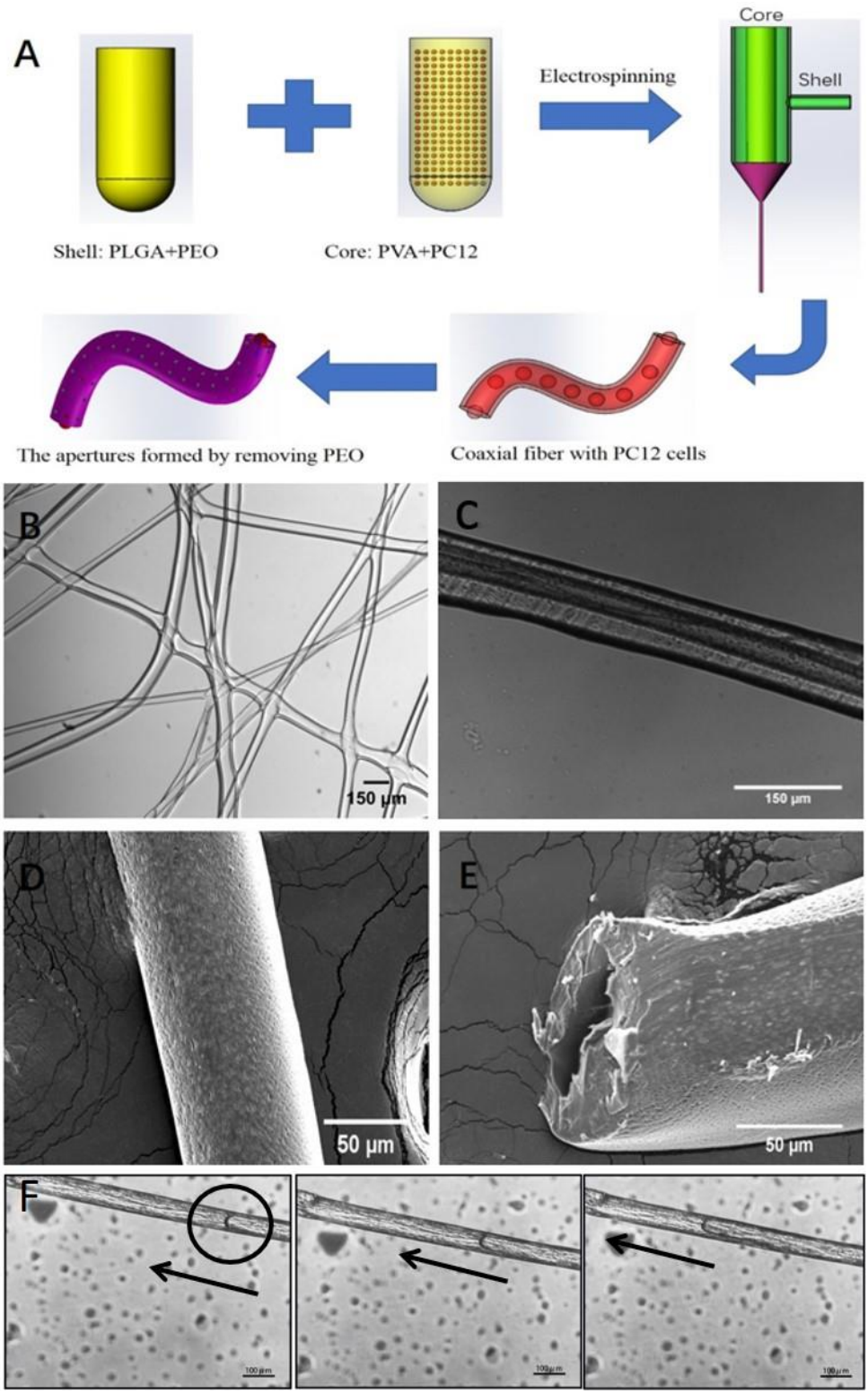

Figure 4-1. (A) Schematic illustration of fabrication of coaxial PLGA\PVA coaxial microfibers with PC12 cells encapsulation; (B, C) Optical microscope images of coaxial fibers; (D, E) SEM images showing porous and hollow structure of microfibers; (F) Optical microscope images of water flowing inside a hollow coaxial microfiber.

4.3.2 Parametric optimization

4.3.2.1 Selection of factors and levels

Design of Experiments (DOE) is a convenient method to evaluate influence of various process parameters/factors on the output. It allows experiments to be designed in a systematic manner for gathering data, helping manage process inputs to get the best possible output, and producing desirable results compared with randomly conducted experiments [58]. There are several parameters affecting morphology and size of the fibers during electrospinning. In this study, three key process inputs i.e. polymer solution concentration, applied voltage and flow rate were selected to study their effect on the process output, i.e. the coaxial fiber external diameter. Three levels were selected for each factor and were set as low, medium and high. The selected variables and values corresponding to each setting (low, medium and high) for all three factors have been summarized in **Appendix A5.**

The first part of the study involved keeping two factors constant and varying the third to understand the specific influence of each level set on the response. Several experiments were conducted each having different concentrations of the shell polymer (PLGA) in solution to determine the range within which fibers could be obtained i.e. between 10% and 15%. When the polymer concentration was below 10%, it was observed that the fibers obtained had a diameter around 15 µm, which is too small for encapsulation of cells whose size ranges between 9-15 µm. When the concentration was above 15%, fibers with a much larger diameter (>100 µm) were obtained, which is likely to cause material wastage and unstable jetting. A range of voltages between 10 kV and 14 kV was found to be optimum for creation of electric field for the electrospinning. Low voltages (<5 kV) are not strong enough to stretch the optical fiber to overcome the viscoelasticity and surface tension of the

polymer solution; large voltages (>17 kV) created a corona phenomenon at the tip of the needle. The range of optimum flow rates for the outer shell (PLGA/PEO=5:1) was found to be between 30 ml/h-50 ml/h for production of coaxial fibers having a uniform diameter. When the flow rate exceeds 50 ml/h, there is a high chance for the occurrence of droplet ejection and formation of beads. A PVA core solution concentration of 6% was found to be optimum; very low concentrations (<4%) again resulted in beaded fiber morphology, while higher concentrations (>7%) resulted in uneven mixing of cells with the solution.

Next, DOE was applied to determine the experimental run order for collecting data and to assess the significance and interdependence of the three selected factors on the process output. In this study, the focus of DOE is on the shell fiber diameter because the core solution is subsequently removed during cell culture, and the structure of the fiber is mainly determined by shell. Analysis of variance (ANOVA) for the three factors influencing the coaxial fiber diameter (outer fiber diameter) was calculated via Minitab and is shown in **Appendix A6** along with the experimental design matrix **Appendix A7.**

4.3.2.2 Analysis of results

Figure 4-2A-I shows how process response i.e. outer diameter of the coaxial fibers behaved at different experimental settings corresponding to variations in the factors selected for performing DOE. As observed from the images, fiber diameter was found to decrease with increase in voltage, but increased with increase in both flow rate and polymer solution concentration which is consistent with the theory of electrospinning [3]. Surface plots were then created based on the data collected, showing the response of the output on varying the inputs (**Figure 4-2J-L**). The plots clearly demonstrate that both flow rate and polymer solution concentration have a

significant influence on coaxial fiber diameter. In contrast, influence of voltage on process output was not as significant, the diameter remaining well below 100 µm for all three levels from low to high.

The size of a PC12 cell as measured using optical microscopy falls in the range of 10-14 µm. A shell fiber diameter falling between 50~100 µm was considered to be optimum for encapsulation of a large number of cells within the fiber. In this regard, based on the data captured in **Figure 4-2J-L**, the optimized parameters required to fabricate uniform fibers with a diameter falling in the above-mentioned range were determined to be: a shell polymer solution concentration of 15%, voltage of 10 kV and a flow rate of 50 ml/h. Maintaining the factors at these levels resulted in production of coaxial fibers with an average fiber diameter of ~75 µm. Simultaneous increase in concentration and flowrate also resulted in fabrication of very large coaxial fibers with diameters ranging from 100-500 µm, capable of encapsulating a much larger number of cells. However, there is also a higher chance of contact between organic solvents used for dissolution of the shell polymer and dispersed cells in this case. The regression model equation obtained via Minitab is shown in **Equation (4.1)** along with factors selected for optimization.

$$D = 37.91 + 11.8725X - 4.9575Y + 5.0725Z + 8.4538X^2 + 0.1988Y^2 + 3.9188Z^2 - 4.3025XY + 3.9575XZ - 1.3075YZ \quad \text{(4.1)}$$

where D is the diameter of the coaxial fiber (in µm), X is the concentration (in %), Y is the applied voltage (in kV), and Z is the flow rate (in ml/h).

It can be observed from the above equation that concentration of the polymer solution is the most significant factor affecting the output i.e. diameter of coaxial fiber. The flow rate comes next, whereas voltage was found to be the least influential

of the three. This is in line with the data obtained and assessed via optical microscopy as shown in **Figure 4-2**. The equation further indicates that concentration of the polymer solution has a marked interactive relationship with both applied voltage and flow rate in affecting the magnitude of the response i.e. fiber diameter, which is consistent with other findings [67]. However, the interaction between voltage and flow rate was comparatively less significant and consistent with the P-value (**Appendix A6**). In addition, the model was found to have an R-squared value of 99.46%, indicating a good fitting.

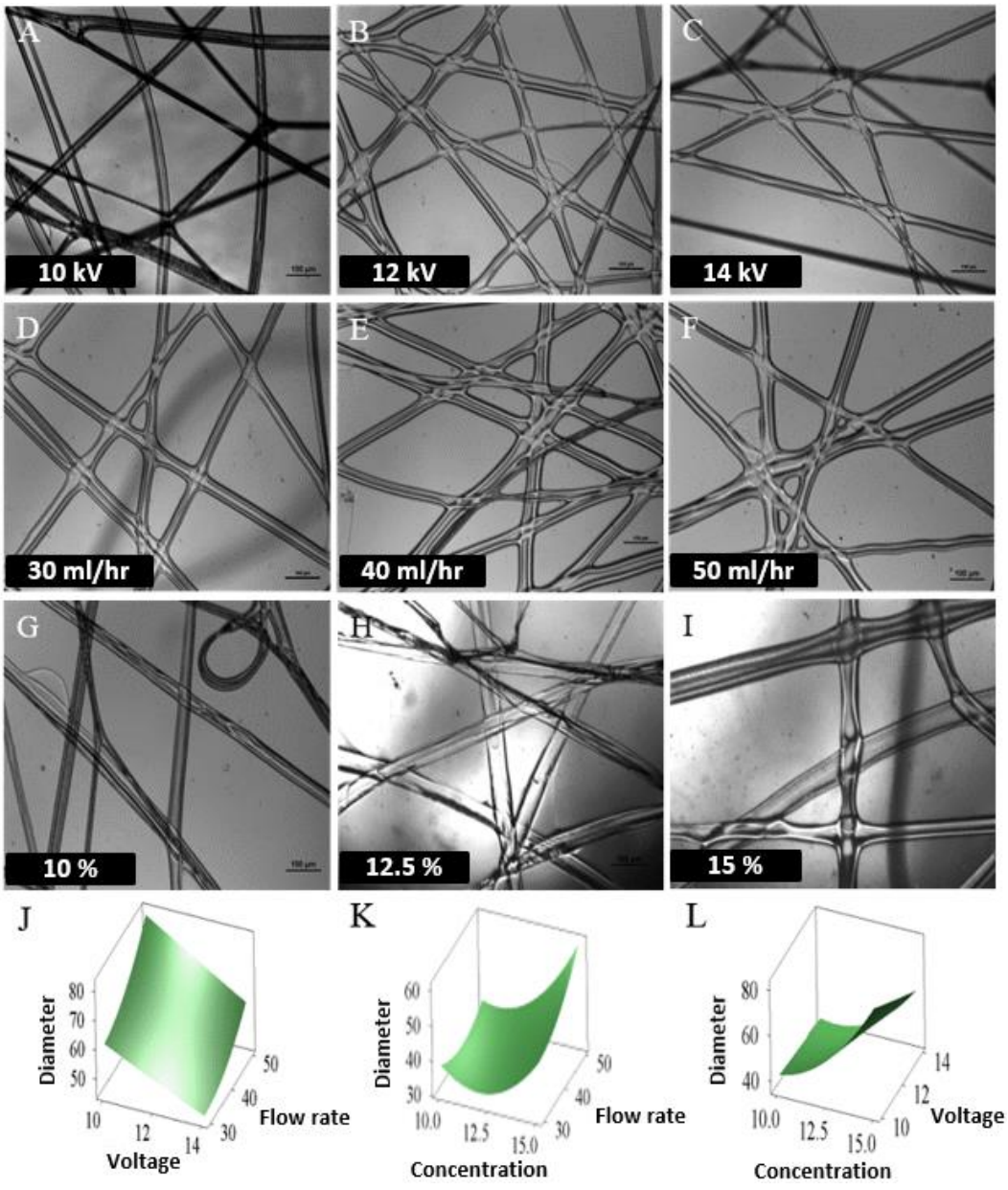

Figure 4-2. (A-I) Optical Images (Scale bar: 100 µm) of coaxial fibers fabricated on varying selected factors i.e. concentration (%), flowrate (ml/h) and voltage (kV) respectively;(A-C) 10%; 30 ml/h; 10,12 and14 kV respectively, (D-F) 10%; 30, 40 and 50 ml/h respectively; 12 kV; (G-I) 10%, 12.5% and 15% respectively; 50 ml/h; 12 kV; (J) Surface plot of diameter vs voltage, flow rate; (K) surface plot of diameter vs concentration, flow rate; (L) surface plot of diameter vs concentration, voltage.

4.3.3 Effect of PLGA and PEO mass fractions on pore size

The principle used for creation of pores is based on the dissolution capability of PEO in both organic and aqueous solutions. The polymer rich-phase comprised of PLGA gives the coaxial fiber its structure, whereas both PEO and PVA are removed subsequently by dissolution in aqueous solution/culture media, the former producing pores on the shell surface and the latter giving the fiber its hollow structure. It follows that an increase in concentration of PEO in the shell polymer solution will result in the creation of a larger number of pores on its subsequent removal after electrospinning. However, concentration of PEO should not exceed a certain threshold as this may result in the production of large cracks in the shell, ultimately leading to its disintegration.

Figure 4-3A shows the cross-section of a coaxially electrospun hollow microfiber after dissolution of both PVA and PEO. From the zoomed in views **Figure 4-3B-C**, it can clearly be observed that the shell layer is covered with pores from the outer wall to inner wall due to the removal of PEO. Most of these pores are connected with one another so that the cavities formed within (due to removal of PVA) are linked to the outer surface, which is beneficial for enhanced transport of oxygen, nutrient and other essential metabolites necessary for cellular activities. **Figure 4-3D-E** are partial enlarged views of the microfiber sample, illustrating some of the interconnected pores created between inner and outer walls of the PLGA shell after dissolution.

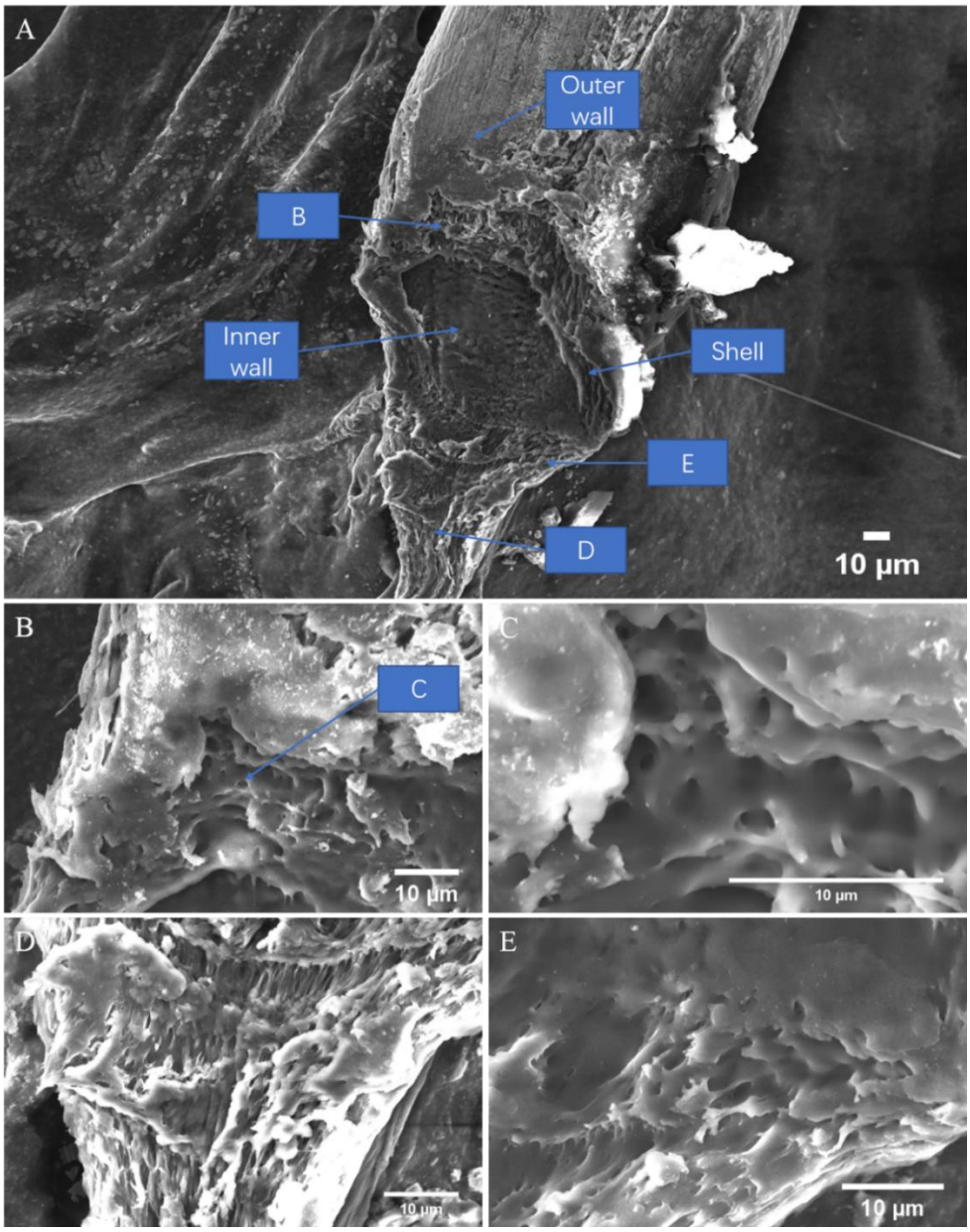

Figure 4-3. (A) SEM image showing overview of a hollow microfiber comprised of a porous shell; (B, D, E) are zoomed in views of image (A); (C) is the partial enlarged view of image (B).

Pores created on the inner wall of the fiber were difficult to assess quantitatively, and hence statistical distributions of pore size shown in **Figure 4-4** are based on the measurements of pores present on the surface of the outer wall of the shell. Different porogen concentrations (PEO) were observed to produce varied sizes of apertures on the shell fiber, and also simultaneously affect morphology of the electrospun fibers as shown in **Figure 4-4**. All experiments for preparation of fiber samples were

conducted with the electrospinning process factors set at values as optimized previously. It must be noted that PLGA cannot completely dissolve in chloroform once the mass fraction exceeds 1:1.

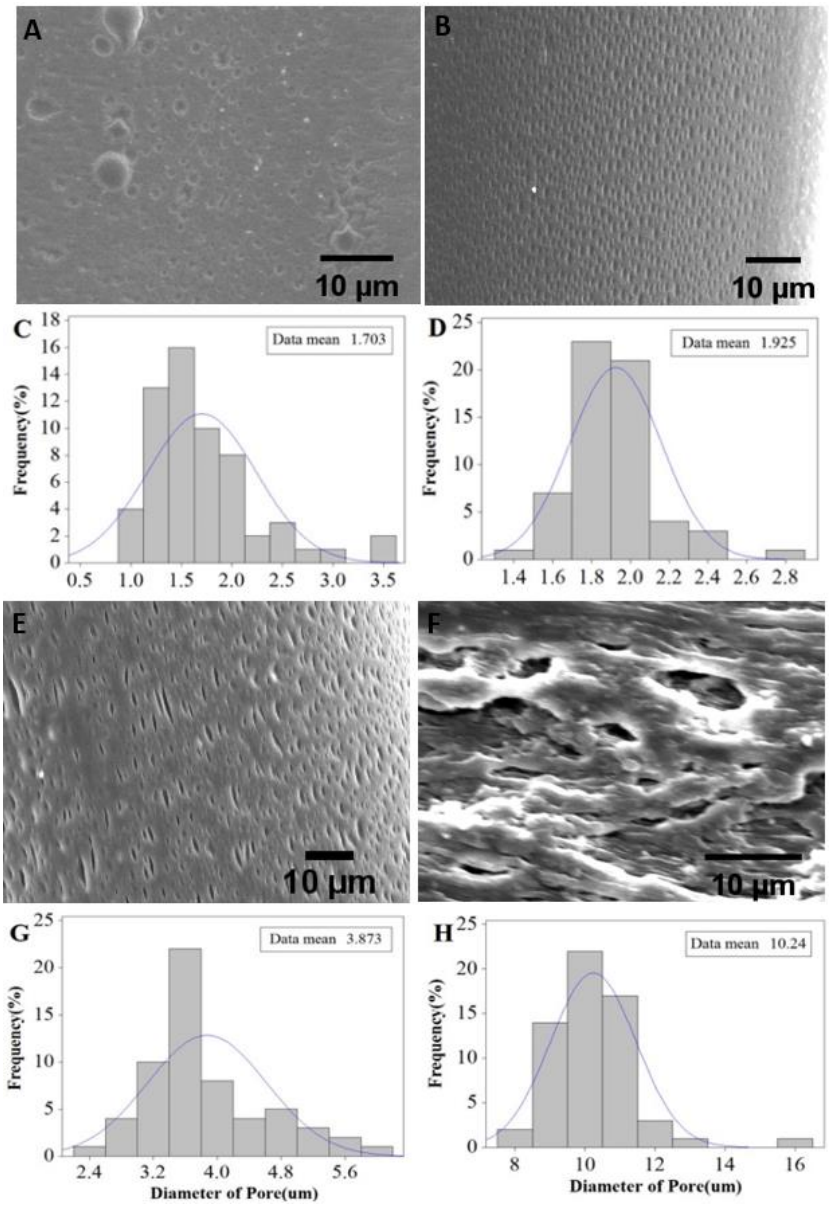

Figure 4-4. (A, B, E, F) SEM images of coaxial fibers produced at mass ratios of (PLGA:PEO) 15: 1, 5: 1, 3: 1 and 1.5: 1 respectively; (C, D, G, H) Histograms of pore size measurements in corresponding images.

Using MATLAB, a fitting curve was drawn to illustrate the relationship between the pore diameter and different mass ratios of PLGA and PEO (**Figure 4-5**). The

equation of the curve obtained meets our findings as illustrated in the histograms.

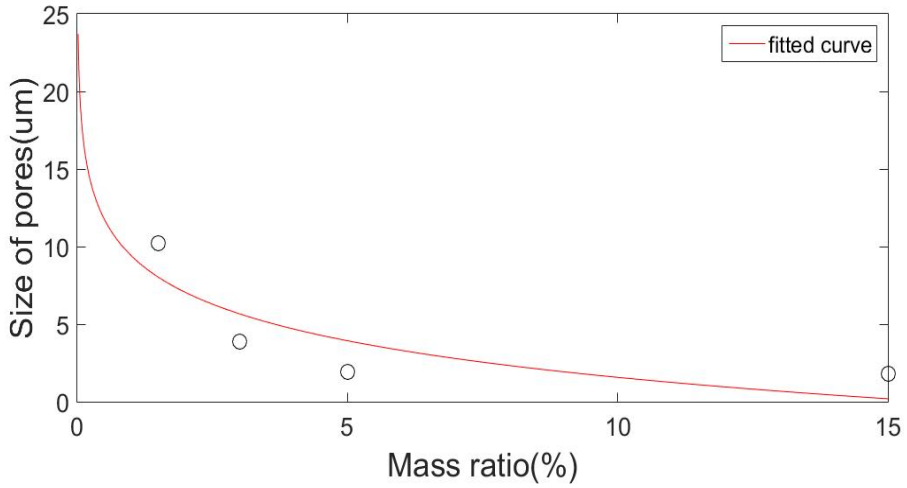

Figure 4-5. The fitting curve of different mass ratios vs mean size of pores.

$$P = 9.406 - 3.404 * \log_e M \quad \textbf{(4.2)}$$

where P is pore diameter (in μm), and M is the mass ratio (in %).

As validated by **Equation (4.2)** of the fitting curve (**Figure 4-5**), it was observed that larger mass fractions of PEO caused larger pores to form on the surface of the shell fiber and are also uniformly distributed throughout the surface. It is assumed that this applies to the entire shell structure as PEO is equally distributed in the shell after electrospinning; on its removal by water/culture media, the pores should be created uniformly throughout the shell. When the mass ratio approaches 1.5:1 (PLGA:PEO), the size of apertures created are large (**Figure 4-4F**), resulting in the formation of cracks which may ultimately lead to the disintegration of the fiber structure. This may result in cells migrating outside of the hollow fibers, which is not consistent with the purpose of this study i.e. to constrain the growth of cells within the hollow fibers to form a 3D network. On the other hand, a bigger pore diameter may also ensure a higher efficiency of transporting nutrients, oxygen and metabolites, which is beneficial for cell growth and proliferation. Considering both

the above-mentioned points, a mass fraction of 3:1 is optimum for creation of an appropriate pore size of ~3.8 µm, that is 15% PLGA mixed with 5% PEO. When mass ratios are further reduced to 15:1 and 5:1, the diameters of the pores are ~1.70 µm and ~1.92 µm respectively which are too low. Increasing the mass ratio to 1:1 results in pore diameters of ~10.2 µm, which is too large and leads to formation of cracks on the shell surface.

4.3.4 *In vitro* cell culture

4.3.4.1 Cell encapsulation and growth

To evaluate the application of this optimized hollow porous microfiber system for *in vitro* 3D neuronal culture in tissue engineering applications, PC12 cells derived from a pheochromocytoma of the rat adrenal medulla were used, as they can easily differentiate into neuron-like cells with long processes [59]. The cells were subcultured and passaged in T-75 flasks and on reaching the required number was mixed with PVA solution, which in turn was prepared using cell culture media. This was used as the core polymer solution and core-sheath electrospinning was carried out inside a biosafety cabinet (BSC) to obtain core-shell microfibers with cells encapsulated inside. The microfiber samples were collected on glass coverslips and immediately transferred into a 6-well plate containing cell culture media for further culture and placed inside the 37°C incubator overnight. The next day, culture media was removed, and the cells were stained with 4′,6-diamidino-2-phenylindole (DAPI) diluted in Phosphate-buffered saline (PBS) to visually assess encapsulation of cells inside the microfibers using fluorescence microscopy.

It was observed that majority of the cells were encapsulated within the hollow fiber and were attached to the inside wall of the shell layer, occupying about 20-50% of the surface depending on the diameter and size of the fiber. **Figure 4-6A-B** shows

both optical and fluorescence images of 3D hollow microfibers with cells encapsulated within one day after the electrospinning, therefore verifying the feasibility of the hollow fibers for culturing of cells *in vitro*. The cells were found to align themselves along the direction of the microfiber due to the constraints of the shell structure, highlighting the potential of this design for aligned cell culture; for example, in neurons where external cues and guidance may be necessary for the formation of neuronal networks. After 3 days of culture, the cells were found to spread throughout the length of the microfiber as shown in **Figure 4-6C**.

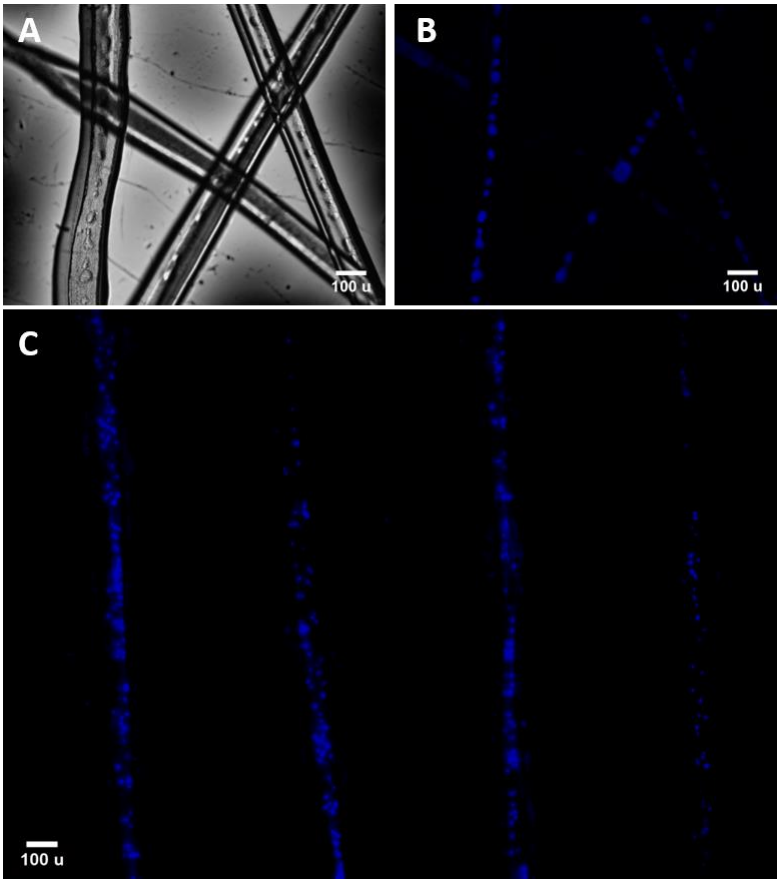

Figure 4-6. (A-B) Optical and corresponding fluorescence microscopy images of PC12 cells inside hollow coaxial microfibers on D1; (C) Fluorescence microscopy image showing cell distribution inside hollow coaxial microfibers on D3; DAPI was used to stain nuclei (blue).

Furthermore, the same experiment was carried out by varying the concentration of the shell solution (PLGA) to obtain a wide range of fiber diameters ranging from 75-

450 µm. On staining with DAPI on day 1, the smaller diameter fibers (below 100 µm) were observed to have fewer cell clusters and the cells were spread out in a relatively more uniform manner inside the hollow fiber (**Figure 4-7A-B)**. On the contrary, bigger diameter fibers contained more cells, the cells tended to form clusters and were far apart from each other as shown in **Figure 4-7C-D**. Clustering of the cells may be due to the lack of functionalization of the fiber surface with protein coatings such as collagen or laminin on the shell to make it more conducive for attachment of cells. In addition, cell numbers are required in the case of bigger diameter fibers to ensure a more even distribution of cells on the inside surface depending on application. This demonstrates the flexibility of this platform for creating a range of hollow fibers with different diameters for various tissue engineering applications.

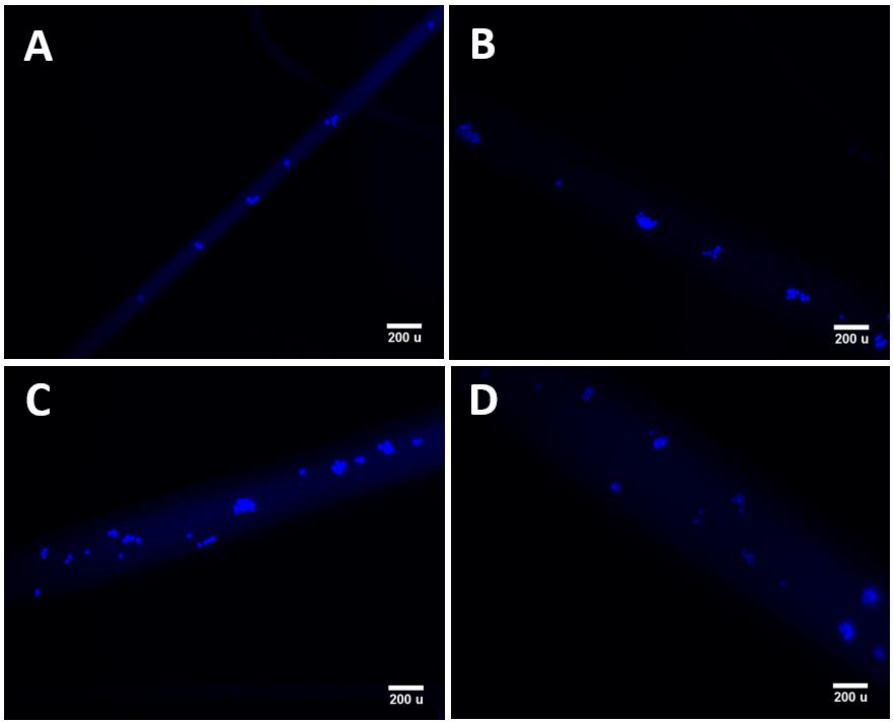

Figure 4-7. (A-D) Fluorescence microscopy images of PC12 cells inside hollow coaxial microfibers with increasing diameters ranging from 90-490 µm; DAPI was used to stain nuclei (blue).

4.3.4.2 Cell viability

The viability of PC12 cells attached within the hollow microfibers after the electrospinning process was assessed on days 3 and 7, in order to ascertain the long-term biocompatibility and cytotoxicity of the substrate. Corresponding fluorescence microscopy images are shown in **Figure 4-8A-B** and **Figure 4-8C-D** respectively. As observed, the encapsulated PC12 cells cultured inside the hollow microfibers showed excellent survival after the electrospinning process at both timepoints. The results indicate that the high voltage utilized during electrospinning is not detrimental to the cell survival and they continue to adhere and grow normally inside the hollow structure of the microfibers. Furthermore, the hollow microfiber platform was observed to support cell survival for a period of 7 days after encapsulation, thus confirming the feasibility of this substrate for long term *in vitro* culture. In addition, it was observed that in samples having smaller fiber diameters (<100 µm), the cells showed excellent survival with few or no dead cells, whereas in bigger diameter fibers, the cells were very sparsely distributed, and most cells did not survive. As mentioned previously, this is perhaps owing to uneven and low distribution of cells inside the fibers as well as exposure to toxic solvent. However, in the smaller diameter fibers the cells were found to survive and proliferate occupying 30-50% of available fiber surface during the three days of culture. The results demonstrate that the encapsulated cells are not only able to survive the electrospinning process but also capable of remaining viable within the entrapped environment for long periods. Although organic solvents such as chloroform can easily cause cell degeneration and death, in this study, cells and polymer solutions were loaded separately into two syringes and the cells were mixed with PVA solution prepared using culture media to maintain viability. Rapid solvent evaporation and fiber solidification all greatly

reduce the time of direct contact between cells and organic solvent, ensuring cell survival and further growth.

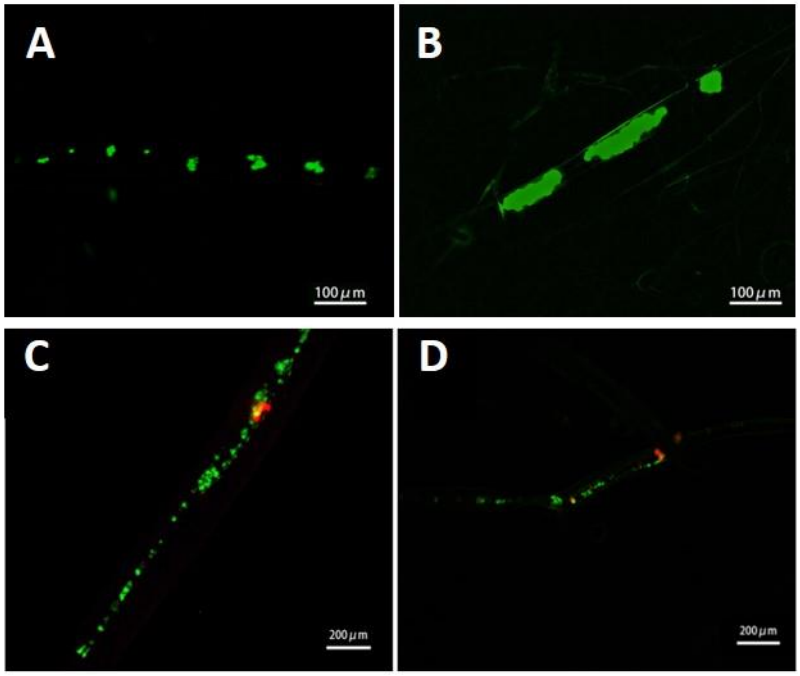

Figure 4-8. Fluorescence microscopy images of cell viability analysis: Live\dead viability test performed on D3 (A-B) and D7 (C-D) after electrospinning; Green: Calcein AM indicating live cells, red: Ethidium homodimer indicating dead cells.

Taken together, we have developed a tunable 3D hollow microfiber-based platform fabricated via coaxial electrospinning for supporting long-term *in vitro* culture of encapsulated cells encapsulated. Although, cell electrospinning has been investigated in previous studies [27, 41], to the best of our knowledge, the present findings represent the first description of hollow and porous microfibers for enhanced transfer of essential nutrition and metabolic waste between interior and exterior environments. In addition, we have also studied the effect of fiber diameter on cell distribution and viability, demonstrating the biocompatibility of this platform for long-term cell culture.

While this substrate holds potential for constrained and directional cell culture i.e. in the case of neuronal or muscle tissues, the system is not without limitations. For

instance, the large number of process parameters/materials involved makes it challenging to consistently fabricate core-sheath fibers with a uniform diameter. In addition, this also increases the risk of external contamination, especially in stem cell-based cultures which normally do not rely on antibiotics such as penicillin-streptomycin, as they can induce changes in gene expression and regulation [60]. Furthermore, the presence of toxic organic solvents such as chloroform during the fabrication process is another limiting factor in using this process for encapsulating more sensitive cell lines. PLGA is intrinsically superhydrophobic and requires additional post-processing steps such as plasma treatment to improve surface wettability for facilitating cell adhesion and infiltration of culture media. The direct fabrication of cell-scaffold structure also leaves no room for additional biomolecular functionalization of the fiber surface, which is essential for human pluripotent stem cell-derived neuronal adhesion as well as formation of neurites [61]. The high flow rates of polymer solutions utilized during the coaxial electrospinning process in turn necessitates suspension of large cell numbers within the core PVA solution to avoid sparse distribution of cells within the fibers during the subsequent fabrication process. Although this is convenient when using rapidly proliferating immortalized cell lines, it can be challenging to generate large numbers of cells when working with patient-derived iPS cell lines. Further work is required to develop this platform, both to achieve a controlled cellular distribution within the microfibers and to explore how it can be optimized to build functional 3D tubular *in vitro* neuronal networks.

4.4 Conclusion

We have successfully developed a tunable, porous and hollow microfiber-based platform for *in vitro* cell culture via coaxial electrospinning by making use of a core-

shell spinneret. DOE methodology (via Minitab) was utilized to determine the experimental run order in optimizing the key process parameters and building a model equation using regression analysis to estimate the effects of varying inputs on the process response i.e. outer fiber diameter. The electrospinning parameters were optimized to a polymer solution concentration of 15%, applied voltage of 10 kV and a polymer solution flow rate of 50 ml/h to produce uniform coaxial fibers with an average diameter of ~75 µm. In addition, the effect of different PLGA and PEO mass fractions on pore size was studied and the best ratio of these two polymers was determined to be 3:1 to create appropriately sized pores inside the shell as well as maintain the mechanical integrity of the fiber construct. Finally, the feasibility of this hollow and porous microfibrous substrate for cell encapsulation and growth was examined by mixing PC12 cells inside the core PVA solution prior to electrospinning.

The encapsulated cells were observed to attach, survive and proliferate within the hollow microfibers for a period of 7 days. Moreover, the cells cultured within the coaxial fibers have the advantage of being protected from the outside environment. The pores created in the shell serve as conduits for enhanced exchange of nutrients and other biomolecules necessary for cellular activities. Taken together, the results demonstrate the potential of this porous, hollow microfiber-based platform for constrained and guided *in vitro* cell culture in tissue engineering. The flexibility of the microfiber system in enabling control over the degree of permeability, fiber diameter and confinement of encapsulated cells signifies its potential for designing biohybrids having practical applications in biosensors, bioremediation and regenerative medicine.

References

[1] C.P. Barnes, S.A. Sell, E.D. Boland, D.G. Simpson, G.L. Bowlin, Nanofiber technology: designing the next generation of tissue engineering scaffolds, Advanced drug delivery reviews 59(14) (2007) 1413-33.

[2] J.T.S. Pettikiriarachchi, C.L. Parish, M.S. Shoichet, J.S. Forsythe, D.R. Nisbet, Biomaterials for Brain Tissue Engineering, Australian Journal of Chemistry 63(8) (2010) 1143-1154.

[3] D.H. Reneker, A.L. Yarin, Electrospinning jets and polymer nanofibers, Polymer 49(10) (2008) 2387-2425.

[4] R. Murugan, S. Ramakrishna, Nano-featured scaffolds for tissue engineering: a review of spinning methodologies, Tissue engineering 12(3) (2006) 435-47.

[5] L.A. Smith, P.X. Ma, Nano-fibrous scaffolds for tissue engineering, Colloids and surfaces. B, Biointerfaces 39(3) (2004) 125-31.

[6] D.I. Braghirolli, D. Steffens, P. Pranke, Electrospinning for regenerative medicine: a review of the main topics, Drug Discovery Today 19(6) (2014) 743-753.

[7] X. Wang, B. Ding, B. Li, Biomimetic electrospun nanofibrous structures for tissue engineering, Materials Today 16(6) (2013) 229-241.

[8] D. Liang, B.S. Hsiao, B. Chu, Functional electrospun nanofibrous scaffolds for biomedical applications, Advanced drug delivery reviews 59(14) (2007) 1392-412.

[9] Y.Z. Zhang, B. Su, J. Venugopal, S. Ramakrishna, C.T. Lim, Biomimetic and bioactive nanofibrous scaffolds from electrospun composite nanofibers, International journal of nanomedicine 2(4) (2007) 623-638.

[10] Z.-M. Huang, Y.Z. Zhang, M. Kotaki, S. Ramakrishna, A review on polymer nanofibers by electrospinning and their applications in nanocomposites, Composites Science and Technology 63(15) (2003) 2223-2253.

[11] T.J. Sill, H.A. von Recum, Electrospinning: Applications in drug delivery and tissue engineering, Biomaterials 29(13) (2008) 1989-2006.

[12] B.A. Blakeney, A. Tambralli, J.M. Anderson, A. Andukuri, D.J. Lim, D.R. Dean, H.W. Jun, Cell infiltration and growth in a low density, uncompressed three-dimensional electrospun nanofibrous scaffold, Biomaterials 32(6) (2011) 1583-90.

[13] D.W. Hutmacher, Scaffold design and fabrication technologies for engineering tissues--state of the art and future perspectives, Journal of biomaterials science. Polymer edition 12(1) (2001) 107-24.

[14] B. Sun, Y.Z. Long, H.D. Zhang, M.M. Li, J.L. Duvail, X.Y. Jiang, H.L. Yin, Advances in three-dimensional nanofibrous macrostructures via electrospinning, Progress in Polymer Science 39(5) (2014) 862-890.
[15] X. Wang, B. Ding, G. Sun, M. Wang, J. Yu, Electro-spinning/netting: A strategy for the fabrication of three-dimensional polymer nano-fiber/nets, Progress in Materials Science 58(8) (2013) 1173-1243.
[16] Y. Yokoyama, S. Hattori, C. Yoshikawa, Y. Yasuda, H. Koyama, T. Takato, H. Kobayashi, Novel wet electrospinning system for fabrication of spongiform nanofiber 3-dimensional fabric, Materials Letters 63(9) (2009) 754-756.
[17] E. Kostakova, D. Lukas, P. Pokorny, M. Seps, Study of polycaprolactone wet electrospinning process, eXPRESS Polymer Letters 8 (2014) 554-564.
[18] M. Kim, G. Kim, Highly porous electrospun 3D polycaprolactone/β-TCP biocomposites for tissue regeneration, Materials Letters 120 (2014) 246-250.
[19] Y.H. Lee, J.H. Lee, I.-G. An, C. Kim, D.S. Lee, Y.K. Lee, J.-D. Nam, Electrospun dual-porosity structure and biodegradation morphology of Montmorillonite reinforced PLLA nanocomposite scaffolds, Biomaterials 26(16) (2005) 3165-3172.
[20] S. Kidoaki, I.K. Kwon, T. Matsuda, Mesoscopic spatial designs of nano- and microfiber meshes for tissue-engineering matrix and scaffold based on newly devised multilayering and mixing electrospinning techniques, Biomaterials 26(1) (2005) 37-46.
[21] X. Zhang, F. Han, A. Syed, E.M. Bukhari, B.C.J. Siang, S. Yang, B. Zhou, W.-j. Wen, D. Jiang, Fabrication of highly modulable fibrous 3D extracellular microenvironments, Biomedical Microdevices 19(3) (2017) 53.
[22] S. Wu, B. Duan, P. Liu, C. Zhang, X. Qin, J.T. Butcher, Fabrication of Aligned Nanofiber Polymer Yarn Networks for Anisotropic Soft Tissue Scaffolds, ACS applied materials & interfaces 8(26) (2016) 16950-16960.
[23] A. Tamayol, M. Akbari, N. Annabi, A. Paul, A. Khademhosseini, D. Juncker, Fiber-based tissue engineering: Progress, challenges, and opportunities, Biotechnology advances 31(5) (2013) 669-87.
[24] Z. Sun, E. Zussman, A.L. Yarin, J.H. Wendorff, A. Greiner, Compound Core–Shell Polymer Nanofibers by Co-Electrospinning, Advanced Materials 15(22) (2003) 1929-1932.

[25] F. Yi, D.A. LaVan, Poly(glycerol sebacate) Nanofiber Scaffolds by Core/Shell Electrospinning, Macromolecular bioscience 8(9) (2008) 803-806.
[26] H. Li, Y. Xu, H. Xu, J. Chang, Electrospun membranes: control of the structure and structure related applications in tissue regeneration and drug delivery, Journal of Materials Chemistry B 2(34) (2014) 5492-5510.
[27] Y. Wu, V.D. Ranjan, Y. Zhang, A Living 3D In Vitro Neuronal Network Cultured inside Hollow Electrospun Microfibers, Advanced Biosystems 2(5) (2018) 1700218.
[28] S. Zhang, M.A. Greenfield, A. Mata, L.C. Palmer, R. Bitton, J.R. Mantei, C. Aparicio, M.O. de la Cruz, S.I. Stupp, A self-assembly pathway to aligned monodomain gels, Nat Mater 9(7) (2010) 594-601.
[29] M. Yamada, R. Utoh, K. Ohashi, K. Tatsumi, M. Yamato, T. Okano, M. Seki, Controlled formation of heterotypic hepatic micro-organoids in anisotropic hydrogel microfibers for long-term preservation of liver-specific functions, Biomaterials 33(33) (2012) 8304-15.
[30] Y. Zuo, X. He, Y. Yang, D. Wei, J. Sun, M. Zhong, R. Xie, H. Fan, X. Zhang, Microfluidic-based generation of functional microfibers for biomimetic complex tissue construction, Acta Biomaterialia 38 (2016) 153-162.
[31] S.-J. Shin, J.-Y. Park, J.-Y. Lee, H. Park, Y.-D. Park, K.-B. Lee, C.-M. Whang, S.-H. Lee, “On the Fly” Continuous Generation of Alginate Fibers Using a Microfluidic Device, Langmuir 23(17) (2007) 9104-9108.
[32] T.C. Lim, M.F. Leong, H. Lu, C. Du, S. Gao, A.C. Wan, J.Y. Ying, Follicular dermal papilla structures by organization of epithelial and mesenchymal cells in interfacial polyelectrolyte complex fibers, Biomaterials 34(29) (2013) 7064-72.
[33] M.F. Leong, J.K. Toh, C. Du, K. Narayanan, H.F. Lu, T.C. Lim, A.C. Wan, J.Y. Ying, Patterned prevascularised tissue constructs by assembly of polyelectrolyte hydrogel fibres, Nat Commun 4 (2013) 2353.
[34] A.C. Wan, M.F. Leong, J.K. Toh, Y. Zheng, J.Y. Ying, Multicomponent fibers by multi-interfacial polyelectrolyte complexation, Adv Healthc Mater 1(1) (2012) 101-5.
[35] H. Onoe, T. Okitsu, A. Itou, M. Kato-Negishi, R. Gojo, D. Kiriya, K. Sato, S. Miura, S. Iwanaga, K. Kuribayashi-Shigetomi, Y.T. Matsunaga, Y. Shimoyama, S. Takeuchi, Metre-long cell-laden microfibres exhibit tissue morphologies and functions, Nat Mater 12(6) (2013) 584-90.

[36] H. Onoe, S. Takeuchi, Cell-laden microfibers for bottom-up tissue engineering, Drug Discovery Today 20(2) (2015) 236-246.
[37] Y. Yu, H. Wen, J. Ma, S. Lykkemark, H. Xu, J. Qin, Flexible Fabrication of Biomimetic Bamboo-Like Hybrid Microfibers, Advanced Materials 26(16) (2014) 2494-2499.
[38] A. Kang, J. Park, J. Ju, G.S. Jeong, S.H. Lee, Cell encapsulation via microtechnologies, Biomaterials 35(9) (2014) 2651-63.
[39] E. Kang, G.S. Jeong, Y.Y. Choi, K.H. Lee, A. Khademhosseini, S.H. Lee, Digitally tunable physicochemical coding of material composition and topography in continuous microfibres, Nat Mater 10(11) (2011) 877-83.
[40] S.N. Jayasinghe, S. Irvine, J.R. McEwan, Cell electrospinning highly concentrated cellular suspensions containing primary living organisms into cell-bearing threads and scaffolds, Nanomedicine (London, England) 2(4) (2007) 555-67.
[41] A. Townsend-Nicholson, S.N. Jayasinghe, Cell Electrospinning: a Unique Biotechnique for Encapsulating Living Organisms for Generating Active Biological Microthreads/Scaffolds, Biomacromolecules 7(12) (2006) 3364-3369.
[42] E. Zussman, Encapsulation of cells within electrospun fibers, Polymers for Advanced Technologies 22(3) (2011) 366-371.
[43] Y. Xiong, Y.-S. Zeng, C.-G. Zeng, B.-l. Du, L.-M. He, D.-P. Quan, W. Zhang, J.-M. Wang, J.-L. Wu, Y. Li, J. Li, Synaptic transmission of neural stem cells seeded in 3-dimensional PLGA scaffolds, Biomaterials 30(22) (2009) 3711-3722.
[44] L. Zhou, J. Tu, G. Fang, L. Deng, X. Gao, K. Guo, J. Kong, J. Lv, W. Guan, C. Yang, Combining PLGA Scaffold and MSCs for Brain Tissue Engineering: A Potential Tool for Treatment of Brain Injury, Stem cells international 2018 (2018) 5024175-5024175.
[45] M. Pang, T. Shu, R. Chen, C. Liu, L. He, Y. Yang, A. Bardeesi, C.-K. Lin, L.-M. Zhang, X. Wang, B. Liu, L.-M. Rong, Neural precursor cells generated from Induced pluripotent stem cells with gelatin sponge-electrospun PLGA/PEG nanofibers for spinal cord injury repair, International Journal of Clinical and Experimental Medicine (2016).
[46] L.E. Sperling, K.P. Reis, L.G. Pozzobon, C.S. Girardi, P. Pranke, Influence of random and oriented electrospun fibrous poly(lactic-co-glycolic acid) scaffolds on

neural differentiation of mouse embryonic stem cells, Journal of Biomedical Materials Research Part A 105(5) (2017) 1333-1345.
[47] C.M. Hwang, S.K. Kim, J.H. Kim, A. Khademhosseini, S.H. Lee, Differentiation of human neural progenitor cells on PLGA microfibers, 2009 IEEE 35th Annual Northeast Bioengineering Conference, 2009, pp. 1-2.
[48] E.-z. Yang, G.-w. Zhang, J.-g. Xu, S. Chen, H. Wang, L.-l. Cao, B. Liang, X.-f. Lian, Multichannel polymer scaffold seeded with activated Schwann cells and bone mesenchymal stem cells improves axonal regeneration and functional recovery after rat spinal cord injury, Acta Pharmacologica Sinica 38(5) (2017) 623-637.
[49] Manuel Pérez-Garnes, J.A. Barcia, U. Gómez-Pinedo, M. Pradas, Ana, Vallés-Lluch, Materials for Central Nervous System Tissue Engineering, Intech2014.
[50] P. Gentile, V. Chiono, I. Carmagnola, P.V. Hatton, An overview of poly(lactic-co-glycolic) acid (PLGA)-based biomaterials for bone tissue engineering, Int J Mol Sci 15(3) (2014) 3640-59.
[51] H.K. Makadia, S.J. Siegel, Poly Lactic-co-Glycolic Acid (PLGA) as Biodegradable Controlled Drug Delivery Carrier, Polymers (Basel) 3(3) (2011) 1377-1397.
[52] G. Paradossi, F. Cavalieri, E. Chiessi, C. Spagnoli, M.K. Cowman, Poly(vinyl alcohol) as versatile biomaterial for potential biomedical applications, Journal of Materials Science: Materials in Medicine 14(8) (2003) 687-691.
[53] J.M. Anderson, M.S. Shive, Biodegradation and biocompatibility of PLA and PLGA microspheres, Advanced drug delivery reviews 64 (2012) 72-82.
[54] N.G. Rim, C.S. Shin, H. Shin, Current approaches to electrospun nanofibers for tissue engineering, Biomedical materials (Bristol, England) 8(1) (2013) 014102.
[55] J. Guan, K.L. Fujimoto, M.S. Sacks, W.R. Wagner, Preparation and characterization of highly porous, biodegradable polyurethane scaffolds for soft tissue applications, Biomaterials 26(18) (2005) 3961-3971.
[56] G.R. Mitchell, K.-h. Ahn, F.J. Davis, The potential of electrospinning in rapid manufacturing processes, Virtual and Physical Prototyping 6(2) (2011) 63-77.
[57] S.R. Coles, D.K. Jacobs, J.O. Meredith, G. Barker, A.J. Clark, K. Kirwan, J. Stanger, N. Tucker, A design of experiments (DoE) approach to material properties optimization of electrospun nanofibers, Journal of Applied Polymer Science 117(4) (2010) 2251-2257.

[58] R.A. Fisher, Design of Experiments, British Medical Journal 1(3923) (1936) 554-554.
[59] G. Guroff, PC12 Cells as a Model of Neuronal Differentiation, in: J.E. Bottenstein, G. Sato (Eds.), Cell Culture in the Neurosciences, Springer US, Boston, MA, 1985, pp. 245-272.
[60] A.H. Ryu, W.L. Eckalbar, A. Kreimer, N. Yosef, N. Ahituv, Use antibiotics in cell culture with caution: genome-wide identification of antibiotic-induced changes in gene expression and regulation, Scientific reports 7(1) (2017) 7533-7533.
[61] A. Hyysalo, M. Ristola, M.E.L. Mäkinen, S. Häyrynen, M. Nykter, S. Narkilahti, Laminin α5 substrates promote survival, network formation and functional development of human pluripotent stem cell-derived neurons in vitro, Stem Cell Research 24 (2017) 118-127.

CHAPTER 5 Wet electrospun synthetic polymer-based fibrillar substrate

The work presented in **Chapters 5** and **6** is largely based on the following publication: Vivek Damodar Ranjan, Lifeng Qiu, Jolene Wei-Ling Lee, Xuelong Chen, Se Eun Jang, Chou Chai, Kah-Leong Lim, Eng-King Tan, Yilei Zhang, Wei Min Huang, Li Zeng. "A microfiber scaffold-based 3D *in vitro* human neuronal culture model of Alzheimer's disease." *Biomaterials Science* 8 (17) (2020) 4861-4874. http://dx.doi.org/10.1039/D0BM00833H.

5.1 Background

As discussed in **Chapter 4**, conventional electrospinning involves the continuous deposition of fibers on a flat plate or aluminum foil collector, eventually forming a 2D mat-like structure with closely packed fibers. The inherently small pore size of such 2D electrospun mats do not allow adequate cellular infiltration or tissue ingrowth, resulting in monolayer culture with cells attaching and growing only on the topmost layer of fibers [1]. A fluid-based collector consisting of a beaker filled with a low surface tension liquid such as ethanol or isopropanol can be used alternatively, to fabricate 3D macroporous, non-woven scaffolds which permits higher cell infiltration and thus forms the basis of a technique called wet electrospinning [2].

In this study, we electrospin PLGA fibers into a grounded, highly concentrated ethanol solution to fabricate microtopographic scaffolds, aimed at achieving 3D *in vitro* neuronal culture via subsequent encapsulation of hESC derived neural progenitors. Various scaffold parameters such as fiber diameter, pore size, porosity and hydrophilicity of the fibrillar substrate were optimized to enhance cellular

infiltration, distribution, attachment, viability and neuronal differentiation inside the scaffold. In addition, fluorescent calcium imaging was carried out to assess the ability of the 3D microfiber scaffolds to support formation of neural circuits as well as facilitate spontaneous electrophysiological spiking activity of encapsulated neurons. Calcium (Ca) ions are intracellular messengers and play a key role in multiple intracellular signaling pathways in neurons, thereby controlling several significant functions in the central nervous system such as cellular proliferation, migration, differentiation and the formation of neural networks including the initiation of long term potentiation/depression in synaptic plasticity [3].

5.2 Materials and Methods

5.2.1 Fabrication of 3D microfiber scaffolds

PLGA (L-lactide/Glycolide ratio of 82/18; inherent viscosity midpoint = 1.8 dl/g) was purchased from Purac. The precursor solutions were prepared by dissolving the polymer in a binary solvent comprised of chloroform and dimethylformamide (DMF) at concentrations optimized to obtain continuous fibers with a consistent diameter. The polymer solution was fed into a 1 ml plastic syringe with a stainless-steel 20G blunt needle, mounted on a syringe pump (Longer pump LSP01-1A) and connected to the positive electrode of a high-voltage DC power supply (Dongwen High Voltage). 2D fibrous mats were fabricated by deposition of fibers on a grounded aluminum foil collector placed at a working distance of 10 cm from the needle.

Fabrication of 3D microfiber scaffolds involves 3 distinct steps. Firstly, microfibers were deposited into a grounded borosilicate beaker containing 95% ethanol by spinning for a duration of 90 seconds [2]. The low surface tension of ethanol allows fibers to sink below the surface giving it a 3D structure. Next, 3D microfibers were

transferred to a 48-well plate where ethanol is replaced by washing thoroughly in deionized (DI) water, the volume of DI water varied as necessary for tuning pore size. In order to ensure uniform distribution, fibers are homogenized in solution through orbital shaking (Cole Parmer Compact Orbital Shaker; 230 VAC, 50 Hz) at 250 rpm for 4 hours. This generates aqueous solutions containing different concentrations of electrospun fibers, solutions with lower fiber concentration yielding higher pore size values. In particular, 40 mg of polymer solution was electrospun and fibers were dispersed into 7.5 ml, 11 ml and 15 ml of DI water to yield aqueous solutions having concentrations of 5.3, 3.6 and 2.6 $mg \cdot ml^{-1}$ respectively. The homogenized fiber solutions were lyophilized for 24 hours to conserve its 3D geometry, obtaining fluffy and cylindrical microfibrous scaffolds composed of 10 mm diameter and 3 mm thickness. These were dried under vacuum at room temperature for an additional 24 hours to remove all traces of cytotoxic residual organic solvents utilized during the fabrication process.

5.2.2 Characterization of fiber diameter and pore size

Fiber diameter and surface morphology of 2D and 3D electrospun PLGA microfibers were analyzed using a field emission scanning electron microscope (FE-SEM, JEOL 6340F). The electrospun 2D fiber mats were sputter coated with gold for 20 seconds using a current of 20 mA (JEOL JFC 1600 Auto Fine Coater) and studied under the FE-SEM at an accelerating voltage in the range of 5-8 kV. In the case of 3D scaffolds, sputter coating step was omitted to prevent fibers from collapsing and causing damage to its 3D structure; a lower accelerating voltage of 1-3 kV along with a fast scanning rate was utilized to visualize the fibers. Fiber morphology and diameter were analyzed at 5000× magnification, whereas 250×-1000× magnifications were used to identify and estimate approximate pore size of

scaffolds. ImageJ software (National Institutes of Health) was used to analyze pore size distribution and fiber diameters for a minimum of 40 random samples in five SEM micrographs for both 2D and 3D fiber constructs respectively (n=3).

5.2.3 Porosity measurement

Gravimetric method and liquid displacement methods were used to determine the total porosity of lyophilized 3D PLGA microfiber scaffolds. Gravimetry involves the use of equation "Total porosity = 1- [(m/v)/ϱ_m]" where "m" is mass of scaffold (g), "v" is the volume of scaffold (cm^3) and ϱ_m is the density of PLGA (1.32 $g.cm^{-3}$). The geometry of the scaffold was measured using a caliper. Liquid displacement method makes use of the Archimedes principle to determine porosity fraction. The scaffolds are first immersed in 5 ml (V_1) of ethanol inside a measuring tube and the increase in volume is measured (V_2). Twelve hours later, scaffolds were removed to measure remaining volume of ethanol in the tube (V_3). The porosity fraction is then calculated using the equation "Total porosity = $(V_1-V_3)/(V_2-V_3)$".

5.2.3 Plasma treatment and sterilization

Air plasma treatment of electrospun 3D PLGA microfiber scaffolds was carried out using a PDC-001 plasma cleaner (Harrick Scientific Corporation). Lyophilized scaffolds were placed in the plasma cleaner chamber and plasma discharge was applied for 120 seconds with radio frequency power set as 30W under vacuum mode. X-ray photoelectron spectroscopy (XPS) measurement was performed on an AXIS Supra X-ray photoelectron spectrometer (Kratos Analytical Ltd). Plasma treated scaffolds were transferred to a new 24-well plate and sterilized by ultraviolet (UV) irradiation for 1 hour followed by pre-treatment with 70% ethanol overnight. Finally, scaffolds were washed thoroughly with sterilized DI water 3-4 times to remove all traces of ethanol before surface coating.

5.2.4 Water contact angle measurement

The water contact angle for 3D PLGA microfiber scaffolds was measured before and after plasma treatment using an optical tensiometer (Dyne Technology) equipped with a camera via sessile drop technique. Uniform 2D fiber mats of 100 µm thickness were electrospun on square glass coverslips placed on the grounded aluminum foil (5 samples). DI water was used for drop formation on the fiber mat with a droplet size of 10 µl. Contact angle is defined as the angle made by the intersection of the liquid/solid interface and the liquid/air interface. Mean value of both left and right contact angles on 5 different regions of interest on 3 samples was determined. This value is a measure of surface wettability, which in turn reflects the hydrophilicity of the scaffolds. All experiments were conducted in ambient conditions and were performed at least 5 times per sample.

5.2.5 Compression testing

The compressive mechanical properties of 3D PLGA microfiber scaffolds were determined by compression testing using MTS criterion Model 43 Electromechanical Universal Test System, with a crosshead speed of 10 mm/min. 3D PLGA microfibers were freeze dried in a 24-well plate to obtain cylindrical scaffolds corresponding to the dimensions of the well (∅ 18 mm and 12.5 mm in height). Mechanical testing was done to determine stiffness of the scaffold in both dry and wet conditions (5 samples each). For testing under wet condition, scaffolds were pre-wetted with phosphate-buffered saline (PBS) at 37^{o}C. A small preload was applied to each sample before the compression test to ensure that the entire scaffold surface was in contact with the plates. The compression stress-strain curves were plotted for both groups of samples; strain was calculated using displacement of the crosshead and Young's modulus (E) in each case was determined by analyzing

average slope of the initial linear portion of the graph (below 40% compressive strain).

5.2.6 Surface coating of 3D PLGA microfiber scaffolds

First, 0.005% Poly-L-Ornithine (PLO) (Sigma) solution was used to soak the 3D scaffolds followed by incubation at 37^{o}C for 24 hours. Next, the scaffolds were washed gently with DI water and laminin (Life Technologies Corporation) at a working concentration of 20 µg/ml diluted in DMEM/F12 culture media (Gibco) was used to coat them, again followed by incubation at 37^{o}C for 48 hours. Finally, excess laminin was aspirated, and appropriate culture media added to commence cell seeding.

5.2.7 hESC maintenance and neuronal differentiation

Human embryonic stem cells (hESC) were obtained from ES Cell International. The cells were maintained in mTeSR1 media (StemCell Technologies) on Matrigel coated dishes (Corning). Media change was performed daily until 70% confluency was obtained. To expand hESC/iPSC cultures, dispase (StemCell Technologies) was used to dissociate cells into clumps. ROCK inhibitor (10 µM) was added into media during either passage, freezing and thawing steps to promote cell survival. hESC were differentiated into frontal cortical neurons using Dual SMAD inhibition protocol in both 2D and 3D culture formats [4]. Briefly, to initiate embryonic body (EB) formation, cells were dissociated with accutase (Gibco) at D2 and seeded onto 6-well culture plates (Thermo Fisher Scientific) in mTeSR1 media supplemented with ROCK inhibitor. From D0-D4, media was replaced with Dual SMAD inhibition media containing DMEM/F12 (Gibco), Neurobasal media (Gibco), non-essential amino acids (Gibco), GlutaMAX (Gibco), N2 supplement (Life Technologies), B27 supplement with vitamin A (Life Technologies), 0.1 µM

LDN193189 (Stemgent) and 10 µM SB431542 (Cellagen Tech) every 2 days until D5. Thereafter, EBs were transferred into Matrigel coated dishes with daily media change until D12. At this stage, induced neural progenitor cells (NPC) were dissociated using accutase and re-plated onto Matrigel coated dishes in NPC maintenance media (DMEM/F12 with glutamine, B27 supplement without vitamin A, N2 supplement and 20ng/ml bFGF (StemCell Technologies) with daily media change.

Cells continue to remain at NPC stage from D12 until media is replaced with neuronal differentiation media. At passage 3-6, NPC were seeded onto 3D scaffolds (2.5×10^6 cells/cm^2) respectively. Cell seeding density and cell suspension volume for scaffolds was optimized to 5×10^6 cells and 200 µl per scaffold respectively. After seeding, scaffolds were immediately placed on an orbital shaker and agitated for 20 minutes at 70 rpm, to ensure deeper and uniform cell penetration to all regions within the scaffold [5]. Thereafter, top up of NPC maintenance medium was done and samples were incubated at 37ºC with 5% CO_2. Media change was done daily with neuronal differentiation media containing neurobasal media, non-essential amino acids, GlutaMAX, B27 with vitamin A, 2.5µM DAPT (Tocris), 10ng/ml BDNF (Sigma), 10ng/ml GDNF (Sigma), 200µM ascorbic acid (Sigma) and 0.5mM db-cAMP (Sigma) until D19 after which the cells were harvested..

5.2.8 Immunocytochemistry

Immunofluorescence staining was performed to characterize phenotypic changes to cells that occurred over the course of proliferation or differentiation culture. Cell-laden samples were rinsed in 1×PBS and fixed using 4% paraformaldehyde (Hito) for 30 min at room temperature. Next, cells were permeabilized in 0.1% Triton X-

100 (Biochemica) for 30 min and blocked in 1% bovine serum albumin (BSA) (Sigma) for 45 min at room temperature. Cells were then incubated overnight at 4^{o}C with primary antibodies: mouse anti-TuJ1 (1:400, Millipore), rabbit anti-Ki67 (1:200, Abcam), mouse anti-Nestin (1:400, Millipore). Cells were then fluorescently labelled with appropriate secondary antibodies: goat anti-rabbit Alexa Fluor 555 (1:250, Invitrogen) and donkey anti-mouse Alexa Fluor 488 (1:250, Invitrogen) overnight at 4^{o}C, and counterstained with fluorescent nuclear dye 4′,6-diamidino-2-phenylindole dihydrochloride (DAPI, 1:200, Sigma). To examine cell apoptosis, terminal deoxynucleotidyl transferase (TdT)-mediated dUTP nick-end labelling (TUNEL) staining assay was done according to manufacturer's protocol (Roche).

5.2.9 Cryosectioning and immunofluorescence confocal microscopy

Cell-laden labelled microfiber scaffolds were embedded in Tissue-Tek O.C.T. Compound (Sakura) at -20^{o}C. Thereafter, a cryotome was used to obtain frozen sections of 40 µm thickness which were mounted on poly-lysine adhesive glass slides using Dako fluorescent mounting medium. Confocal scanning laser microscopy (Olympus Fluoview FV1000) was used to capture fluorescence/bright-field images of both coverslips as well as 3D scaffold sections at desired magnifications. Five random, separate fields for each sample were recorded followed by image analysis using custom ImageJ macros for region of interest (ROI) selection and cell counting. Constant image size, magnification, and imaging parameters were used for all measurements. Positive cells were defined as cells with fluorescence intensity three times or more above background level. First, the images were split into separate channels using stack viewing option in ImageJ [6]. The images were then converted to binary style and the pixel intensity threshold values were adjusted to a suitable level to identify individual cells. In the case of images

containing densely packed cells, the watershed segmentation algorithm within ImageJ was used to delineate nuclear boundaries in both 2D and 3D binary images after converting them to masks [7]. Next, the Analyze Particles tool was used to filter out different sizes of particles and count only those objects which are very circular by adjusting the Circularity range numbers in the segmented images. This process of cell counting was done for all channels in each image which correspond to the specific antibodies stained including DAPI. Finally, the average percentage ratios of the total cell number stained for each marker to that of DAPI were determined and the corresponding data were plotted using bar charts for the respective groups (2D and 3D).

5.2.10 Primary neuronal culture

Brains of D18 embryos obtained from pregnant Sprague Dawley rats were dissected using a pair of forceps to isolate the cortex under a microscope. Cortical neurons were obtained from the tissue using papain dissociation protocol and then plated on to laminin coated 3D PLGA electrospun scaffolds placed inside glass bottom dishes at a seeding density of 10-15 million cells/ml. The scaffolds are then shaken using an orbital shaker for 15 mins to ensure an even spread of cells. For 2D controls, the glass bottom dishes were coated with poly-d-lysine (PDL) and cells were seeded at a density of 120000-200000 cells/ml. Neurobasal media supplemented with l-glutamine, pen-strep, B27 and 10% FBS is topped up to 3 ml. Culture media (without FBS) is changed once every two days subsequently and culture is continued for 2 weeks.

5.2.11 Calcium imaging

Cells were stained using Hoechst 33342 (1:1000, Abcam) and Fluo-4 AM (1:100, Thermo Fisher Scientific) on D16 according to manufacturer's protocol. The

staining solution was diluted using PBS supplemented with glucose (Thermo Fisher Scientific). Live cell imaging was carried out on a widefield fluorescent microscope after 30-60 mins of incubation at 37ºC. A 20× objective, auto exposure of 20 ms, gain multiplier of 60, conversion gain of 3.7× and light intensity rating of 8 are used to capture times lapse images of calcium transients of the live cells at 37ºC in both 2D and 3D formats.

5.2.12 Statistical analysis

All experiments were performed in triplicates at a minimum of three independent events, and the results presented are representative data sets. Statistical analysis was performed using unpaired Student's two-tailed *t*-test. Quantitative data were expressed as mean ± standard deviation (SD). Differences were considered statistically significant when $p^* < 0.05$ (GraphPad, Prism).

5.3 Results and Discussion

5.3.1 Fabrication and characterization of 3D PLGA microfiber scaffolds

PLGA was chosen for electrospinning due to its well-documented biodegradability, non-cytotoxicity, sterilizability and biocompatibility [8, 9]. Moreover, it is synthetic and therefore circumvents the immunogenicity and variability issues of animal derived Matrigel used in previous AD models. In addition, neural stem cell culture on 2D films of PLGA has been shown to elicit increased neural differentiation and neurite outgrowth compared with other commonly used polymers such as poly(L-lactide-co-ε-caprolactone) (PLCL) and poly(L-lactic acid) (PLLA) [10].

Firstly, the fabrication process parameters were tuned to obtain randomly oriented, continuous, bead-less microfibers with a uniform diameter using conventional electrospinning (**Table 5-1**). 2D fiber mats obtained using this method had a fiber

diameter ranging between 1-2 µm and pore size ranging between 2-15 µm, resulting in closely packed planar structures with compact layering of fibers. Each layer sits directly below the other preventing infiltration of rounded cells whose size typically ranges between 5-20 µm [11] into inner regions of the scaffold.

Table 5-1. Optimized process parameters for fabrication of PLGA scaffolds.

Electrospinning parameters - PLGA	
Inherent Viscosity (dl/g)	1.5 - 2.0
Concentration (%)	10
Chloroform : DMF	7:3
Flow Rate (ml/hr)	0.8
Needle	20 G blunt
Working Distance(cm)	10
Voltage (kV)	10

Scaffolds fabricated via traditional electrospinning produce fibers with diameters ranging around few hundred nanometers, mimicking native ECM in its fibrillary structure and not in terms of spatial characteristics [12]. Nanofibrous substrates have low porosities and poor pore distribution with pore sizes ranging less than 10 µm, composed of densely packed planar pseudo-3D structures hindering volumetric cell infiltration [13]. This results in cells experiencing a 2D growth pattern which is similar to Petri dish-based monolayer cultures [14]. An optimum pore size is vital for allowing cells to penetrate inside the scaffold, at the same time encapsulating and preventing them from dropping directly to the bottom.

Consequently, we used a wet-electrospinning technique [2], replacing the solid aluminum collector with a grounded ethanol bath to increase fiber dispersion and reduce fiber bonding (**Figure 5-1A**). Ethanol is a low surface tension liquid and

allows fibers starts to sink beneath the surface giving the scaffold its 3D structure. The concentration of ethanol was then optimized, higher concentrations allowing better suspension of the fibers inside the bath. Pore size decreased with increase in concentration of 3D microfiber solutions (**Figure 5-1B**). This trend continued until a threshold was reached after which no change in pore size was observed. Maximum pore size and interfiber spacing were obtained by dispersing microfibers in DI water at a concentration of 2.6 $mg \cdot ml^{-1}$. Interfiber spacing within the 3D PLGA scaffolds ranged between 10-100 µm and the average pore size was 35.04 ± 21.09 µm. SEM imaging was utilized to delineate the morphology of 2D and 3D microfiber constructs (**Figure 5-1C)**. 2D mats were composed of fibers which were mostly straight, whereas wet-electrospun fibers had a loose, curved structure though all process parameters were identical.

Pore size of wet electrospun 3D scaffolds was significantly larger ($p < 0.001$) than corresponding 2D mats (**Figure 5-1D-E**), however, no significant change was observed in average diameter of individual PLGA fibers (1.96 ± 0.16 µm) between them. Various pore shapes were randomly distributed within the 3D microstructure in an interconnected fashion. In addition, fiber diameter was maintained between 1-2 µm to increase pore size and interconnectivity [15], thus ensuring a true 3D environment for cell infiltration, attachment and growth. It is also a key topographic factor in regulating neural stem cell (NSC) fate, with diameters below 500 nm resulting in higher degree of cell spreading and proliferation, ultimately leading to differentiation of NSC into glia [16, 17]. On the contrary, as fiber diameter increases (~1 µm), cells are reported to show decreased migration, spreading and proliferation, preferentially differentiating into neuronal lineage [16, 18].

In addition to pore size and pore interconnectivity, porosity is another key factor which dictates the extent of cellular infiltration, tissue ingrowth and diffusion of essential molecules into the scaffold. The average porosity fraction of the lyophilized 3D PLGA microfiber scaffolds as measured using both gravimetric and liquid displacement methods was ~0.988. This confirms that the wet electrospun scaffolds have large, interconnected pores with significantly lower fiber packing densities compared with 2D fiber mats, thereby enabling cells to infiltrate easily into its inner regions. Taken together, highly porous microfiber scaffolds of 2-10 mm thickness with an average pore size of ~40 μm were fabricated. The cell-seeding paradigm was optimized subsequently via orbital shaking to achieve deep and uniform cell-infiltration of more than 1 mm from the scaffold surface.

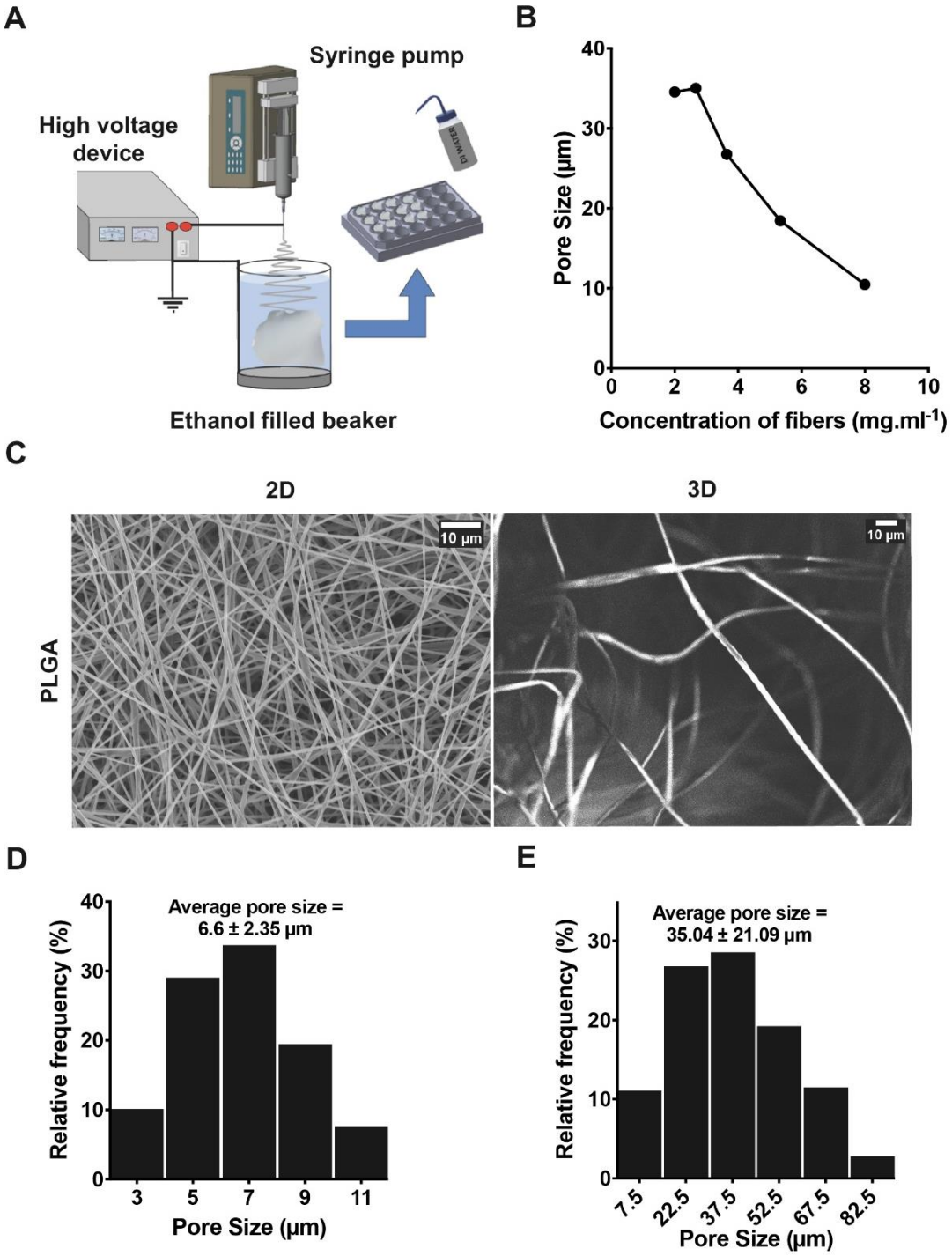

Figure 5-1. Preparation and pore size optimization of 3D PLGA microfiber scaffolds. (A) Schematic of wet-electrospinning process; (B) Variation in pore size of 3D PLGA scaffold with changing microfiber concentration; (C) FE-SEM micrographs showing microfiber morphology and distribution in 2D and 3D scaffolds respectively (Scale bar: 10 µm); Pore size distribution of PLGA (D) 2D & (E) 3D microfiber scaffolds; Data is expressed as mean ± SD (n = 3).

5.3.2 3D PLGA microfiber scaffolds exhibit enhanced wettability after surface treatment

PLGA is intrinsically superhydrophobic in nature, its contact angle ranging over 140^{o}, and prohibiting wetting of the porous structure by water/cell culture media. Hence, scaffolds were subjected to atmospheric air plasma treatment to bring the contact angle down to an intermediate wettability range (~77^{o}), facilitating cell attachment as well as infiltration of culture media [19]. Maintaining the polymer fiber surface at intermediate wettability has been shown to maximize both cell adhesion and protein coating adsorption, which is vital in preventing cell clustering/clumping [20, 21]. A significant reduction in contact angle ($p < 0.001$) from 139.56^{o} ± 1.56^{o} to 77.4^{o} ± 7.47^{o} was obtained after plasma treatment (**Figure 5-2A**), thus improving hydrophilicity of the PLGA scaffolds.

Changes in chemical compositions of PLGA fiber surfaces before and after plasma treatment were investigated by XPS. Low resolution XPS spectra for PLGA (a) before and (b) after plasma treatment are presented (**Figure 5-2B**). It shows two main contributions corresponding to C1s at ~285 eV and O1s located at ~531 eV due to the chemical structure of PLGA, characterized by presence of oxygen in the polymeric chain, and the O/C content being slightly increased after plasma treatment. In addition, high-resolution XPS measurements indicated a shift showing increase in the ratio of carbonyl group in the plasma treated sample and a corresponding decrease in –C–O– bonds, again contributing to hydrophilicity of the sample (**Appendix A8)** [22]. Plasma treatment renders fibers amenable to functionalization via adsorption of biomolecules for improving cell adhesion. In this regard, laminin was incorporated on both 2D and 3D substrate surfaces via physical adsorption to provide integrin binding receptors for cells of neural lineage, promote

NPC adhesion including differentiation into neurons and neurite outgrowth [23]. Physical adsorption of laminin was further enhanced using a pre-adsorbed poly-l-ornithine (PLO) layer on both 2D and 3D substrate surfaces [24, 25], thereby augmenting cell-material interactions without dramatically affecting morphological features of the scaffold.

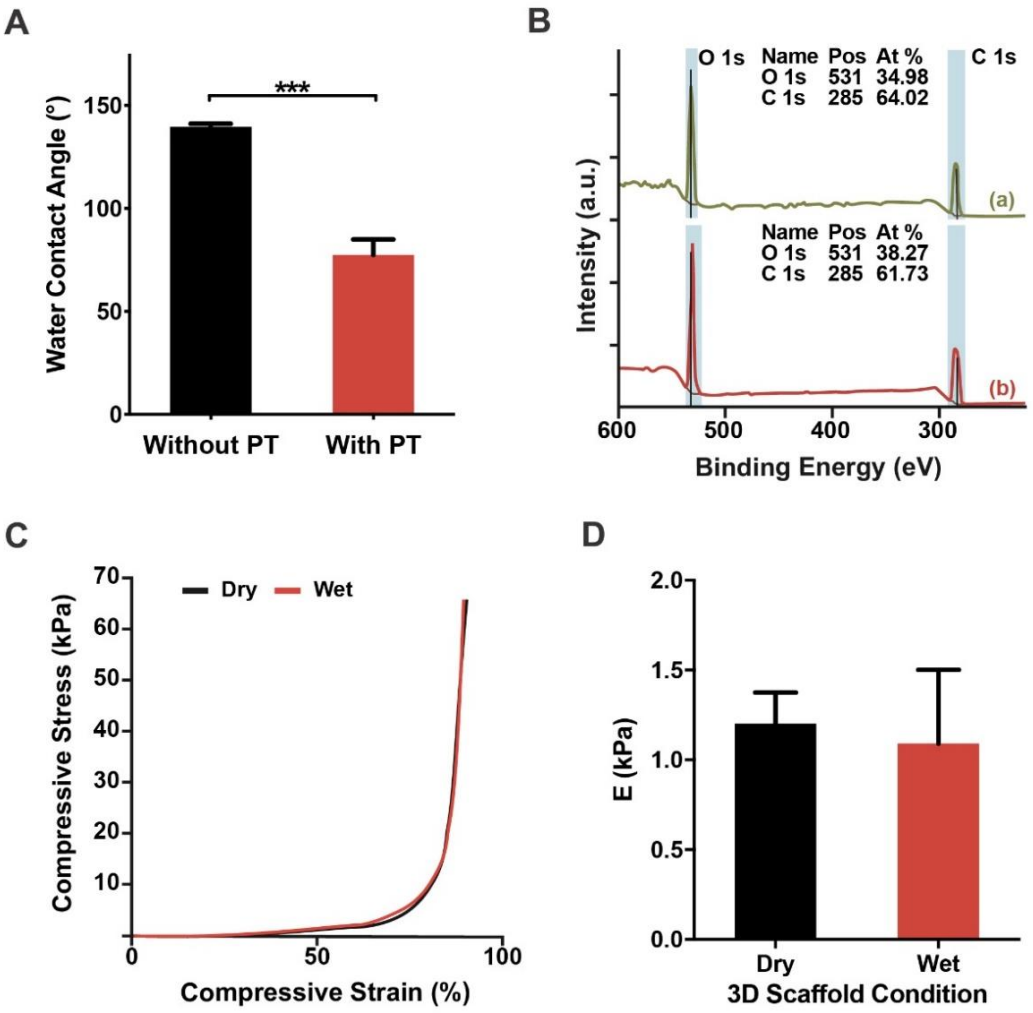

Figure 5-2. Characterization of 3D PLGA microfiber scaffolds. (A) Water contact angles of 3D microfibrous scaffolds before and after plasma treatment; (B) Low resolution XPS spectra of PLGA microfiber surface (a) without and (b) with atmospheric air plasma treatment (300 s); (C) Stress-strain curves obtained for 3D PLGA microfiber scaffolds tested under dry and wet conditions; (D) Compressive moduli determined for dry and wet condition testing; Data is expressed as mean ± SD (n = 5), ***$p < 0.001$.

5.3.3 3D PLGA microfiber scaffolds are comparable to brain ECM in terms of matrix stiffness

In addition to physical and geometric cues, stem cells can mechanosense the stiffness of their microenvironment, which plays a major role in modulating cell survival, growth and lineage/phenotype-specific differentiation [26] Softer substrates (<1 kPa) have been shown to promote neuronal differentiation, whereas stiffer substrates (~10 kPa) lead to glial differentiation [27]. The resistance which a cell feels when it deforms the ECM is measured by the elastic constant E of the matrix or microenvironment. Lyophilized 3D PLGA microfiber scaffolds displayed good elasticity/resilience and could be pressed to large deformations without failure. On removal of compressive force, the scaffolds nearly regained their original shapes instantaneously. In addition, the mechanical properties of microfiber scaffolds in wet state i.e. in PBS at 37^{o}C was also assessed in order to simulate body conditions.

The engineering stress-strain curves for 3D PLGA scaffolds in both dry and wet conditions are as plotted (**Figure 5-2C**). The patterns were similar in both cases i.e. large strains being observed for small load increments, and subsequent marked continuous stiffening with increasing compression loads. A linear elastic regime was observed when compressive strain < 40% and a sharp stress-increasing regime for higher strains. When compressive strain increased beyond 60%, it led to complete pore collapse and clogging leading to a densification regime. Compression moduli of 1.2 ± 0.17 kPa and 1.09 ± 0.4 kPa were obtained for dry and wet conditions respectively (**Figure 5-2D**), no significant difference in stiffness being observed between them. These values are close to the stiffness of brain ECM, elastic modulus of brain tissue ranging around 0.5-1 kPa [28]. This confirms that wet-electrospun 3D PLGA microfibrous scaffolds are capable of mimicking mechanical properties

of *in vivo* conditions, thus promoting more realistic physiological responses compared with Petri dishes/glass cover slips which have flat, stiff surfaces. The high standard deviation could be a result of the randomized pore distribution within the scaffold microstructure. Furthermore, the ultimate compressive strengths of scaffolds were determined for both conditions (**Appendix A8**), a significant difference being observed between dry and wet states ($p < 0.01$). The reason might be that the presence of PBS within the fibrous matrix offers additional resistance at higher compressive loads in contrast with dry scaffolds.

5.3.4 3D PLGA microfiber scaffolds enhance infiltration, uniform distribution and neurite formation

Next, to test the neural differentiation efficiency on 3D PLGA scaffolds, hESC/iPSC-derived NPCs were seeded on PLGA 3D scaffolds and cultured following the neuronal differentiation timeline (**Figure 5-3A**). NPCs seeding was done on both functionalized 2D Petri-dishes/cover slips and 3D microfiber scaffolds on day 12 (D12). Fluorescence imaging of the scaffold cross-section indicated cell infiltration to be greater than 1 mm from the top surface of the scaffold; the seeded cells were uniformly distributed in all regions as a result of orbital seeding (**Figure 5-3B (i-iii)**). Omission of this orbital shaking process immediately after seeding caused majority of cells to accumulate on the top surface of scaffold, lowering cell penetration into inner regions (**Appendix A9**). This demonstrates the necessity as well as effectiveness of orbital seeding in evenly distributing large cell numbers throughout the bulk of the scaffold compared with static surface seeding used in most 3D scaffold-based cultures [5]. In addition, cell density and cell–cell contact are key factors in modulating *in vitro* differentiation and proliferation [29], and

homogeneous seeding of cells is necessary for ensuring adequate cell–cell interactions within the scaffold microstructure.

Majority of iPSC-derived NPCs showed $TuJ1^+$ staining while undifferentiated cells stained positive for Nestin as observed one day after cell seeding (**Appendix A9**). The differentiation rates of iPSC line - 8529 as observed in **Figure 5-3B (iii)** were observed to be similar to the hESC line, a common differentiation protocol and culture timeline being used for all stem cell lines. PLGA microfiber scaffolds supported cell proliferation, identified by $Ki67^+$ staining and neuronal differentiation of hESC-derived NPCs, identified by $TuJ1^+$ staining (**Figure 5-3B (iv-v)**). Neurite formation was observed around some of the cells (indicated by white arrows), attaching and aligning themselves along the randomly distributed microfibers which serve as the framework for contact guidance (**Figure 5-3B (v)**). SEM imaging was used to delineate the morphology of neurons encapsulated between fibers. Cells were observed to attach and grow within the fibrous structure, the cell bodies being encapsulated between multiple fibers (**Figure 5-3B (vi) -** red arrows indicate cell bodies). This gave cells a 3D spatial orientation enabling growth of neurites in all three dimensions. In addition, cell bodies retained a spherical shape contrary to flat, spread out structures commonly observed in 2D monolayer cultures. Taken together, the results confirm the capability of the PLGA microfiber substrate in enabling 3D cellular culture as well as supporting uniform distribution, proliferation and neuronal differentiation of stem cell-derived NPCs. In addition, our seeding paradigm allows deep cellular penetration compared with most existing scaffold-based 3D culture models which rely on static seeding with a cellular infiltration ranging between 200-800 μm [14, 30-32].

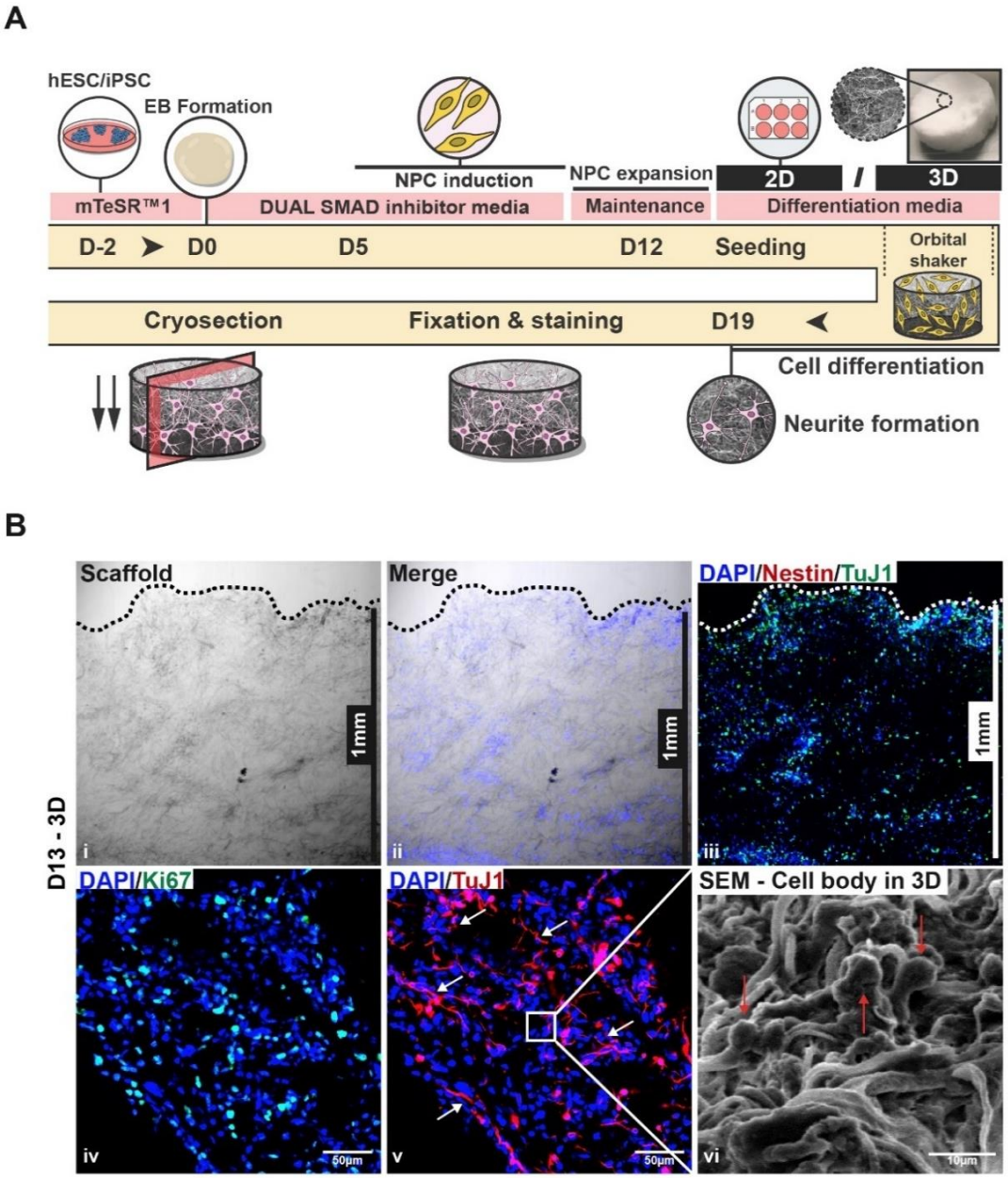

Figure 5-3. Encapsulation and characterization of NPC inside 3D PLGA microfiber scaffolds. (A) Schematic of hESC/iPSC derived neuronal culture illustrating orbital seeding (80 rpm; 20 mins), differentiation protocol and timeline followed for 2D and 3D cultures; (B) Confocal fluorescent microscopy images indicating (i) cross-section of 3D microfiber scaffold after sectioning (dotted line indicates top surface of 3D scaffold); (ii, iii) cell infiltration, distribution and differentiation of iPSC-derived NPCs (8529 cell line) inside 3D scaffold as assessed via staining for TuJ1 (green) and Nestin (red) markers on D13; (iv) cell proliferation assessed by Ki67 (green) marker and (v) cell differentiation with neurite formation indicated by TuJ1 (red) marker of hESC-derived NPCs on D13; Nuclei were counterstained with DAPI (blue); (vi) SEM image of scaffold cross-section showing cell morphology and attachment on microfibers at 2000× magnification.

5.3.5 3D PLGA microfiber scaffolds support long-term cell viability

Cell viability is a key criterion in the development of 3D scaffolds aimed at *in vitro* tissue engineering applications. The material of the scaffold needs to be non-toxic as well as biocompatible taking into account the specific cell/tissue type used in culture. This is vital in neurodegenerative disease modeling applications where encapsulated cells remain within the scaffold for long culture durations in order differentiate, mature and elicit disease pathologies. We quantified cell death inside the electrospun 3D PLGA microfiber scaffolds via immunostaining on D13 and D19 using TUNEL assay. TUNEL can identify DNA fragmentation, a characteristic of both apoptotic as well as necrotic cells. The corresponding representative confocal images of the labeled and cryosectioned scaffolds are illustrated in **Figure 5-4A**. The percentage cell death normalized to DAPI is presented in **Figure 5-4B** for quantitative comparison. Only 2.82 ± 0.47% of cells stained positive for TUNEL on D13. This implies that more than 95% of cells survived one day after seeding. However, a significant increase in cell death was observed by D19, with approximately 9.95 ± 1.66% of cells showing TUNEL positive staining. This is still indicative of a survival rate of ~90% for human stem cell-derived neurons cultured within the microfibrous scaffolds, thereby indicating the excellent cell viability offered by this system compared with existing 3D cell culture platforms [33]. In conclusion, the *in vitro* cell viability analysis of 3D PLGA scaffolds demonstrates the non-cytotoxicity and biocompatibility of this platform for long-term NPC-derived neuronal culture.

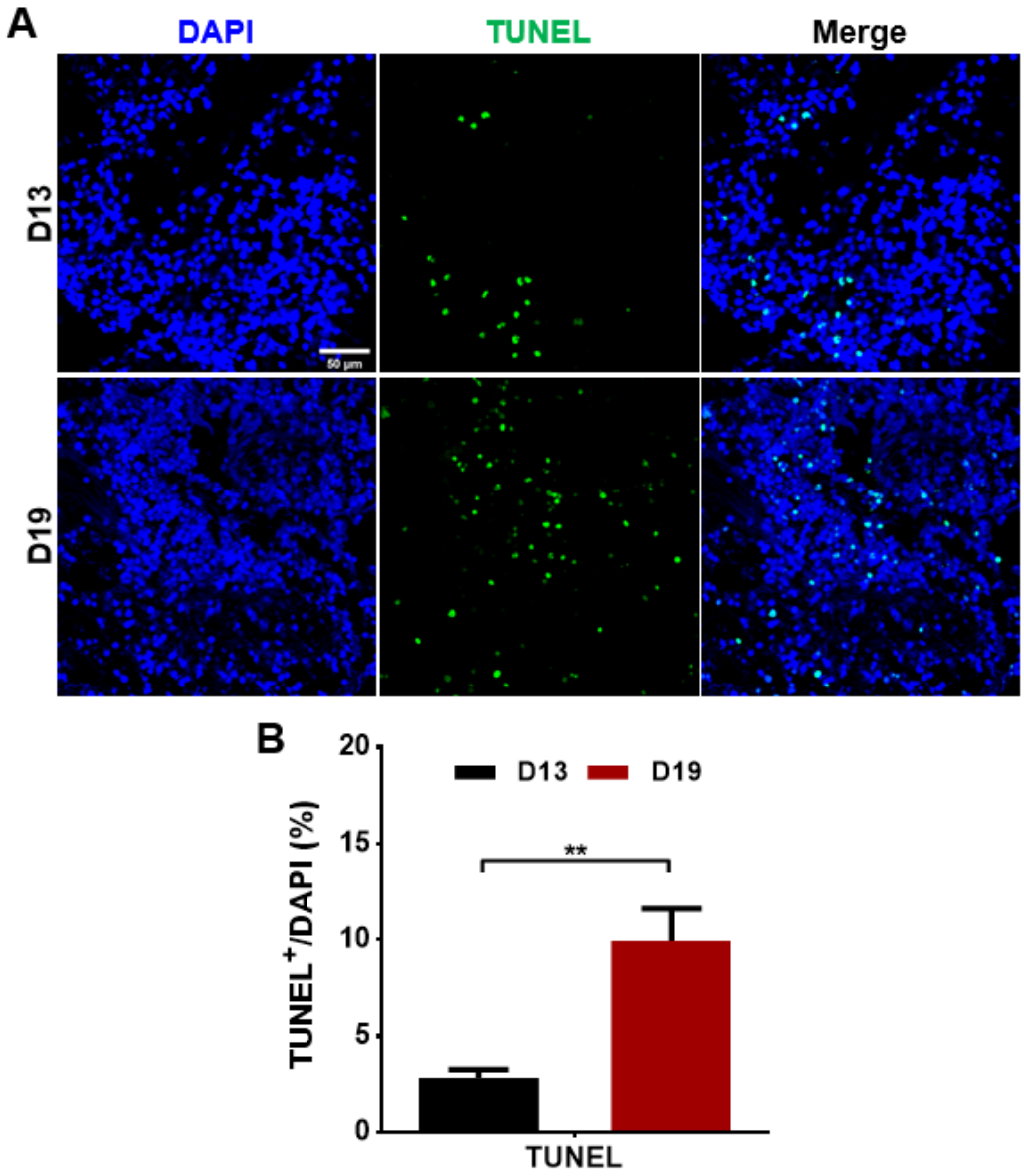

Figure 5-4. (A) Confocal fluorescent microscopy images indicating cell death inside the 3D microfiber scaffolds stained for TUNEL (green) on D13 and D19; Nuclei were counterstained with DAPI (blue); (B) Quantification of immunostaining results showing percentage positive staining of TUNEL marker normalized to DAPI on D13 and D19; Data is expressed as mean ± SD (n = 3), *$p < 0.05$, **$p < 0.01$.

5.3.6 3D PLGA microfiber scaffolds support spontaneous electrophysiological spiking activity of encapsulated neurons

Calcium imaging helps examine the link between electrical activity in neurons to the movements of calcium ions into the cells and vice versa [34]. Calcium transients are more pronounced when there is an increase in the concentration of intracellular

calcium due to Ca inflow across the cell membrane, which in turn is linked to electrophysiological activity of the neurons. Neuronal culture systems in 3D are more appropriate for electrophysiological studies than planar counterparts. Spontaneous electrophysiological activities of 2D and 3D neuronal networks in culture were analyzed using fluorescent calcium imaging analysis. **Figure 5-5A-D** shows Fluo-4 calcium imaging time-lapse images carried out on D16 for both 2D and 3D cortical neuronal cultures. The cells in the 2D format were observed to fire synchronously whereas the firing in the 3D format was random (non-synchronous) in some cases and synchronous in others. This is consistent with other studies which have reported 2D neuronal networks to exhibit high levels of bursting activity and synchronization along with low levels of random spike activity and a high level of synchronization [35]. In contrast, 3D neuronal network dynamics exhibit a wider repertoire of activities with less global synchrony [36]. There was a lot of background observed in 3D imaging owing to the out of focus light when using a wide field microscope. This made it very challenging to visualize the firing of neurons manually in the case of 3D culture. In both culture formats, several cells did not show any calcium transients possibly indicating their inactivity. Taken together, the calcium imaging analysis demonstrates the capability of the PLGA microfibrous scaffolds to support formation of neural circuits and facilitate electrophysiological activity of encapsulated neurons. It must also be noted that the kinetics of the dye used in this study is much slower compared with neuronal action potential spikes, and therefore the change in fluorescence of the calcium indicator is deemed to be analogous to a convolved action potential.

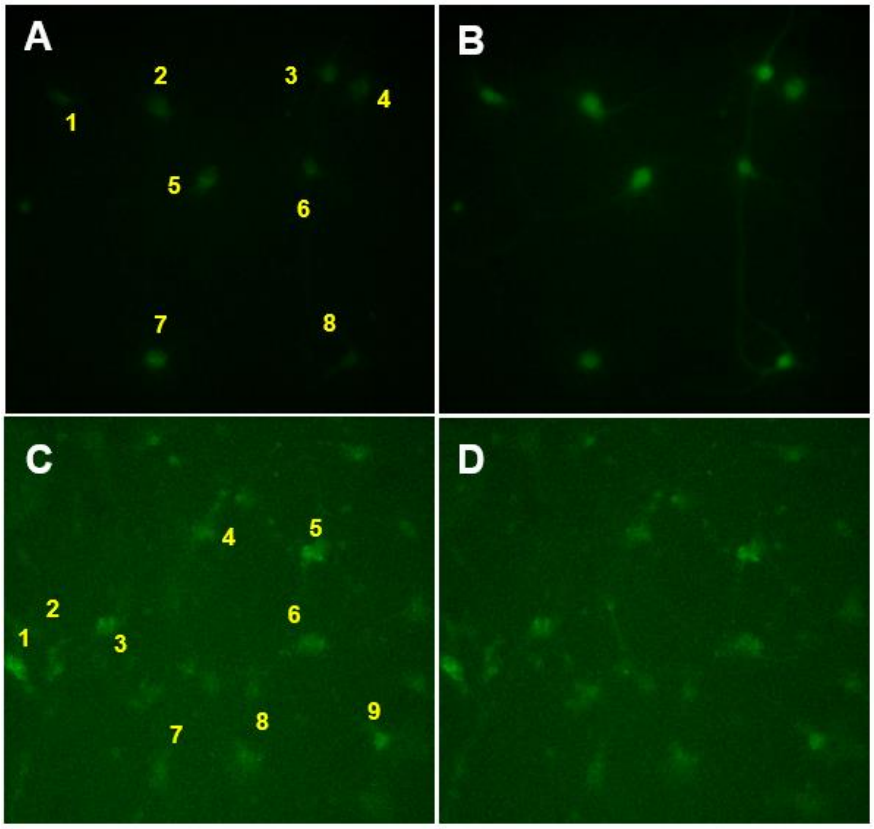

Figure 5-5. Fluorescent calcium time-lapse live cell imaging data; Time lapse images of cortical neurons in 2D culture at different timepoints (A) Exhibiting no activity; (B) exhibiting synchronous bursts; (C-D) time lapse images of cortical neurons in 3D culture exhibiting random spiking and non-synchronous bursting activity; Inset numbers indicate active neurons showing calcium transients.

5.4 Conclusion

In summary, the work presented here demonstrates that wet electrospun PLGA microfibrous scaffolds are capable of supporting human 3D *in vitro* NPC culture and neuronal differentiation. The scaffolds are optimized to have a large pore size and porosity, enabling deep cellular infiltration and uniform distribution of seeded cells from the upper surface compared with most existing platforms. The fibers also serve as a framework for growth of neurites along their surface, which is essential for interaction and function of neurons. Moreover, the cell bodies are in contact with multiple fibers at the same time, thus retaining a spherical structure with a 3D orientation unlike the flat, spread out morphology observed in tissue culture plate

based 2D cultures. Hydrophilicity of the PLGA fibers was enhanced using plasma treatment to enable adsorption of laminin, a key ECM protein which improves NPC adhesion, neuronal differentiation as well as neurite outgrowth. The stiffness of the fibrous substrate was comparable with the elasticity of brain tissue which plays a significant role in promoting realistic physiological responses for regulation of cell fate, survival and growth *in vitro*. Furthermore, fluorescent calcium imaging confirmed the ability of the 3D microfiber scaffolds to support both neurite outgrowth as well as formation of neural circuits exhibiting spontaneous electrophysiological spiking activity.

While our study represents a proof-of-concept that microfibrillar polymer-based scaffolds can serve as a scalable 3D neuronal culture platform, the system is not without limitations. For instance, the micro-architecture of the scaffold cannot be controlled precisely due to random deposition of fibers when electrospinning leading to inconsistent inter-fiber spacing. The opacity of the 3D scaffold composed of hundreds of layers of fibers makes it difficult to perform live cell imaging or visualize neurite formation and outgrowth in real time. Plasma treatment of soft materials such as the 3D PLGA scaffolds used here can cause aging of the modified surface and lead to a degradative effect on the substrate. A very high cell seeding density was necessary to facilitate uniform distribution of cells throughout the macroporous scaffold. Moreover, separation/harvesting of cells encapsulated inside the fibrous structure for further expansion is challenging. Nevertheless, the results show promise for using this synthetic, standardizable, reproducible and easy to implement 3D microfiber substrate-based culture platform for *in vitro* stem-cell derived neuronal modeling of AD.

References

[1] J. Rnjak-Kovacina, A.S. Weiss, Increasing the Pore Size of Electrospun Scaffolds, Tissue Engineering Part B: Reviews 17(5) (2011) 365-372.

[2] Y. Yokoyama, S. Hattori, C. Yoshikawa, Y. Yasuda, H. Koyama, T. Takato, H. Kobayashi, Novel wet electrospinning system for fabrication of spongiform nanofiber 3-dimensional fabric, Materials Letters 63(9) (2009) 754-756.

[3] C. Grienberger, A. Konnerth, Imaging calcium in neurons, Neuron 73(5) (2012) 862-85.

[4] S.M. Chambers, C.A. Fasano, E.P. Papapetrou, M. Tomishima, M. Sadelain, L. Studer, Highly efficient neural conversion of human ES and iPS cells by dual inhibition of SMAD signaling, Nat Biotechnol 27(3) (2009) 275-80.

[5] P. Thevenot, A. Nair, J. Dey, J. Yang, L. Tang, Method to analyze three-dimensional cell distribution and infiltration in degradable scaffolds, Tissue engineering. Part C, Methods 14(4) (2008) 319-31.

[6] J. Schindelin, I. Arganda-Carreras, E. Frise, V. Kaynig, M. Longair, T. Pietzsch, S. Preibisch, C. Rueden, S. Saalfeld, B. Schmid, J.-Y. Tinevez, D.J. White, V. Hartenstein, K. Eliceiri, P. Tomancak, A. Cardona, Fiji: an open-source platform for biological-image analysis, Nature Methods 9 (2012) 676.

[7] L. Vincent, P. Soille, Watersheds in digital spaces: an efficient algorithm based on immersion simulations, IEEE Transactions on Pattern Analysis and Machine Intelligence 13(6) (1991) 583-598.

[8] J.T.S. Pettikiriarachchi, C.L. Parish, M.S. Shoichet, J.S. Forsythe, D.R. Nisbet, Biomaterials for Brain Tissue Engineering, Australian Journal of Chemistry 63(8) (2010) 1143-1154.

[9] L.E. Sperling, K.P. Reis, L.G. Pozzobon, C.S. Girardi, P. Pranke, Influence of random and oriented electrospun fibrous poly(lactic-co-glycolic acid) scaffolds on neural differentiation of mouse embryonic stem cells, Journal of Biomedical Materials Research Part A 105(5) (2017) 1333-1345.

[10] S.H. Bhang, J.S. Lim, C.Y. Choi, Y.K. Kwon, B.-S. Kim, The behavior of neural stem cells on biodegradable synthetic polymers, Journal of Biomaterials Science, Polymer Edition 18(2) (2007) 223-239.

[11] B. Sun, Y.Z. Long, H.D. Zhang, M.M. Li, J.L. Duvail, X.Y. Jiang, H.L. Yin, Advances in three-dimensional nanofibrous macrostructures via electrospinning, Progress in Polymer Science 39(5) (2014) 862-890.
[12] C.P. Barnes, S.A. Sell, E.D. Boland, D.G. Simpson, G.L. Bowlin, Nanofiber technology: designing the next generation of tissue engineering scaffolds, Advanced drug delivery reviews 59(14) (2007) 1413-33.
[13] S. Soliman, S. Sant, J.W. Nichol, M. Khabiry, E. Traversa, A. Khademhosseini, Controlling the porosity of fibrous scaffolds by modulating the fiber diameter and packing density, Journal of biomedical materials research. Part A 96(3) (2011) 566-74.
[14] J. Wu, Y. Hong, Enhancing cell infiltration of electrospun fibrous scaffolds in tissue regeneration, Bioactive Materials 1(1) (2016) 56-64.
[15] J. Rnjak-Kovacina, A. Weiss, Increasing the Pore Size of Electrospun Scaffolds, Tissue engineering. Part B, Reviews 17 (2011) 365-72.
[16] G.T. Christopherson, H. Song, H.Q. Mao, The influence of fiber diameter of electrospun substrates on neural stem cell differentiation and proliferation, Biomaterials 30(4) (2009) 556-64.
[17] L. Moroni, R. Licht, J. de Boer, J.R. de Wijn, C.A. van Blitterswijk, Fiber diameter and texture of electrospun PEOT/PBT scaffolds influence human mesenchymal stem cell proliferation and morphology, and the release of incorporated compounds, Biomaterials 27(28) (2006) 4911-4922.
[18] A.L. Carlson, N.K. Bennett, N.L. Francis, A. Halikere, S. Clarke, J.C. Moore, R.P. Hart, K. Paradiso, M. Wernig, J. Kohn, Z.P. Pang, P.V. Moghe, Generation and transplantation of reprogrammed human neurons in the brain using 3D microtopographic scaffolds, Nat Commun 7 (2016) 10862.
[19] W.M. Saltzman, T.R. Kyriakides, Chapter 20 - Cell Interactions with Polymers A2 - Lanza, Robert, in: R. Langer, J. Vacanti (Eds.), Principles of Tissue Engineering (Fourth Edition), Academic Press, Boston, 2014, pp. 385-406.
[20] W.M. Saltzman, T.R. Kyriakides, Chapter 20 - Cell Interactions with Polymers, in: R. Lanza, R. Langer, J. Vacanti (Eds.), Principles of Tissue Engineering (Fourth Edition), Academic Press, Boston, 2014, pp. 385-406.
[21] C.P. Stallard, K.A. McDonnell, O.D. Onayemi, J.P. O'Gara, D.P. Dowling, Evaluation of Protein Adsorption on Atmospheric Plasma Deposited Coatings

Exhibiting Superhydrophilic to Superhydrophobic Properties, Biointerphases 7(1) (2012) 1-12.
[22] A.M. Pappa, V. Karagkiozaki, S. Krol, S. Kassavetis, D. Konstantinou, C. Pitsalidis, L. Tzounis, N. Pliatsikas, S. Logothetidis, Oxygen-plasma-modified biomimetic nanofibrous scaffolds for enhanced compatibility of cardiovascular implants, Beilstein journal of nanotechnology 6 (2015) 254-62.
[23] P. Liesi, D. Dahl, A. Vaheri, Neurons cultured from developing rat brain attach and spread preferentially to laminin, Journal of Neuroscience Research 11(3) (1984) 241-251.
[24] H. Song, C.F. Stevens, F.H. Gage, Astroglia induce neurogenesis from adult neural stem cells, Nature 417(6884) (2002) 39-44.
[25] M.M. Daadi, In Vitro Assays for Neural Stem Cell Differentiation, in: T. Zigova, P.R. Sanberg, J.R. Sanchez-Ramos (Eds.), Neural Stem Cells: Methods and Protocols, Humana Press, Totowa, NJ, 2002, pp. 149-155.
[26] A.J. Engler, S. Sen, H.L. Sweeney, D.E. Discher, Matrix elasticity directs stem cell lineage specification, Cell 126(4) (2006) 677-89.
[27] K. Saha, A.J. Keung, E.F. Irwin, Y. Li, L. Little, D.V. Schaffer, K.E. Healy, Substrate modulus directs neural stem cell behavior, Biophysical journal 95(9) (2008) 4426-38.
[28] B.S. Elkin, E.U. Azeloglu, K.D. Costa, B. Morrison, 3rd, Mechanical heterogeneity of the rat hippocampus measured by atomic force microscope indentation, Journal of neurotrauma 24(5) (2007) 812-22.
[29] L.A. Solchaga, E. Tognana, K. Penick, H. Baskaran, V.M. Goldberg, A.I. Caplan, J.F. Welter, A rapid seeding technique for the assembly of large cell/scaffold composite constructs, Tissue engineering 12(7) (2006) 1851-63.
[30] Q.L. Loh, C. Choong, Three-Dimensional Scaffolds for Tissue Engineering Applications: Role of Porosity and Pore Size, Tissue Engineering Part B: Reviews 19(6) (2013) 485-502.
[31] S.H. Choi, Y.H. Kim, M. Hebisch, C. Sliwinski, S. Lee, C. D'Avanzo, H. Chen, B. Hooli, C. Asselin, J. Muffat, J.B. Klee, C. Zhang, B.J. Wainger, M. Peitz, D.M. Kovacs, C.J. Woolf, S.L. Wagner, R.E. Tanzi, D.Y. Kim, A three-dimensional human neural cell culture model of Alzheimer's disease, Nature 515(7526) (2014) 274-8.

[32] D. Zhang, M. Pekkanen-Mattila, M. Shahsavani, A. Falk, A.I. Teixeira, A. Herland, A 3D Alzheimer's disease culture model and the induction of P21-activated kinase mediated sensing in iPSC derived neurons, Biomaterials 35(5) (2014) 1420-8.
[33] J. Gopinathan, I. Noh, Recent trends in bioinks for 3D printing, Biomaterials Research 22(1) (2018) 11.
[34] F.B. Neubauer, J.N. MacLean, Calcium Imaging in Neuroscience, eLS, John Wiley & Sons, Ltd2001.
[35] M. Frega, M. Tedesco, P. Massobrio, M. Pesce, S. Martinoia, Network dynamics of 3D engineered neuronal cultures: a new experimental model for in-vitro electrophysiology, Sci Rep 4 (2014) 5489.
[36] M. Tedesco, M. Frega, S. Martinoia, M. Pesce, P. Massobrio, Interfacing 3D Engineered Neuronal Cultures to Micro-Electrode Arrays: An Innovative In Vitro Experimental Model, Journal of visualized experiments : JoVE (105) (2015) e53080.

CHAPTER 6 3D *in vitro* human neuronal modeling of AD

The work presented in **Chapters 5** and **6** is largely based on the following publication: Vivek Damodar Ranjan, Lifeng Qiu, Jolene Wei-Ling Lee, Xuelong Chen, Se Eun Jang, Chou Chai, Kah-Leong Lim, Eng-King Tan, Yilei Zhang, Wei Min Huang, Li Zeng. "A microfiber scaffold-based 3D *in vitro* human neuronal culture model of Alzheimer's disease." *Biomaterials Science* (2020). http://dx.doi.org/10.1039/D0BM00833H.

6.1 Evaluation and comparison of 3D scaffold platforms based on design criteria

Three different platforms were developed for achieving 3D *in vitro* neuronal culture as discussed in the preceding chapters. These include: a graphene oxide hydrogel-based electroconductive substrate fabricated via physical crosslinking (**Chapter 3**); a synthetic polymer-based, hollow microfiber substrate fabricated via core-shell electrospinning (**Chapter 4**); and a synthetic polymer-based, non-woven fibrillar substrate fabricated via wet electrospinning (**Chapter 5**). Each substrate was studied independently and has its own advantages and limitations. The next step is to compare them with one another in terms of the array of properties required for 3D neuronal culture matrices, and then select the most suitable substrate for 3D *in vitro* human stem cell-derived neuronal modeling of AD.

In the following tables, a concise review and comparison of all three substrates is presented based on the general design criteria for *in vitro* scaffolding. These include both physical/structural properties of the substrate (**Table 6-1**) and the biological properties necessary for interfacing it with neuronal cultures (**Table 6-2**).

Table 6-1. Comparison of physical/structural properties of *in vitro* scaffolding platforms.

	SCAFFOLD DESIGN CRITERIA – PHYSICAL/STRUCTURAL PROPERTIES							
	Ease of fabrication	Scalability	Porosity	Interconnected pore network	Hydrophilicity	Surface functionalization	Mechanical properties	Conducti
ked sed el	✓	✓✓	✓✓	✓✓	✓	✓	✓	✓
pun te	✓✓	✓	✓	✓	✗	✗	✓	✗
	✓✓✓	✓✓✓	✓✓✓	✓✓✓	✓✓✓	✓✓	✓✓✓	✗

Table 6-2. Comparison of biological properties of *in vitro* scaffolding platforms.

E	SCAFFOLD DESIGN CRITERIA – BIOLOGICAL PROPERTIES							
	Cell seeding/encapsulation	Cell infiltration	Cell distribution	3D culture	Cell viability	Cell proliferation	Neuronal differentiation	Neurit formati
inked based ogel	✓✓✓	✓✓✓	✓✓✓	✓✓	✓✓✓	✓✓✓	✓✓✓	✗
	✓✓	✓	✓	✓	✓✓	✓	✗	✗

spun r- rate								
r-	✓	✓✓	✓✓	✓✓✓	✓✓✓	✓✓✓	✓✓✓	✓

Both the graphene oxide-based hydrogel and the coaxially electrospun PLGA hollow microfiber-based substrate are direct cell-scaffold fabrication techniques which provide the advantage of generating the scaffold while simultaneously encapsulating cells. In contrast, the wet electrospun non-woven fiber-based substrate requires passive cell seeding i.e. after scaffold fabrication [1], where cells are laid on top of the scaffold and allowed to infiltrate the scaffold over time. An additional orbital seeding step is necessary in this case to ensure deep infiltration and uniform distribution of cells throughout the scaffold construct. However, this also provides opportunities for making additional surface modification or surface treatments which is not possible with the other two substrates. For instance, plasma treatment to enhance both hydrophilicity of the fiber surface as well as surface adsorption of ECM-related biomolecules such as laminin could be performed on the PLGA wet-electrospun scaffolds. This improved neuronal cell attachment and enabled neurite formation, leading to the formation of neural circuits. On the other hand, both the graphene oxide hydrogel and hollow microfiber scaffolds were hydrophobic in nature, causing cells to clump together and limiting the formation of neurites and neuronal networks. Although the graphene-based hydrogel offers the additional advantage of conductivity, further work is required to improve the hydrophilicity as well as the mechanical integrity of the scaffold for use as a long-term *in vitro* culture platform.

Taken together, the PLGA wet-electrospun, non-woven, microfiber-based substrate demonstrates the most potential as a simple, standardizable, reproducible and easy to implement 3D culture system for promoting neuronal attachment, growth and differentiation. Moreover, polymeric fibrous scaffolds possess excellent ECM attributes such as large surface-area-to-volume ratio, high porosity and a fibrillar

structure which facilitates neurite contact guidance as well as efficient diffusion of nutrients and waste [2]. In addition, tailoring of the fiber diameter as well as spatial orientation has been shown to regulate both neural stem cell proliferation and neural differentiation [3, 4].

Next, we leverage on these advantages and combine the electrospun microfibrous PLGA scaffolds with FAD patient iPSC-derived neurons to develop a novel, proof-of-concept 3D *in vitro* platform for modeling AD. Conventional Petri dish-based 2D cultures were used as monolayer controls for a comparative assessment of cell phenotypes and recapitulation of AD pathologies (**Figure 6-1**). Although electrospun scaffolds have widely been used in neural tissue engineering applications [5], to the best of our knowledge, the present findings represent the first description of interfacing polymer-based fibrillar scaffolds with FAD patient iPSC-derived neurons for 3D *in vitro* modeling of early-stage AD pathogenesis.

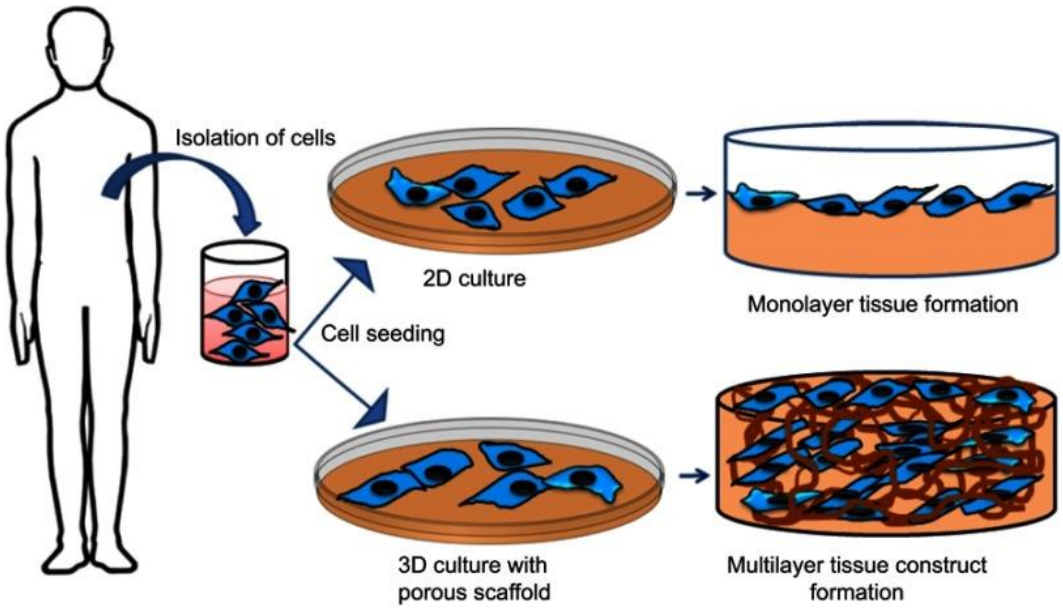

Figure 6-1. Schematic representation of 2D and 3D cultures (Adapted from [6])

6.2 Materials and Methods

6.2.1 Derivation of iPS cells

FAD fibroblasts (AG09908, AG06840) and control fibroblasts (AG04148, AG08529) were obtained from Coriell Cell Repository. Fibroblasts were reprogramed to iPSC via transfection of Nanog, Lnc28, Oct4, klf2, c-myc, Sox2. Somatic reprogramming of fibroblasts was performed using a modification of the EBNA-1 based episomal reprogramming method described by Okita *et al.* [7] Episomal vectors, namely, pCXLE-hOCT3/4-shp53-F, pCXLE-hSK, and pCXLE-hUL were commercially available from Addgene. Fibroblasts cell lines were dissociated using 1× trypsin/EDTA solution. Cells were counted and 6×10^5 cells were pelleted and resuspended in 100 µL Buffer R from the Neon Transfection System 100 µL Kit (Life Technologies, MPK10096). The cell suspension was mixed with 1 µg each of the 3 reprogramming vectors and loaded into a 100 µL Neon® Tip. Transfection was performed on the Neon electroporation device (Life Technologies MPK5000) using the following parameters: 1650 V, 10 ms, 2 pulses. Transfected cells were distributed evenly into 3 wells of a 6-well plate (BD Falcon) and maintained in complete DMEM medium (DMEM high glucose, 10% FBS, 1× GlutaMAX, 100 µM non-essential amino acid, 1 mM sodium pyruvate, 100 µM β-mercaptoethanol, all from Life Technologies) without antibiotics for 7 days with medium change every other day. At D7, cells were dissociated using 1× trypsin/EDTA solution prior to cell counting.

From here on, previously mentioned Okita *et al.* protocol has been optimized and modified to meet the needs for feeder-free iPS derivation. Total of 1×10^5 cells were plated/well of Matrigel (Becton-Dickinson) coated 6-well plate in complete DMEM medium. The following day, the medium was replaced with 1:1 mixture of complete

DMEM and defined pluripotent stem cell medium mTeSR1 (StemCell Technologies). From next day on, conditioned media was replaced with fresh mTeSR1 media with media change being performed every other day. When iPS colonies reach about ~0.5-1 mM in diameter (around 3 weeks post-transfection onward), they were manually picked under bright field microscopy and each colony placed in a single well of Matrigel coated 24-well plate (Nunc). Cells were detached using Dispase (StemCell Technologies) when ~50% confluency was reached and transferred into Matrigel-coated 6-well plate. Subsequently, cells were passaged 1:3 by dissociation with 0.5 mM EDTA when they reached near confluence. Newly passaged cells were cultured overnight in media containing 10 μM ROCK inhibitor Y-27632.

6.2.2 hESC/iPSC maintenance and neuronal differentiation

Human embryonic stem cells (hESC) were obtained from ES Cell International. Human ESC/iPSC were maintained in mTeSR1 media (StemCell Technologies) on Matrigel coated dishes (Corning). Media change was performed daily until 70% confluency was obtained. To expand hESC/iPSC cultures, dispase (StemCell Technologies) was used to dissociate cells into clumps. ROCK inhibitor (10 μM) was added into media during either passage, freezing and thawing steps to promote cell survival. hESC and iPSC were differentiated into frontal cortical neurons using Dual SMAD inhibition protocol in both 2D and 3D culture formats [8]. Briefly, to initiate embryonic body (EB) formation, cells were dissociated with accutase (Gibco) at D2 and seeded onto 6-well culture plates (Thermo Fisher Scientific) in mTeSR1 media supplemented with ROCK inhibitor. From D0-D4, media was replaced with Dual SMAD inhibition media containing DMEM/F12 (Gibco), Neurobasal media (Gibco), non-essential amino acids (Gibco), GlutaMAX (Gibco),

N2 supplement (Life Technologies), B27 supplement with vitamin A (Life Technologies), 0.1µM LDN193189 (Stemgent) and 10µM SB431542 (Cellagen Tech) every 2 days until D5. Thereafter, EBs were transferred into Matrigel coated dishes with daily media change until D12. At this stage, induced neural progenitor cells (NPC) were dissociated using accutase and re-plated onto Matrigel coated dishes in NPC maintenance media (DMEM/F12 with glutamine, B27 supplement without vitamin A, N2 supplement and 20ng/ml bFGF (StemCell Technologies) with daily media change.

Cells continue to remain at NPC stage from D12 until media is replaced with neuronal differentiation media. At passage 3-6, NPC were seeded onto surface modified coverslips (2×10^5 cells/cm^2), 6-well plates (2×10^5 cells/cm^2) and 3D scaffolds (2.5×10^6 cells/cm^2) respectively. Cell seeding density and cell suspension volume for scaffolds was optimized to 5×10^6 cells and 200 µl per scaffold respectively. After seeding, scaffolds were immediately placed on an orbital shaker and agitated for 20 minutes at 70 rpm, to ensure deeper and uniform cell penetration to all regions within the scaffold [9]. Thereafter, top up of NPC maintenance medium was done and samples were incubated at 37ºC with 5% CO_2. Media change was done daily with neuronal differentiation media containing neurobasal media, non-essential amino acids, GlutaMAX, B27 with vitamin A, 2.5µM DAPT (Tocris), 10ng/ml BDNF (Sigma), 10ng/ml GDNF (Sigma), 200µM ascorbic acid (Sigma) and 0.5mM db-cAMP (Sigma) until D19 after which the cells were harvested. The hESC line was used for characterization and comparison of cell viability, proliferation and differentiation and the iPSC lines were used for investigation of Aβ and p-tau pathologies. The differentiation culture protocol, timeline and culture

media used for all patient-derived iPSC lines are the same as that used for the hESC line illustrated in the previous chapter (**Figure 5-3A**).

6.2.3 Immunocytochemistry

Immunofluorescence staining was performed to characterize phenotypic changes to cells that occurred over the course of proliferation or differentiation culture. Cell-laden samples were rinsed in 1×PBS and fixed using 4% paraformaldehyde (Hito) for 30 min at room temperature. Next, cells were permeabilized in 0.1% Triton X-100 (Biochemica) for 30 min and blocked in 1% bovine serum albumin (BSA) (Sigma) for 45 min at room temperature. Cells were then incubated overnight at 4^{o}C with commercially available primary antibodies: mouse anti-TuJ1 (1:400, Millipore), rabbit anti-Ki67 (1:200, Abcam), mouse anti-NeuN (1:400, Millipore), rabbit anti-cleaved caspase-3 (1:400, Cell Signaling), mouse anti-GFAP (1:400, Abcam). Cells were then fluorescently labelled with appropriate secondary antibodies: goat anti-rabbit Alexa Fluor 555 (1:250, Invitrogen) and donkey anti-mouse Alexa Fluor 488 (1:250, Invitrogen) overnight at 4^{o}C, and counterstained with fluorescent nuclear dye 4′,6-diamidino-2-phenylindole dihydrochloride (DAPI, 1:200, Sigma).

6.2.4 Cryosectioning and immunofluorescence confocal microscopy

Cell-laden labelled microfiber scaffolds were embedded in Tissue-Tek O.C.T. Compound (Sakura) at -20^{o}C. Thereafter, a cryotome was used to obtain frozen sections of 40 µm thickness which were mounted on poly-lysine adhesive glass slides using Dako fluorescent mounting medium. Confocal scanning laser microscopy (Olympus Fluoview FV1000) was used to capture fluorescence/bright-field images of both coverslips as well as 3D scaffold sections at desired magnifications. Five random, separate fields for each sample were recorded

followed by image analysis using custom ImageJ macros for region of interest (ROI) selection and cell counting. Constant image size, magnification, and imaging parameters were used for all measurements. Positive cells were defined as cells with fluorescence intensity three times or more above background level. First, the images were split into separate channels using stack viewing option in ImageJ [10]. The images were then converted to binary style and the pixel intensity threshold values were adjusted to a suitable level to identify individual cells. In the case of images containing densely packed cells, the watershed segmentation algorithm within ImageJ was used to delineate nuclear boundaries in both 2D and 3D binary images after converting them to masks [11]. Next, the Analyze Particles tool was used to filter out different sizes of particles and count only those objects which are very circular by adjusting the Circularity range numbers in the segmented images. This process of cell counting was done for all channels in each image which correspond to the specific antibodies stained including DAPI. Finally, the average percentage ratios of the total cell number stained for each marker to that of DAPI were determined and the corresponding data were plotted using bar charts for the respective groups (2D and 3D, D13 and D19).

6.2.5 Gene expression qPCR analysis

Both 2D and 3D samples were homogenized in 1 ml of QIAzol lysis reagent (Qiagen) and total RNA was isolated with RNeasy kit (Qiagen) according to manufacturer's instructions. Reverse transcription polymerase chain reaction (RT-PCR) was carried out using iScript cDNA synthesis kit (Bio-rad). Synthesized cDNA products were subjected to real-time quantitative PCR (qPCR) using LightCycler 96 system (Roche) with All-in-One™ qPCR mix (GeneCopoeia).

Relative mRNA expression levels of target genes were calculated based on 2ΔΔCt formula and normalized to 2D monolayer controls.

6.2.6 Enzyme-linked Immunosorbent Assay (ELISA) and Western blot

Protein extraction was performed using PBS containing 1% Triton in the presence of phosphatase and protease inhibitors (MedChem Express). Cells were lysed in lysis buffer for 30 min on ice and agitated every 10 min. Scaffold cultures were homogenized for an additional 30 seconds before agitation to force cells out of the scaffold. Samples were centrifuged at 18,506 g at 4°C for 15 min. Cell supernatant was collected, and protein concentration was quantified using DC protein assay (Bio-rad) analyzed with infinite M200 plate reader (Tecan). ELISA was carried out to quantify total level of amyloid-beta (1-42) (Aβ42) using Human Amyloid-β (1-42) High-sensitive ELISA kit (Wako). Western blot was carried out using 20 μg of total protein lysate per sample with primary antibodies (1:1000 mouse anti-phospho-Tau (AT8) (Thermo Fisher Scientific) and 1:1000 mouse anti-β-actin (Cell Signalling Technology).

6.2.7 Statistical analysis

All experiments were performed in triplicates at a minimum of three independent events, and the results presented are representative data sets. Statistical analysis was performed using unpaired Student's two-tailed *t*-test. Quantitative data were expressed as mean ± standard deviation (SD). Differences were considered statistically significant when $p^* < 0.05$ (GraphPad Prism).

6.3 Results

6.3.1 3D PLGA microfiber scaffolds support long-term survival of stem cell-derived NPCs and differentiated neurons

We quantified cell death in 2D and 3D cultures using cleaved caspase 3 (CC3) cell apoptosis marker detection via immunostaining on both D13 and D19 (**Figure 6-2A**), and percentage cell death normalized to DAPI for quantitative comparison (**Figure 6-2B**). On D13, 1.88 ± 0.24% and 3.67 ± 1.71% of total cells stained positive for CC3 in 2D and 3D cultures respectively ($p < 0.05$). This indicates that more than 95% of cells encapsulated within the microfibrous scaffolds survived one day after seeding. A significant increase ($p < 0.05$) in cell death was observed in 3D culture by D19, with approximately 4.17 ± 1.34% and 11.49 ± 2.49% of total cells staining positive for CC3 in 2D and 3D cultures respectively. However, this survival rate of ~90% for stem cell-derived neurons after a week of culture within the PLGA microfibrous scaffolds demonstrates the excellent biocompatibility of this platform, and is comparable with cell viability data (ranging between 80-90%) observed in various existing 3D neural cell culture platforms [3, 12, 13].

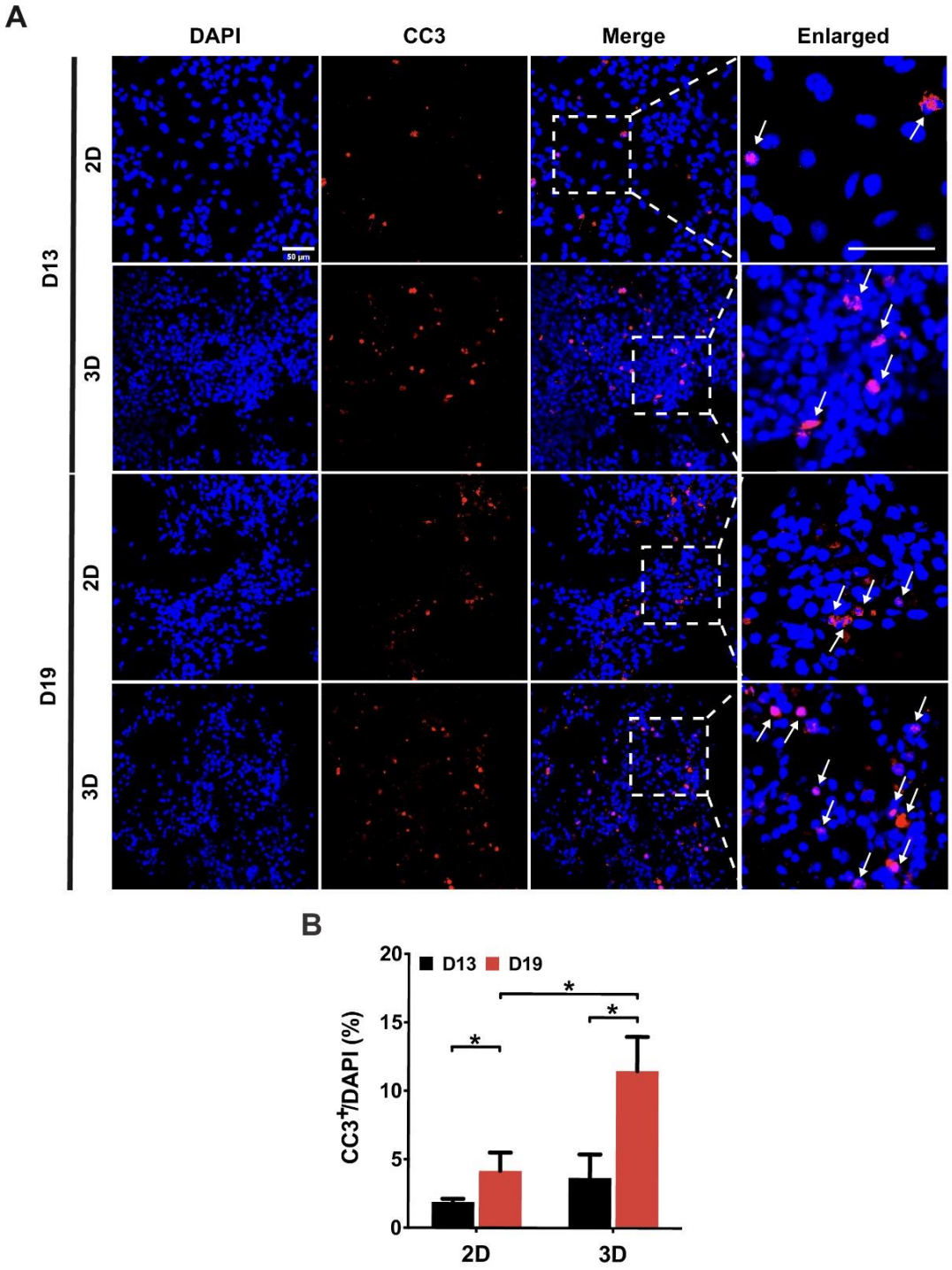

Figure 6-2. 3D PLGA microfiber scaffolds support survival of encapsulated cells. (A) Confocal fluorescent microscopy images indicating cell death in both 2D and 3D cultures stained for cleavage caspase 3 (CC3) (red) marker on D13 and D19; Nuclei were counterstained with DAPI (blue); (B) Quantification of immunostaining results showing percentage positive staining of cell death marker CC3 normalized to DAPI for D13 and D19; Data is expressed as mean ± SD (n = 3), *$p < 0.05$, **$p < 0.01$; Scale bar: 50 µm.

6.3.2 3D PLGA microfiber scaffolds reduce cell proliferation rates compared with 2D monolayer culture

To examine whether 3D microfiber scaffolds regulate proliferation of the stem-cell derived NPCs we quantified percentage of proliferative cells, identified by positive Ki67 staining on both D13 and D19 and comparing them with 2D controls (**Figure 6-3A**). 43.47 ± 4.5% of total cells in 2D monolayer culture were $Ki67^+$ on D13, indicating that majority of the cells continued to proliferate one day after seeding (**Figure 6-3B**). In contrast, 3D culture within microfiber scaffolds induced significant reduction ($p < 0.001$) in percentage cell proliferation, with only 14.58 ± 3.39% of total cells staining showing $Ki67^+$ positive staining. However, 2D cultures also showed a significant decrease ($p < 0.01$) in number of proliferative cells by D19, with only 14.98 ± 3.92% of total cells staining $Ki67^+$. In similar fashion, cell proliferation numbers showed a more pronounced decrease ($p < 0.05$) in 3D cultures, only 6.19 ± 1.99% of total cells staining $Ki67^+$ after one week of culture (**Figure 6-3B**). To further confirm immunocytochemistry results, we characterized expression levels of Ki67 for both 2D and 3D cultures on D19 using qPCR for specific gene targets (**Appendix A10**). We observed a nearly twofold decrease ($p < 0.05$) in Ki67 expression for 3D scaffold-based culture compared with 2D controls (**Figure 6-3C**). These results clearly demonstrate that 3D PLGA microfibrous scaffold-based culture induces significant reduction in NPC proliferative rates, compared with conventional 2D monolayer culture.

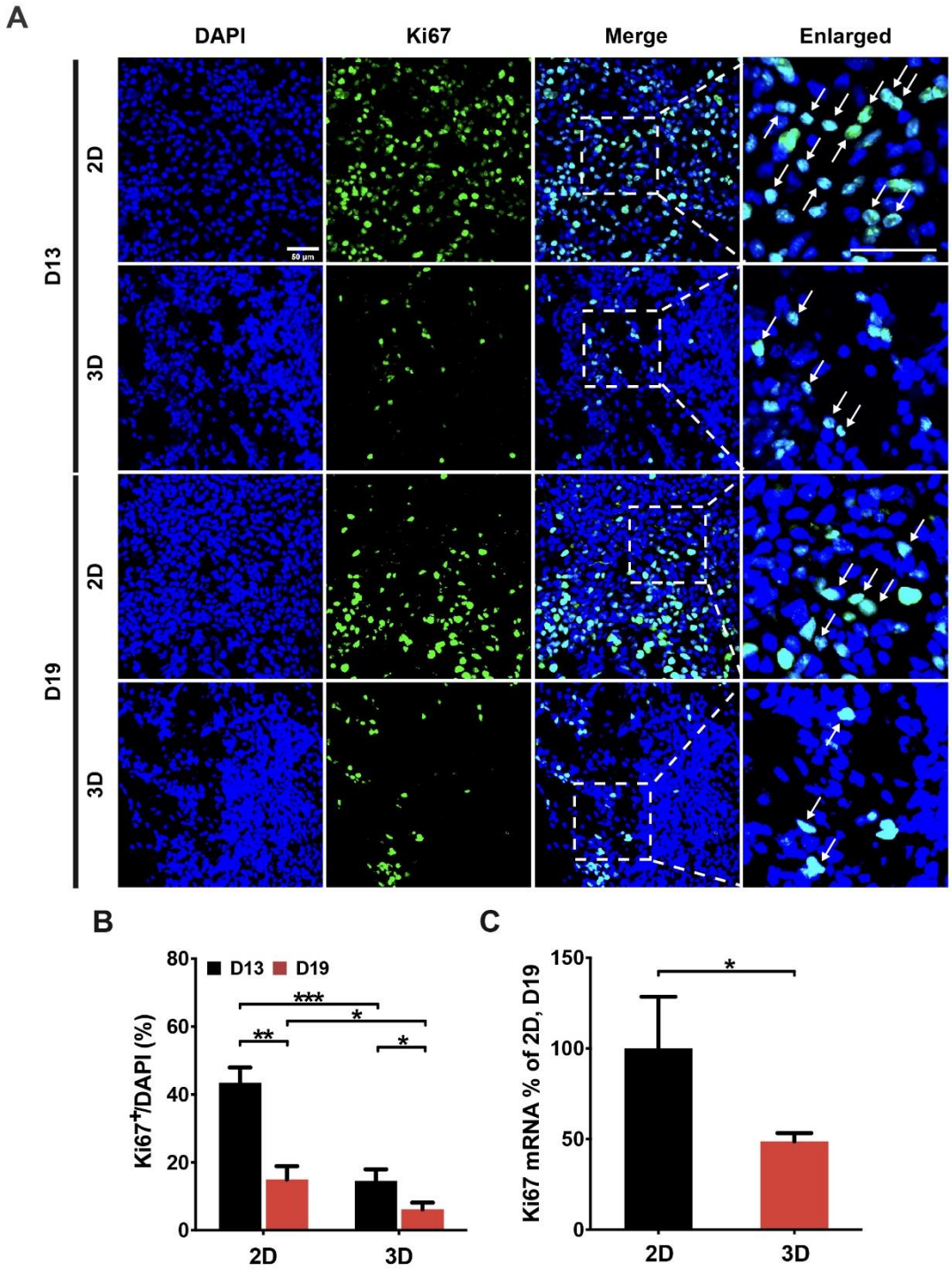

Figure 6-3. 3D PLGA microfiber scaffolds decrease cell proliferation rates. (A) Confocal fluorescent microscopy images indicating hESC derived NPC proliferation in both 2D and 3D cultures as stained for Ki67 (green) marker on D13 and D19; Nuclei were counterstained with DAPI (blue); (B) Quantification of immunostaining results showing percentage positive staining of cell proliferation marker Ki67 normalized to DAPI for D13 and D19; (C) qPCR analysis of Ki67 expression in cells cultured via 2D and 3D formats on D19; Data is expressed as mean ± SD (n = 3), *$p < 0.05$, **$p < 0.01$, ***$p < 0.001$; Scale bar: 50 µm.

6.3.3 3D PLGA microfiber scaffolds accelerate neuronal differentiation compared with 2D monolayer culture

To investigate and compare efficiency of cell differentiation between the 2 platforms, the NPCs were differentiated, and expression of different neuronal and glial markers was investigated at the protein level. We quantified neuronal differentiation in both 2D and 3D cultures by detection of neuronal lineage marker β3-tubulin (TuJ1) via immunofluorescence staining on D13; maturation of neurons was in turn quantified by detection of mature neuronal marker NeuN on D19 (**Figure 6-4A**). In addition, corresponding glial differentiation was assessed by detection of astrocyte marker GFAP (**Appendix A11**). We found that 3D culture significantly enhanced neuronal differentiation ($p < 0.001$) on D13, nearly 30.72 ± 1.15% of total cells were $TuJ1^+$, compared with 2.78 ± 0.04% for 2D controls (**Figure 6-4B**). However, no glial differentiation was observed in both 2D and 3D cultures at this time. By D19, 15.93 ± 3.81% of total cells were $NeuN^+$ in 3D culture, again significantly greater than 2D controls ($p < 0.01$) which showed negligible (~0.05%) NeuN expression. In similar fashion, 3D cultured cells showed a pronounced expression of GFAP with 5.12 ± 1.00% of total cells staining positive on D19, in contrast to 2D controls ($p < 0.001$) which did not show any positive staining at both timepoints (**Appendix A11**). To further validate staining results for neuronal differentiation, we assessed expression levels of NeuN on D19 for both conditions using qPCR. An eightfold increase ($p < 0.001$) in NeuN expression was obtained for 3D culture compared with 2D controls (**Figure 6-4C**), confirming the capability of the microfibrous substrate in promoting highly efficient neuronal differentiation, glial differentiation as well as accelerated maturation of neurons within a week of culture.

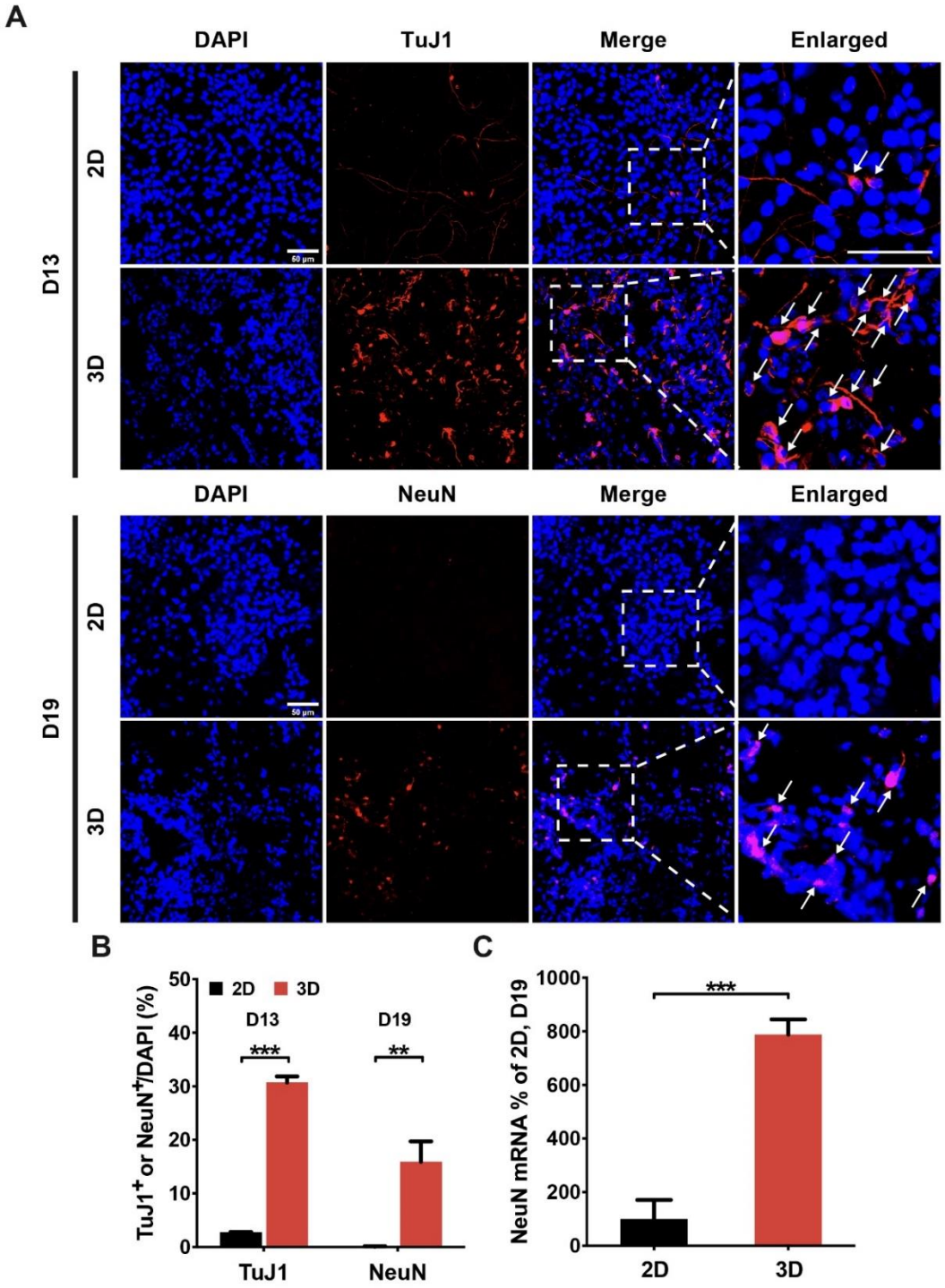

Figure 6-4. 3D PLGA microfiber scaffolds accelerate neuronal differentiation. (A) Confocal fluorescent microscopy images indicating hESC derived neuronal differentiation in 2D and 3D cultures stained for TuJ1 (red) and NeuN (red) markers on D13 and D19 respectively; Nuclei were counterstained with DAPI (blue); (B) Quantification of immunostaining results showing percentage positive staining of neuronal differentiation markers Tuj1 and NeuN normalized to DAPI for D13 and D19; (C) qPCR analysis of NeuN expression in cells cultured via 2D and 3D formats on D19; Data is expressed as mean ± SD (n = 3), **$p < 0.01$, ***$p < 0.001$; Scale bar: 50 µm.

6.3.4 3D PLGA microfiber scaffolds amplify pathogenic Aβ42 and p-tau levels in FAD-iPSC derived neurons

To determine if 3D PLGA scaffold-based culture mediates upregulation of pathogenic Aβ42 expression in iPSC-derived neurons, we quantified Aβ42 levels of cells lines with FAD mutations (6840 and 9908) and compared them to non-demented age-matched controls (4148 and 8529) on D19. Details on the origin of above-mentioned cell lines have been summarized (**Table 6-3**).

Table 6-3. Overview of iPSC lines utilized for AD pathogenesis study.

ID	Description	Gene	Mutations	Sex	Age at Sampling	Race
AG04148	AD Ctrl	-	-	M	56	Caucasian
AG08529	AD Ctrl	-	-	F	60	Caucasian
AG06840	FAD, Type 3	PSEN1	ALA246GLU	M	56	Caucasian
AG09908	FAD, Type 4	PSEN2	ASN141ILE	F	81	Caucasian

The pluripotency of fibroblast-derived iPSCs was characterized by immunocytochemistry (**Appendix A12**). Aβ42 expression levels obtained for all differentiated neuronal cell lines were normalized to corresponding total Aβ42 levels obtained for control 8529 (**Figure 6-5A** for 2D and **Figure 6-5B** for 3D) cultures respectively. As expected, the controls expressed lower levels of Aβ42 compared with FAD cell lines. Although a significant difference ($p < 0.05$) in Aβ42 expression between FAD neurons and controls was observed in both 2D and 3D cultures, a twofold amplification in Aβ42 levels between diseased and control cell lines was observed only in the case of 3D culture, this difference being more pronounced for 6840 ($p < 0.01$) (**Figure 6-5B**). We further accessed the expression of specific genes linked to the APP pathway, namely PSEN1 and ADAM17 (**Appendix A10**), through

qPCR at D19 and observed similar trends to Aβ42 expression (**Appendix A13**). However, no significant amplification was observed between 2D and 3D cultures which suggest various levels of post-transcriptional and post-translational modifications not explored in this study. These results clearly indicate that 3D neuronal culture within the PLGA microfiber scaffolds elicits an enhancement of pathogenic Aβ42 levels in FAD neurons compared with 2D monolayer-based controls.

Next, both 2D and 3D cultures on D19 were characterized by western blot for presence of p-tau (**Figure 6-5C**). After normalizing all readings to the non-demented cell line 8529, our results showed elevated levels of p-tau expression in FAD line 6840 in comparison with controls; this trend being observed in both 2D and 3D cultures. In addition, 3D cultures displayed more pronounced levels of p-tau (31.8 ± 17.4%) compared with 2D cultures (14.4 ± 7.9%) (**Figure 6-5D-E)**. This is in line with other published reports where negligible p-tau expression was detected in 2D and 3D cultures for FAD line 9908 [14, 15]. Although both FAD cell lines were previously reported to show elevated Aβ42 levels, no abnormal tau accumulation was detected in 9908 which is in agreement with our observations. Taken together, our findings reinforce our hypothesis that 3D culture within PLGA microfiber scaffolds serves as a suitable *in vitro* model to recapitulate pathogenic characteristics of FAD-iPSC derived neurons.

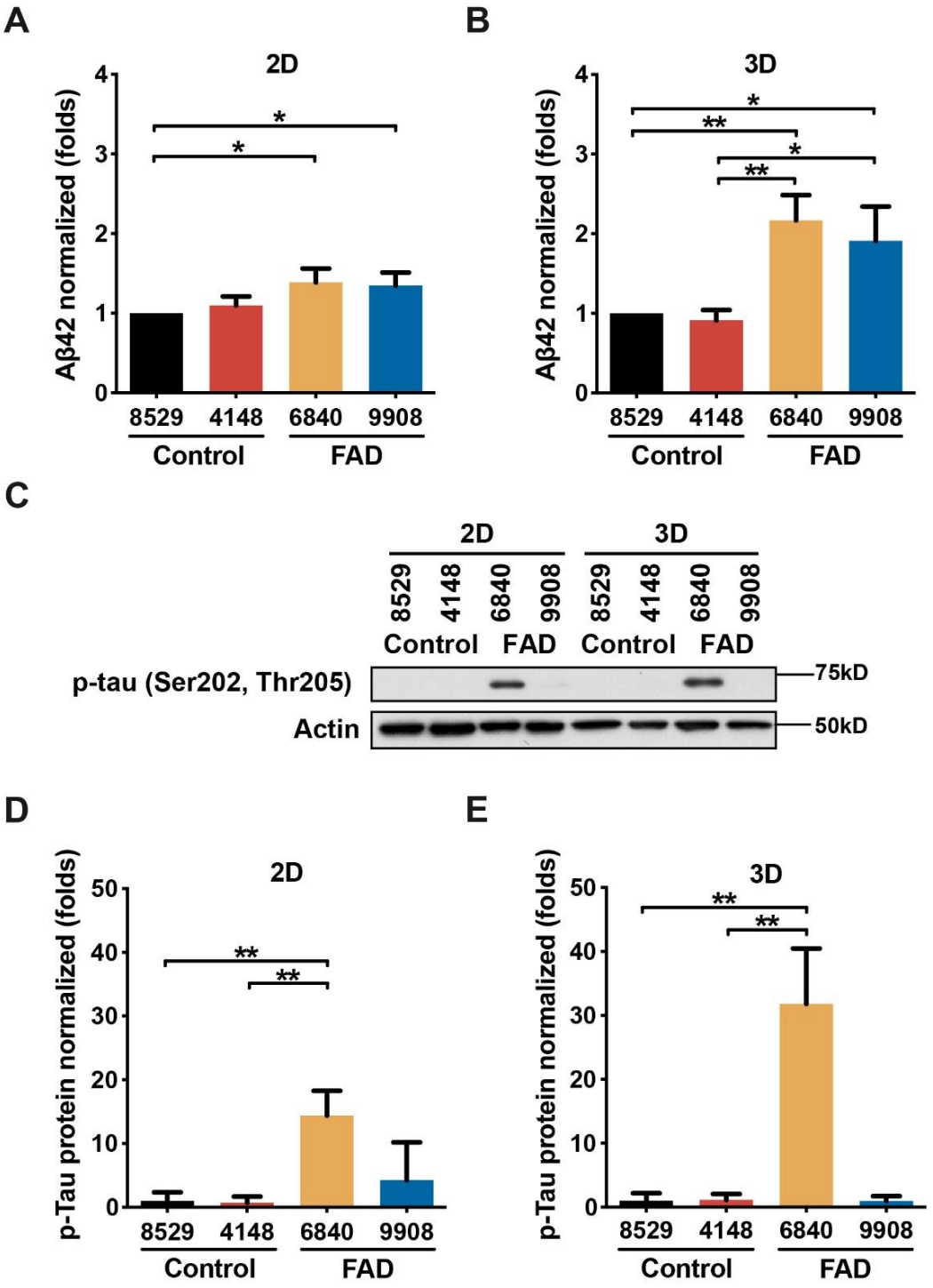

Figure 6-5. 3D PLGA microfiber scaffolds amplify expression of AD pathogenic markers. (A) ELISA analysis of Aβ42 expression levels in controls (8529, 4148) and FAD (6840, 9908) cell lines normalized to 8529 cell line on D19 for 2D culture and (B) 3D culture; (C) Western blot depicting levels of p-tau in control and FAD cell lines for 2D and 3D cultures; Quantification of p-tau levels based on western blot in control and FAD cell lines normalized to 8529 cell line on D19 for (D) 2D culture and (E) 3D culture; Data is expressed as mean ± SD (n = 3), *$p < 0.05$, **$p < 0.01$.

6.4 Discussion

Inaccessibility of the human brain makes it desirable to study AD pathogenesis and degeneration on appropriate 3D model systems of brain cultures to bridge knowledge gaps encountered in preceding animal/2D models. In the present study, we investigate the influence of electrospun 3D fibrous substrates on cellular phenotypes including recapitulation of pathogenic hallmarks in a human neuronal culture model of AD.

3D culture of stem-cell derived NPC within the PLGA scaffolds resulted in significant enhancements in neuronal differentiation of encapsulated neural progenitors within one week of culture, indicated by the dramatically elevated TuJ1 and NeuN expression levels compared with Petri dish-based monolayer controls. This could be the result of enhanced cell confinement within the microfibrous substrate [16] which limits motility-induced aggregation, leading to increased engagement of neural cell-adhesion molecules such as L1 or N-cadherin [17], in turn diminishing residual proliferative cell numbers) and enhancing neuronal differentiation profiles [18]. To sum up, the structural morphology of the 3D microfibrous substrate and its low matrix stiffness, in combination with biochemical cues present in culture media not only lowers cell proliferation rates, but also drives highly efficient neuronal differentiation which is consistent with previous reports [19, 20]. In addition, the microfiber scaffolds supported glial differentiation but to a lower extent which is in agreement with aforementioned arguments, whereas glial cells were totally absent in 2D culture.

The accelerated differentiation of patient iPSC-derived neurons cultured within the 3D PLGA substrate may have caused adequate maturation and aging of neuronal cells, resulting in expression of elevated Aβ42 and p-tau levels in the diseased cell

lines. More importantly, recapitulation of both pathologies was more pronounced and consistent compared with the same cell lines in 2D monolayer culture conditions. This spontaneous and robust incidence of disease hallmarks in the 3D microfibrous culture platform confirms its feasibility as an *in vitro* model for investigation of early-stage AD pathogenesis. However, the duration of neuronal culture in this study was inadequate to elicit late-stage pathological hallmarks of AD including amyloid plaques and neurofibrillary tangles [21], which typically requires 9-14 weeks of culture as observed in previous 3D culture models [22-25]. In addition, insufficient maturation and aging of neuronal cells may have led to the low levels of pathogenic Aβ species seen in this platform compared to physiological levels as observed in the AD human brain [26]. These limitations have been reported in other 2D [27, 28] and 3D [23] iPSC-derived neuronal models of AD despite longer culture durations. The levels of Aβ species generated from FAD iPSC-derived neurons might not be sufficient to form Aβ plaques and other Aβ-triggered pathogenic events. Although previous 3D models of AD utilizing Matrigel matrix have produced 10~1000-fold higher levels of Aβ compared to iPSC-derived FAD neurons [22, 24, 25], they utilize fluorescence-activated cell sorting (FACS) enrichment protocols to generate FAD ReNcell VM cell line (ReN cells), an immortalized hNPC line producing high levels of pathogenic Aβ species by overexpressing human APP and PSEN1 with multiple FAD mutations. This artificial elevation of pathologies via gene manipulation and engineered cell lines is not representative of early stage pathogenesis observed in the AD human brain.

Nevertheless, the results demonstrate the benefit of using a synthetic, standardizable, reproducible and easy to implement 3D culture system for *in vitro* modeling of AD. In future studies, coupling efficiency of 3D microfibers with ECM biomolecules

could be enhanced to enable longer-term culture of AD neurons for recapitulation of late stage pathological hallmarks including amyloid plaques and neurofibrillary tangles. PLGA could be replaced with conductive materials such as polypyrrole (PPy) enabling electrical stimulation of cells during culture, thereby serving as an *in vitro* platform for modulating cell behavior and facilitating non-invasive brain stimulation studies [29]. Furthermore, it could be utilized for *in vivo* transplantation studies to generate differentiated cells for regenerative medicine applications.

6.5 Conclusion

Taken together, the present findings represent the first demonstration of interfacing 3D synthetic polymer-based fibrillar scaffolds with iPSC-derived human neuronal cultures so as to robustly recapitulate and accelerate early-stage AD pathogenesis. We demonstrate good cell viability, significant reduction in cell proliferation, highly efficient neuronal differentiation and accelerated maturation of stem-cell derived NPCs cultured within the tunable 3D PLGA microfiber scaffolds compared with conventional Petri dish-based 2D monolayer cultures. Furthermore, differentiated neurons in 3D PLGA scaffold-based culture exhibited significant amplification of pathogenic Aβ42 and p-tau levels between diseased and healthy age-matched controls. The expression of pathogenic markers in 3D culture was also more pronounced compared with 2D monolayer cultures, demonstrating its feasibility for robust recapitulation and spontaneous acceleration of early-stage AD pathogenesis. We foresee further broadening of the use of our 3D platform to develop culture models of other complex neurodegenerative diseases as well as evaluation and characterization of prospective therapeutic candidates.

References

[1] L.A. Solchaga, E. Tognana, K. Penick, H. Baskaran, V.M. Goldberg, A.I. Caplan, J.F. Welter, A rapid seeding technique for the assembly of large cell/scaffold composite constructs, Tissue engineering 12(7) (2006) 1851-63.

[2] J.T.S. Pettikiriarachchi, C.L. Parish, M.S. Shoichet, J.S. Forsythe, D.R. Nisbet, Biomaterials for Brain Tissue Engineering, Australian Journal of Chemistry 63(8) (2010) 1143-1154.

[3] L.E. Sperling, K.P. Reis, L.G. Pozzobon, C.S. Girardi, P. Pranke, Influence of random and oriented electrospun fibrous poly(lactic-co-glycolic acid) scaffolds on neural differentiation of mouse embryonic stem cells, Journal of Biomedical Materials Research Part A 105(5) (2017) 1333-1345.

[4] G.T. Christopherson, H. Song, H.Q. Mao, The influence of fiber diameter of electrospun substrates on neural stem cell differentiation and proliferation, Biomaterials 30(4) (2009) 556-64.

[5] Q. Xu, L. Jin, C. Li, S. Kuddannayai, Y. Zhang, The effect of electrical stimulation on cortical cells in 3D nanofibrous scaffolds, RSC Advances 8(20) (2018) 11027-11035.

[6] R. Geetha Bai, K. Muthoosamy, S. Manickam, A. Hilal-Alnaqbi, Graphene-based 3D scaffolds in tissue engineering: fabrication, applications, and future scope in liver tissue engineering, Int J Nanomedicine 14 (2019) 5753-5783.

[7] K. Okita, Y. Matsumura, Y. Sato, A. Okada, A. Morizane, S. Okamoto, H. Hong, M. Nakagawa, K. Tanabe, K. Tezuka, T. Shibata, T. Kunisada, M. Takahashi, J. Takahashi, H. Saji, S. Yamanaka, A more efficient method to generate integration-free human iPS cells, Nat Methods 8(5) (2011) 409-12.

[8] S.M. Chambers, C.A. Fasano, E.P. Papapetrou, M. Tomishima, M. Sadelain, L. Studer, Highly efficient neural conversion of human ES and iPS cells by dual inhibition of SMAD signaling, Nat Biotechnol 27(3) (2009) 275-80.

[9] P. Thevenot, A. Nair, J. Dey, J. Yang, L. Tang, Method to analyze three-dimensional cell distribution and infiltration in degradable scaffolds, Tissue engineering. Part C, Methods 14(4) (2008) 319-31.

[10] J. Schindelin, I. Arganda-Carreras, E. Frise, V. Kaynig, M. Longair, T. Pietzsch, S. Preibisch, C. Rueden, S. Saalfeld, B. Schmid, J.-Y. Tinevez, D.J. White, V.

Hartenstein, K. Eliceiri, P. Tomancak, A. Cardona, Fiji: an open-source platform for biological-image analysis, Nature Methods 9 (2012) 676.
[11] L. Vincent, P. Soille, Watersheds in digital spaces: an efficient algorithm based on immersion simulations, IEEE Transactions on Pattern Analysis and Machine Intelligence 13(6) (1991) 583-598.
[12] L. D'Aiuto, J. Naciri, N. Radio, S. Tekur, D. Clayton, G. Apodaca, R. Di Maio, Y. Zhi, P. Dimitrion, P. Piazza, M. Demers, J. Wood, C. Chu, J. Callio, L. McClain, R. Yolken, J. McNulty, P. Kinchington, D. Bloom, V. Nimgaonkar, Generation of three-dimensional human neuronal cultures: application to modeling CNS viral infections, Stem cell research & therapy 9(1) (2018) 134-134.
[13] D. Lam, H.A. Enright, S.K.G. Peters, M.L. Moya, D.A. Soscia, J. Cadena, J.A. Alvarado, K.S. Kulp, E.K. Wheeler, N.O. Fischer, Optimizing cell encapsulation condition in ECM-Collagen I hydrogels to support 3D neuronal cultures, Journal of Neuroscience Methods 329 (2020) 108460.
[14] C. Gonzalez, E. Armijo, J. Bravo-Alegria, A. Becerra-Calixto, C.E. Mays, C. Soto, Modeling amyloid beta and tau pathology in human cerebral organoids, Molecular psychiatry 23(12) (2018) 2363-2374.
[15] T. Yagi, D. Ito, Y. Okada, W. Akamatsu, Y. Nihei, T. Yoshizaki, S. Yamanaka, H. Okano, N. Suzuki, Modeling familial Alzheimer's disease with induced pluripotent stem cells, Hum Mol Genet 20(23) (2011) 4530-9.
[16] A.L. Carlson, C.A. Florek, J.J. Kim, T. Neubauer, J.C. Moore, R.I. Cohen, J. Kohn, M. Grumet, P.V. Moghe, Microfibrous substrate geometry as a critical trigger for organization, self-renewal, and differentiation of human embryonic stem cells within synthetic 3-dimensional microenvironments, FASEB journal : official publication of the Federation of American Societies for Experimental Biology 26(8) (2012) 3240-51.
[17] A.L. Carlson, N.K. Bennett, N.L. Francis, A. Halikere, S. Clarke, J.C. Moore, R.P. Hart, K. Paradiso, M. Wernig, J. Kohn, Z.P. Pang, P.V. Moghe, Generation and transplantation of reprogrammed human neurons in the brain using 3D microtopographic scaffolds, Nat Commun 7 (2016) 10862.
[18] J.F. Cherry, N.K. Bennett, M. Schachner, P.V. Moghe, Engineered N-cadherin and L1 biomimetic substrates concertedly promote neuronal differentiation, neurite extension and neuroprotection of human neural stem cells, Acta Biomater 10(10) (2014) 4113-26.

[19] A.J. Engler, S. Sen, H.L. Sweeney, D.E. Discher, Matrix elasticity directs stem cell lineage specification, Cell 126(4) (2006) 677-89.
[20] B. Carlberg, M.Z. Axell, U. Nannmark, J. Liu, H.G. Kuhn, Electrospun polyurethane scaffolds for proliferation and neuronal differentiation of human embryonic stem cells, Biomedical materials (Bristol, England) 4(4) (2009) 045004.
[21] C. D'Avanzo, J. Aronson, Y.H. Kim, S.H. Choi, R.E. Tanzi, D.Y. Kim, Alzheimer's in 3D culture: challenges and perspectives, Bioessays 37(10) (2015) 1139-48.
[22] S.H. Choi, Y.H. Kim, M. Hebisch, C. Sliwinski, S. Lee, C. D'Avanzo, H. Chen, B. Hooli, C. Asselin, J. Muffat, J.B. Klee, C. Zhang, B.J. Wainger, M. Peitz, D.M. Kovacs, C.J. Woolf, S.L. Wagner, R.E. Tanzi, D.Y. Kim, A three-dimensional human neural cell culture model of Alzheimer's disease, Nature 515(7526) (2014) 274-8.
[23] W.K. Raja, A.E. Mungenast, Y.T. Lin, T. Ko, F. Abdurrob, J. Seo, L.H. Tsai, Self-Organizing 3D Human Neural Tissue Derived from Induced Pluripotent Stem Cells Recapitulate Alzheimer's Disease Phenotypes, PLoS One 11(9) (2016) e0161969.
[24] S.H. Choi, Y.H. Kim, L. Quinti, R.E. Tanzi, D.Y. Kim, 3D culture models of Alzheimer's disease: a road map to a "cure-in-a-dish", Mol Neurodegener 11(1) (2016) 75.
[25] J. Park, I. Wetzel, I. Marriott, D. Dréau, C. D'Avanzo, D.Y. Kim, R.E. Tanzi, H. Cho, A 3D human triculture system modeling neurodegeneration and neuroinflammation in Alzheimer's disease, Nature Neuroscience 21(7) (2018) 941-951.
[26] J. Wang, D.W. Dickson, J.Q. Trojanowski, V.M. Lee, The levels of soluble versus insoluble brain Abeta distinguish Alzheimer's disease from normal and pathologic aging, Exp Neurol 158(2) (1999) 328-37.
[27] C.R. Muratore, H.C. Rice, P. Srikanth, D.G. Callahan, T. Shin, L.N. Benjamin, D.M. Walsh, D.J. Selkoe, T.L. Young-Pearse, The familial Alzheimer's disease APPV717I mutation alters APP processing and Tau expression in iPSC-derived neurons, Hum Mol Genet 23(13) (2014) 3523-36.
[28] M.A. Israel, S.H. Yuan, C. Bardy, S.M. Reyna, Y. Mu, C. Herrera, M.P. Hefferan, S. Van Gorp, K.L. Nazor, F.S. Boscolo, C.T. Carson, L.C. Laurent, M. Marsala, F.H. Gage, A.M. Remes, E.H. Koo, L.S. Goldstein, Probing sporadic and

familial Alzheimer's disease using induced pluripotent stem cells, Nature 482(7384) (2012) 216-20.
[29] E. Tomaskovic-Crook, Q. Gu, S.N.A. Rahim, G.G. Wallace, J.M. Crook, Conducting Polymer Mediated Electrical Stimulation Induces Multilineage Differentiation with Robust Neuronal Fate Determination of Human Induced Pluripotent Stem Cells, Cells 9(3) (2020).

CHAPTER 7 Conclusion & Future work

7.1 Summary

Alzheimer's disease (AD) is the most common form of dementia characterized by progressive memory loss and impairment of cognitive functions, ultimately leading to death. The key to understanding AD aetiology lies in developing effective disease models, which should ideally recapitulate all aspects pertaining to the disease. A plethora of techniques have been developed by researchers for modeling AD such as *in silico*, *in vivo*, 2D and 3D *in vitro* culture platforms. Over the last few decades, research into AD pathogenesis has predominantly focused on animal and 2D *in vitro* models. Although both approaches have provided valuable insights into AD aetiology, neither has fully reproduced the pathological events observed in human AD patients [1]. Recent advancements in tissue culture techniques and stem cell technologies have led to the development of 3D *in vitro* disease models, which are relatively more representative of the complex *in vivo* microenvironments present inside native tissues. However, existing 3D neuronal models of AD utilize engineered cell lines overexpressing mutant genes to artificially elevate pathological expression or rely on cell-aggregate cultures possessing heterogeneities in composition, biological properties and cell differentiation stages.

In this regard, we utilized a tissue engineering approach to develop three novel biomaterial-based scaffolding platforms for achieving 3D cellular culture, each substrate specifically aimed at supporting neuronal differentiation and long-term neuronal culture. These include: a graphene oxide hydrogel-based electroconductive substrate fabricated via physical crosslinking; a synthetic polymer-based, hollow microfiber substrate fabricated via core-shell electrospinning; and a synthetic polymer-based, non-woven fibrillar substrate fabricated via wet electrospinning.

Next, we characterized, reviewed and compared all three substrates based on the general design criteria for 3D *in vitro* scaffolding i.e. in terms of both physical/structural properties as well as biological requirements. Although both the electroconductive hydrogel and hollow microfiber-based substrates facilitated direct fabrication of cell-scaffold structure, they are limited by their hydrophobicity and lack of surface functionalization, which in turn hindered neurite outgrowth and formation of neuronal networks. In contrast, the PLGA wet-electrospun, non-woven microfiber substrate demonstrated the most potential as a simple, standardizable, reproducible and easy to implement 3D culture system for promoting attachment, growth, neuronal differentiation and formation of neural circuits. Stem cell-derived NPC culture within the 3D microfiber substrate reduced cell proliferation and significantly accelerated neural differentiation into neuronal and astro/glial cells compared with 2D monolayer controls.

Finally, we interfaced the 3D scaffolds with FAD patient iPSC-derived human neuronal cultures to develop a novel 3D *in vitro* model of AD. The differentiated neurons in 3D PLGA scaffold-based culture exhibited significant amplification in pathogenic amyloid-beta 42 (Aβ42) and phospho-tau levels between diseased and age-matched controls. Furthermore, the spontaneous expression levels of these pathogenic markers in 3D culture was more pronounced compared with corresponding 2D monolayer control cultures. Taken together, the present findings represent the first demonstration of interfacing 3D synthetic polymer-based fibrillar scaffolds with iPSC-derived human neuronal cultures so as to robustly recapitulate and accelerate early-stage AD pathogenesis (**Figure 7-1**). They also highlight the several advantages of a 3D microenvironment over conventionally used monolayer

cultures in terms of enhancing expression of neuronal markers as well as replication of disease pathologies.

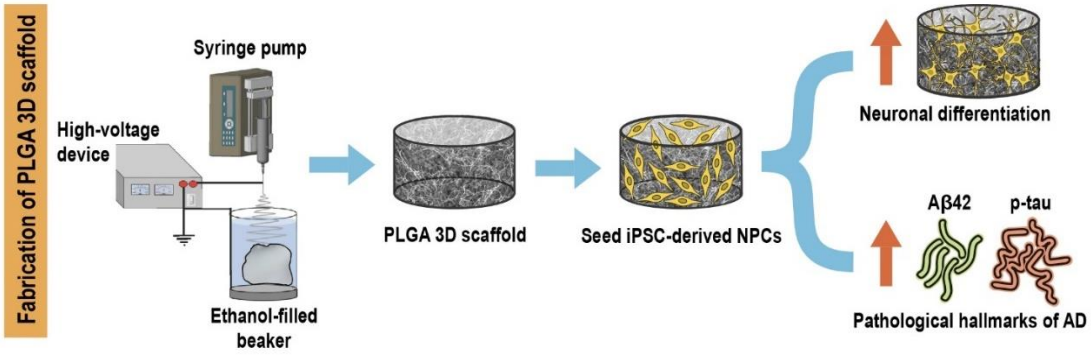

Figure 7-1. Schematic illustrating summary of the 3D *in vitro* AD modeling work done in this thesis.

7.2 Limitations and Potential solutions

Some of the major limitations of this study along with potential solutions are listed below.

- Utilizing iPS cell lines for disease modeling

  The discovery of iPS cell technology has spurred the development of a plethora of *in vitro* disease models recapitulating pathological characteristics hitherto not observed in animal models. However, variability within iPS cell lines along with the heterogeneities arising within their clones caused by genetic or epigenetic variations limits the reproducibility of these models [2]. Moreover, iPSCs derived from healthy individuals were used as controls, which could have an entirely different genetic background compared with cells derived from AD patients. In this case, isogenic cell lines derived from AD-iPSCs where mutations have been corrected to wild-type using gene editing technologies such as transcription activator-like effector nucleases (TALENs) or CRISPR could be more appropriate for use as non-demented controls [3, 4].

- Replication of late-stage AD hallmarks and biological aging

  Lack of robust AD hallmarks in our 3D model might be a result of production of lower levels of pathogenic Aβ species, especially Aβ42, compared to AD patients along with insufficient maturation and aging of neuronal cells. This limitation has been reported in other 2D [5, 6] and 3D [7] iPSC-derived neuronal models despite longer culture durations. The levels of Aβ species generated from FAD iPSC-derived neurons might not be sufficient to form Aβ plaques and other Aβ-triggered pathogenic events. The relative developmental age of the iPSC-derived neurons used for modeling AD does not consider the fact that patients typically develop the disease in their fifth decade. Biological aging and underlying cellular pathways in late-onset diseases such as AD is hard to reproduce in an *in vitro* setting [8]. This could be addressed by integrating scaffold-based cultures with organ-on-a-chip or bioreactor technologies to extend cultivation times, resulting in higher maturity levels [9]. Furthermore, transplanting them into an *in vivo* physiological environment such as an animal brain has been successfully shown to facilitate vascularization, paving the way for modeling diseases under conditions physiologically resembling the native context [10].

- Use of both SAD and FAD cell lines for comprehensive modeling of AD

  Pathological phenotypes between SAD and FAD associated cell lines have been observed to be inconsistent in previous studies [6, 11]. Hence, a much larger sample size comprising of both AD formats is necessary to fully understand the reasons behind these heterogeneities. Although our 3D culture model has characterized some of the early-stage pathways connected to FAD, the more prevalent sporadic form has not been represented. In addition, the functional

roles of AD associated proteins such as APP and PSEN1 also needs to be investigated [8, 12]. Both genetic and environmental risk factors associated with AD should be considered in future models; for instance, neurotoxins could be used in conjunction with AD mutations, thereby rendering more comprehensive representations of the sporadic form.

- Lack of vascularization in 3D *in vitro* culture

  Similar to organoid cultures, scaffold-based cultures also lack vascularization which could affect neurogenesis and later stage development of neuronal tissue owing to difficulties involved in delivering essential nutrients and signaling molecules akin to native *in vivo* conditions [13]. Combining the 3D scaffold-based platform with microfluidic perfusion chambers can enable fluid flow via micro-scale channels aimed at substituting *in vivo* vasculature for sustaining longer-term cell growth [14]. This is necessary for neurodegenerative disease modeling which require very long culture durations for comprehensive and robust recapitulation of disease pathologies. Microfluidic devices provide additional advantages such as the ability to co-culture different cell types, spatial control of cell culture, material versatility, fluidic control as well as generation of molecular gradients [15, 16]. They also help analyze organ-level functions at the cellular level in a controlled fashion, and hence are more representative of native *in vivo* microenvironments compared with static 2D/3D cultures [17].

- Structural/physical limitations of using wet electrospun microfibrous scaffolds

  The micro-architecture of the scaffold cannot be controlled precisely due to random deposition of fibers when electrospinning leading to inconsistent inter-fiber spacing. In addition, the opacity of the 3D scaffold composed of hundreds of layers of fibers makes it difficult to perform live cell imaging or visualize

neurite formation and outgrowth in real time. Plasma treatment of soft materials can cause aging of the modified surface and lead to a degradative effect on the substrate [18]. A very high cell seeding density was necessary to facilitate uniform distribution of cells throughout the macroporous scaffold. This is especially challenging when utilizing patient-derived stem cell lines due to the low yields obtained during subculture in comparison with rapidly proliferating immortalized cell lines. Moreover, separation/harvesting of cells encapsulated inside the 3D fibrous structure for further expansion is another limiting factor in the use of these scaffolds.

7.3 Future directions

In the context of the results obtained, several future directions are proposed in the following section to advance this disease modeling study in terms of both fabrication and characterization.

- The coupling efficiency of 3D microfibers with ECM biomolecules such as laminin could be further strengthened via covalent immobilization or blended electrospinning techniques [19] to enable longer-term culture of AD neurons. This could facilitate recapitulation of later stage pathological hallmarks such as amyloid plaques and neurofibrillary tangles.
- Human body responds to electrical fields and its principal component of neural communication is the action potential generated at the neuronal synapse. This implies that a substrate developed for neuronal culture should ideally possess electrical conductivity. Electrical stimulation has been reported to enhance cell proliferation, migration, differentiation [20] and even attenuate disease pathogenesis [21]. However, the substrate material used in this work i.e. PLGA is electrically nonconductive. In this case, electrospun PLGA could be replaced

with conductive materials such as polypyrrole (PPy) enabling electrical stimulation of cells during culture, thereby serving as a 3D *in vitro* platform for modulating cell behavior and facilitating non-invasive brain stimulation studies. Further work on surface functionalization of the graphene oxide-based electroconductive hydrogel could be explored to improve its hydrophilicity as well as incorporate cell adhesion motifs for enhancing cell–matrix interactions.

- Hypoxic or ischemic events such as stroke have been reported to stimulate amyloidogenic Aβ production and are linked to increased reactive oxygen species (ROS) production [22]. The influence of such environmental insults on intracellular cellular homeostasis including their influence on Aβ/p-tau levels [23] can be assessed by interfacing the scaffold-based AD culture with a microfluidic hypoxia device capable of mimicking native *in vivo* conditions. Microphysiological systems (MPSs) can be engineered to create specialized culture microenvironments, enabling the use of 3D matrices with continuous perfusion and live cell imaging facility for monitoring *in vitro* cellular activities in real-time [16, 24]. They can be interfaced with 3D scaffold-based cultures to simulate cerebral hypoperfusion by supplying controlled quantities of oxygen and glucose to cells via built-in microchannels and thereby facilitating the study of variable microenvironments in regulating AD pathologies [25].
- Increasing evidence suggests the substantial involvement of immunological mechanisms in the pathogenic cascade of AD [26]. The role of glial cells including their sustained activation, recruitment and initiation of inflammatory response in human AD brains which contribute to neuronal damage [14] needs to be investigated in future studies.

- Future *in vitro* models could be used to analyze the role of metals such as zinc (Zn), copper (Cu) and iron (Fe) in Aβ misfolding and plaque aggregation which have been attributed to alterations in metal homeostasis [27-29]. Some studies have even hinted at the influence of the gut microbiome in regulating neuro-inflammation and Aβ levels [30, 31], which again demonstrates the diverse assortment of factors to be considered in AD research.
- The mechanisms involved in the regulation of calcium homeostasis are compromised in AD including influx, compartmentalization and efflux of calcium from the neurons [32]. AD neurodegeneration has also been associated with synaptic dismantling and progressive decrease in neuronal activity [33]. Conventional methods of extracellular electrophysiology such as multielectrode array (MEA) allows measurement of spiking activity of only up to several hundred neurons. In this regard, fluorescent cellular-calcium imaging in combination with deep learning techniques can be used to compare collective spiking responses of neural populations in diseased versus healthy cells, and then assess whether changes in neuronal activity patterns occur in the presence of amyloid plaques [34]. Calcium imaging can help correlate electrical activity in neurons to intercellular movements of calcium ions [35].
- The 3D microfiber substrate-based *in vitro* culture can be used to investigate the impact of β-secretase inhibitors and γ-secretase modulator treatments on Aβ/p-tau levels in AD cell lines, therefore serving as a potential high-throughput drug screening platform. This can accelerate AD drug discovery by supplementing the expensive, high-maintenance and time-consuming *in vivo* trials presently utilized for testing candidate drugs [36] (**Figure 7-2**). HTS enables rapid and parallel testing of numerous drugs, thereby speeding up the dug development

timeline and reducing chances of failure in human clinical trials. In addition, these trials could also be used to assess and confirm potential connections/correlations existing among the major hallmarks of AD [1].

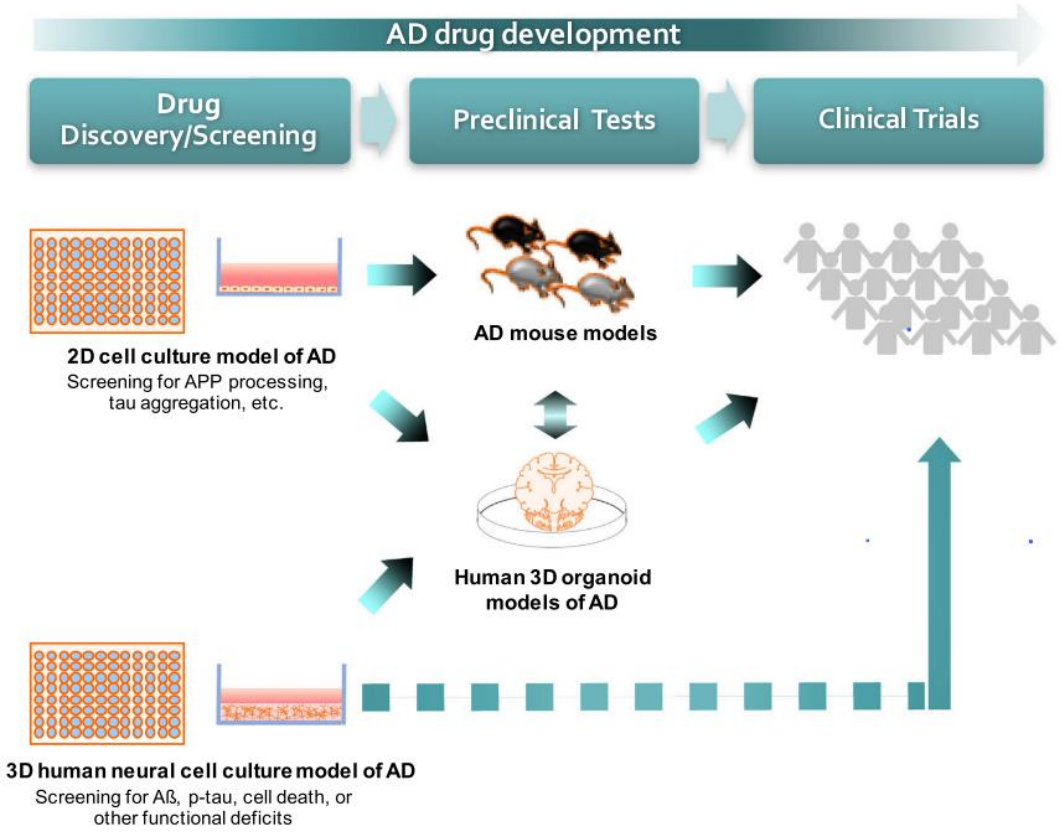

Figure 7-2. Application of AD models in drug development (Adapted from [1]).

7.4 References

[1] S.H. Choi, Y.H. Kim, L. Quinti, R.E. Tanzi, D.Y. Kim, 3D culture models of Alzheimer's disease: a road map to a "cure-in-a-dish", Mol Neurodegener 11(1) (2016) 75.

[2] P. Cahan, G.Q. Daley, Origins and implications of pluripotent stem cell variability and heterogeneity, Nat Rev Mol Cell Biol 14(6) (2013) 357-68.

[3] J. Yang, S. Li, X.B. He, C. Cheng, W. Le, Induced pluripotent stem cells in Alzheimer's disease: applications for disease modeling and cell-replacement therapy, Mol Neurodegener 11(1) (2016) 39.

[4] J. Muffat, Y. Li, R. Jaenisch, CNS disease models with human pluripotent stem cells in the CRISPR age, Curr Opin Cell Biol 43 (2016) 96-103.

[5] C.R. Muratore, H.C. Rice, P. Srikanth, D.G. Callahan, T. Shin, L.N. Benjamin, D.M. Walsh, D.J. Selkoe, T.L. Young-Pearse, The familial Alzheimer's disease APPV717I mutation alters APP processing and Tau expression in iPSC-derived neurons, Hum Mol Genet 23(13) (2014) 3523-36.

[6] M.A. Israel, S.H. Yuan, C. Bardy, S.M. Reyna, Y. Mu, C. Herrera, M.P. Hefferan, S. Van Gorp, K.L. Nazor, F.S. Boscolo, C.T. Carson, L.C. Laurent, M. Marsala, F.H. Gage, A.M. Remes, E.H. Koo, L.S. Goldstein, Probing sporadic and familial Alzheimer's disease using induced pluripotent stem cells, Nature 482(7384) (2012) 216-20.

[7] W.K. Raja, A.E. Mungenast, Y.T. Lin, T. Ko, F. Abdurrob, J. Seo, L.H. Tsai, Self-Organizing 3D Human Neural Tissue Derived from Induced Pluripotent Stem Cells Recapitulate Alzheimer's Disease Phenotypes, PLoS One 11(9) (2016) e0161969.

[8] C. Arber, C. Lovejoy, S. Wray, Stem cell models of Alzheimer’s disease: progress and challenges, Alzheimer's Research & Therapy 9 (2017) 42.

[9] T. Takebe, B. Zhang, M. Radisic, Synergistic Engineering: Organoids Meet Organs-on-a-Chip, Cell Stem Cell 21(3) (2017) 297-300.

[10] A.A. Mansour, J.T. Gonçalves, C.W. Bloyd, H. Li, S. Fernandes, D. Quang, S. Johnston, S.L. Parylak, X. Jin, F.H. Gage, An in vivo model of functional and vascularized human brain organoids, Nature Biotechnology 36 (2018) 432.

[11] T. Kondo, M. Asai, K. Tsukita, Y. Kutoku, Y. Ohsawa, Y. Sunada, K. Imamura, N. Egawa, N. Yahata, K. Okita, K. Takahashi, I. Asaka, T. Aoi, A. Watanabe, K.

Watanabe, C. Kadoya, R. Nakano, D. Watanabe, K. Maruyama, O. Hori, S. Hibino, T. Choshi, T. Nakahata, H. Hioki, T. Kaneko, M. Naitoh, K. Yoshikawa, S. Yamawaki, S. Suzuki, R. Hata, S. Ueno, T. Seki, K. Kobayashi, T. Toda, K. Murakami, K. Irie, W.L. Klein, H. Mori, T. Asada, R. Takahashi, N. Iwata, S. Yamanaka, H. Inoue, Modeling Alzheimer's disease with iPSCs reveals stress phenotypes associated with intracellular Abeta and differential drug responsiveness, Cell Stem Cell 12(4) (2013) 487-96.

[12] H.K. Lee, C. Velazquez Sanchez, M. Chen, P.J. Morin, J.M. Wells, E.B. Hanlon, W. Xia, Three Dimensional Human Neuro-Spheroid Model of Alzheimer's Disease Based on Differentiated Induced Pluripotent Stem Cells, PLoS One 11(9) (2016) e0163072.

[13] I. Kelava, M.A. Lancaster, Dishing out mini-brains: Current progress and future prospects in brain organoid research, Developmental Biology 420(2) (2016) 199-209.

[14] J. Park, I. Wetzel, I. Marriott, D. Dréau, C. D'Avanzo, D.Y. Kim, R.E. Tanzi, H. Cho, A 3D human triculture system modeling neurodegeneration and neuroinflammation in Alzheimer's disease, Nature Neuroscience 21(7) (2018) 941-951.

[15] V. van Duinen, S.J. Trietsch, J. Joore, P. Vulto, T. Hankemeier, Microfluidic 3D cell culture: from tools to tissue models, Curr Opin Biotechnol 35 (2015) 118-26.

[16] M. Jorfi, C. D'Avanzo, D.Y. Kim, D. Irimia, Three-Dimensional Models of the Human Brain Development and Diseases, Advanced healthcare materials 7(1) (2017).

[17] S.N. Bhatia, D.E. Ingber, Microfluidic organs-on-chips, Nat Biotechnol 32(8) (2014) 760-72.

[18] M. Asadian, K.V. Chan, M. Norouzi, S. Grande, P. Cools, R. Morent, N. De Geyter, Fabrication and Plasma Modification of Nanofibrous Tissue Engineering Scaffolds, Nanomaterials (Basel, Switzerland) 10(1) (2020).

[19] H.S. Koh, T. Yong, C.K. Chan, S. Ramakrishna, Enhancement of neurite outgrowth using nano-structured scaffolds coupled with laminin, Biomaterials 29(26) (2008) 3574-82.

[20] C. Chen, X. Bai, Y. Ding, I.-S. Lee, Electrical stimulation as a novel tool for regulating cell behavior in tissue engineering, Biomaterials Research 23(1) (2019) 25.
[21] P.E. Silva, R. de Cássia Marqueti, K. Livino-de-Carvalho, A.E.T. de Araujo, J. Castro, V.M. da Silva, L. Vieira, V.C. Souza, L.O. Dantas, G. Cipriano Jr, O.T. Nóbrega, N. Babault, J.L.Q. Durigan, Neuromuscular electrical stimulation in critically ill traumatic brain injury patients attenuates muscle atrophy, neurophysiological disorders, and weakness: a randomized controlled trial, Journal of Intensive Care 7(1) (2019) 59.
[22] M. Vijayan, P.H. Reddy, Stroke, Vascular Dementia, and Alzheimer's Disease: Molecular Links, J Alzheimers Dis 54(2) (2016) 427-443.
[23] L. Qiu, G. Ng, E.K. Tan, P. Liao, N. Kandiah, L. Zeng, Chronic cerebral hypoperfusion enhances Tau hyperphosphorylation and reduces autophagy in Alzheimer's disease mice, Sci Rep2016.
[24] Cook, P. Tom, S. Stephen, Y. Jiajie, S. Emily, S. Michael, V. Jason, J.V. Jeremy, S. Linda, P.P. Julia, L. Iris, V. Nicholas, G. Mario, E.L. Matthew, Z. Zhe, W. Xin, A.B. Laurie, A.L. Douglas, L.C. Rebecca, C. Catherine, R.T. Steven, L.S. Cynthia, J.H. David, R. Gaurav, L.T. David, C. Murat, C.D.E. Linda G. Griffith, C. Wen Li Kelly, G. Emily, K. Timothy, R.S. Luis, M.B. Brij, F. Duncan, K. Jared, M. Christian, T. Nikolaos, V. Jorge, D. Christi, Interconnected Microphysiological Systems for Quantitative Biology and Pharmacology Studies, Scientific Reports 8(1) (2018) 4530.
[25] M.D. Brennan, M.L. Rexius-Hall, L.J. Elgass, D.T. Eddington, Oxygen control with microfluidics, Lab Chip 14(22) (2014) 4305-18.
[26] M.T. Heneka, M.J. Carson, J. El Khoury, G.E. Landreth, F. Brosseron, D.L. Feinstein, A.H. Jacobs, T. Wyss-Coray, J. Vitorica, R.M. Ransohoff, K. Herrup, S.A. Frautschy, B. Finsen, G.C. Brown, A. Verkhratsky, K. Yamanaka, J. Koistinaho, E. Latz, A. Halle, G.C. Petzold, T. Town, D. Morgan, M.L. Shinohara, V.H. Perry, C. Holmes, N.G. Bazan, D.J. Brooks, S. Hunot, B. Joseph, N. Deigendesch, O. Garaschuk, E. Boddeke, C.A. Dinarello, J.C. Breitner, G.M. Cole, D.T. Golenbock, M.P. Kummer, Neuroinflammation in Alzheimer's disease, Lancet Neurol 14(4) (2015) 388-405.
[27] C.J. Maynard, A.I. Bush, C.L. Masters, R. Cappai, Q.X. Li, Metals and amyloid-β in Alzheimer's disease, Int J Exp Pathol 86(3) (2005) 147-59.

[28] A.I. Bush, W.H. Pettingell, G. Multhaup, M. d Paradis, J.P. Vonsattel, J.F. Gusella, K. Beyreuther, C.L. Masters, R.E. Tanzi, Rapid induction of Alzheimer A beta amyloid formation by zinc, Science (New York, N.Y.) 265(5177) (1994) 1464-7.

[29] C.S. Atwood, R.D. Moir, X. Huang, R.C. Scarpa, N.M. Bacarra, D.M. Romano, M.A. Hartshorn, R.E. Tanzi, A.I. Bush, Dramatic aggregation of Alzheimer abeta by Cu(II) is induced by conditions representing physiological acidosis, J Biol Chem 273(21) (1998) 12817-26.

[30] M.R. Minter, C. Zhang, V. Leone, D.L. Ringus, X. Zhang, P. Oyler-Castrillo, M.W. Musch, F. Liao, J.F. Ward, D.M. Holtzman, E.B. Chang, R.E. Tanzi, S.S. Sisodia, Antibiotic-induced perturbations in gut microbial diversity influences neuro-inflammation and amyloidosis in a murine model of Alzheimer's disease, Sci Rep 6 (2016) 30028.

[31] S. Bhattacharjee, W.J. Lukiw, Alzheimer's disease and the microbiome, Front Cell Neurosci 7 (2013) 153.

[32] J. Wang, C. Sun, Calcium and Neurogenesis in Alzheimer's Disease, Frontiers in Neuroscience 4(194) (2010).

[33] M.A. Busche, G. Eichhoff, H. Adelsberger, D. Abramowski, K.H. Wiederhold, C. Haass, M. Staufenbiel, A. Konnerth, O. Garaschuk, Clusters of hyperactive neurons near amyloid plaques in a mouse model of Alzheimer's disease, Science (New York, N.Y.) 321(5896) (2008) 1686-9.

[34] E.A. Pnevmatikakis, D. Soudry, Y. Gao, T.A. Machado, J. Merel, D. Pfau, T. Reardon, Y. Mu, C. Lacefield, W. Yang, M. Ahrens, R. Bruno, T.M. Jessell, D.S. Peterka, R. Yuste, L. Paninski, Simultaneous Denoising, Deconvolution, and Demixing of Calcium Imaging Data, Neuron 89(2) (2016) 285-99.

[35] F.B. Neubauer, J.N. MacLean, Calcium Imaging in Neuroscience, eLS, John Wiley & Sons, Ltd2001.

[36] A. Kumar, A. Singh, Ekavali, A review on Alzheimer's disease pathophysiology and its management: an update, Pharmacological reports : PR 67(2) (2015) 195-203.

APPENDIX

Appendix A1. Preparation of Graphene Oxide.

Graphene oxide (GO) was prepared according to the modified Hummer's method. First, 60 ml concentrated sulfuric acid was introduced into a 250 ml three-neck flask with mechanical stirring and ice-water bath. Next, graphite power (2.5 g) and sodium nitrate (1.25 g) were mixed with the acid, leading to green color slurry. After the mixture cooled down (<10 ^{o}C), potassium permanganate (7.5 g) was added slowly into above solution by five parts with each quota 1.5 g. Afterwards, the system was allowed to react at 35^{o}C for 2 h and 50^{o}C for 2 h, resulting in a very viscous and dark brown paste. Then, 100 ml deionized water was slowly added to cool down the reaction and maintained for another 15 min. The muddy-like mixture obtained was poured into a 2 L beaker with ~700 ml DI water inside. With the addition of H_2O_2 (30 ml, 30%), the solution turned bright yellow color, which is usually an indicator of successful reaction. Dilute hydrochloric acid (fume acid: water = 1:9) was then added, and the deposition part was washed by DI water repeatedly using centrifuge until the pH of supernatant remain constant. Finally, the graphene oxide obtained was concentrated in water using a centrifuge.

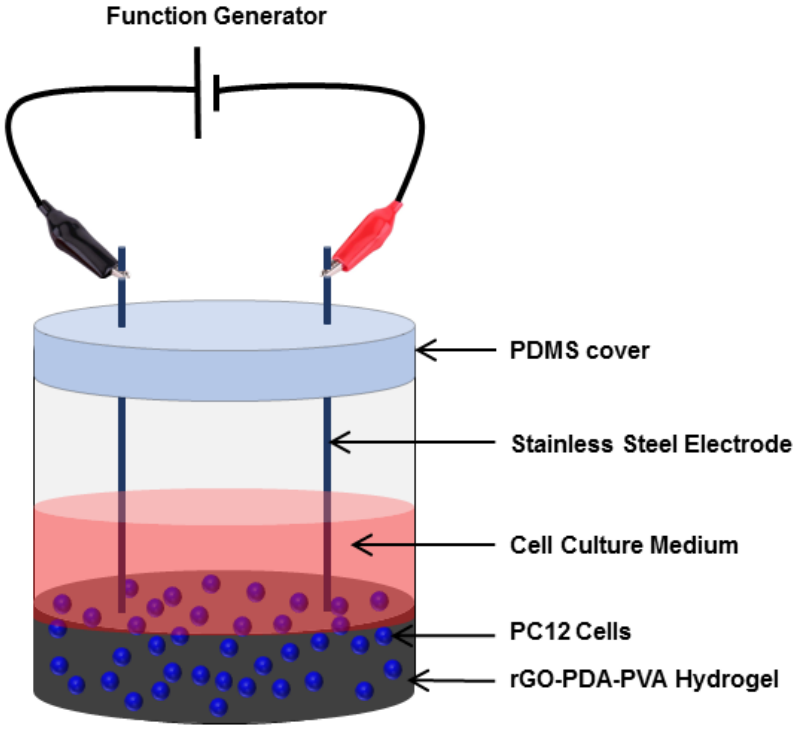

Appendix A2. 3D view of electrical stimulation setup inside each culture well.

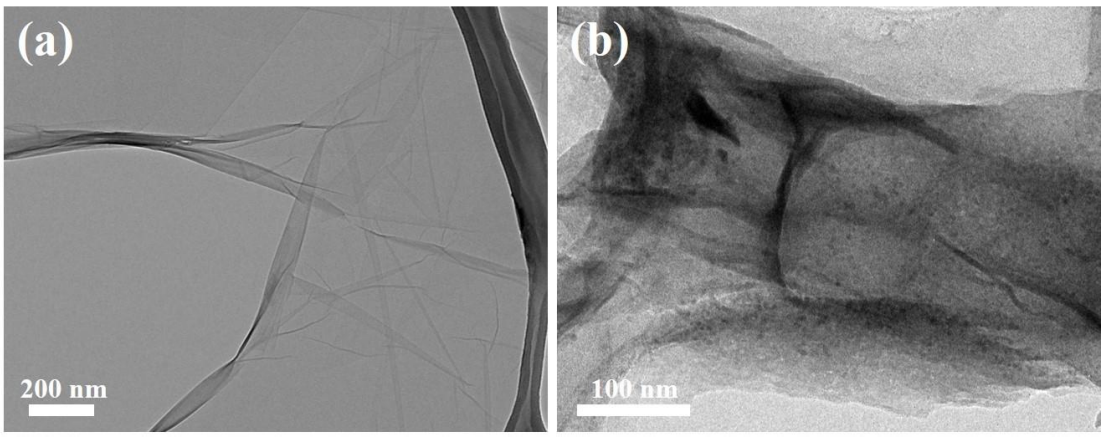

Appendix A3. TEM of (a) GO and (b) rGO-PDA.

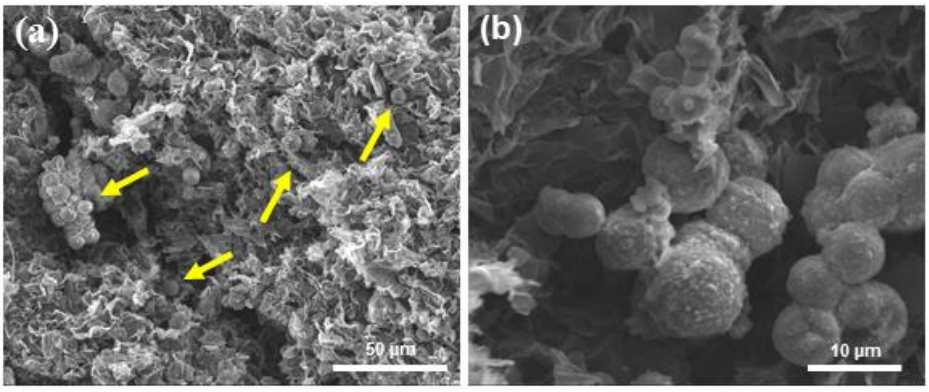

Appendix A4. SEM images of PC12 cells grown inside the 3D scaffold 7 days after cell seeding (a) without and (b) with electrical stimulation; Inset arrows indicate cell clusters.

Appendix A5. Selected variables and levels for DOE.

Factor Name	Factor Letter	Low Setting	Medium Setting	High Setting
Concentration	A	10%	12.5%	15%
Voltage	B	10 kV	12 kV	14 kV
Flow rate	C	30 ml/h	40 ml/h	50 ml/h
Response	Diameter of coaxial fiber (μm)			

Appendix A6. ANOVA Table, Diameter of coaxial fiber.

Source	Degree of freedom	Seq SS	Adj SS	Adj MS	F	P
A	2	2501.37	2501.37	1250.69	308.66	0
B	2	462.67	462.67	23134	57.09	0
C	2	660.18	660.18	330.09	81.46	0
A*B	4	188.94	188.94	47.24	11.66	0.002
A*C	4	185.29	185.29	46.32	11.43	0.002
B*C	4	28.14	28.14	7.04	1.74	0.235
Error	8	32.42	32.42	4.05		
Total	26	4059.01				

Appendix A7. Design matrix of experimental results.

Run Order	Concentration (%)	Voltage (kV)	Flow rate (ml/hr)	Diameter 1 (µm)	Diameter 2 (µm)	Diameter 3 (µm)
1	10	10	30	34.37	33.56	34.55
2	10	10	40	35.9	36.1	36.33
3	10	10	50	40.98	39.88	42.14
4	10	12	30	35.65	34.85	35.1
5	10	12	40	37.6	37.03	38.65
6	10	12	50	39.62	37.96	38.69
7	10	14	30	29.95	28.7	30.22
8	10	14	40	35.03	34.87	36.03
9	10	14	50	35.55	35.94	35.33
10	12.5	10	30	41.7	42.65	39.99
11	12.5	10	40	47.83	45.98	46.86
12	12.5	10	50	52.71	51.86	52.33
13	12.5	12	30	33.05	31.98	32.66
14	12.5	12	40	37.91	37.02	38.32
15	12.5	12	50	47.58	47.03	44.76
16	12.5	14	30	33.95	33.43	33.55
17	12.5	14	40	38.6	38.11	38.65
18	12.5	14	50	39.75	39	40.23
19	15	10	30	52.98	53.43	51.96
20	15	10	40	66.7	65.92	66.43
21	15	10	50	77.18	78.14	78.36
22	15	12	30	53.03	52.64	52.88
23	15	12	40	57.93	57.23	57.12
24	15	12	50	72.83	72.03	73.11
25	15	14	30	40.36	40.85	39.77
26	15	14	40	48.62	48.23	47.98
27	15	14	50	57.13	57.77	56.81
Low						
Medium						
High						

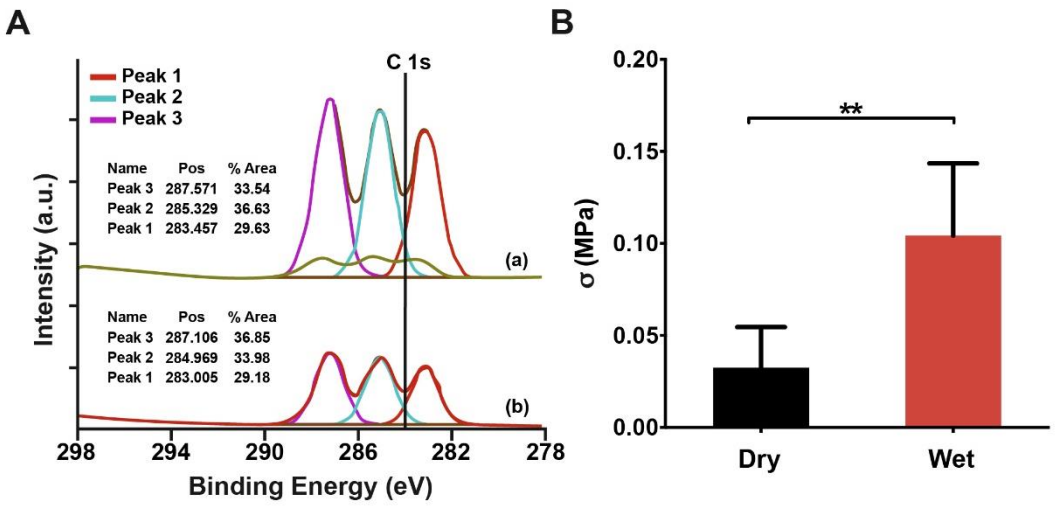

Appendix A8. Characterization of 3D PLGA microfiber scaffolds. (A) High-resolution XPS spectra of C1s region of PLGA microfiber surface (a) without and (b) with atmospheric air plasma treatment (300 s); (B) Ultimate compressive strengths (σ) of 3D PLGA microfibrous scaffolds obtained for mechanical testing under dry and wet conditions; Data is expressed as mean ± SD (n = 5), $^{**}p < 0.01$.

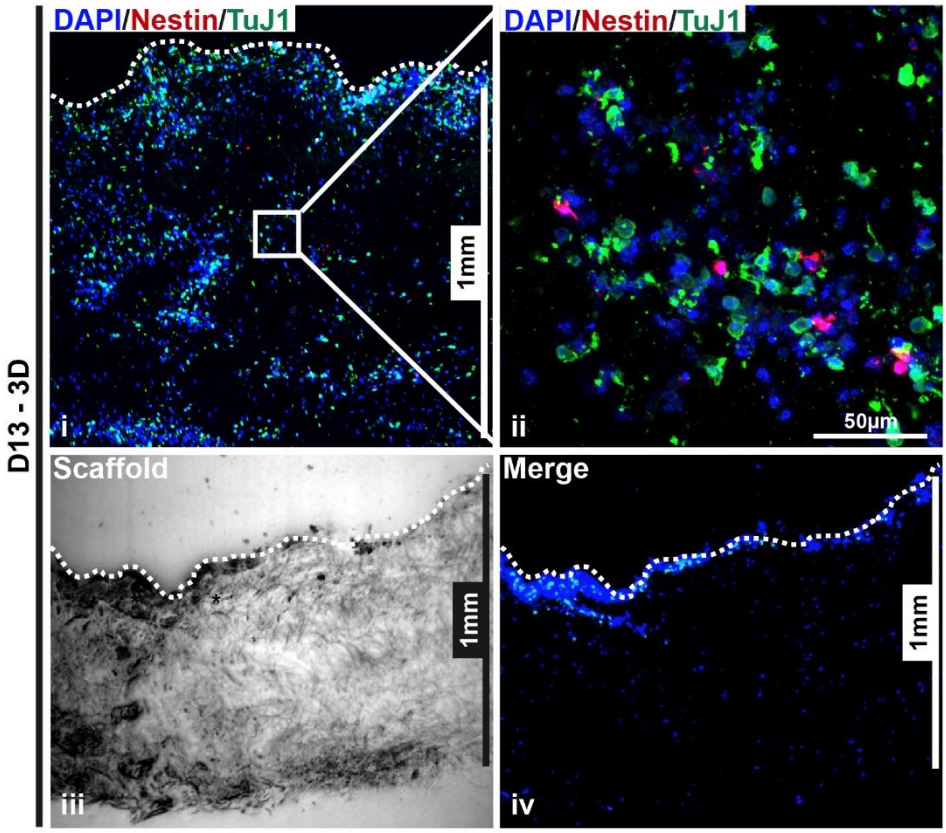

Appendix A9. Encapsulation and characterization of iPSC-derived NPC inside 3D PLGA microfiber scaffolds. Confocal fluorescent microscopy images indicating (i-ii) differentiation of iPSC-derived NPCs (8529 cell line) inside 3D scaffold as assessed via staining for TuJ1 (green) and Nestin (red) markers on D13; (iii) cross-section of 3D microfiber scaffold after sectioning (dotted line indicates top surface of 3D scaffold); (iv) cell infiltration and distribution of D13 differentiated NPC inside 3D scaffold without orbital shaking as assessed via staining for Ki67 (green) and DAPI (blue) markers.

Appendix A10. Primer sequences used for specific gene targets for qPCR

Target Gene		Primer sequence (5’-3’)
Ki67	F	ACGCCTGGTTACTATCAAAAGG
	R	CAGACCCATTTACTTGTGTTGGA
TuJ1	F	CACCCAGCAGATGTTCGATG
	R	CTTCACGTTGTTGGGGATCC
NeuN	F	GCGGCTACACGTCTCCAACATC
	R	ATCGTCCCATTCAGCTTCTCCC
PSEN1	F	ACAGGTGCTATAAGGTCATCCA
	R	CAGATCAGGAGTGCAACAGTAAT
ADAM17	F	GGCAAATGTGAGAAAC
	R	TGGACAAGAATGCTGAAAGGA
Actin	F	GCGCAAGTTAGGTTTTGTCA
	R	AGATGTGGACAGCAAGCAG

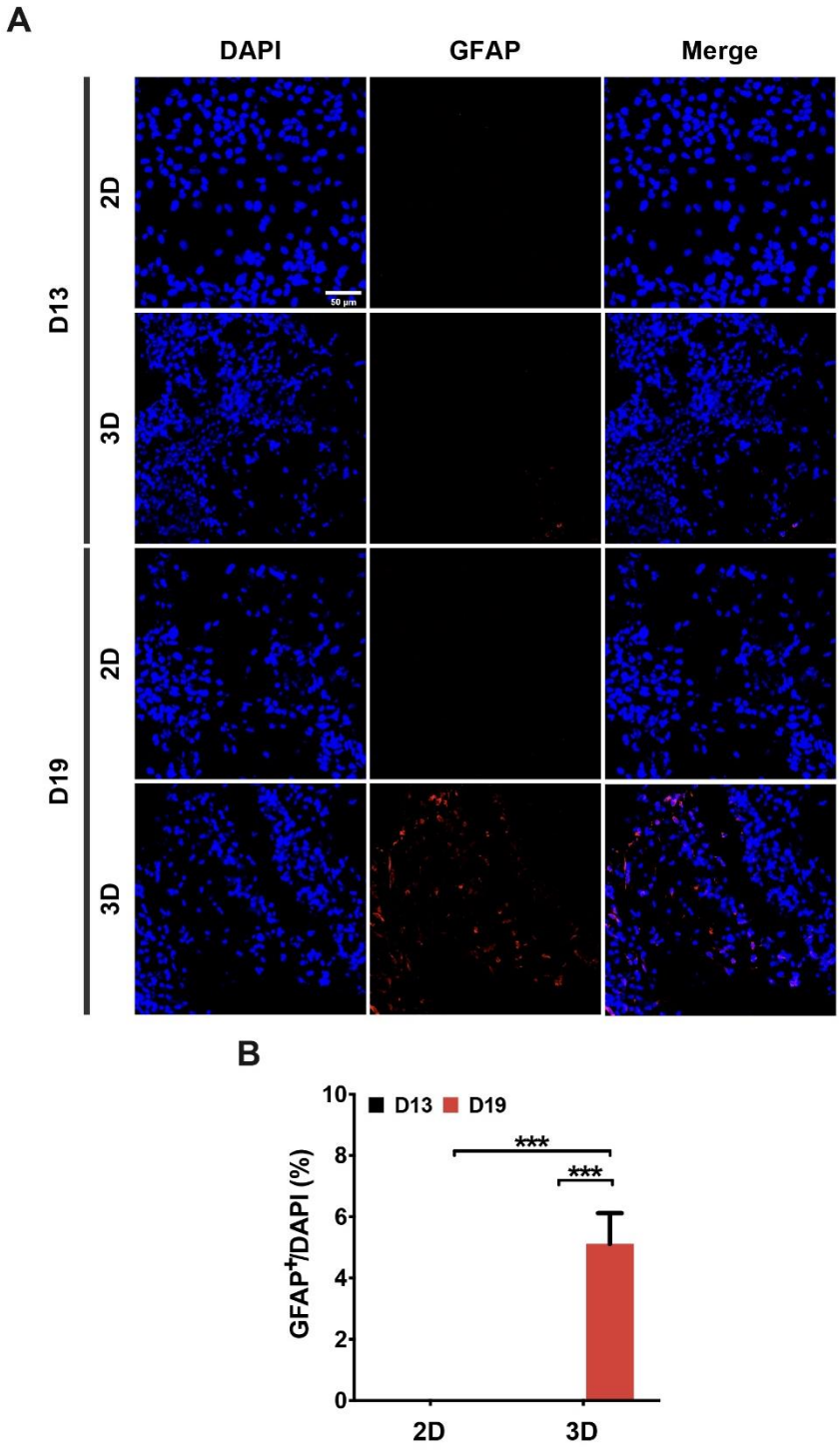

Appendix A11. Comparison of glial differentiation between 2D and 3D cultures. (A) Confocal fluorescent microscopy images indicating glial differentiation in 2D and 3D cultures stained for GFAP (red) marker on D13 and D19 respectively; Nuclei were counterstained with DAPI (blue); (B) Quantification of immunostaining results showing percentage positive staining of glial differentiation markers normalized to

DAPI for D13 and D19; Data is expressed as mean ± SD (n = 3), **$p < 0.01$, ***$p < 0.001$; Scale bar: 50 µm.

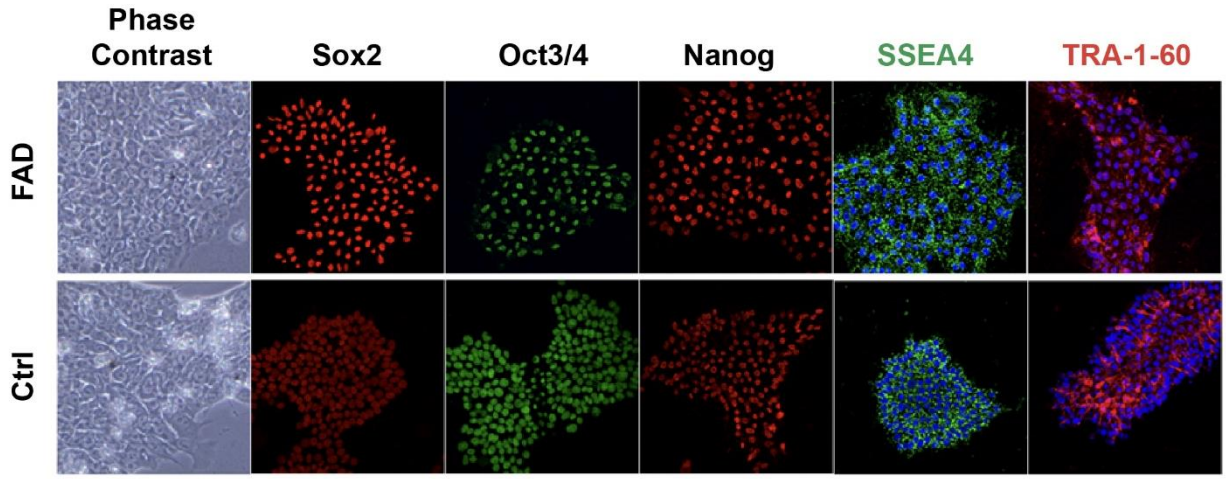

Appendix A12. Confocal fluorescent microscopy images indicating pluripotency of iPSCs. Fibroblast-derived iPSCs were immunostained and positive for various iPSC markers such as SOX2, OCT4, Nanog, SSEA4, and TRA-1-60; Nuclei were counterstained with DAPI (blue).

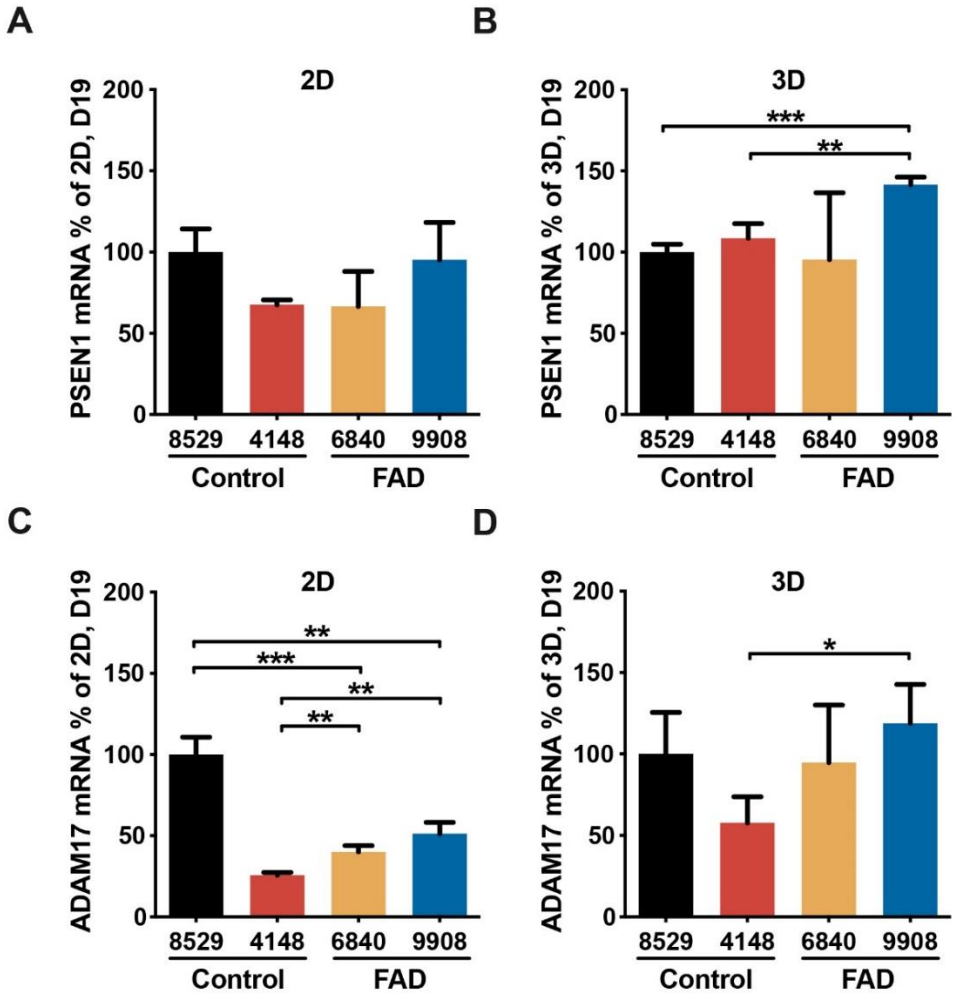

Appendix A13. 3D culture elevates expression of specific genes linked to the APP pathway. qPCR analysis of APP-linked pathway genes in D19 FAD-iPSC derived neurons; PSEN1 expression in (A) 2D culture and (B) 3D culture; ADAM17 expression in (C) 2D culture and (D) 3D culture; Data is expressed as mean ± SD (n = 3), *$p < 0.05$, **$p < 0.01$, ***$p < 0.001$.